

STATISTICAL THERMODYNAMICS AND HOMOGENEOUS
NUCLEATION OF ATOMIC MICROCLUSTERS

JOHN A. McINNES
DEPARTMENT OF PHYSICS
BEDFORD COLLEGE
UNIVERSITY OF LONDON

A THESIS PRESENTED IN FULFILLMENT OF THE REQUIREMENT
FOR THE DEGREE OF DOCTOR OF PHILOSOPHY OF THE
UNIVERSITY OF LONDON

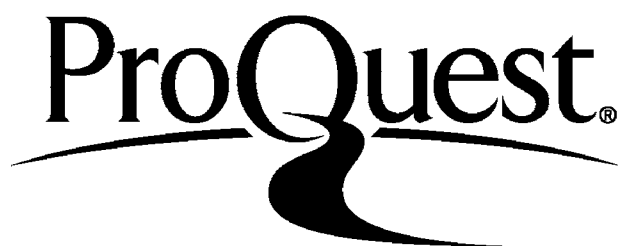
ProQuest Number: 10098962

All rights reserved

INFORMATION TO ALL USERS

The quality of this reproduction is dependent upon the quality of the copy submitted.

In the unlikely event that the author did not send a complete manuscript and there are missing pages, these will be noted. Also, if material had to be removed, a note will indicate the deletion.



ProQuest 10098962

Published by ProQuest LLC(2016). Copyright of the Dissertation is held by the Author.

All rights reserved.

This work is protected against unauthorized copying under Title 17, United States Code.
Microform Edition © ProQuest LLC.

ProQuest LLC
789 East Eisenhower Parkway
P.O. Box 1346
Ann Arbor, MI 48106-1346

Acknowledgements


This research has been carried out under the supervision of Dr. M.R. Hoare, Reader in Theoretical Physics, at Bedford College, University of London. I owe Dr. Hoare a great debt of gratitude for his guidance, friendship and encouragement over the last few years.

I am grateful to the advisory and operations staff both past and present at Bedford College Computer Unit, and especially to Dr. P. Pal for many hours of useful discussion and an extremely generous allocation of computing time. I would also like to thank Dr. J.A. Barker for advice on the computer generation of stereo images.

Acknowledgement of the facilities provided by the University of London Computing Centre, the Atomic Energy Research Establishment, Harwell, and the Quantum Chemistry Program Exchange, University of Indiana, U.S.A., is made, and thanks given to the Science Research Council, London, who financed this research.

January 1976

John A. McInnes



Abstract

A systematic investigation is carried out of the multiplicity of potential energy minima for up to 13 atoms interacting under central two-body potentials of Lennard-Jones and Morse type. The sets of minima discovered by various growth algorithms are believed to be virtually exhaustive of all possible N-atom isomers for the potentials used, with $N < 14$. These are classified according to the presence of crystallographic or non-crystallographic (5-fold) symmetry, and their energy distributions are statistically analyzed. It is shown that non-crystallographic configurations predominate in structures of both greatest and least binding energy. A striking result is the extreme sensitivity of the number of possible stable minima to variations in the range and softness of the pair potential. Thus, of no fewer than 988 energetically distinct minima for 13 Lennard-Jones (6-12) atoms, only some 36 are supported by the Morse ($\alpha = 3$) potential.

A vibrational analysis is performed for each configuration and the resulting vibrational frequencies are used to construct an approximation to the multi-configuration partition function (MCPF). This partition function is compared with the corresponding single-configuration partition function derived from the most stable cluster (SCPF). Thermodynamic properties for monatomic systems of rare gases, based on a rigid rotor/harmonic oscillator (RRHO) approach, are obtained via both single- and multi-configuration partition functions. It is seen that the validity of the single-configuration approximation depends strongly upon the distribution of isomer energies and less strongly upon the number of these isomers. From the computed partition functions equilibrium constants and relative concentrations are estimated, as

is the size of the critical nucleus at various pressures. The first five reduced virial coefficients are calculated and a correspondence between the equilibrium constants and Mayer's Cluster Integrals presented.

The use of graph theory in the enumeration of geometrically distinct isomers in 3 and higher dimensional spaces is noted, and adjacency matrices for some specific isomers constructed. Inspection of these matrices enables one to determine how compact the corresponding structures are.

Introduction

The development of fast digital computers has made possible a systematic investigation of the potential energy surfaces of microscopic N -atom clusters, with $N < 14$. A knowledge of the minima in these surfaces enables one to determine thermodynamic properties and equilibrium constants of very small microclusters by applying statistical mechanical techniques based on the rigid rotor/harmonic oscillator (RRHO) approximation (Hill (1960)). Ultimately one is able to determine the sizes of critical nuclei at various temperatures and pressures.

Several researchers (Reed (1952), Stogryn and Hirschfelder (1959), Andres and Boudart (1965), Courtney (1966), Buckle (1969), Burton (1970a,b,1971a,1972a,b), McGinty (1971,1972,1973), Bonissent and Mutaftschiev (1973) and Hoare and Pal (1971a,1972a,b,1975)) have investigated an N -body approach to the statistical mechanical properties of microclusters from a potential energy surface standpoint. Only the last three groups cited above, however, have attempted a systematic investigation of the potential energy surfaces of microclusters. McGinty (1971) has optimized argon clusters in f.c.c. and h.c.p. form by use of molecular dynamical techniques whilst Hoare and Pal have 'grown' clusters by starting with intuitively sound bases and proceeding along a well-defined growth pattern. Bonissent and Mutaftschiev (1973) have constructed different configurations for $N \leq 9$ by a similar process. The present work extends and modifies previous data for clusters ranging from the 2-atom dimer to the 13-atom icosahedron. Rouvray (1975) provides an interesting review of early attempts at isomer enumeration. Once all isomers for specified N have been

enumerated it becomes possible to construct a multi-configuration partition function (MCPF) and hence to calculate multi-configuration thermodynamic properties. McGinty (1972) has noted that the single-configuration partition function (SCPF) is only an approximation to the MCPF and recognizes that more information about the multiplicity of configurations is required to calculate more accurate values of cluster thermodynamic properties. Kristensen et al (1974) have investigated these properties using molecular dynamics; Eters and Kaelberer (1975) present thermodynamic data for very small aggregates of rare gas atoms which are obtained in a similar fashion. An outstanding advantage of computer simulations is that in principle all regions of phase space may be explored.

To represent the interatomic forces between the constituent atoms of a cluster the Lennard-Jones 6-12 potential is used in the major part of this thesis; a Morse ($\alpha=3$) potential is introduced to determine the effect of range and hardness of a potential on the isomer multiplicity. The multiplicity is seen to be extremely sensitive to the range and hardness of the applied potential. Each cluster is permitted to relax in all coordinates under both the Lennard-Jones and Morse potentials until it is mechanically stable in potential energy terms; the numbers, energies and energy distributions of the relaxed configurations provide a basis from which the MCPF may be calculated. The vibrational frequencies of the clusters are assumed to be harmonic and are determined by a method described by Gwinn (1971). The clusters are then treated as an ensemble of ideal gas molecules in thermodynamic equilibrium with the monomeric vapour in a heat reservoir; a full statistical mechanical treatment leads to the determination of cluster thermodynamic properties and equilibrium constants. Cluster symmetry

factors are required to determine the rotational sub-partition functions; these are dependent upon the assumption that the cluster acts as a rigid rotor. A basic premise in the RRHO approximation is that the atoms vibrate harmonically about their equilibrium positions. Although anharmonic effects and liquid-like properties become pronounced at reduced temperatures greater than approximately .3 (Burton (1971a)), harmonic calculations may still be undertaken at higher reduced temperatures if the calculations are viewed in the same perspective as the cell model of the liquid state (McGinty (1971)). Harmonic approximations have been used by Reed (1952) for small nitrogen clusters and by Burton (1969,1970a,b,1971b,1972a,b), McGinty (1971,1972,1973) and Hoare and Pal (1972a,b,1975), for rare gas clusters. Once the rotational and vibrational sub-partition functions have been constructed one may proceed to a multi-configurational treatment of the cluster thermodynamics. Comparison of the MCPF results and SCPF results is made - the SCPF is that partition function associated with the most stable cluster for each N-value. An estimate of the validity of the SC approximation may therefore be made. This comprehensive treatment leads to the evaluation of free energies, internal energies, entropies and heat capacities, whilst the principle of detailed balance enables one to estimate relative equilibrium concentrations and equilibrium constants. Configurational thermodynamic properties, relevant to the theory of the glass transition (Kauzmann (1948), Goldstein (1972)), are calculated in order to determine whether the atomistic model presented in this work is able to model the glass transition.

The size dependence of low temperature heat capacities has been studied by Fröhlich (1937), Montroll (1950), Burton (1970a,1971a)

and Hoare and Pal (1972a,1975). Burton has calculated the heat capacities of small argon clusters by invoking the concept of surface energies; Hoare and Pal approached the problem from an atomistic viewpoint. Jura and Pitzer (1952) have studied the heat capacity in cubic configurations by considering standing waves in slabs of elastic cube. In the present work the vibrational heat capacities of the rare gases are shown to be non-linear in T^3 at very low temperatures.

Thermodynamic stabilities in terms of Gibbs free energy may be combined with the kinetic approach to homogeneous nucleation (Farkas (1927)) which with the previously mentioned condition of mechanical stability enables the relative stabilities of the various isomeric forms to be determined. Thermodynamic stability implies the determination of the least extravagant cluster in free energy terms - thus from the stationary values of the Gibbs free energy of formation determined via the MCPF the size of the critical nucleus may be estimated for various gases at different temperatures and pressures. Calculation of the free energy of formation from the MCPF bypasses any need to extend the classical concepts of surface free energies to clusters of microscopic proportions. A link is therefore formed between classical nucleation theory (Gibbs (1906), Becker and Döring (1925), Volmer and Weber (1925) and Zeldovich (1942) and an explicit treatment of the mechanics of microscopic N -atom clusters which as yet seems not possible for clusters containing more than a few atoms. The classical theory predicts results compatible with experimental cloud chamber studies but the extension of this theory to the size range studied here, i.e. $2 \leq N \leq 13$, becomes invalid when one attempts to integrate the concepts of surface energies into a truly microscopic approach.

Theoretical studies on nucleation processes are centred around the premise that in the limit the bulk stable phase is part of an infinite crystal, and consequently imply areas of local or non-local order. X-ray diffraction studies show an increase in order as a liquid approaches its freezing point; Gingrich (1943) has provided evidence of ordered structures in argon whilst Farges et al (1973) have indicated the existence of local solid-like symmetries in clusters of argon formed by expansion through a nozzle at supersonic velocities. A similar technique has been used by Leckenby and Robbins (1966), Milne and Greene (1967) and Milne, Vandegrift and Greene (1970) to determine the equilibrium constants of microscopic clusters. An atomistic theory such as that proposed by Walton (1962) becomes necessary to explain the structure of microcrystallites, in which it is probable that ordered regions exist which have no long-range order or any relationship to regular lattice structures.

The virial coefficients of a Lennard-Jones gas may be expressed in terms of cluster equilibrium constants (Woolley (1953), Leckenby and Robbins (1968), Spurling and Mason (1969)); estimates of the first five reduced coefficients are determined in the present work. Hirschfelder et al (1954) have compiled extensive tables of reduced second and third virial coefficients, whilst Barker (1975) and Barker et al (1966) have published values of the second, fourth and fifth reduced coefficients. The expansion coefficients of Kihara (1951) enable the third reduced coefficients to be calculated. Comparisons of the coefficients determined in this thesis are made with the published data. By considering the virial equation of state a relationship between the Mayer cluster integrals (Mayer and Mayer (1940)) and the virial coefficients is established.

Following Randić (1974) adjacency matrices for some distinct configurations are constructed and a description of a graph-theoretic procedure which enables one to determine the number of distinct graphs (clusters) on N vertices (atoms) in three and higher dimensional spaces is presented. Gutman et al (1975), in Part XII of a series of papers analyzing the topological properties of conjugated compounds by a similar approach, includes references to previous works in this series which amplify the uses of graph theory in theoretical physics and chemistry.

Summary of Arrangement of Thesis

Growth schemes; L-J optimizations; multiplicity of L-J isomers with energy statistics and distributions; Morse optimizations and isomer multiplicity.

Harmonic oscillator vibrational analysis; construction of vibrational SCPF and MCPF for neon, argon, krypton and xenon clusters. Vibrational thermodynamic properties of finite clusters; comparison of MCPF data and SCPF data; calculations of relative equilibrium concentrations and equilibrium constants.

Gibbs free energies of formation; estimates of critical nuclear sizes; approximations to L-J virial coefficients; the uses of graph theory in isomer enumeration problems.

<u>Contents</u>	Page
Acknowledgements	2
Abstract	3
Introduction	5
Chapter 1	
1.1 The Potential Energy Surface	15
1.2 Growth Patterns	22
1.3 Optimization Techniques	30
1.4 Minimization by the Method of Conjugate Gradients	33
Chapter 2	
2.1 Lennard-Jones Clusters: $2 \leq N \leq 13$	35
2.2 Minimal Energy Configurations	36
2.3 Tetrahedral Isomers	43
2.4 Octahedral Isomers	45
2.5 Bernal Structures and the Cube	49
2.6 Discussion	50
Chapter 3	
3.1 Amorphous Solids and the Glassy State	59
3.2 The Multiplicities of Morse ($\alpha=3$) Isomers	60

Chapter 4

4.1	The Vibrational Motion of Clusters	66
4.2.1	The Transformation to Normal Coordinates	67
4.2.2	The Kinetic Energy Matrix \underline{T}	68
4.2.3	The Potential Energy Matrix \underline{V}	69
4.2.4	Diagonalization of the \underline{V} Matrix	69
4.3	The Frequency Spectra of Real Systems	70
4.4	Cluster Zero Point Energies	76
4.5	The Maximum Number of Vibrational Levels of L-J 6-12 Dimers	79

Chapter 5

5.1	Basic Statistical Thermodynamics	82
5.2	The Single-Configuration Approximation	83
5.3	The Multi-Configuration Approximation	85
5.4	Equilibrium Constants and Relative Equilibrium Concentrations	88

Chapter 6

6.1	Introduction	91
6.2	Vibrational Single-Configuration Internal Energies	91
6.3	Vibrational Single-Configuration Free Energies	92
6.4	Vibrational Single-Configuration Entropies	95
6.5	Vibrational Single-Configuration Heat Capacities	102
6.6	Configurational Thermodynamic Properties	112

Chapter 7

7.1	Introduction to the Multi-Configuration Approach	117
7.2	Vibrational Partition Functions	118
7.3	Vibrational Free Energies	122
7.4	Vibrational Internal Energies	125
7.5	Vibrational Entropies	127
7.6	Vibrational Heat Capacities	130
7.7	Conclusion	131

Chapter 8

8.1	Introduction	133
8.2	Equilibrium Constants	133
8.3	Discussion of Tables 35 to 38	134
8.4	Relative Equilibrium Concentrations	141
8.5	Discussion of Relative Equilibrium Concentrations	145

Chapter 9

9.1	An Introduction to Nucleation Theory	149
9.2	Free Energies of Formation of Atomic Clusters	153
9.3	Critical Nuclei	156

Chapter 10

10.1	Introduction	161
10.2	Virial Coefficients	162
10.3	Results and Discussion	165
10.4	Mayer Cluster Integrals	169

Chapter 11	
11.1 The Uses of Graph Theory in Isomer Enumeration	170
11.2 Adjacency Matrices: their Classification and Ordering	171
11.3 Adjacency Matrices of Some Specific Structures	173
11.3.1 The Dimer	173
11.3.2 The Equilateral Triangle and Linear Chain	173
11.3.3 The Tetrahedron	174
11.3.4 Some 5-Vertex Structures	174
11.3.5 Some 6-Vertex Structures	176
11.3.6 The Distorted Pentagonal Bipyramid	177
11.3.7 The Cube	178
11.3.8 The Icosahedron	178
11.4 The Generation of the Complete Set of Anisomorphic Graphs on a Given Number of Vertices	180
References and Bibliography	183
Appendix A	195
Description of Major Computer Programs and Auxiliary Programs	
Appendix B	200
Vibrational Multi-Configuration Thermodynamic Functions	
Appendix C	204
Cluster Distributions in Configuration Space	
Appendix D	206
Standard Gibbs Free Energies of Formation	

Chapter 1

1.1 The Potential Energy Surface

The potential energy of an N-atom cluster located in coordinate space by the vectors $\{\underline{r}_1, \underline{r}_2, \dots, \underline{r}_N\}$ may be expressed in terms of some applicable potential energy function $V(\underline{r}_1, \underline{r}_2, \dots, \underline{r}_N)$, where this function contains both repulsive and attractive components, with the latter tending to draw the N-atoms into some stable compact configuration. In this work the potential energy surface is taken to be the resultant of central 2-body forces, enabling the potential energy to be written

$$V(\underline{r}_1, \underline{r}_2, \dots, \underline{r}_N) = \sum_{i=1}^{N-1} \sum_{j>i}^N V(|\underline{r}_i - \underline{r}_j|) \quad (1.1)$$

where $V(r)$ is an appropriate potential. In the major part of this thesis $V(r)$ is chosen to be the Lennard-Jones 6-12 potential applicable to rare gas clusters.

i.e.

$$\tilde{V}(r) = 4\epsilon \left[\left(\frac{\sigma}{r} \right)^{12} - \left(\frac{\sigma}{r} \right)^6 \right] \quad (1.2)$$

where σ is that value of r for which $\tilde{V}(r) = 0$ and ϵ is the depth of the potential energy well.

Equation (1.2) may be scaled such that both the pair energy (ϵ) and the equilibrium distance ($2^{1/6}\sigma$) are equal to unity. This leads to

$$\left. \begin{aligned} V(r) &= \frac{1}{r^{12}} - \frac{2}{r^6} \\ V'(r) &= -\frac{12}{r^7} \left[\frac{1}{r^6} - 1 \right] \\ V''(r) &= \frac{12}{r^8} \left[\frac{13}{r^6} - 7 \right] \end{aligned} \right\} \quad (1.3)$$

where ' and " signify 1st and 2nd derivatives with respect to distance respectively. These equations are presented in Figure 1. This scaling removes any necessity to refer to particular atomic aggregates by name, whilst enabling the potential energy of any particular species at absolute zero to be easily obtained by insertion of the appropriate values of σ and ϵ . The L-J 6-12 potential represented by equation (1.3) is merely a specific case of the more general Mie potential, given in equation (1.4):

$$V(r) = \frac{1}{(n-m)} \left[\frac{n}{r^m} - \frac{m}{r^n} \right] \quad (1.4)$$

Subsequently, the potential energy surface is investigated using a long-range Morse potential, equation (1.5) below:

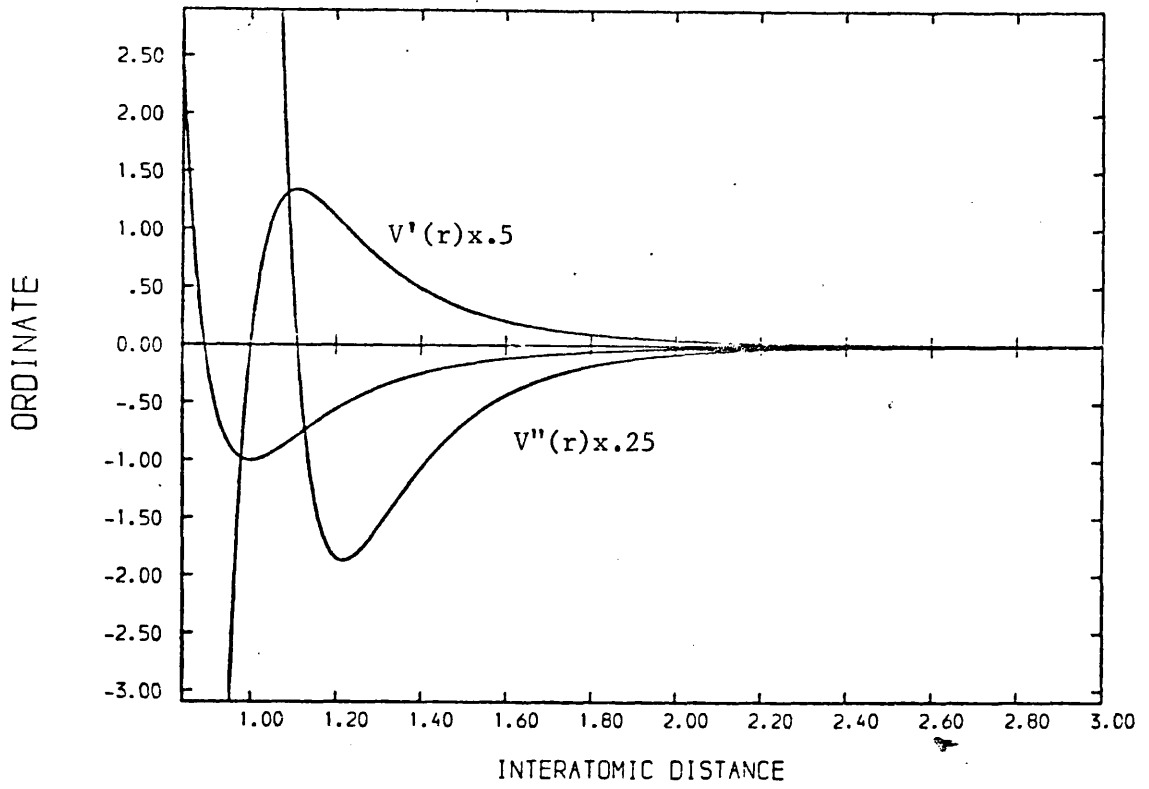
$$V(r) = [1 - \exp\{3(1-r)\}]^2 - 1 \quad (1.5)$$

Although the functional form of the potential in (1.1) may be specified and evaluated at any point almost nothing may be said about the location and characteristics of these minima in the potential energy surface embedded in a $(3N-5)$ -dimensional space. In general sufficient conditions for the existence of at least one stable configuration are that $V(r)$ is:

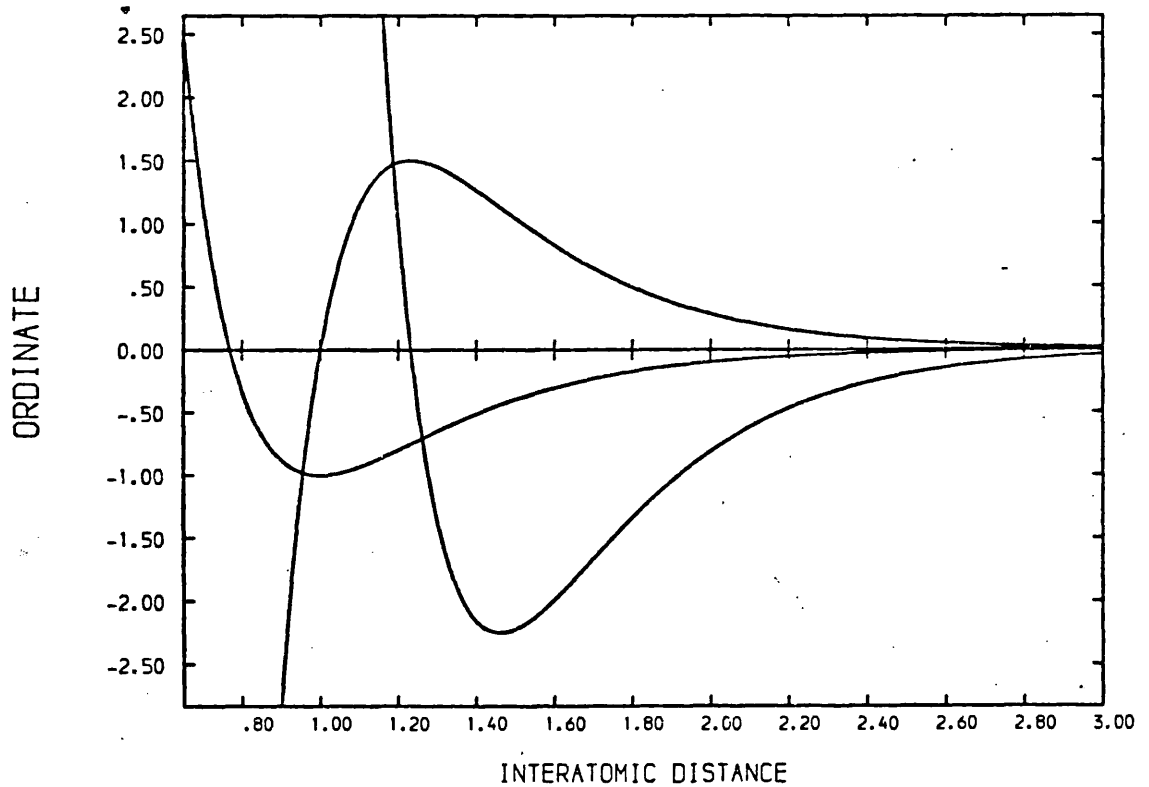
- (i) differentiable
- (ii) bounded below
- (iii) convex at infinity
- (iv) positive infinite at $r = 0$.

These conditions ensure the existence of a greatest lower bound for $V\{\underline{r}_1\}$. The polyhedron formed in co-ordinate space corresponding

Figure 1



L-J POTENTIAL ; 1ST AND 2ND DERIVATIVES

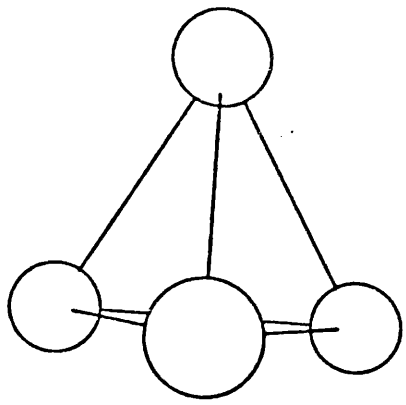


MORSE POTENTIAL ; 1ST AND 2ND DERIVATIVES

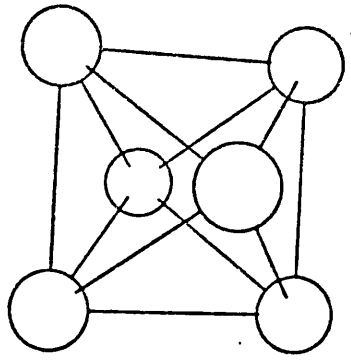
to the set of vectors $\{\underline{r}_i\}$ evidently may be considered as $N!$ points in configuration space differing only in the numbering of the atoms.

One inescapable fact is that the potential energy surface contains a considerable number of local minima, some of which correspond to stable isomeric forms, whilst others represent metastable configurations. At these latter 'saddle-point' configurations atoms 'pop-over' from one configuration to another: the effective dimensionality of these saddle-points depends on the number of co-operatively-moving atoms involved. Internal popping-through motions in general correspond to saddle-points of higher dimensionality than those associated with surface popping-through, since the distortion of internal neighbouring regions involves the co-operative movements of a greater number of atoms than does surface distortion.

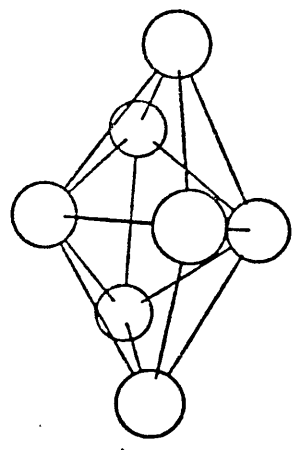
The precise number of local minima is shown to be extremely sensitive to the range and hardness of the potential function used, but one may say with certainty that at each local minimum all partial derivatives $(\partial V/\partial \xi_i)$ of the potential function vanish, with all 2nd derivatives $(\partial^2 V/\partial \xi_i \partial \xi_j)$ being positive definite, where $\{\xi_i\}$ are the bond lengths. The principal radii of curvature of any particular minimum in the potential energy surface may then be obtained from the eigenvalues of the Hessian matrix of 2nd derivatives; physically these eigenvalues correspond to the normal mode frequencies of vibration governing small motions. Only for $2 \leq N \leq 4$ is it possible to give unequivocal minimum configurations: these are, for $N = 2, 3$ and 4 respectively:- the dumb bell, the equilateral triangle, and the regular tetrahedron. For $N \geq 5$ the problem becomes non-trivial



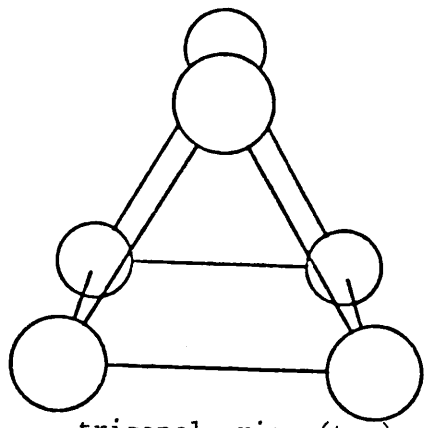
tetrahedron



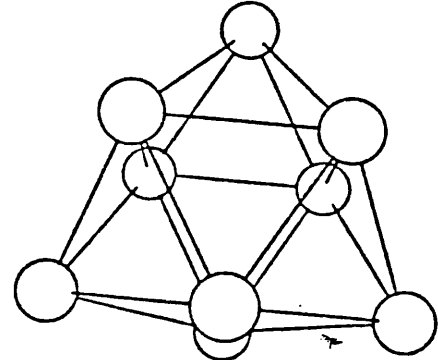
octahedron



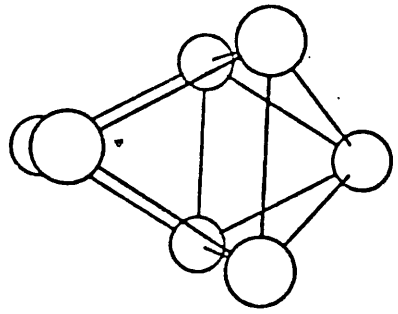
pentagonal bipyramid



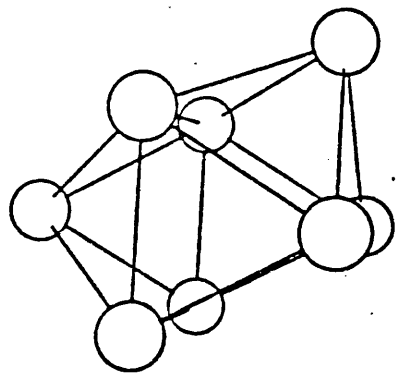
trigonal prism (t.p)



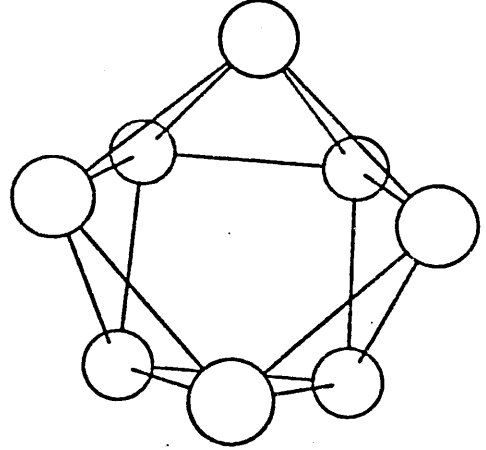
t.p + 3 caps



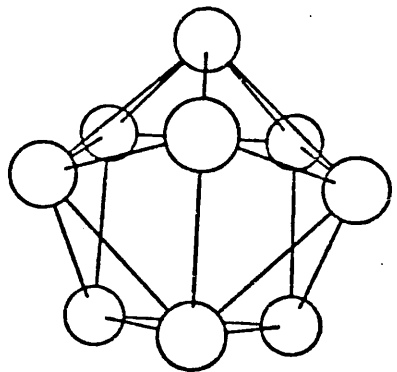
t.p + 1 cap



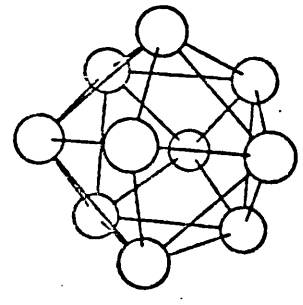
t.p + 2 caps



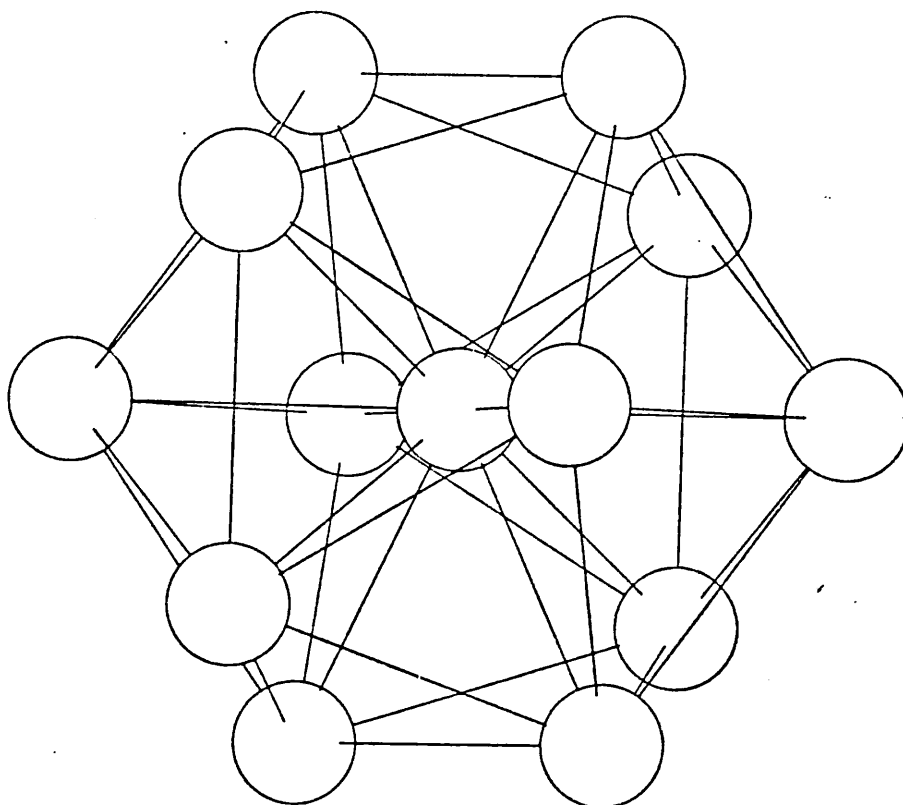
square antiprism (S.a)



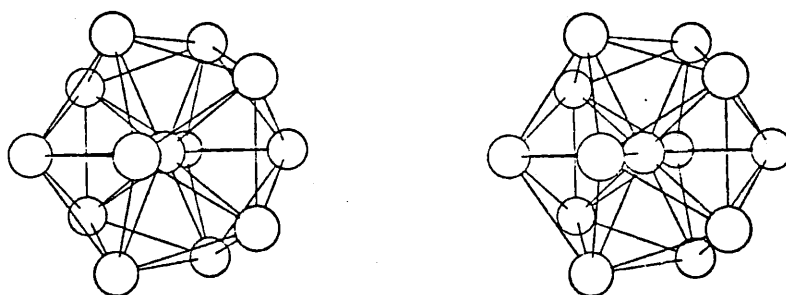
S.a + 1 cap



S.a + 2 caps



13-atom icosahedron



Stereo icosahedral pair

in that the number of interatomic distances $\left[\frac{1}{2}N(N-1)\right]$ exceeds the number of co-ordinates required $[3N-6]$. Early attempts to locate possible minima followed the tradition of sphere-packing (e.g. Coxeter (1961); Fejes (1964)), with investigations into the close-packing of hard-spheres being carried out by Boerdijk (1952), Bagley (1965), Nicholas (1968) and van Hardeveld and Hartog (1969). Werfelmeier (1937) precedes all these authors in his description of sphere-packing experiments. Adams and Matheson (1972) have used a computer to generate random close-packing of hard-spheres. Hoare and Pal (1971a) attempted a systematic enumeration of all possible structures with $N \leq 9$, as did Bonissent and Mutaftschiev (1973). However, Hoare and Pal permitted growth of an $(N+1)$ -atom cluster only via the most stable N -atom cluster: this procedure leads to incorrect isomer multiplicities for $N \geq 8$, a fact pointed out by Bonissent and Mutaftschiev (1973). It becomes necessary to find an algorithm which is capable of discovering at least a large proportion of minima for $N > 5$, if not all of them. The key to such an algorithm lies in the generation of hard-sphere clusters (loc. cit) in rigid contact. By the addition of an $(N+1)$ th sphere to a surface facet of an N -hard-sphere cluster it is possible to locate regions of configuration space which may produce a local minimum energy. Full minimization of the potential energy function for the $(N+1)$ -hard-sphere cluster confirms or denies the existence of this particular local minimum. In such a fashion hard-sphere clusters may be 'grown' in the computer from some appropriate base structure to locate possible minimal regions of configuration space, and the properties of these regions of space investigated.

1.2 Growth Patterns

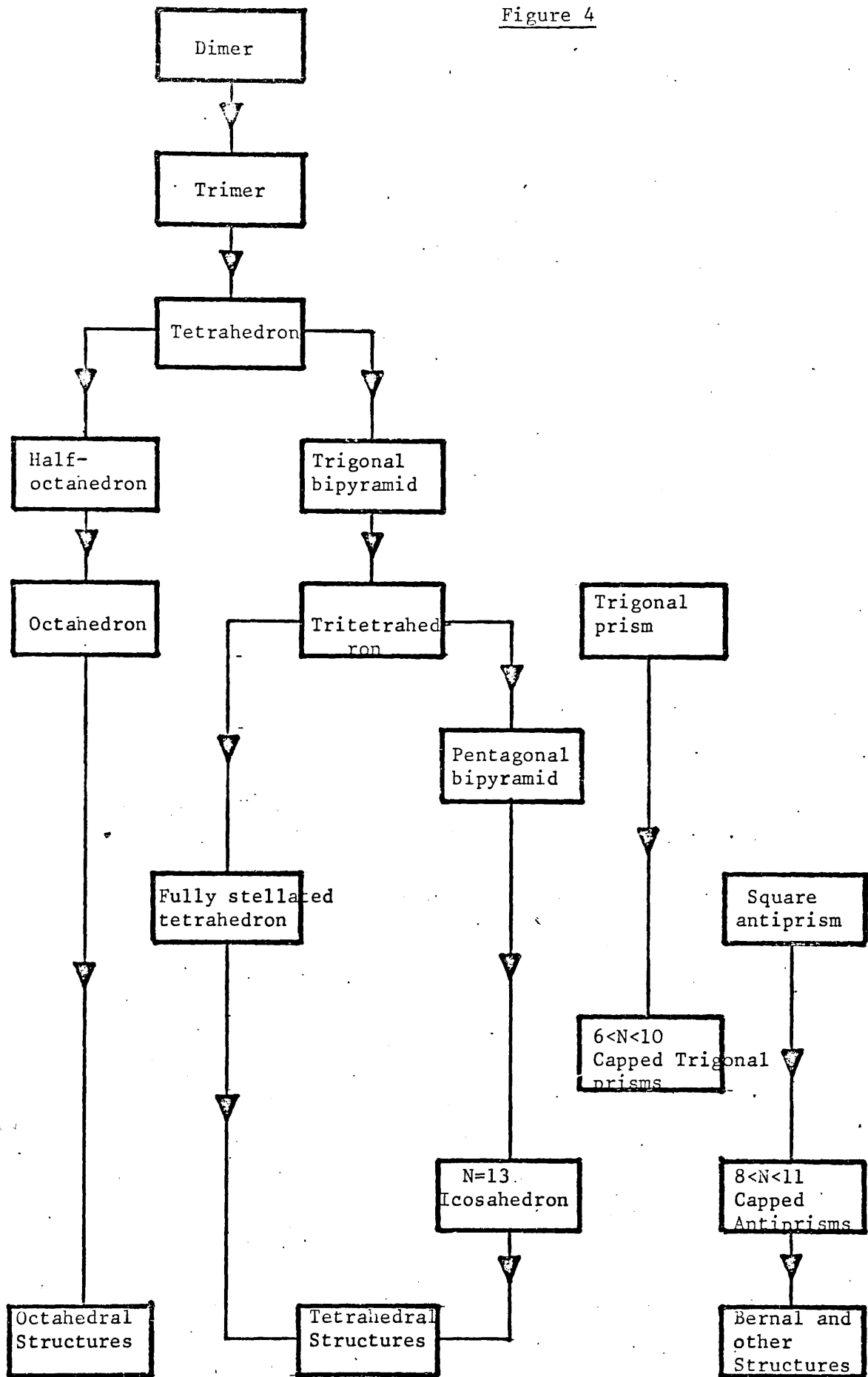
Hard sphere clusters are grown from 2 basic non-lattice 'seed-structures':

- (i) the 4-atom tetrahedron and
- (ii) the 6-atom octahedron.

The pentagonal (7-atoms) seed, referred to by Hoare and Pal (1971a), spontaneously appears from the tetrahedral growth scheme and consequently pentagonally grown structures are absorbed into the tetrahedral group. Other seed-structures used include the Archimedean antiprism plus one or two caps, and the fully-capped trigonal bipyramid. These other seeds generate clusters which are not accessible via the tetrahedral or octahedral routes, and have been chosen from Bernal's list of canonical polyhedra (Bernal (1959), (1960), (1964)). All of the previously mentioned seed-structures are illustrated in Figure 2. The 8-atom regular cube is shown to be unstable under a Lennard-Jones potential, collapsing to a tetrahedral structure. Consequently it is not used as a seed structure.

A systematic enumeration of all possible N-atom structures involves the growth of minimal structures from all the basic seeds by making all possible positionings of additional atoms on their surfaces. Every N-atom minimum obtained must then be examined for uniqueness and geometrically indistinguishable structures deleted from the list of bases for the next generation. A sufficient condition for the geometric uniqueness of two clusters is that the distance matrices $[D_{ij}] = [|\underline{r}_i - \underline{r}_j|]$ should be different for some choices of numbering. A more easily computed, although weaker, condition for the same is that the diagonalized inertia tensors in

Figure 4



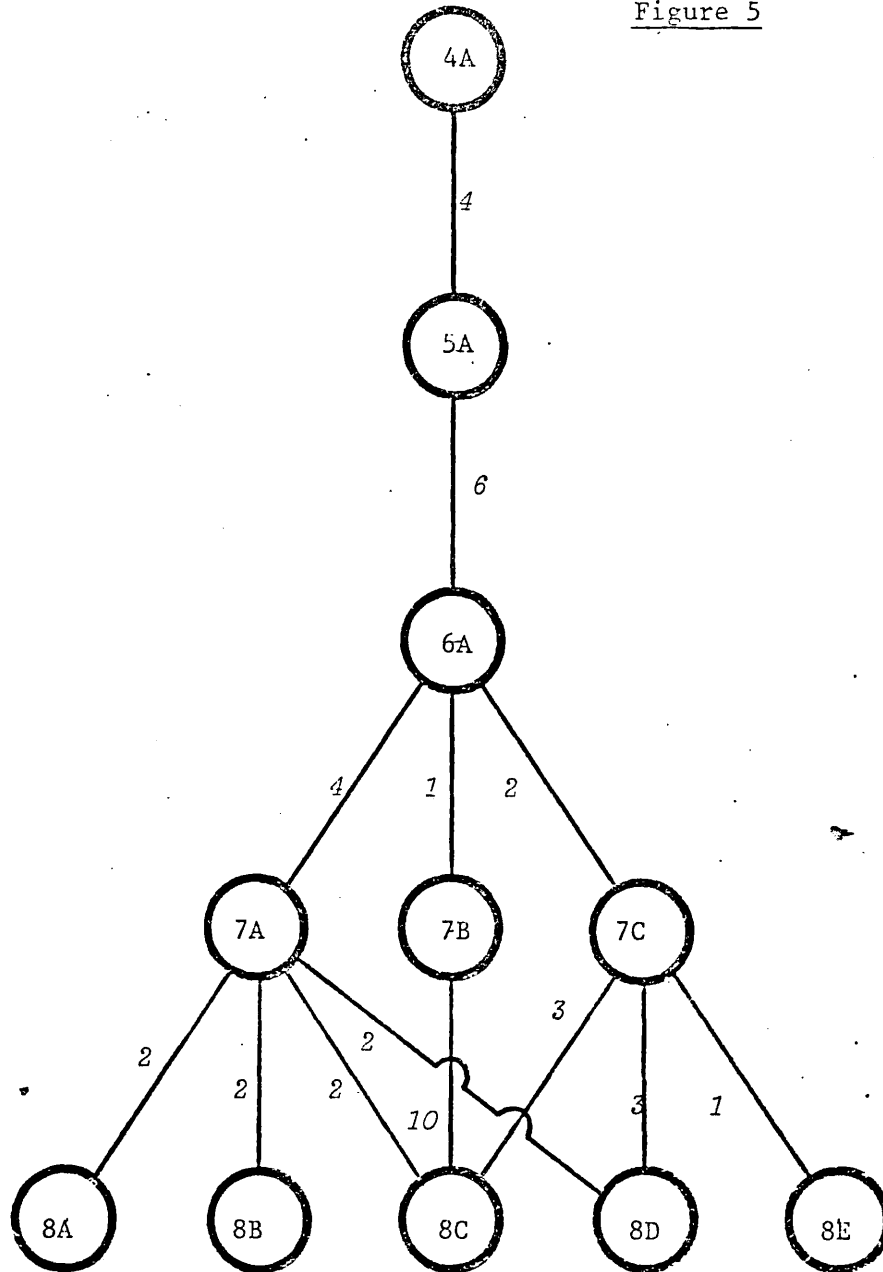
The Genesis of Growth

the centre of mass reference frame of each of the clusters should differ. These conditions, however, do not distinguish between enantiomorphic pairs which occur for $N \geq 6$. To test whether a structure possesses a plane of symmetry (and therefore does not possess an enantiomorph) we may use the fact that, if a plane or planes of symmetry is (are) present, two of the principal axes of the inertia ellipsoid will lie in this plane (one of these planes), (Symon (1967)). The absence of a plane of symmetry is therefore established by testing the symmetry of the 3 planes determined by the principal axes.

The following growth algorithm may then be used (Hoare and McInnes (1976)).

- 1) Choose a seed-structure of N -atoms and relax to its minimum in the required potential. Keeping this configuration fixed, test the structures obtained by adding an additional atom to each surface facet in turn. Store all geometrically distinct configurations.
- 2) Relax these configurations to their true $(N+1)$ atom minimum. Confirm that they remain distinct and delete any which collapse to previously generated structures.
- 3) Take each of the $(N+1)$ atom structures discovered in this way and repeat the procedures under 1) and 2) above, using it in place of the seed-structure.
- 4) Terminate the sequence when computing time becomes unreasonable. Pick a new seed-structure and restart, checking each new minimum for distinctness against the full list for all previous sites.

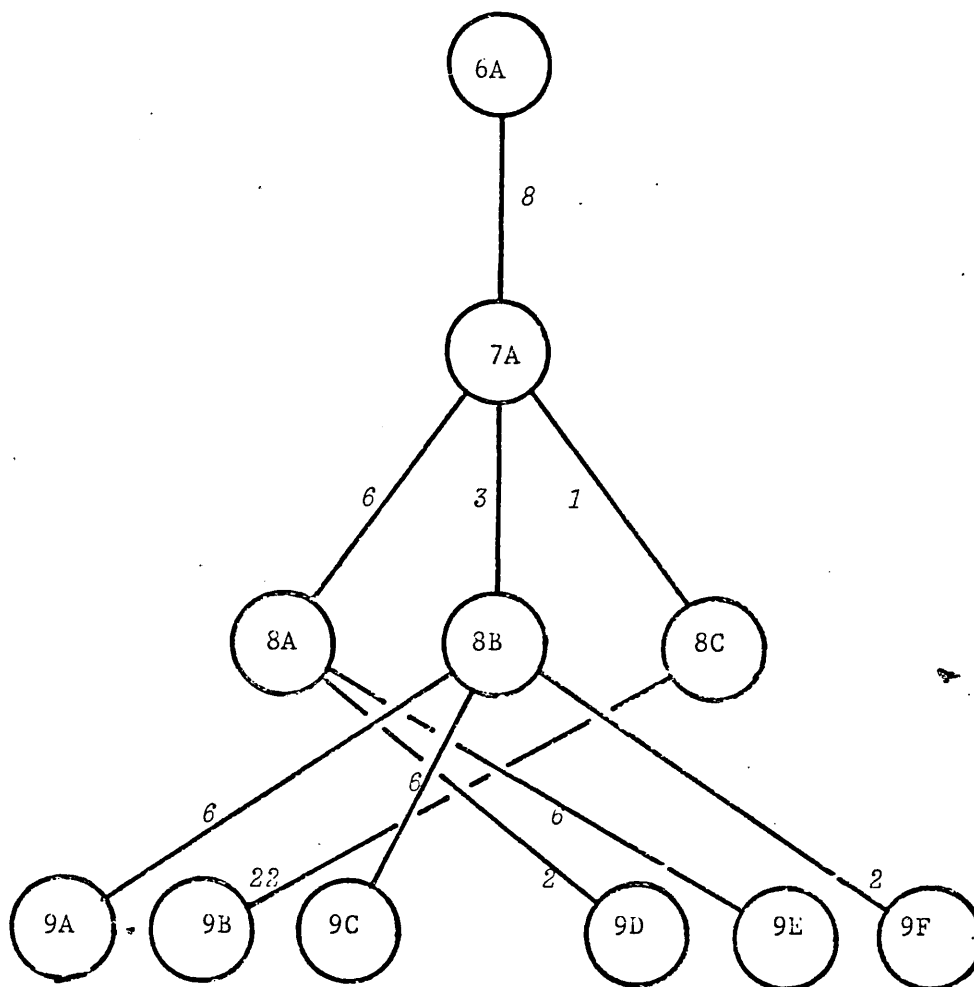
Figure 5



Interrelationships for Tetrahedral Minima of up to 8 L-J Atoms

The italic numbers identify the number of equivalent surface facets for a particular growth step; the letters in each circle identify the structures. 4A(tetrahedron); 5A(double tetrahedron); 6A,7A,8A (Boerdijk spiral); 7B (pentagonal bipyramid); 7C (incomplete stellated tetrahedron); 8B (irregular figure); 8C (pentagonal bipyramid + 1); 8D (skewed tetrahedral figure); 8E (fully stellated tetrahedron).

Figure 6



Inter-relationships for Octahedral Minima of up to 9 L-J

Atoms

The italic numbers identify the number of equivalent surface facets for a particular growth step; the letters in each circle identify the structures. The various structures may be identified by reference to Figure 9. Structure A is more stable than structure B, which is more stable than structure C, etc.

A flow chart for this growth algorithm is presented in Figure A1, Appendix A.

Table 1 contains the basic geometrical properties of the two major seed structures used, and of some very compact structures.

TABLE 1

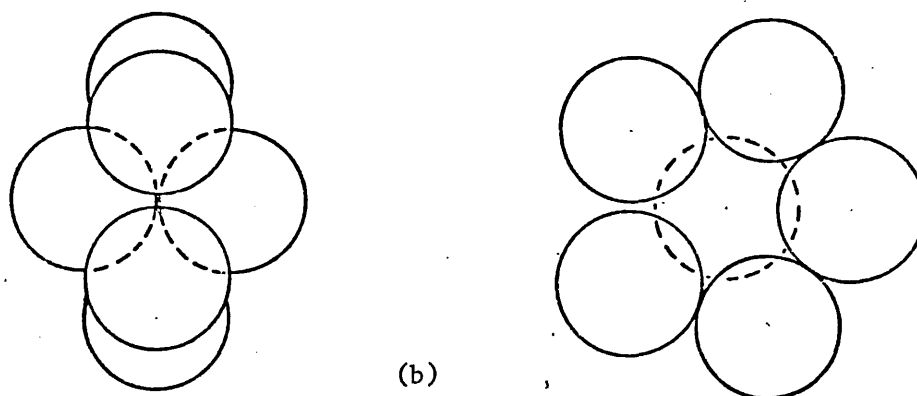
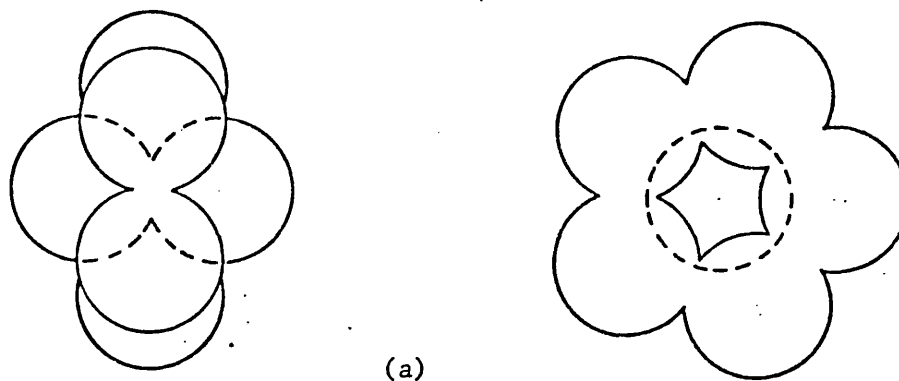
<u>Structure</u>	<u>N</u>	<u>No. of Vertices</u>	<u>No. of Faces</u>	<u>Symmetry Group</u>	<u>Symmetry Operations</u>	<u>Description of Structure</u>
Tetrahedron	4	4	4	T_d	12	Spherical top
Octahedron	6	6	8	O_h	24	Spherical top
Pentagonal Bipyramid	7	7	10	D_{5h}	10	Symmetric top
Icosahedron	13	12	20	$I_n(Y_n)$	60	Spherical top

Using this algorithm the L-J 6-12 minima for $N \leq 13$ are generated. At $N=13$ there exists the important icosahedral configuration with 12 atoms grouped around a central 13th. This structure, shown in Figure 3, provides another possible growth seed, although all structures based on a 13-atom icosahedron are accessible from the 4-atom tetrahedral seed, in the same way that pentagonal structures based around the 7-atom pentagonal bipyramid, shown in Figure 2, are themselves accessible from the tetrahedral seed. Hoare and Pal (1972b) have investigated the geometry of spherical face-centred-cubic clusters, based on the 6-atom octahedron, although all but one of their structures are larger than those considered here. Closely allied to the octahedral clusters are the cuboctahedral unit cell configuration and the hexagonal close packed structure. However, as Burton (1970, 1971a), McGinty (1971) and Hoare and Pal (1972b) have shown, these structures relax into the icosahedral configuration

under a Lennard-Jones 6-12 potential. Burton's relaxation appears incomplete as although his final structure possesses full icosahedral symmetry it is extended in the radial direction, leading to a lower binding energy/atom than that calculated by Hoare and Pal (1972b). This method of growing spherical clusters was introduced by Benson and Shuttleworth (1951) and extended by van Hardeveld and Hartog (1969) in their investigation of the variation in the number of surface atoms on metal crystals of differing structures, and in the work of Nishioka et al (1971) who have calculated the replacement partition functions of small f.c.c. crystals. Unlike the interpretation of tetrahedral growth given by Hoare and Pal (1971a), who defined a growth path bypassing the 7-atom pentagonal bipyramid, tetrahedrally grown clusters defined in this work include all clusters able to be grown from the 4-atom tetrahedral seed. Figure 4 illustrates the relationships between the various seed-structures and their corresponding families, whilst Figures 5 and 6 identify the first stages in the tree-like interrelationships of minima of the tetrahedral and octahedral families respectively.

It is of interest to note that the enumeration of hard spheres in contact becomes considerably protracted due to the existence of clearance regions inherent in hard-sphere packings, which arise through the space-filling deficit of tetrahedra. When a realistic potential is imposed and the hard-sphere structures 'relaxed' these clearance regions 'heal-up', often producing symmetric pentagonal motifs. Figure 7 illustrates the healing-up of the clearance region present in the 7-atom pentagonal bipyramid structure. Permutations of these clearance gaps around a structure lead to several additional stable structures, all of which relax to an

Figure 7



The Clearance Gap in Hard-Sphere Isomers

The clearance region shown above (b) arises when seven hard spheres are packed in an imperfect pentagonal bipyramid. On relaxation the gap of $7^{\circ} 20'$ heals up and a configuration with perfect D_{5h} symmetry results.

identical structure when a potential such as the Lennard-Jones 6-12 is applied. Hard sphere enumeration is also possible by graph theoretic methods (see Chapter 11), related to the simpler problem of counting 'animals' of N adjacent points on a lattice (Harary (1967)), but a greater physical insight is provided by the growth sequences described above.

Once a set of hard-sphere clusters has been generated it is necessary to minimize equation (1.1), i.e. the cluster potential energy function, for each member of this set. Procedures to minimize functions of many variables are described in the following section.

1.3 Optimization Techniques

The optimization procedures used to minimize equation (1.1) may be considered as falling into three major groups.

(i) The energies of various simple lattice structures are derived by summing the interatomic potential energy contributions for some realistic potential. In their estimations of the surface energies of f.c.c. and b.c.c. crystals Benson and Shuttleworth (1951), and Nicholas (1968) have calculated lattice energies in this way. Nishioka et al (1971) also followed this procedure in the first stages of their calculations of the replacement partition functions of small f.c.c. crystals.

(ii) By scaling the lattice constants and allowing atoms positioned at some preselected lattice sites to relax within the overall symmetry, a search for an energy minimum may be made. Allpress and Sanders (1970), in their study of a number of metallic f.c.c. clusters,

were the first to apply this method. Burton (1970a) carried out similar calculations but allowed independent relaxation of different layers to accommodate the experimentally well-known phenomenon (Vook and Otoono (1967)) of surface relaxation. This method of relaxed lattice optimization, although an improvement on the fixed lattice procedure described in (i) above, is liable to disguise the fact that the 'final' structure obtained may be physically non-realistic with some potential functions. It is possible for a valley to exist in the energy surface which is only accessible by permitting completely free relaxation in all the variables. A notable example of this type of structure is the simple 8-atom cube: this structure, when allowed to relax freely under a Lennard-Jones 6-12 potential, has insufficient attraction along the diagonals to maintain full cubic symmetry, and consequently collapses to a tetrahedral structure.

(iii) By removing all restraints and permitting full relaxation in all $3N$ variables the cluster has the freedom of complete rearrangement of its constituent atoms. In this rearrangement initial symmetries may dissolve and final completely different symmetries may spontaneously emerge. Since in any system in which atoms nucleate in space it is possible for any initial configuration to be present, full relaxation is necessarily required to reach the true minimum in the potential energy surface, unless this minimum coincidentally possesses an initial lattice symmetry. Sinclair and Pollard (1970), in their studies of the equilibrium configurations of arrays near crystal defects, used a sophisticated full relaxation technique, whilst McGinty (1971) relaxed compact f.c.c. lattice configurations by moving each atom in the direction of force acting

on it through a distance proportional to this force. Burton (1971a) and Hoare and Pal (1971a,1971b,1972a,1972b) have systematically optimized f.c.c. clusters and amorphous packings respectively. Barker, Hoare and Finney (1975) have optimized the inner 999-atom core of the Bernal random close-packed structure: this optimization, involving 2997 variables, appears to involve the greatest number of variables used in a full relaxation procedure to date. Bonissent and Mutaftschiev (1973) have also used a full relaxation technique in a study of the stability of very small clusters.

With either an increasing number of atoms or an increasing variety of different isomeric forms containing the same number of atoms it becomes essential to discover faster and more efficient full relaxation procedures. Hoare and Pal (1971a,1971b,1972a,1972b) used a simple but slow sectioning procedure (Wilde and Brightler 1967), which is not appropriate to the minimization of very large multiplicities of isomers. Possible minimization methods include the method of steepest descent (Householder (1953)) and the conjugate gradient minimization technique (Fletcher and Powell (1963), Fletcher (1972)), the latter having been developed from a procedure described by Davidon (1959). This latter method, used also by Barker, Hoare and Finney (1975), is utilised in this work. It is superior to the method of steepest descent in that the search direction on each iteration contains an explicit reference to the search direction obtained on the previous iteration. A brief outline of the method of conjugate gradients is given below; Fletcher (1972) provides a fuller description. Figure A2 in Appendix A presents a flow chart for the computer program used.

1.4 Minimization by the Method of Conjugate Gradients

Given a function $V(\underline{x})$ of $3N$ variables, the method of conjugate gradients involves linear searching such that given an approximation \underline{x}_k on the k^{th} iteration, a direction \underline{S}_k may be chosen and \underline{x}_{k+1} calculated from:

$$\underline{x}_{k+1} = \underline{x}_k + \alpha_k \underline{S}_k \quad (1.6)$$

where α_k is chosen so that $V(\underline{x}_{k+1})$ minimizes $V(\underline{x}_k + \alpha \underline{S}_k)$ for all α . Quadratic termination is achieved by choosing the search directions $\underline{S}_i, \underline{S}_j$ to be mutually conjugate to the Hessian matrix \underline{G} of 2nd derivatives

ie.

$$\underline{S}_i^T \underline{G} \underline{S}_j = 0, \text{ for all } i, i \neq j \quad (1.7)$$

where the superscript T denotes transpose.

The gradient vector \underline{g}_k of the function to be minimized is used to calculate the search directions on each iteration by the following prescription:

$$\underline{S}_k = \begin{cases} -\underline{g}_k & : k=1 \\ -\underline{g}_k + \beta_k \underline{S}_{k-1} & : k>1 \end{cases} \quad (1.8)$$

It is evident from (1.8) that for $k = 1$ the search directions are merely the directions of steepest descent; for $k>1$ the directions involve the directions of steepest descent of the current iteration plus the search directions from the previous iteration multiplied by some scalar β_k . This scalar in general involves the directions of steepest descent obtained from the previous iteration (Fletcher and Reeves (1964), Fletcher (1971)). Four points to note when

minimizing general (i.e. non-quadratic) functions by this method are:

- (i) the starting configuration should be as near as possible to the final configuration.
- (ii) in some convoluted $3N$ -dimensional surfaces convergence may be extremely slow due to, for example, movement down a banana-shaped valley (Rosenbrock (1960)). Periodic reversion to the steepest descent direction instead of the usual search direction avoids 'trapping' in convoluted areas of the surface, provided such reversions are not more frequent than every $3N$ iterations, whilst retaining quadratic convergence for harmonic functions.
- (iii) the formal requirement for \underline{x}_i to be at a minimum is the gradient vector $\underline{g}_k = 0$. Computational rounding errors make this requirement unobtainable, so iterations need to be continued until a complete cycle of $3N$ iterations, starting from a steepest descent search, produces no reduction in $V(\underline{x})$.

(iv) since equation (1.7) may not be solved exactly for α_k with non-quadratic functions some approximate solution is required. The method used in this work is described by Davidon (1959) and implemented by Fletcher and Powell (1963). Various tests may be made for satisfactory values of α (Fletcher (1972)), but this linear search problem still remains formidable. Both cubic interpolation (Fletcher and Reeves (1964)) and extrapolation are used to revise the values of α . Fletcher (1970) removes the linear search problem entirely by replacing the quadratic termination problem by one of monotonic convergence of an approximating matrix to the inverse Hessian.

The minimization program used in subsequent Chapters is based on a program supplied by the Theoretical Physics Division, A.E.R.E., at Harwell.

Chapter 2

2.1 Lennard-Jones Clusters: $2 < N \leq 13$

Starting from some basic seed-structure a systematic application of the growth algorithm previously described, using a Lennard-Jones 6-12 potential (equations 1.3), results in a family of soft-sphere Lennard-Jones (L-J) isomers. The members of such a family are designated tetrahedral, octahedral or Bernal structures, depending upon the original seed. By removing the requirement that the parent structure is relaxed to a minimum in the applied potential it is possible to generate a family of hard-sphere (H-S) isomers; however the clearance regions inherent in H-S structures (see Figure 7) lead to the production of very many more H-S than L-J clusters. Consequently computing time restrictions cause the termination of H-S isomer enumeration at $N=11$. Several geometrically distinct H-S structures relax under the applied potential to forms equivalent in both energy and morphology. Reference to Tables 2 to 4 illustrates this fact - these tables contain the calculated numbers of H-S and L-J isomers belonging to the tetrahedral, octahedral and Bernal families. Since clusters containing 6 or more atoms may exist in both left- and right-handed forms the total number of L-J isomers is examined for chirality: the results of this investigation are contained in Table 5. The necessity of including enantiomorphs in the multi-configuration partition function is emphasised by the contents of this table. Fitting the multiplicity data of Table 5 to an exponential curve results in the following generating function for the number of isomers $g(N)$ containing more than thirteen atoms;

$$g(N) \approx \exp\{-2.5176 + 0.3572N + 0.0286N^2\} \quad (2.1)$$

Equation (2.1) predicts 3279 stable isomers for $N=14$ and 10753 for $N=15$.

<u>Table 2</u>			<u>Table 3</u>			<u>Table 4</u>			<u>Table 5</u>		
<u>N</u>	<u>H-S</u>	<u>L-J</u>	<u>N</u>	<u>H-S</u>	<u>L-J</u>	<u>N</u>	<u>H-S</u>	<u>L-J</u>	<u>N</u>	<u>Total</u>	<u>Enants.</u>
4	1	1	6	1	1	9	2	1	4	1	0
5	1	1	7	1	1	10	9	3	5	1	0
6	1	1	8	4	3	11	>19	16	6	2	1
7	3	3	9	9	6	12	*>14	53	7	4	1
8	6	5	10	40	29	13	*>66	167	8	8	1
9	23	11	11	136	60				9	18	3
10	73	25	12	*	142				10	57	11
11	337	69	13	*	338				11	145	19
12	*	171							12	366	47
13	*	483							13	988	131

*signifies computing time restrictions.

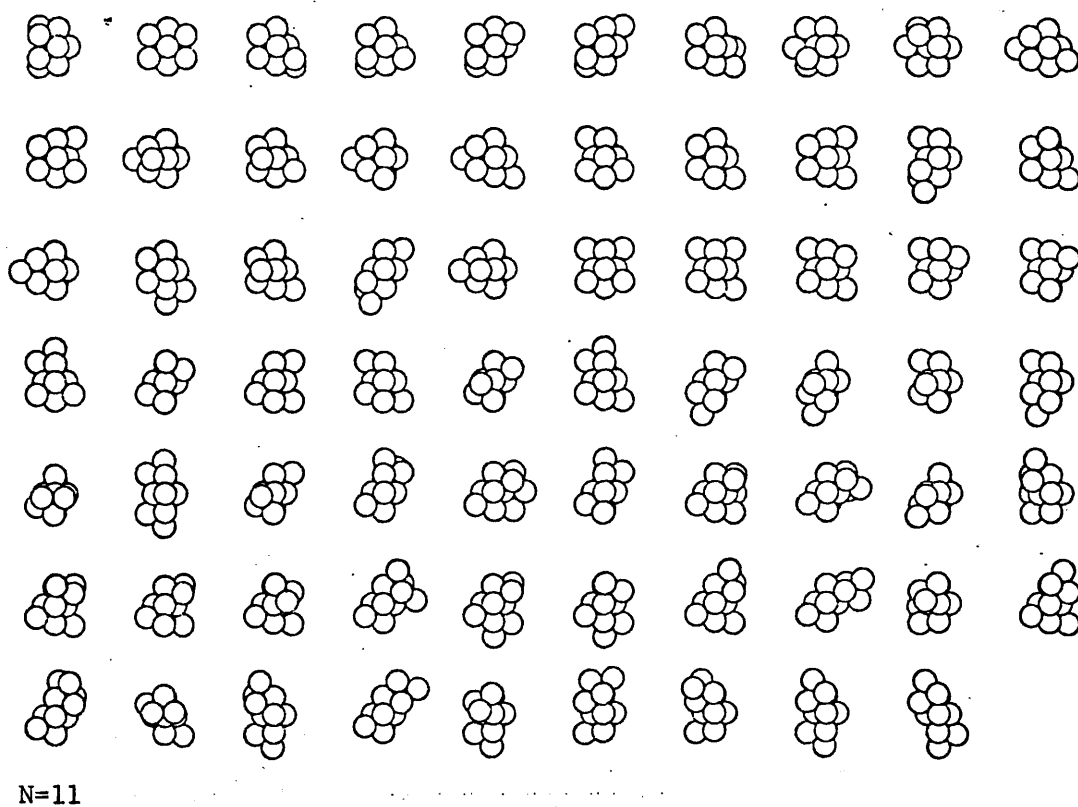
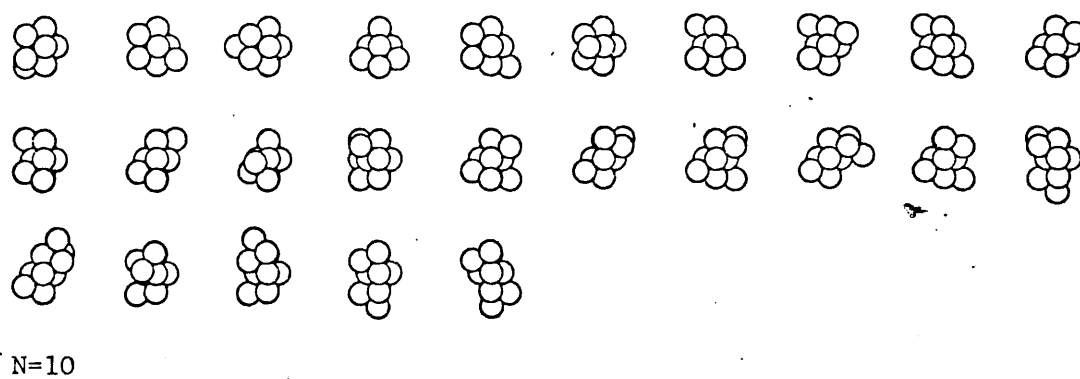
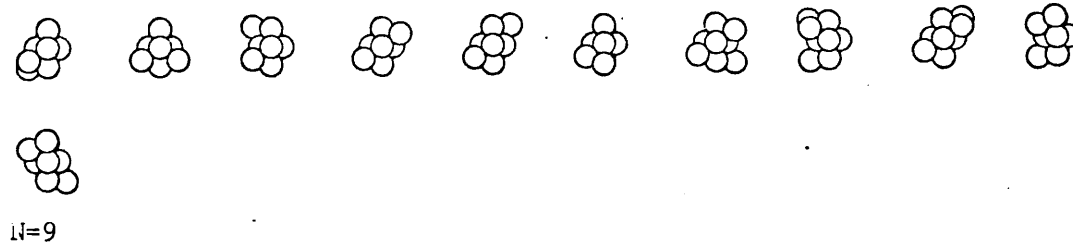
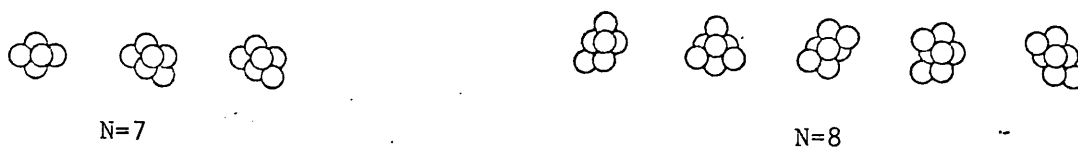
Tables 2 to 4 present the respective numbers of hard-sphere and Lennard-Jones 6-12 isomers for the tetrahedral, octahedral and Bernal sub-groups. Table 5 contains the total number of isomers in the range $4 \leq n \leq 13$ and the number of enantiomorphs present in this range.

Figures 8 to 11 show the various subsets of minima for $N \leq 12$. Since the lists of minima for $N=13$ are too great to present *in toto* Figures 12 and 13 illustrate some of the most and least stable minima in this category. In each case the most stable structure appears at the top left-hand side with isomers in descending order of binding energy along the rows. One immediately notes the trend towards more extended structures as the binding energy decreases. The Boerdijk spiral configuration (Boerdijk (1952)), resembling a chain of tetrahedra face to face, is easily identified in the figures of tetrahedral clusters. It is interesting to note that these extended structures are not the least stable available but are followed in the figures by many others of less systematic extended structure.

2.2 Minimal Energy Configurations

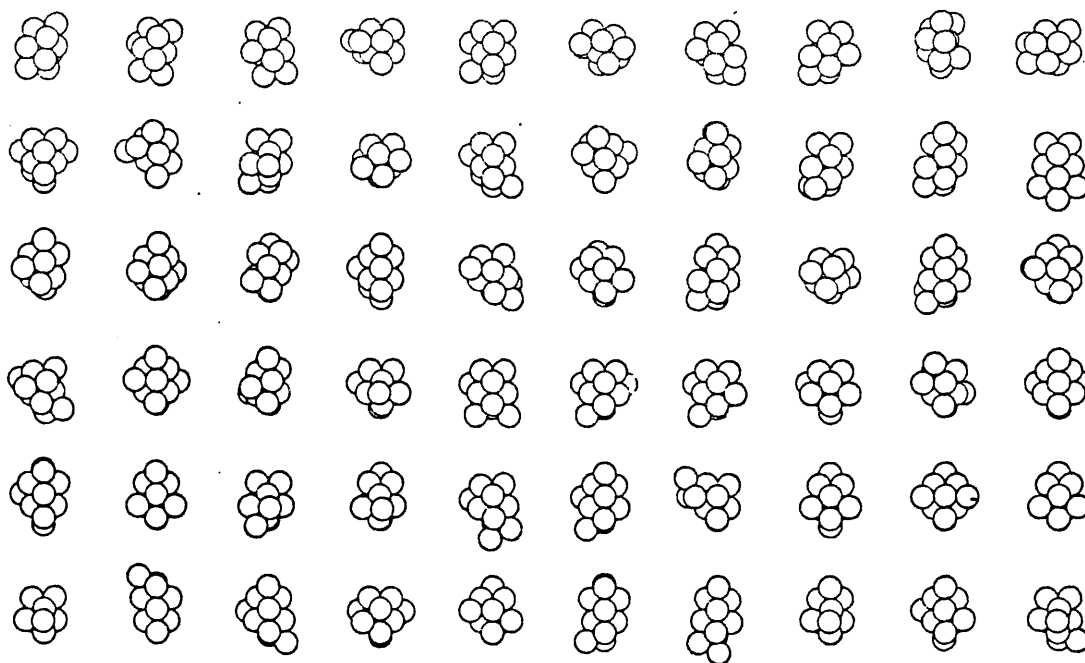
The morphologies and scaled potential energies of the most stable L-J isomers are presented in Table 6. One notices the tendency for the compact structures to possess high symmetry. Information in this

Figure 8

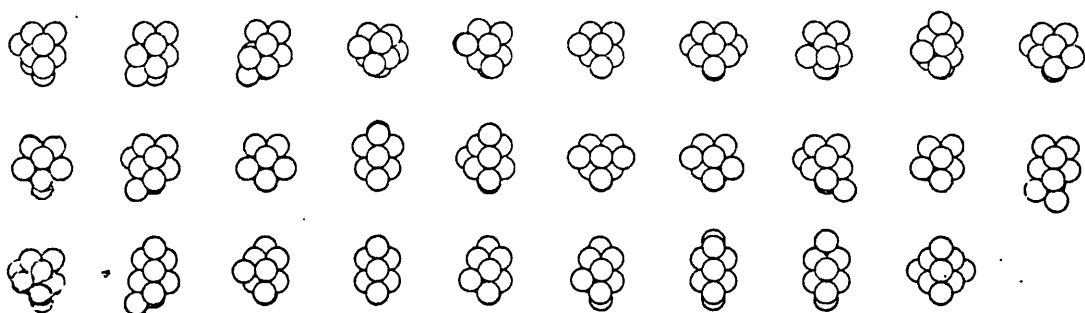


Tetrahedral Isomers

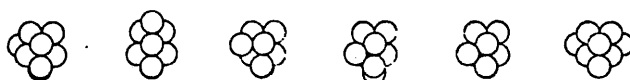
Figure 9



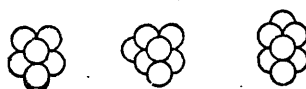
N = 11



N = 10



N = 9



N = 8

Octahedral L-J Isomers: $7 < N < 12$

table is subsequently used in the calculations of rotational partition functions. Energies quoted in this and subsequent tables, as well as throughout the text, have the minus sign suppressed.

Table 6

N	V(N)*	Subset [†]	Point Group	Symmetry Operations	Description of Structure	Principal Moments of Inertia
2	1.0000	-	C ₂	2	Dimer, unit side	0.5000, 0.5000, 0.0000.
3	3.0000	-	C ₃	3	Equilateral triangle, unit side. Symmetric top.	1.0000, 1.0000, 0.5000.
4	6.0000	T	T _d	12	Tetrahedron, unit side. Spherical top.	1.0000, 1.0000, 1.0000.
5	9.1039	T	D _{3h}	6	Trigonal bipyramid. Symmetric top.	1.8245, 1.8245, 1.0029.
6	12.7121	O	O _h	24	Octahedron, spherical top.	1.9820, 1.9820, 1.9820.
7	16.5054	T	D _{5h}	10	Pentagonal bipyramid. Symmetric top.	3.6285, 2.3370, 2.3370.
8	19.8214	T	C _{1h}	1	Pentagonal bipyramid + 1. Asymmetric top.	4.6574, 3.6944, 2.6679.
9	24.1134	T	C _{2v}	2	Pentagonal bipyramid + 2. Asymmetric top.	5.6316, 4.3395, 3.3402.
10	28.4225	T	C _{3v}	3	Pentagonal bipyramid + 3. Symmetric top.	6.5102, 4.6021, 4.6017.
11	32.7659	T	G _{2v}	2	Pentagonal bipyramid + 4. Asymmetric top.	7.1325, 5.9453, 5.1933.
12	37.9676	T	C _{5v}	5	Pentagonal bipyramid + 5. Symmetric top.	7.5465, 6.4154, 6.4152.
13	44.3268	T	I _h	60	Oblate structure. Icosahedron. Spherical top.	7.4315, 7.4313, 7.4312.

* Minus sign suppressed throughout.

† T: tetrahedral subset; O: octahedral subset

Morphologies of the most stable L-J isomers

For all values of N except $N=6$ the most stable structure is a member of the tetrahedral family. The minimal energy 6-atom structure is the octahedron, with full octahedral symmetry. For $N=2$ and $N=3$ the minimal energy configurations are the linear dimer and the planar equilateral triangle respectively. With distances scaled as in equations (1.3) both of these structures have interatomic spacings of 1 unit. The 4-atom tetrahedron is the first non-planar structure: all atoms are in mutual contact with an interatomic spacing of 1 unit. For $N=5$ one finds the first occurrence of non-nearest neighbours in the trigonal bipyramid: this structure may be considered as two tetrahedra back to back sharing a common base. The edges of this base are distended by .15% to 1.0015 units with the peak to peak distance contracted by approximately .4% to 1.6267 units. The 6-atom octahedron has a base side of .9955 units with a peak to peak distance of 1.4079 units: this peak to peak distance represents a contraction of .45%. The 7-atom pentagonal bipyramid has an axial distance of 1.0225 units, an edge distance of .9935 units, and a planar 5-membered ring with an interatomic spacing of 1.00145 units. These latter interatomic distances differ from those cited by Hoare and Pal (1971a); nevertheless the structure maintains full D_{5h} symmetry and is marginally more stable, (energy 16.5054), i.e. possesses higher binding energy, than Hoare and Pal's bipyramid (energy 16.5049).

Minimal clusters for $N>7$ follow the Werfelmeier sequence (Werfelmeier (1937)) - the sequence of structures obtained on adding atoms around the fivefold axis of the pentagonal bipyramid. This sequence culminates with the regular icosahedron at $N=13$. The most stable 9-atom structure has two adjacent atoms added to the pentagonal bipyramid (see Figure 8). By following the Werfelmeier sequence

Figure 10

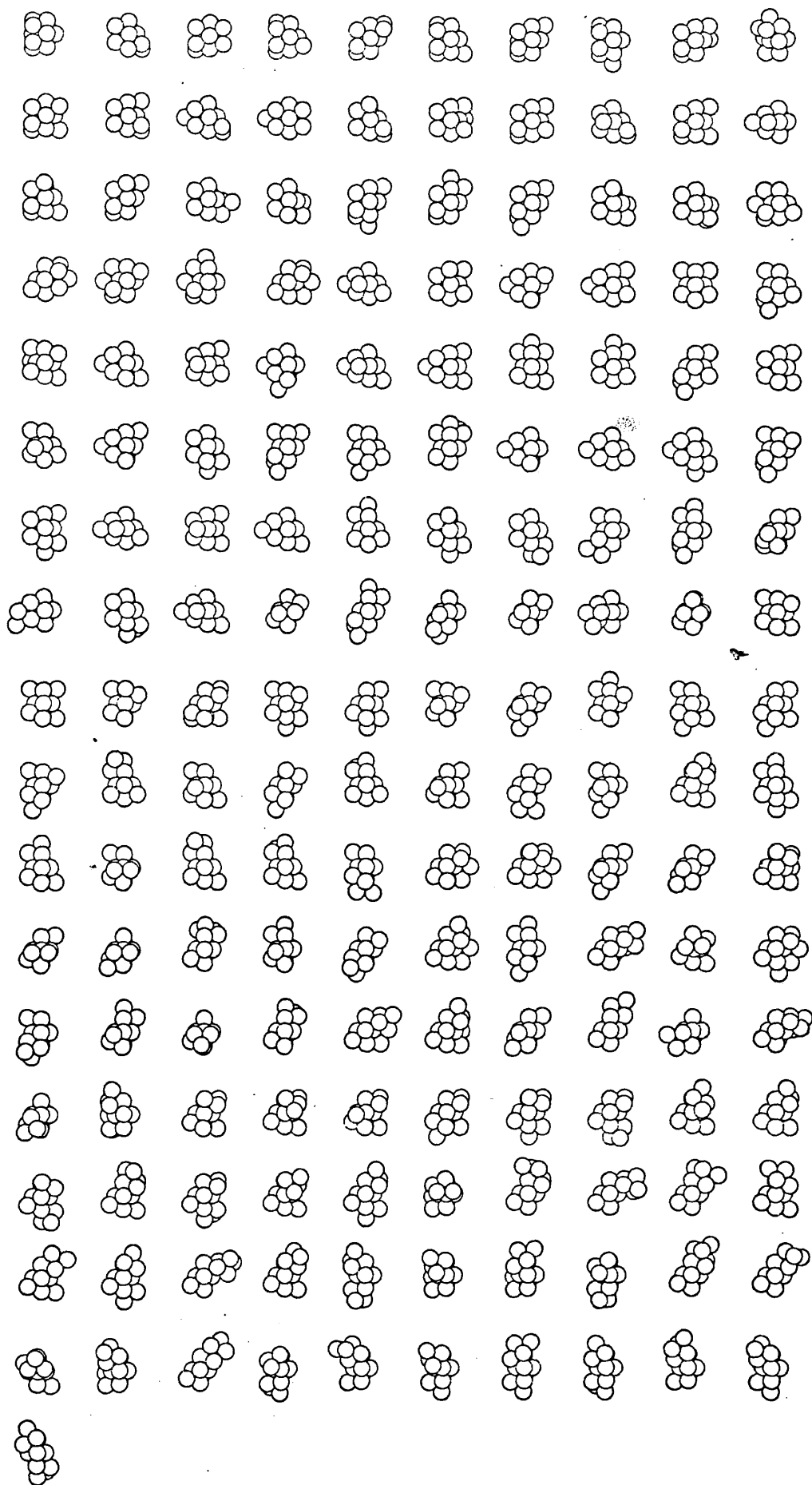
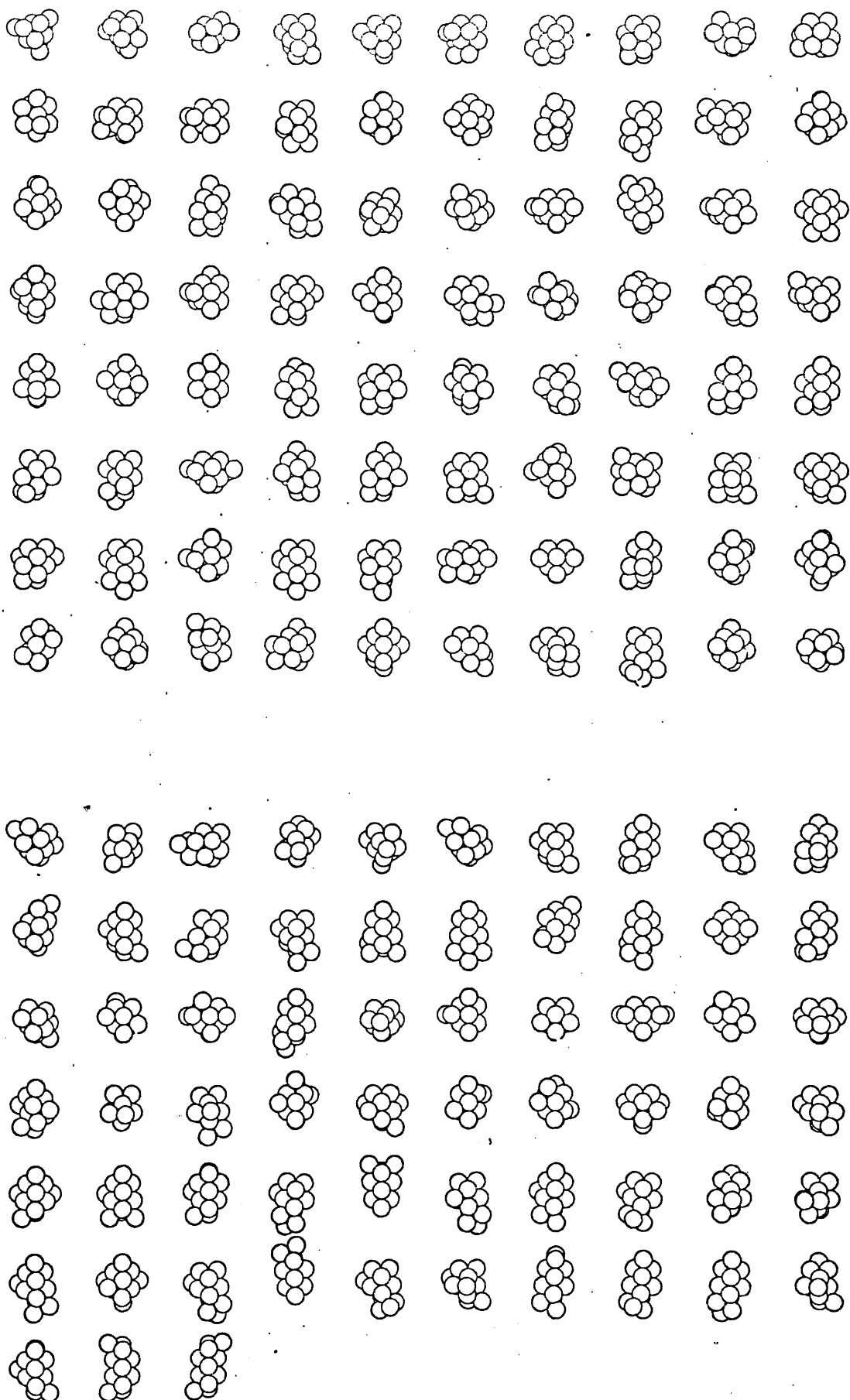
12-atom tetrahedral isomers

Figure 11

Octahedral 12-atom Isomers

one arrives at the oblate 12-atom cluster which may be recognised as the icosahedron minus one atom. Addition of a thirteenth atom to the five-coordinated site at the apex of this cluster produces the icosahedron with twelve peripheral atoms arranged symmetrically about the central one. The twelve radial bonds are contracted to .9638 units while the sides of the equilateral triangles covering the surface are distended to 1.0134 units, thus producing the peripheral to radial bond ratio of 1.0515 characteristic of icosahedral structures. Although it is not possible to be certain that such a structure is the absolute minimal one for 13-atoms it is almost inconceivable that a structure with higher binding energy could exist.

2.3 Tetrahedral Isomers

For $3 < N < 6$ only tetrahedral L-J structures exist, since the 5-atom square pyramid, composed of a fifth atom added to a planar square of four atoms, is found from its frequency spectrum to be metastable. This structure, with an energy $V(5)=8.4806$ and belonging to the point group C_{4v} , collapses to the trigonal bipyramid described in the previous section. The tetrahedral 6-atom structure comprises three tetrahedra packed face to face, forming a Boerdijk spiral configuration. This configuration, with energy $V(6)=12.3029$ and symmetry C_{2h} , may exist in both left- and right-handed forms.

By adding atoms to three of the faces of a tetrahedron the 7-atom partially stellated tetrahedron, energy $V(7)=15.5932$, is formed. Addition of a fourth atom to the final face of the basic tetrahedron results in the 8-atom fully stellated tetrahedron, energy $V(8)=18.9761$. Subsequent addition of atoms to the faces of the fully stellated tetrahedron generates that set of clusters referred to by Hoare and Pal

(1971a) as 'tetrahedral isomers'. Hoare and Pal designate those structures grown by the addition of atoms to a pentagonal bipyramid 'pentagonal isomers'. The set of tetrahedral isomers referred to in this work includes both the tetrahedral and pentagonal structures of Hoare and Pal's work.

Table 7 contains the results of the statistical analyses of all tetrahedral binding energies. The measures of skewness and kurtosis (Spiegel (1961)) in this table indicate the degrees of asymmetry and peakedness of the distributions, taken relative to the normal

Table 7

N	$V_{\max}(N)/N$	$V_{\min}(N)/N$	$\bar{V}(N)/N$	$S^{\dagger} \times 10^2$	Skewness $\times 10$	Kurtosis $\times 10$
2	-	-	.5000	-	-	-
3	-	-	1.0000	-	-	-
4	-	-	1.5000	-	-	-
5	-	-	1.8208	-	-	-
6	-	-	2.0505	-	-	-
7	2.3579	2.2190	2.2682	7.78	6.97	-15.00
8	2.4777	2.3473	2.3815	5.45	14.00	+1.08
9	2.6793	2.4479	2.5315	7.61	3.98	-8.92
10	2.8423	2.5289	2.6318	9.17	5.79	-7.67
11	2.9787	2.5953	2.7327	9.62	3.58	-7.17
12	3.1640	2.6508	2.8083	10.26	4.45	-2.17
13	3.4098	2.7022	2.8828	10.96	4.76	+3.55

\dagger Standard deviation.

Statistical Analysis of Tetrahedral Binding Energies

distribution. A gradual increase in the standard deviations with increasing N is seen for $N > 7$, showing an increasing energy spread, but the skewness and kurtosis of each distribution appear to follow no specific trend. This may be explained when one realises that the latter two measures are extremely sensitive to the morphology of the previous parent generation. If a particular extended N -atom cluster with low binding energy has more available sites for the addition of an $(N+1)$ th atom than does another more compact structure, the mean

binding energy is displaced towards the low energy limit. Additionally, if both compact and extended structures contribute equal numbers of 'daughter' clusters, the distribution curve tends to become flattened.

2.4 Octahedral Isomers

The set of octahedral isomers originates with the 6-atom octahedron, described in Section 2.2. Growth from this seed produces units which, unlike the tetrahedral units, have a space filling characteristic. Examination of the first 8-atom structure in Figure 9 shows an opening of the 4-atom ring - Werfelmeier (1937) identifies this structure as a tetragonal hemihedron of the second kind, with symmetry D_{2h} . Such a cluster may be described as being formed from two identical trapezia interpenetrating in perpendicular planes. The energy of this hemihedron (19.7653) closely approaches that of the overall minimal cluster for 8-atoms, i.e. the pentagonal bipyramid plus one (energy 19.8216). Opening of the octahedral ring may be seen in a number of other isomers presented in Figure 9. Such ring openings occur when one side of the ring is under pressure from two atoms positioned directly opposite one another on opposite sides of the plane containing the ring (see the structures in Figure 9). Three octahedral clusters for $N=8$ and six for $N=9$ are found, in disagreement with the figures of two for $N=8$ and three for $N=9$ quoted by Hoare and Pal (1971a). These clusters, with others, are shown in Figure 9.

A particularly striking 10-atom cluster is the f.c.c. tetrahedron formed by the addition of three atoms to each edge of a tetrahedron. This structure has full tetrahedral symmetry and an energy of 25.7918 units. It is the final 10-atom octahedral cluster in Figure 9, having emerged spontaneously from the octahedral growth sequence. Allpress and Sanders (1970) and Ino (1970), suggest that externally symmetric

Figure 12

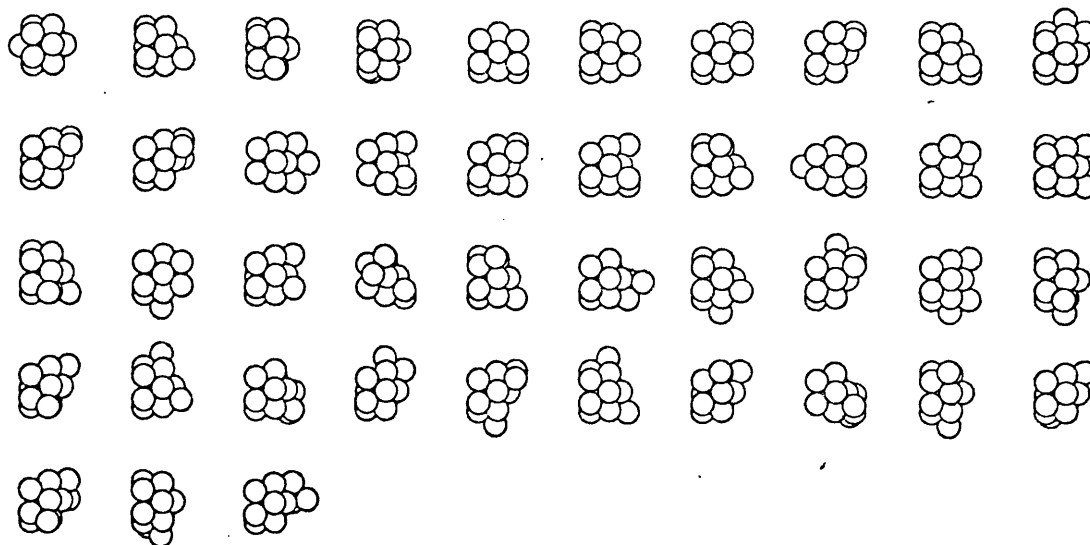
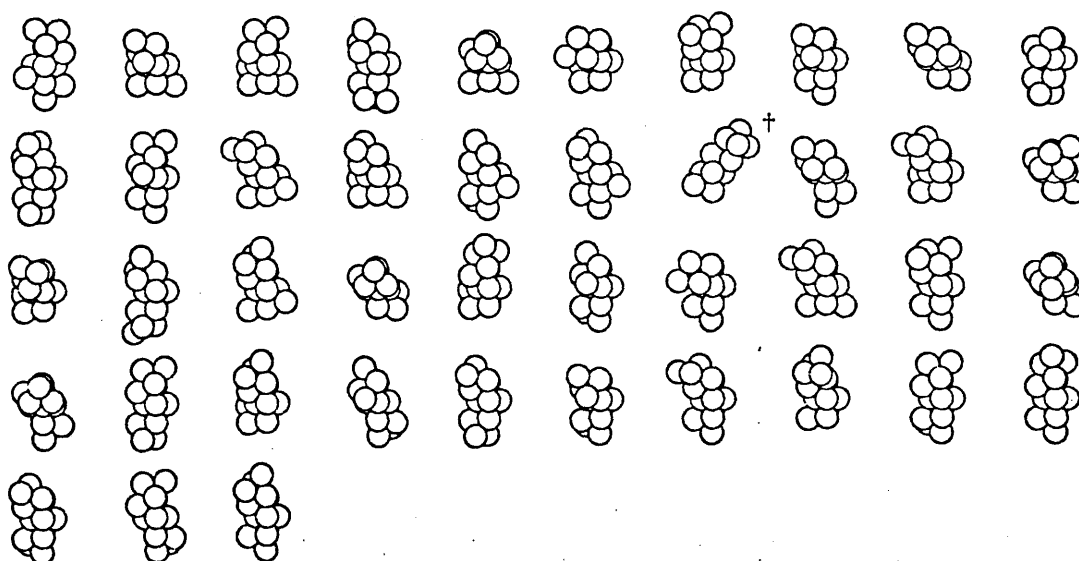
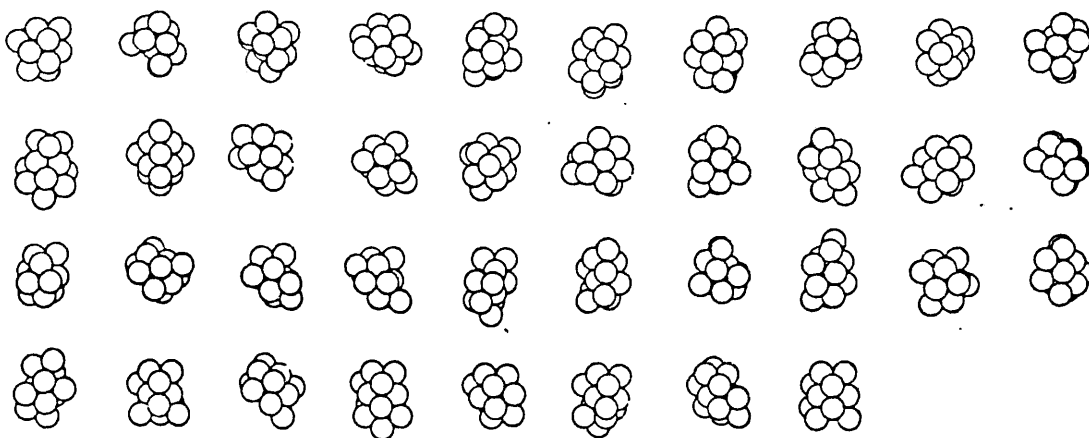
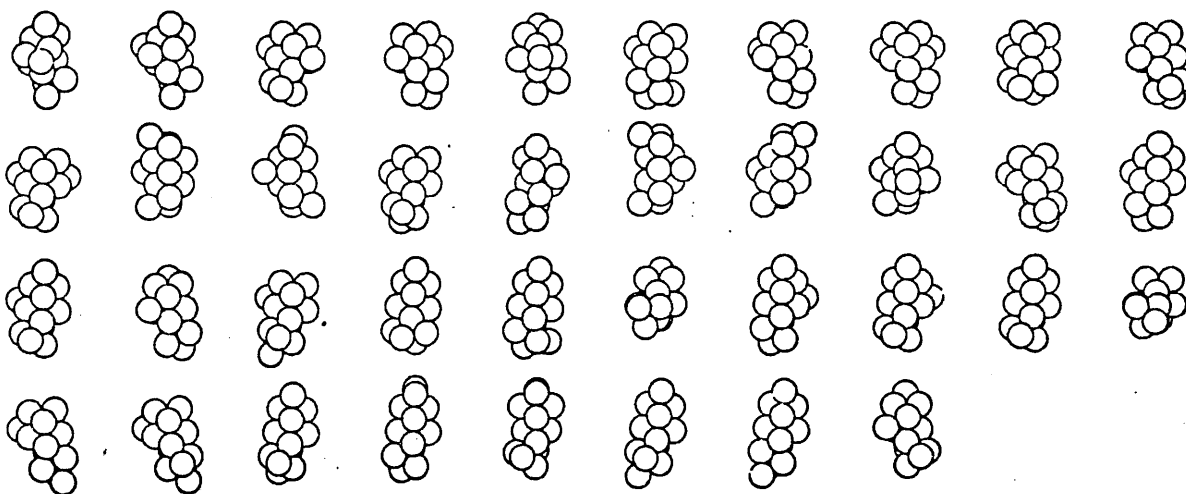
First 43 Tetrahedral 13-atom IsomersLast 43 Tetrahedral 13-atom Isomers† *Boerdijk Spiral*

Figure 13First 38 13-atom Octahedral L-J IsomersLast 38 13-atom Octahedral L-J Isomers

forms such as the f.c.c. tetrahedron may form a basic unit for growth by twinning. Kimoto and Nishida (1967), and Allpress and Sanders (1970) report the observations of pseudo-crystallites with non-lattice symmetries in condensing metal vapours. Such pseudo-crystallites may be formed by the growth of a daughter phase forming a mirror image of such an f.c.c. structure as that mentioned above. In such a fashion larger 'twinned' figures may be constructed. Fukano and Wayman (1969) criticise the extension of such a mechanism to clusters larger than the twinned 23-atom pentagonal bipyramid and advocate a sphere-packing modification in which five atoms are added around the five-fold axis of this cluster. A sixth atom is then added on the symmetry axis. Komoda (1968) suggests the growth of twinned structures by the addition of atoms to the 7-atom pentagonal bipyramid and the 13-atom icosahedron in such a fashion as to preserve the overall shape of the cluster.

Statistical analyses of the octahedral binding energies produce the data contained in Table 8. Examination of this Table shows the standard deviations for all N to be less than those in Table 7 for tetrahedral isomer distributions. Fluctuations in the skewness and kurtosis coefficients may again be attributed to the morphology of the parent structure.

Table 8

N	$V_{\max}(N)/N$	$V_{\min}(N)/N$	$\bar{V}(N)/N$	$S^{\dagger} \times 10^2$	Skewness x10	Kurtosis x10
5 [†]	-	-	1.6961	-	-	-
6	-	-	2.1187	-	-	-
7	-	-	2.2847	-	-	-
8	2.4707	2.3962	2.4218	4.23	7.04	-15.00
9	2.5748	2.4972	2.5472	2.63	-12.22	4.31
10	2.7206	2.5792	2.6518	3.22	5.22	4.81
11	2.8570	2.6986	2.7520	4.14	4.61	-8.50
12	3.0174	2.7295	2.8389	5.48	4.63	1.49
13	3.1038	2.7911	2.9241	6.57	0.86	-4.89

[†] Standard deviation

[‡] Metastable structure

Statistical Analysis of Octahedral Binding Energies

2.5 Bernal and Other Structures

It is possible to construct a number of clusters grown from seeds which are neither tetrahedral nor octahedral. Some such seed-structures, members of Bernal's list of canonical polyhedra (Bernal (1959), (1960), (1964)), are illustrated in Figure 2. The 6-atom trigonal prism is unstable under a Lennard-Jones potential, reforming to the trigonal bipyramid. However the simultaneous addition of three half-octahedral caps forms a stable structure, which has an optimized energy of 23.2698 units and symmetry C_{3h} . The trigonal prism plus one cap reforms to the single 7-atom octahedral structure (energy 15.9350 units), whilst the trigonal prism plus two caps distorts into the 8-atom tetragonal hemihedron (Werfelmeier (1937)), also a member of the octahedral group. The Archimedean antiprism relaxes to a structure with an energy of 22.3567 units - however the frequency spectrum for such a configuration shows it to be metastable. The addition of one cap to the antiprism produces a structure which relaxes to the trigonal prism plus three caps. The 10-atom fully-capped antiprism (energy 26.7712, symmetry C_{4v}) is stable and therefore may be used as a seed structure.

An investigation into the stability under a L-J potential of the 8-atom cube shows the collapse of such a structure to the fully stellated tetrahedron (energy 18.9761 units). Optimizing the cube under the constraint that cubic symmetry is preserved produces a cluster with an energy of 15.1771 units. The danger of such a constraint is well illustrated by the collapse of this structure to a tetrahedral configuration on the removal of the constraint - the cube has insufficient attraction along the diagonals to support itself under a Lennard-Jones 6-12 potential.

Bennett (1972) describes a 10-atom structure, composed of 2 adjacent octahedra, which relaxes to the most stable octahedral structure.

As in the previous two sections a statistical analysis of the binding energies for each value of N is performed: the results of these analyses are presented in Table 9. One immediately notes the almost constant standard deviation for Bernal clusters and the tendency for the kurtosis coefficients of the distributions to approach that of the normal distribution with increasing N .

Table 9

N	$V_{\max}(N)/N$	$V_{\min}(N)/N$	$\bar{V}(N)/N$	$S^{\dagger} \times 10^2$	Skewness $\times 10$	Kurtosis $\times 10$
9	-	-	2.5855	-	-	-
10	2.7214	2.6695	2.6894	2.80	6.48	-15.00
11	2.8320	2.6481	2.7078	6.13	6.87	5.70
12	2.9619	2.7373	2.8365	5.07	6.69	- 2.73
13	3.0746	2.7630	2.9077	6.24	-1.60	- 1.50

[†] Standard deviation.

Statistical Analyses of Bernal Binding Energies

2.6 Discussion

Figures 5 and 6 illustrate tetrahedral and octahedral interrelationships. The removal of one cluster may result in the loss of several later generation clusters; thus a systematic cluster enumeration is essential. Division of clusters into sub-groups is an aid to classification: however statistical analyses of the total isomer set are required for a description of the system as a whole. The results of such analyses for varying N are presented in Table 10. As in Table 9 the tendency for the standard deviation to remain independent of N is noted. Table 7 shows positive skewness for all

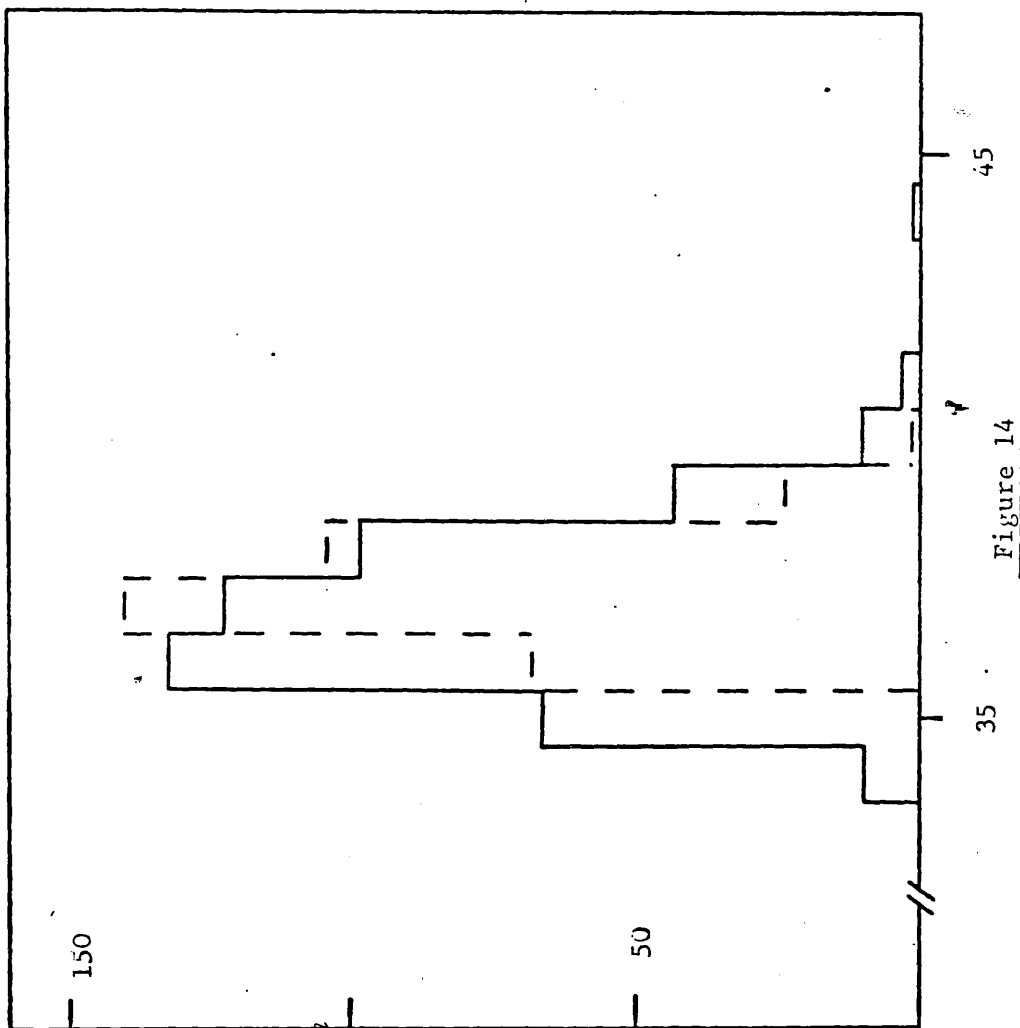


Figure 14

The Distribution of Tetrahedral and Octahedral 13-atom L-J Isomers

The dotted line shows the octahedral distribution to be contained within the tetrahedral distribution. The detached point representing the icosahedron is clearly distinguishable. Energy is given in units of the L-J pair-energy.

Table 10

<u>N</u>	<u>$\bar{V}(N)/N$</u>	<u>$S^{\dagger} \times 10^2$</u>	<u>Skewness x10</u>	<u>Kurtosis x 10</u>
7	2.2702	6.37	6.89	-11.28
8	2.3966	5.14	7.42	-10.08
9	2.5397	6.16	0.79	-3.19
10	2.6450	6.61	2.52	+3.05
11	2.7379	7.52	2.40	0.30
12	2.8243	8.16	1.74	4.80
13	2.9011	9.14	1.33	6.48

[†]Standard deviation

Statistical Analyses of Total Binding Energies

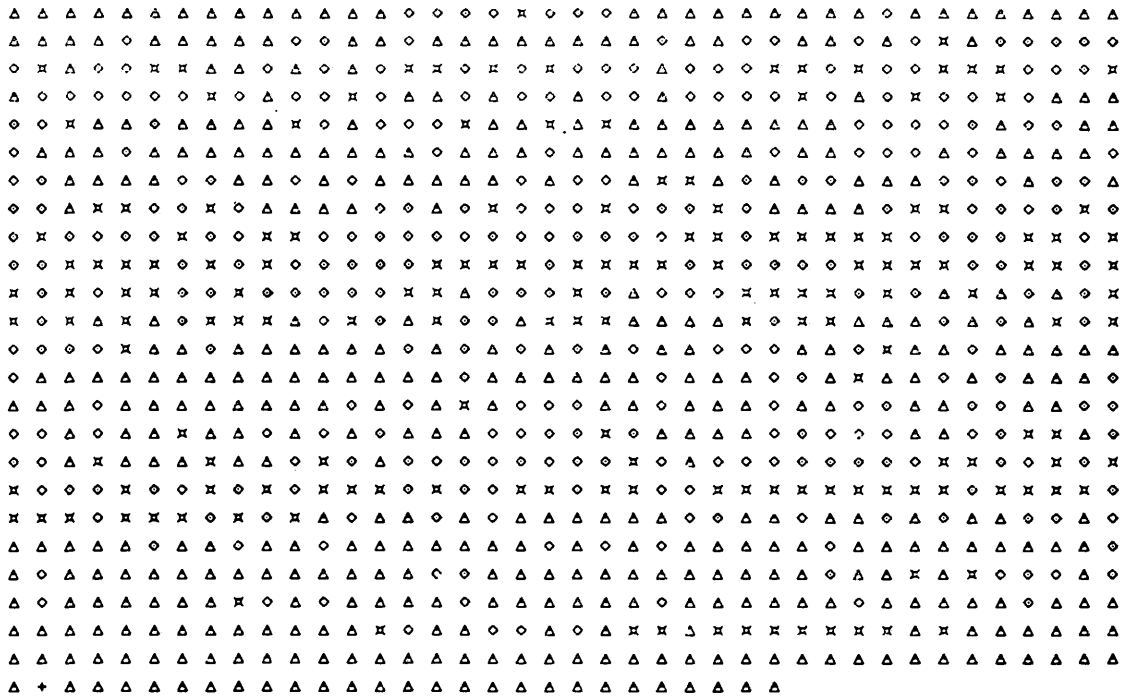
values of N, i.e. the frequency curves of distributions have longer tails to the right of the central maximum. An interpretation of these results is that it is easier to form alternative structures by variation of the less stable, more elongated structures than the more compact units. 9-atom octahedral clusters and 13-atom Bernal clusters exhibit negative skewness, indicating the existence of a larger number of structures with comparatively high binding energies than with low binding energies. From the skewness coefficients in Table 10 one may conclude that overall there exists a greater variety of extended structures than compact structures. The kurtosis coefficients in the same table show the distributions of total binding energies to move from platykurtic, through mesokurtic at N=11, to leptokurtic. In Figure 14 the distributions of tetrahedral and octahedral structures by binding energy for 13-atom L-J clusters are presented. These distributions are noticeably asymmetric, with the detached single point for the icosahedral structure. The latter is separated by 2.8548 units from its closest competitor in energy (respective energies 44.3268 and 41.4720).

Tables 3 and 4 indicate that the octahedral structures in the size range $N \leq 13$ are comparable in number with the tetrahedral types. The binding energies of the former set are more narrowly peaked about the most probable than the latter. Figures 15 and 16 present the statistics of structural types graphically. In these figures each of the three symbols marks a structural type of a particular minimum for a specific N . The minima are arranged in decreasing order of binding energy as in Figures 8 to 13. The predominance of tetrahedral minima at both extremes and the comparatively uniform distribution of other types is clearly distinguishable.

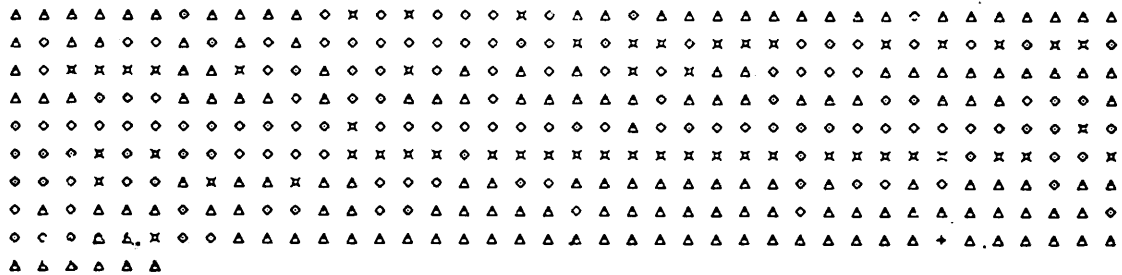
For $N=13$ it is possible to construct highly symmetric figures other than the icosahedron, such as the f.c.c. cuboctahedron which reforms under an L-J potential to the regular icosahedron. This reformation is also noted by Burton (1970a,1971), McGinty (1971), and Hoare and Pal (1972b). The hexagonal close packing (h.c.p.) unit cell structure forms another unstable cluster, collapsing to the icosahedron. The icosahedron may itself be used as a seed-structure to generate larger clusters: by covering all the faces of a regular icosahedron the 33-atom dodecahedron may be constructed.

The binding energies per atom for the most and least stable tetrahedral and octahedral L-J structures, $N \leq 13$, are plotted in Figure 17, as is the binding energy per atom in an infinite f.c.c. crystal (Kihara and Koba (1952)). The inclusion of the octahedral energy range in the tetrahedral range is clearly seen in this figure. To obtain the binding energy of a cluster of a specific gas it is necessary to multiply the scaled energy by the appropriate well-depth ϵ . The L-J parameters for the rare gases are contained in Table 11. Table 12 presents the binding energies per atom of this work's minimal

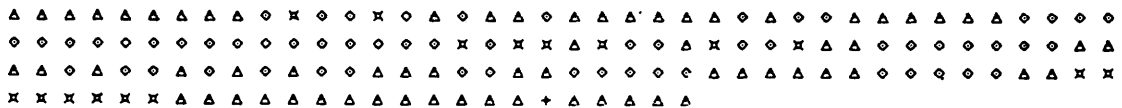
Figure 15



N = 13



N = 12



N = 11

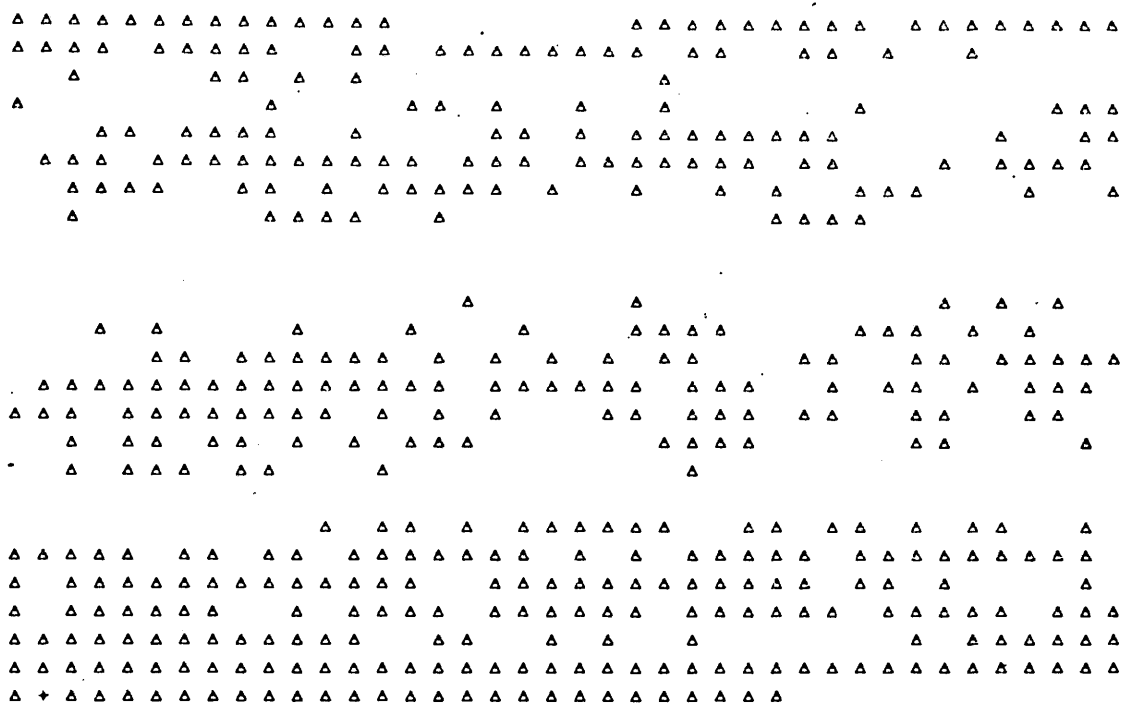


N = 10

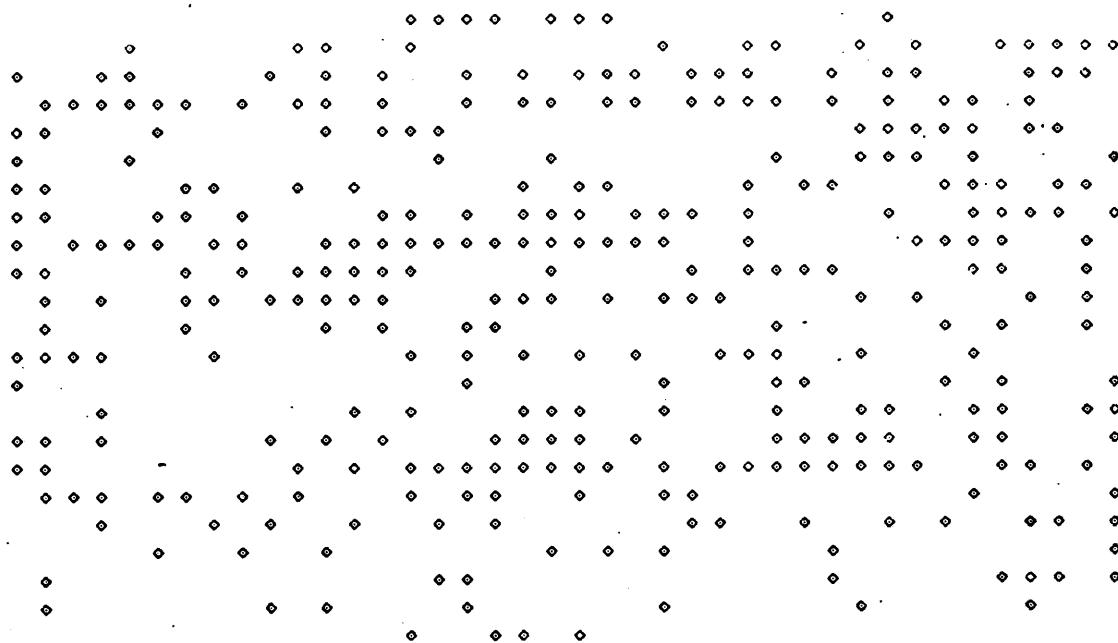
Distribution of Structural Types for L-J Minima

Each structure is coded by a symbol according to type and these are printed in order of decreasing binding energy, illustrating the 'interleaving' of structural types.

△ = tetrahedral; ◇ = octahedral; ✕ = other; † = Boerdijk spiral.



Tetrahedral 13-atom Structures



Octahedral 13-atom Structures

Figure 16

Distribution of Structural Types for 988 L-J 13-atom Minima

See captions to Figure 15.

Table 11

<u>Gas</u>	<u>$\epsilon/k.^{\circ}\text{Abs.}$</u>	<u>$\sigma.\text{mx}10^{10}$</u>	<u>Mass.a.m.u</u>	<u>Melting Temperature.$^{\circ}\text{Abs.}$</u>
Neon	35.60	2.749	20.183	24.48
Argon	119.8	3.405	39.948	83.95
Krypton	171.0	3.60	83.80	116.55
Xenon	221.0	4.10	131.30	161.25

Lennard-Jones Parameters for the Rare Gases

(data from Hirschfelder, Curtiss and Bird (1954)).

clusters and the binding energies obtained by McGinty (1971), in his investigation of growth from close packed lattices. For $N \leq 7$ both

Table 12

<u>N</u>	<u>(a)</u>	<u>(b)</u>
2	.5000	.5000
3	1.0000	1.0000
4	1.5000	1.5000
5	1.8208	1.8207
6	2.1187	2.1186
7	2.3579	2.3578
8	2.4777	2.4706
9	2.6793	2.5512
10	2.8423	2.7189
11	2.9787	2.8254
12	3.1640	2.9691
13	3.4098	3.1901

(a) *this work*

(b) *McGinty (1971)*

Maximum Binding Energy/Atom

sets of energies agree closely; as N increases McGinty's binding energies are lower than those of this work, showing that the preferred minimal configurations, in terms of potential energy at absolute zero, are non-lattice structures in the size range studied. An entropy advantage is also conferred on the non-lattice structures since these forms naturally have greater disorder than the lattice-based

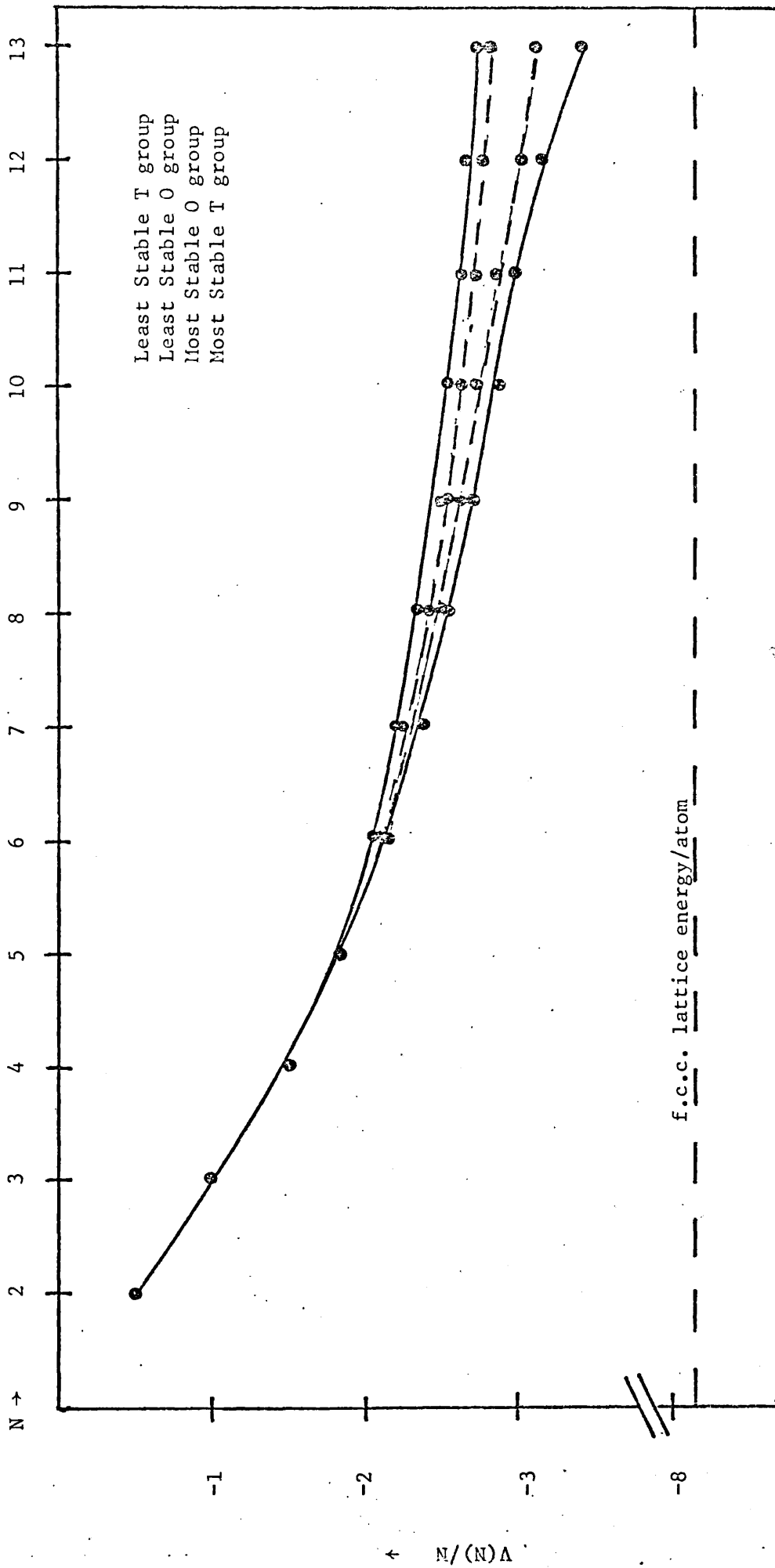


Figure 17

Tetrahedral and Octahedral Binding Energies

structures. Although it has not been possible to obtain unequivocally absolute minima the relative stabilities of various isomeric forms are well-defined. To assess the thermodynamic competition between clusters a statistical mechanical analysis based on the harmonic oscillator approximation is undertaken. In subsequent chapters we investigate the statistical thermodynamics of finite solid-like clusters: more weakly bound clusters possess more strongly pronounced liquid-like characteristics which increase the complexity of cluster partition function determinations.

Chapter 3

3.1 Amorphous Solids and the Glassy State

Dense random packings of hard spheres have been used by a number of authors to provide structural models of amorphous metal alloys (Frank and Kasper (1958,1959), Cargill (1970a,1970b), Polk (1970), Bennett et al (1971), Sadoc et al (1973)), amorphous transition element films (Leung et al (1974a,1974b)), and amorphous germanium and silicon (Polk (1971), Polk and Boudreaux (1973)). Alfrey et al (1943) suggest the migration of 'holes' as a mechanism involved in the formation of glasses (see also Kauzmann (1948)) - Polk (1972) models metallic alloy glasses in terms of Voronoi polyhedra, referring to the 'holes' classified by Bernal (1964). Cohen and Turnbull (1961) consider glass formation in metallic and ionic systems from a sphere-packing standpoint. In this chapter the soft-sphere structures described in Chapter 2 are re-optimized under the influence of a potential chosen to represent the behaviour of amorphous materials. In their investigations of amorphous metals Weaire et al (1971) use Morse potentials with the parameters of Girifalco and Weizer (1959) - following the former authors' example a Morse ($\alpha = 3$) potential is used in this chapter (Figure 1 and equation (1.5)). The set of Morse minima generated from the Lennard-Jones (L-J) set is not necessarily complete since the superposition of the Morse potential on the minimal L-J configurations may result in a 'passing-over' of very shallow minima near the initial points in the configuration space. Nevertheless one may feel reasonably confident that by far the greater part of the Morse minimal set is discovered by this method.

3.2 The Multiplicity of Morse ($\alpha = 3$) Isomers

The application of a Morse ($\alpha = 3$) potential to the L-J cluster set produces a new set of clusters, the members of which have higher binding energies and in general are more compact (Table 13). A surprisingly small fraction of the L-J minima survive in the Morse potential energy surface - see Table 14. If a particular geometric motif is eliminated on changing the range or hardness of the potential, then a whole series of available growth paths are excluded from subsequent generations. Certain tetrahedral configurations, for example the 6-atom trigonal bipyramid, 'open-up' to form octahedral-type minima on the application of the Morse potential. The longer range potential thus shows a tendency to form crystallographic structures, and produces a considerable 'smoothing-out' of the topography of the potential energy surface.

Table 13

<u>N</u>	<u>$\bar{V}(N)/N$</u>	
	<u>L-J</u>	<u>Morse</u>
6	2.1187	2.2574
7	2.2702	2.4723
8	2.3966	2.6715
9	2.5397	2.8875
10	2.6450	3.1050
11	2.7379	3.3047
12	2.8243	3.4774
13	2.9011	3.6608

Comparison of Mean L-J and Morse Binding Energies

Table 14

<u>N</u>	<u>Morse</u>	<u>L-J</u>	<u>H-S</u> [†]
6	1	2	2
7	3	4	4
8	5	8	> 10
9	8	18	> 32
10	16	57	>113
11	24	145	>473
12	22	366	*
13	36	988	*

The Multiplicity of Morse, L-J and Hard-Sphere Isomers

[†] *The numbers quoted for hard-sphere isomers refer only to tetrahedral-type configurations.*

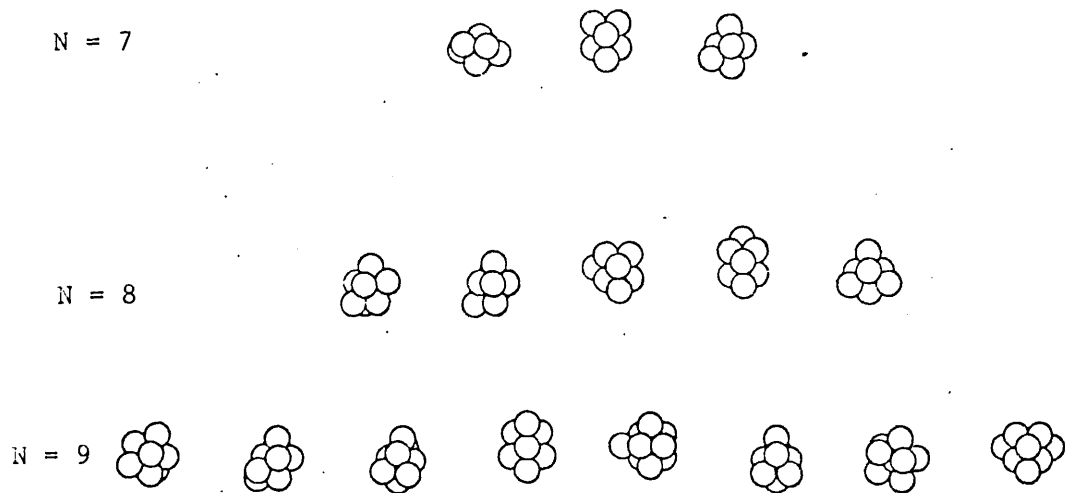
* *Computing time restrictions.*

The reduction in the number of Morse isomers on going from $N = 11$ to $N = 12$ (Table 14) need not seem paradoxical if we reason as follows. The minimal 11-atom cluster is the icosahedron with two adjacent gaps. For the Morse potential it is possible that a number of variations of this structure have a precarious existence close to low saddle points - on the addition of a twelfth atom many of these variants may shrink to arrangements identical in both energy and morphology. The data in Table 14 enable one to produce the following generating function (equation (3.1) for N -atom Morse clusters. Use of (3.1) enables predictions of

$$g(N) = 7.3919 - 3.6151N + 0.4258N^2 \quad (3.1)$$

40 14-atom and 49 15-atom Morse clusters to be made.

Figure 18



Morse Isomers: $6 < N < 10$

Figure 19

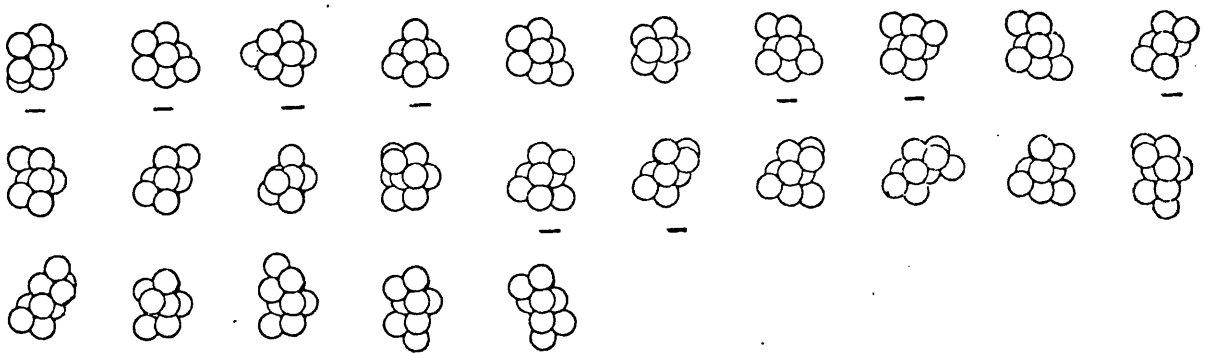
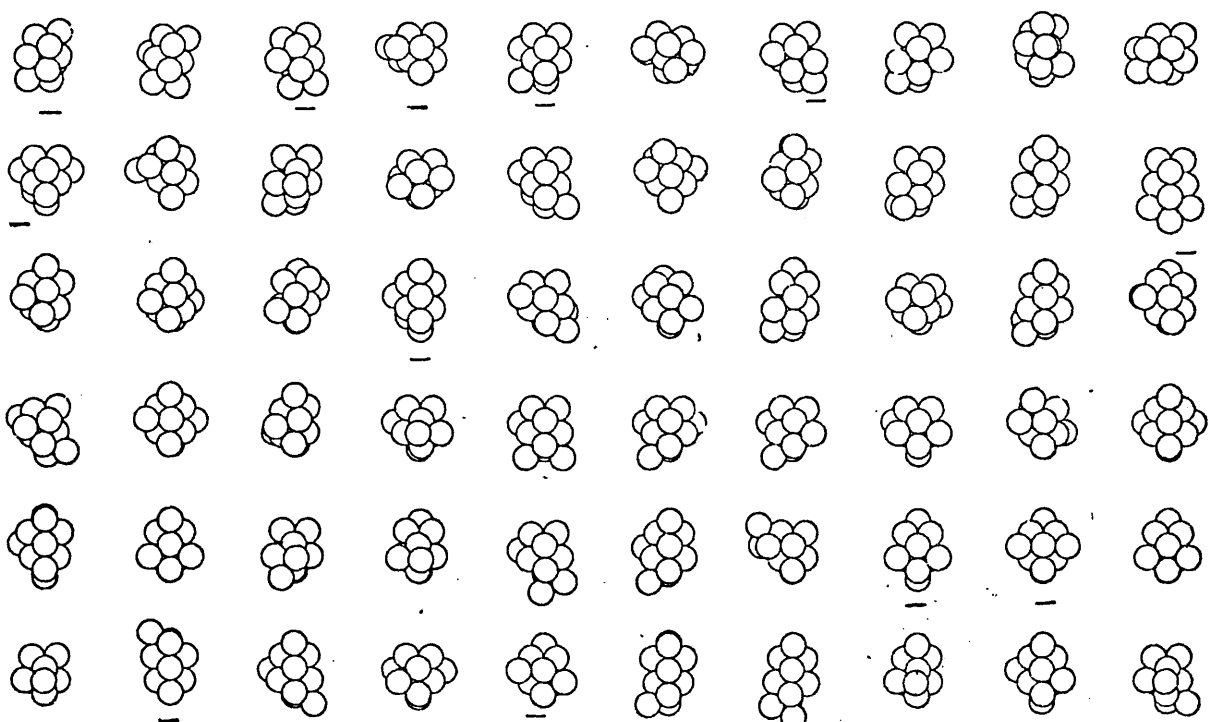


Figure 20



L_J isomers which survive under a Morse potential are underlined

The two 6-atom L-J clusters both relax to an octahedral structure (symmetry O_h) under the Morse potential. This structure has a base length of .9769 units (L-J: .9955), a peak to peak height of 1.3817 units (L-J: 1.4079), and an edge length of .9769 units (L-J: .9955). Its energy is 13.544 units, compared to the L-J octahedral energy of 12.712 units; i.e. there is an energy increase of 6.5%. The Morse pentagonal bipyramid has an energy of 17.5530 units (an increase of 6.3% on the corresponding L-J cluster), an axial length of 1.0926 units (L-J: 1.0225), an edge of length .9799 units (L-J: .9935), and a separation between the members of the five-fold ring of .9564 units (L-J: 1.00145). From these lengths it is apparent that the Morse potential has 'stretched' the pentagonal bipyramid along its five-fold axis; full D_{5h} symmetry is preserved. The energy of the Morse icosahedron is 51.7370 units (L-J: 44.3268). Radial and surface bonds are contracted to approximately 95% of the corresponding L-J lengths, preserving the characteristic icosahedral ratio of 1.0515. The Morse binding energies are shown (Table 14) to be 6-7% greater than the corresponding L-J energies - bond lengths in general contract to 95-98% of the L-J cluster values.

Figure 18 shows a selection of the Morse isomer sets - in this figure the clusters are arranged in order of decreasing binding energy and the interleaving of tetrahedral and octahedral structures is clearly illustrated. Figures 19 and 20 identify some of those distinct L-J clusters which remain distinct under the influence of the Morse potential.

The results of statistical analyses of the energy distributions of N-atom clusters are presented in Table 15. We see that except for

8- and 11-atom clusters the energy distributions possess negative skewness, indicating that more compact than elongated structures exist. This result is a consequence of the strong attractive component of the Morse potential, which distorts the tetrahedral clusters into crystallographic octahedral forms and thereby reduces the number of distinct elongated structures.

Table 15

<u>N</u>	<u>$V_{\max}(N)/N$</u>	<u>$V_{\min}(N)/N$</u>	<u>$\bar{V}(N)/N$</u>	<u>s^{\dagger} x10</u>	<u>Skewness x10</u>	<u>Kurtosis x10</u>
7	2.5076	2.4060	2.4723	.48	- 7.11	-11.18
8	2.7554	2.6262	2.6715	.55	+ 7.61	-10.30
9	2.9754	2.7853	2.8875	.60	- 1.31	- 5.83
10	3.1889	2.9135	3.1050	.78	-12.90	+ 6.60
11	3.4483	3.1675	3.3047	.75	+ 1.95	- 1.85
12	3.6748	3.2595	3.4774	1.25	- 1.91	- 7.19
13	3.9798	3.2397	3.6608	1.83	- 0.60	- 3.35

Statistical Analyses of Total Morse Binding Energies

[†] *Standard deviation.*

The kurtosis coefficients for all $N \neq 10$ indicate that the distribution curves are platykurtic. For 10-atom clusters the energy distribution is leptokurtic and possesses strong negative skewness. This distribution suggests the existence of a variety of compact 10-atom structures and a large number of structures with energies very close to that of the most probable.

From a knowledge of Morse and L-J multiplicities *configurational* thermodynamic properties may be calculated. Gibbs (1960), Adam and Gibbs (1965) and Goldstein (1973a) attribute the glass transition to configurational entropy - the investigations of these authors provide a motivation for the study of configurational thermodynamic properties in Chapter 6.

Chapter 4

4.1 The Vibrational Motion of Clusters

The constituent atoms of the clusters considered here are envisaged as performing small vibrations about an equilibrium configuration whilst the cluster retains its rigid body character. The cluster is defined by its potential energy V and its kinetic energy T with the equilibrium configuration corresponding to zero values of the generalized coordinates $\{q\}$. If the potential energy is expanded in a Taylor series in the displacement and terms higher than quadratic in this expansion ignored, V is expressed as a homogeneous quadratic function in $\{q\}$. The linear terms in the expansion are all zero since the partial derivatives of V with respect to $\{q\}$ must be zero when the $\{q\}$ are zero. Neglect of higher order terms is equivalent to assuming central forces between the atoms. The kinetic energy T is a homogeneous quadratic function of $\{\dot{q}\}$ with coefficients involving $\{q\}$, where the $\dot{}$ signifies a time derivative. Since the $\{q\}$ and $\{\dot{q}\}$ are assumed to be small one may retain only those terms of lowest order in T and thereby replace the coefficients involving $\{q\}$ by those values they assume when the $\{q\}$ are replaced by zeros. Therefore T may be expressed as a homogeneous quadratic function in $\{q\}$ with constant coefficients. If the $\{q\}$ are expressed in terms of normal coordinates the vibrational motions of the cluster may be resolved into a set of normal vibrations. Such vibrations are characterized by the facts that each atom executes simple harmonic motion and that all atoms vibrate in phase with the same frequency. These motions are dependent on the solution of the equations of motion (4.1)

$$\sum_{j=1}^{3N} \frac{d}{dt} \frac{\partial T}{\partial \dot{q}_j} + \frac{\partial V}{\partial q_j} = 0 \quad (4.1)$$

4.2.1 The Transformation to Normal Coordinates

The theory of normal coordinates is comprehensively treated by several authors (e.g. Whittaker (1937), Herzberg (1945), Wilson, Decius and Cross (1955)). In order to understand the following sections some salient points from normal coordinate theory are included below.

The Hamiltonian of a system is written $H = T+V$ where

$$\text{(kinetic energy)} \quad 2T = \sum_{ij} a_{ij} \dot{q}_i \dot{q}_j = \underline{\dot{q}}' \underline{A} \underline{\dot{q}} \quad , \quad (4.2)$$

$$\text{(potential energy)} \quad 2V = \sum_{ij} k_{ij} q_i q_j = \underline{q}' \underline{K} \underline{q} \quad , \quad (4.3)$$

and the prime signifies a matrix transpose. A transformation is required which reduces each of (4.2) and (4.3) to a sum of squares of $3N$ new variables. If the new variables are chosen to be $\{Q\}$, where $Q_i = a_{ii} q_i$, it is shown (Whittaker (1937)) that the kinetic and potential energies take the form

$$2T = \sum_{i=1}^{3N} \dot{Q}_i^2 = \underline{\dot{Q}}' \underline{1} \underline{\dot{Q}} \quad (4.4)$$

$$2V = \sum_{i=1}^{3N} c_i Q_i^2 = \underline{Q}' \underline{C} \underline{Q} \quad (4.5)$$

where $c_i = \frac{a_{ii}}{k_{ii}}$. In matrix language one requires the simultaneous reduction of \underline{A} and \underline{K} to a unit and diagonal matrix respectively.

If mass-weighted Cartesian coordinates are used, the kinetic energy matrix is already a unit matrix. Gwinn (1971) describes a procedure in which the normal coordinates are calculated in such a mass-weighted system. Unlike the methods used in chemical spectroscopy (see for example Wilson, Decius and Cross (1955)), Gwinn's method

involves no separation of rotational and translational motion until the potential energy matrix is diagonalized; consequently five or six zero frequencies are found which provide a useful check on the accuracy of the computation. No coupling between vibrational and rotational motion is assumed. The \underline{V} matrix is generated by the method outlined in 4.2.3, whilst the transformation which diagonalizes \underline{V} is the transformation from Cartesian to normal coordinates. Once the kinetic energy and potential energy matrices are established an orthogonal transformation is required to generate the normal coordinates. Such a transformation is possible since at least one form (the kinetic energy matrix) is positive definite (Whittaker (1937)).

4.2.2 The Kinetic Energy Matrix \underline{T}

The kinetic energy of an N-atom cluster in which each atom has mass m is, in Cartesian coordinates,

$$\underline{T} = \frac{m}{2} \sum_{i=1}^N (\dot{x}_i^2 + \dot{y}_i^2 + \dot{z}_i^2), \quad \text{which may be rewritten in}$$

matrix form as

$$2\underline{T} = \underline{\dot{R}}' \underline{m} \underline{\dot{R}} \quad (4.6)$$

In (4.6) $R_1 = x_1$, $R_2 = y_1$, $R_3 = z_1$, $R_4 = x_2$, etc. In such a form the kinetic energy matrix is already diagonal. If mass-weighted coordinates are used, in which $\{X\} = \{m^{\frac{1}{2}}R\}$, equation (4.6) reduces to

$$2\underline{T} = \underline{\dot{X}}' \underline{1} \underline{\dot{X}} \quad (4.7)$$

i.e. the kinetic energy matrix is reduced to a unit matrix.

4.2.3 The Potential Energy Matrix \underline{V}

The force constant K_{ij} is assumed to be the second derivative with respect to the distance r_{ij} between atoms i and j of the Lennard-Jones potential function. The potential energy matrix may be constructed in the following way (Gwinn (1971)). Considering the general term $K \cdot \delta r_{ij} \cdot \delta r_{\ell m}$, the variation of r_{ij} is written

$$\delta r_{ij} = \sum_k (\partial r_{ij} / \partial R_k) \delta R_k, \quad (4.8)$$

with

$$\frac{\partial r_{ij}}{\partial R_k} = \frac{R_r - R_s}{r_{ij}} = \phi_{k'ij}, \quad (4.9)$$

{ R } as defined in Section 4.2.2 and the coordinates R_k indexed for atom N as $3(N-1)+1$, $3(N-1)+2$, $3(N-1)+3$. In (4.9) the positive sign is taken if k corresponds to atom r , and the negative sign if k corresponds to atom s , with $k' = k$ modulo 3. The coefficients for each δR_i are stored and the process repeated for $\delta r_{\ell m}$. The two series are multiplied together, resulting in terms such as $K \phi_{r'ij} \phi_{s'\ell m} \delta x_r \delta x_s$. The coefficient $K \phi_{r'ij} \phi_{s'\ell m}$ is added to the r - s element of the \underline{V} matrix. Each force constant thus contributes to many elements of this \underline{V} matrix, which is an overlay of all the force constants. The \underline{V} matrix is easily converted to mass-weighted Cartesian coordinates by dividing all of the elements in each row and column by the square root of the mass of a constituent atom.

4.2.4 Diagonalization of the \underline{V} matrix

Once the \underline{V} matrix is established in mass-weighted Cartesian coordinates it only remains for this matrix to be diagonalized using

an orthogonal transformation. It is possible that the resulting diagonal matrix may not be positive definite - such an occurrence results in the production of imaginary frequencies. Physically this result implies that the potential energy surface is convex with respect to infinitesimally small movements of the atoms, indicating that the cluster is metastable or incompletely optimized. An incompletely optimized structure corresponds to one distorted by fictitious forces (Hoare and Pal (1972a)), resulting in an increase in computed frequencies (Rayleigh's Theorem). Since there has been no separation of rotational and translational motions the diagonalization procedure produces five or six zero frequencies, according as the cluster contains two or more atoms. The procedure used to diagonalize \underline{V} is the well-known variable threshold Jacobi method (see, for example, Wilkinson (1965)).

4.3 The Frequency Spectra of Real Systems

The normal vibrations of the optimized clusters described in Chapter 2 are determined by Gwinn's (1971) method and the normal frequencies thus obtained are used to calculate the harmonic partition functions. Chapter 5 details how thermodynamic properties may be estimated by use of these partition functions. Table 17 presents the frequency distribution of the most and least stable clusters in the size range $2 \leq N \leq 13$. Due to the scaling of the Lennard-Jones 6-12 potential (see equation (1.3)) it is necessary to multiply the frequencies in Table 17 by $\left(\frac{\epsilon}{m}\right)^{\frac{1}{2}} \cdot \left(\frac{1}{2^{1/6}\sigma}\right)$. These factors for the four rare gases considered here are calculated from the data in Table 11 and are contained in Table 16.

Table 16

<u>Ne</u>	<u>Ar</u>	<u>Kr</u>	<u>Xe</u>
3.93 x 10 ¹¹	4.13 x 10 ¹¹	3.22 x 10 ¹¹	2.57 x 10 ¹¹

Conversion Factors for Absolute Frequencies

One notes from this table that the argon frequencies are slightly greater than the neon frequencies, even though the argon atoms are almost twice as heavy as the neon atoms. However the argon well depth is nearly four times as deep as the neon well depth - consequently the more massive argon atoms vibrate with higher frequencies than do the neon atoms in a cluster of specified size and configuration. For the heavier clusters of krypton and xenon the frequencies decrease as the mass of the constituent atom increases.

Table 17

<u>N</u>	<u>v_i</u>
2	1.910
3	1.654(2), 2.339
4	1.350(2), 1.910(3), 2.701
5	1.062(2), 1.588, 1.868(2), 1.940(2), 2.516, 2.790
6 ₁	1.339(2), 1.415(3), 2.001(3), 2.451(3), 2.792
6 ₂	.731, .998, 1.451, 1.467, 1.600, 1.827, 1.984, 1.998, 2.148, 2.379, 2.747, 2.866.
7 ₁	1.051(2), 1.466(2), 1.503, 1.604(2), 1.967, 2.195(2), 2.222(2), 2.815, (2), 2.845
7 ₂	.657, .809, 1.097, 1.430, 1.561, 1.637, 1.657, 1.851, 1.978(2), 2.174, 2.451, 2.571, 2.835, 2.975

Table 17 Continued

<u>N</u>	<u>v_i</u>
8 ₁	.726, .996, 1.095, 1.421, 1.495, 1.582, 1.588, 1.670, 1.777, 1.866, 2.075, 2.181, 2.304, 2.364, 2.641, 2.844, 2.855, 3.089.
8 ₂	.536, .758, .834, 1.302, 1.337, 1.539, 1.597, 1.699, 1.829, 1.865, 1.909, 2.079, 2.137, 2.405, 2.547, 2.792, 2.943, 3.017
9 ₁	.953, .969, .999, 1.483, 1.498, 1.513, 1.523, 1.597, 1.667, 1.691, 1.790, 1.864, 2.140, 2.197, 2.389, 2.394, 2.583, 2.785, 2.872, 3.049, 3.283.
9 ₂	.522, .574, .698, 1.192, 1.248, 1.279, 1.525, 1.576, 1.686, 1.844, 1.846, 1.940, 1.956, 1.992, 2.138, 2.300, 2.557, 2.789, 2.814, 3.029, 3.070.
10 ₁	.917(2), 1.099, 1.349(2), 1.451, 1.532(2), 1.640(2), 1.650, 1.856, 1.902(2), 2.043, 2.162, 2.391(2), 2.637(2), 2.796, 2.911, 3.503(2).
10 ₂	.463, .513, .595, .942, 1.106, 1.262, 1.362, 1.472, 1.557, 1.707, 1.822(2), 1.875, 1.938, 1.985, 2.104, 2.109, 2.267, 2.443, 2.784, 2.814, 2.836, 3.602, 3.165
11 ₁	.849, .866, 1.059, 1.188, 1.355, 1.383, 1.452, 1.482, 1.524, 1.625, 1.659, 1.701, 1.779, 1.843, 2.000, 2.032, 2.150, 2.203, 2.282, 2.355, 2.553, 2.611, 2.690, 2.762, 3.068, 3.767, 3.847
11 ₂	.412, .441, .556, .771, 1.027, 1.059, 1.292, 1.401, 1.455, 1.567, 1.683, 1.803, 1.820, 1.825, 1.925, 1.935, 2.029(2), 2.221, 2.233, 2.385, 2.665, 2.828, 2.831, 2.898, 3.154, 3.188

Table 17 Continued

<u>N</u>	<u>ν_i</u>
12 ₁	.850(2), 1.199(2), 1.232, 1.244, 1.387(2), 1.627(4) 1.777(2), 1.809, 2.059(2), 2.084(2), 2.144(2), 2.310, 2.503(2), 2.512(2), 2.636, 3.688, 4.259(2)
12 ₂	.387, .396, .468, .675, .940, 1.003, 1.042, 1.330, 1.395, 1.476, 1.592, 1.699, 1.708, 1.790, 1.827, 1.875, 1.916, 1.965, 2.013, 2.090, 2.182, 2.314, 2.340, 2.557, 2.782, 2.833, 2.858, 2.974, 3.197, 3.227.
13 ₁	1.153(5), 1.564(4), 1.695(5), 1.828(3), 2.148(3), 2.164(4), 2.487(5), 2.693, 4.411(3)
13 ₂	.372, .392, .440, .632, .784, .841, 1.034, 1.174, 1.230, 1.357, 1.430, 1.560, 1.622, 1.658, 1.689, 1.827, 1.864, 1.896, 1.954, 1.974, 2.044, 2.077, 2.256, 2.389, 2.433, 2.489, 2.658, 2.709, 2.852, 2.965, 3.045, 3.294, 3.546

Scaled Vibrational Frequencies of the Most and Least Stable Isomers

Absolute frequencies are obtained by multiplying the scaled frequencies by the relevant factor from Table 16. The numbers in brackets are the numbers of degenerate vibrations.

The data in Table 17 show that the most stable clusters produce a greater number of degenerate vibrations than do the least stable. This is to be expected since in general the most stable clusters possess a higher order of symmetry than the less stable ones. As

the cluster size increases one sees a corresponding spread in frequencies. Acoustic type vibrational modes due to the co-operative movement of neighbouring atoms in the same direction produce the low frequencies, whilst the higher frequencies are due to 'breathing' modes. These latter modes constitute optical type modes, in which there is co-operative displacement of neighbouring atoms in opposite directions. Due to the small size of the clusters it is futile to attempt any identification of surface harmonics. Development of the acoustic modes is limited due to the size of the system: Figure 21 illustrates the tendency for the frequency spectra to split in distinct 'bands', thus making any transition from the bulk to the finite frequency spectrum impossible. Similar behaviour is observed by Dickey and Paskin (1968) in molecular dynamics experiments on platelets; these authors attribute such behaviour to the existence of surface and edge vibrational modes. One notes from the histograms in Figure 21 and from Table 17 the wider frequency spread associated with the less stable clusters, which tend to be irregular extended structures and are therefore capable of accommodating lower acoustic type vibrations. The histograms in Figure 21 show very little resemblance to the frequency spectra of infinite systems (Dickey and Paskin (1968)(1970)) or to the Debye model; however since the largest cluster considered here contains a mere thirteen atoms this result is not unexpected. The decrease in the low frequency end with increasing cluster size is observed; as the number of atoms tends to infinity one expects this decrease to tend to zero. However the finite size of the system establishes a lower limit to the frequency spectrum with small clusters possessing low frequency modes not seen in the bulk solid. Van Hove (1953) predicts

Frequency Histograms of Various Structures

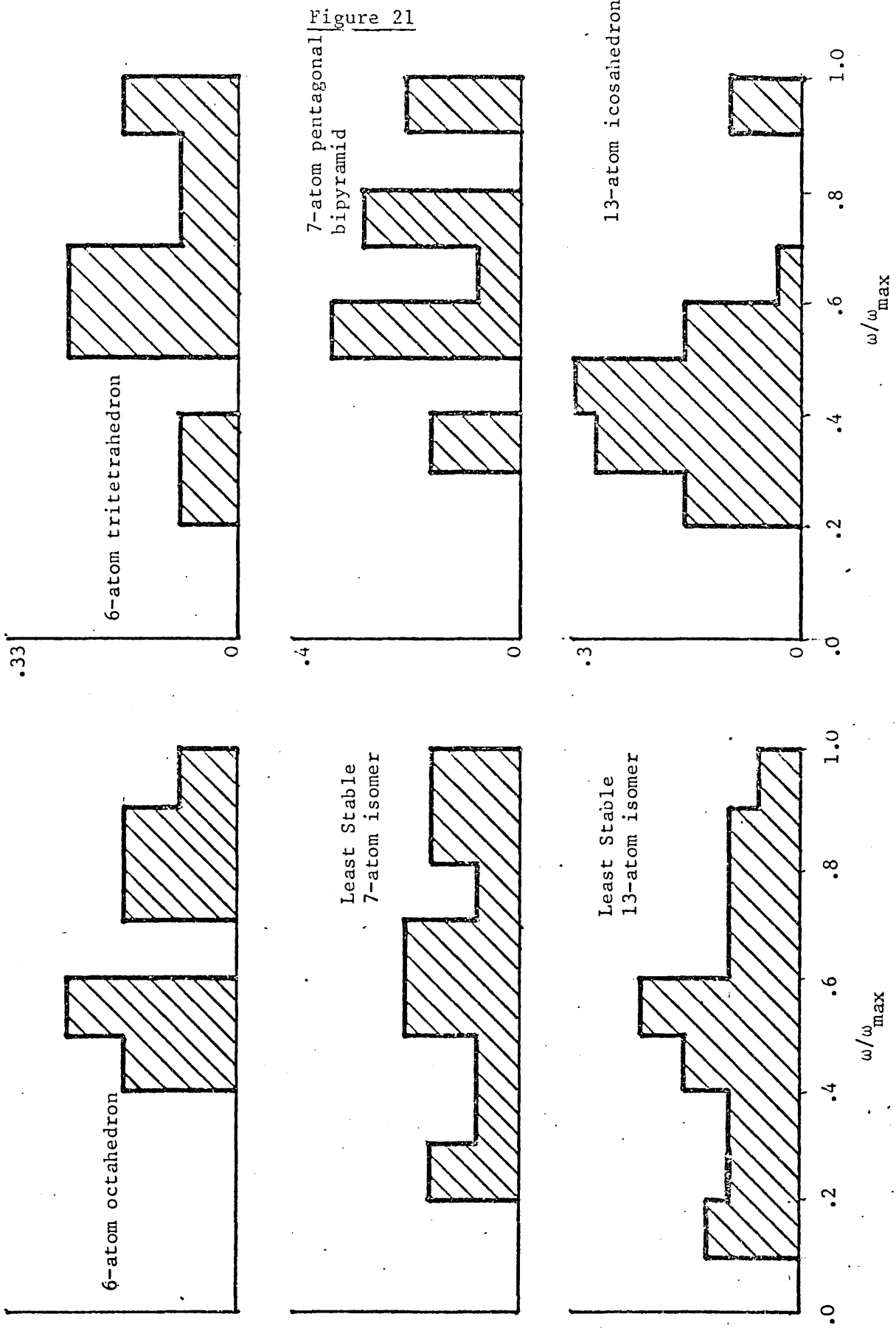


Figure 21

that the frequency distribution function of a crystal, assuming harmonic interatomic forces and periodicity, has singularities, as opposed to the smooth distribution function obtained by, for example, Blackman (1941). The frequency spectrum of the thirteen atom icosahedron (Figure 21) shows a gap which is reminiscent of the structure in the continuous spectra of infinite crystals. Newell (1953) shows such a gap in the frequency distribution of a simple cubic monatomic lattice. Dickey and Paskin (1970) illustrate the decreasing importance of bulk vibrational modes as the surface to volume ratio increases.

The clusters with high configurational symmetry (which in the case of the very small clusters considered here tend to coincide with the most stable clusters) possess frequency spectra which show a marked separation into frequency bands. These bands are due to the presence of degenerate vibrations; Hoare and Pal (1972a,1975) present frequency spectra which show the same qualitative trends as those in Figure 21, although their data are in all cases except one for systems containing more than thirteen atoms. The spectra of finite clusters enables an explanation of the thermodynamic properties described in Chapter 6 to be made.

4.4 Cluster Zero Point Energies

The cluster zero point energy per degree of freedom is calculated from

$$E_{\text{zero}} = \frac{E_{\text{zero}}}{i_{\text{max}}} = \frac{h}{2} \cdot \sum_{i=1}^{i_{\text{max}}} \nu_i \quad (4.10)$$

where the index i runs over all non-zero vibrational frequencies. In Table 18 the mean zero point energies per degree of freedom of clusters containing less than 7 atoms are presented.

Table 19 contains statistical analyses of the cluster zero point energies per degree of freedom for clusters in the range $7 \leq N \leq 13$. It is apparent from this table, taking due regard of the standard deviation, the mean zero point energy per degree of freedom \bar{E}_{zero} remains constant in the size range studied. The distribution curves are all platykurtic and except for $N = 11$ and $N = 12$ show positive skewness. For all N except $N = 8$ the most stable cluster also possesses the highest E_{zero} - for $N = 8$ the maximum value of E_{zero} is possessed by the most stable octahedral structure. The minimum potential energy N -atom clusters, with $7 \leq N \leq 10$, correspond to those clusters with minimum values of E_{zero} - for $N = 11$ and 12 octahedral structures have minimum E_{zero} values, whilst for $N = 13$ an elongated irregular cluster has the minimum E_{zero} . It is possible to conclude that in general clusters with high symmetry and consequently a number of degenerate vibrations possess higher zero point energies than the irregular, low symmetry clusters, which have a wider spread of frequencies (see Figure 21) but few, if any, degenerate vibrations.

Table 18

N	$\max E_{\text{zero}}$	$\min E_{\text{zero}}$	\bar{E}_{zero}	†
2	← $\times 10^4$ →		9.5492	
3			9.4116	
4	as \bar{E}_{zero}		9.2761	
5			9.2413	
6	9.6119	9.2908	9.4514	

Mean Lennard-Jones Zero Point Energies per Degree of Freedom

† absolute energies obtained on multiplying by $\left(\frac{\hbar}{2^{1/6} \sigma} \right) \cdot \left(\frac{\epsilon}{m} \right)^{1/2}$.

Table 19

N	$\max E_{\text{zero}}$	$\min E_{\text{zero}}$	\bar{E}_{zero}	s^{\dagger}	Skewness	Kurtosis
	$\times 10^1$			$\times 10^2$	$\times 10^1$	
7	9.6742	9.2201	9.4165	2.16	2.46	-16.45
8	9.6880	9.2016	9.3840	1.86	4.98	-11.90
9	9.8187	9.1839	9.4483	1.94	1.04	-8.50
10	9.9396	9.1676	9.4544	1.87	+2.00	-5.00
11	10.0159	8.9928	9.4854	2.00	-0.88	-2.76
12	10.1625	8.9275	9.5334	2.04	-0.74	-0.95
13	10.5226	9.1370	9.5595	2.15	+0.75	-0.44

Statistical Analyses of Lennard-Jones Zero Point Energies

Energies in the above table are per degree of freedom; absolute energies may be obtained on multiplying by $\left(\frac{h}{2^{1/6}\sigma}\right) \cdot \left(\frac{\epsilon}{m}\right)^{1/2}$.

\dagger Standard Deviation

Table 20 compares the maximum cluster zero point energies $\{\tilde{E}_{\text{max}}\}$,

(= $i_{\text{max}} \cdot E_{\text{max}}$), and the maximum potential energies at absolute zero. As the size of a cluster increases the zero point energy may make a sizeable contribution to the total cluster energy. However, Table 20 shows that for $2 \leq N \leq 13$ the potential energies at absolute zero are all approximately one order of magnitude larger than the corresponding zero point energies.

Table 20

	<u>N</u>					
	<u>2</u>	<u>3</u>	<u>4</u>	<u>5</u>	<u>6</u>	<u>7</u>
$\dagger i \times \max E_{\text{zero}} \dagger$	0.261	0.773	1.523	2.276	3.157	3.972
$N \times E_{\text{max}} \dagger$	1.654	4.962	9.923	15.06	21.02	27.30
	<u>N</u>					
	<u>8</u>	<u>9</u>	<u>10</u>	<u>11</u>	<u>12</u>	<u>13</u>
$\dagger i \times \max E_{\text{zero}} \dagger$	4.726	5.643	6.529	7.401	8.344	9.504
$N \times E_{\text{max}} \dagger$	32.78	39.88	47.01	54.19	62.79	73.30

Comparison of Maximum Cluster Zero Point Energies and Maximum Lennard-Jones Potential Energies at Absolute Zero for Argon Clusters

\dagger : i is the number of degrees of freedom

\dagger : all energies are measured in Joules $\times 10^{21}$

4.5 The Maximum Number of Vibrational Levels of L-J 6-12 Dimers

In this section the maximum number of vibrational energy levels of a harmonic oscillator in a well of depth ϵ is compared with the maximum number of dimer levels calculated by Stogryn and Hirschfelder (1959) using a WKB approximation. The implications of the discrepancy are noted.

Table 21

	<u>Ne</u>	<u>Ar</u>	<u>Kr</u>	<u>Xe</u>
Harmonic Approx.	1	3	6	9
WKB Calcs. (a)	3	9	16	26

Exact and Harmonic Energy Levels for Lennard-Jones Dimers

(a) *data from Stogryn and Hirschfelder (1959)*

The above table shows that the harmonic approximation predicts fewer dimer energy levels than does the WKB calculation. This result is expected since the harmonic approximation levels are equally spaced, see Table 22, whilst anharmonic effects cause the convergence of levels as higher energies are considered. A knowledge of the maximum number of vibrational dimer states enables one to determine an approximate temperature below which the use of classical mechanics is invalid in the evaluation of the partition functions. Classical statistical mechanics apply when the energy difference between two neighbouring states is very much less than kT . Since the rotational levels are very close we confine our interest to the vibrational states. For example, since Stogryn and Hirschfelder (1959) calculate nine dimer vibrational levels for argon, it may be argued that classical statistical mechanics are valid if $T^* \gg 1/9$. In the above authors' calculations of the maximum number of levels the angular quantum number l is assumed to be zero, since for $l > 0$ the effective potential well is made shallower and narrower, thereby

decreasing the number of energy levels. They state that quantum corrections for argon, krypton and xenon are small for $T^* \gtrsim .5$; for neon T^* needs to be greater than ~ 1.0 .

Table 22

	<u>Neon</u>	<u>Argon</u>	<u>Krypton</u>	<u>Xenon</u>	<u>Principal Quantum No.</u> <u>j</u>
ϵ^\dagger	0.491	1.654	2.361	3.051	
	0.248	0.261	0.204	0.163	0
	-	0.784	0.612	0.488	1
	-	1.307	1.020	0.813	2
	-	-	1.428	1.139	3
	-	-	1.836	1.464	4
	-	-	2.244	1.789	5
	-	-	-	2.115	6
	-	-	-	2.440	7
	-	-	-	2.765	8

Harmonic Energy Levels for Rare Gas Dimers

\dagger *Well depth*

All energies are measured in Joules $\times 10^{21}$

Since the harmonic approximation underestimates the number of levels one would expect the harmonic partition function to underestimate the 'exact' partition function - however a compensating and unfortunately non-separable influence, described in Chapter 10, also exists.

Chapter 5

5.1 Basic Statistical Thermodynamics

At sufficiently low temperatures we may adopt the RK-HO approximation (Farges et.al. (1973)) ; in this case the cluster hamiltonian may be separated into vibrational, rotational and translation components. Such a decomposition enables the cluster partition function $Z(N,T)$ to be written as a product of three sub-partition functions, as in equation (5.1)

$$Z(N,T) = Z_t(N,T)Z_r(N,T)Z_v(N,T)\exp\{-V(N)/kT\} \quad (5.1)$$

where t, r and v identify translational, rotational and vibrational contributions and $V(N)$ is the binding energy of the minimum about which vibration occurs. The thermodynamic functions of a solid-like N -atom cluster at temperature T may be written (Hill (1960)):

Helmholtz Free Energy

$$F(N,T) = -kT \ln Z(N,T) \quad (5.2)$$

Internal Energy

$$E(N,T) = kT^2 \frac{\partial \ln Z(N,T)}{\partial T} \quad (5.3)$$

Entropy

$$S(N,T) = kT \frac{\partial \ln Z(N,T)}{\partial T} + k \ln Z(N,T) \quad (5.4)$$

Heat Capacity

$$C_{vol}(N,T) = 2kT \frac{\partial \ln Z(N,T)}{\partial T} + kT^2 \frac{\partial^2 \ln Z(N,T)}{\partial T^2} \quad (5.5)$$

The partition function to be used in equations (5.2) to (5.5) may be either the single-configuration partition function (SCPF), identified by the subscripts sc, or the multi-configuration partition function (MCPF), identified by the subscripts mc.

5.2 The Single-Configuration Approximation

Assuming the rigid rotor/harmonic oscillator (RRHO) approximation standard texts on statistical thermodynamics (eg. Hill (1960)) present the single-configuration sub-partition functions listed below.

$$Z_{v,sc}(N,T) = \frac{3N-6}{\prod_{i=1} \exp\left[-\frac{h\nu_i}{2kT}\right] \left[1 - \exp\left\{-\frac{h\nu_i}{kT}\right\}\right]^{-1}} \quad (5.6)$$

$$Z_{r,sc}(N,T) = \frac{\pi^{1/2}}{X} \left[\frac{8\pi^2 kT}{h^2}\right]^{3/2} [I_a I_b I_c]^{1/2}, \quad N > 2 \quad (5.7)$$

$$Z_{t,sc}(N,T) = \left[\frac{2\pi m N k T}{h^2}\right]^{3/2} \cdot V: \quad Z_{r,sc}(2,T) = \frac{mkT}{2\hbar} r^{*2} \quad (5.8)$$

In the above equations

ν_i = the normal mode frequencies about the given minimum,

N = the number of atoms present,

T = the absolute temperature,

k = Boltzmann's constant, r^* = equilibrium separation,

X = the cluster symmetry factor, introduced to correct for repeated countings of indistinguishable clusters,

h = Planck's constant, $\hbar = h/2\pi$,

I_a, I_b, I_c = the principal moments of inertia of the cluster,

m = the mass of an individual atom,

V = the volume of the container.

Vibrational motion is considered to be quantised, leading to the quantum vibrational sub-partition function, whilst the rotational motion is assumed to be classical. Such an assumption is justified owing to the large moments of inertia of polyatomic molecules (Abraham and Pound (1968)) - however numerical results for neon indicate the increasing importance of quantum contributions as the atomic mass decreases.

Use of equations (5.1) and (5.6) to (5.8) with equations (5.2) to (5.5) produces the following equations for the single-configuration thermodynamic functions

$$\begin{aligned}
 {}_{sc}F(N,T) &= -kT \ln \left\{ \prod_{i=1}^{3N-6} \exp \left[-\frac{h\nu_i}{2kT} \right] \left[1 - \exp \left(-\frac{h\nu_i}{kT} \right) \right]^{-1} \right\} + V(N) \\
 {}_{sc}F_v(N,T) &= -kT \ln \left\{ \left[\frac{2\pi m N k T}{h^2} \right]^{3/2} V \right\} - kT \ln \left\{ \frac{[\pi I_a I_b I_c]^{1/2}}{\chi} \left[\frac{8\pi^2 k T}{h^2} \right]^{3/2} \right\} \\
 {}_{sc}F_t(N,T) & \qquad \qquad \qquad {}_{sc}F_r(N,T) \qquad (5.9)
 \end{aligned}$$

$$\begin{aligned}
 {}_{sc}E(N,T) &= \sum_{i=1}^{3N-6} \left[\frac{h\nu_i}{\exp(h\nu_i/kT) - 1} \right] + \frac{h}{2} \sum_{i=1}^{3N-6} \nu_i + V(N) + 3kT \\
 {}_{sc}E_v(N,T) & \qquad \qquad \qquad {}_{sc}E_t(N,T) + \\
 & \qquad \qquad \qquad {}_{sc}E_r(N,T) \qquad (5.10)
 \end{aligned}$$

$$\begin{aligned}
 {}_{sc}S(N,T) &= k \sum_{i=1}^{3N-6} \left\{ \left[\frac{h\nu_i/kT}{\exp(h\nu_i/kT) - 1} \right] - \ln \left[1 - \exp(-h\nu_i/kT) \right] \right\} \\
 {}_{sc}S_v(N,T) & \qquad \qquad \qquad {}_{sc}S_t(N,T) \qquad (5.11) \\
 &+ k \left[\frac{3}{2} - \frac{F_t(N,T)}{kT} \right] + k \left[\frac{3}{2} - \frac{F_r(N,T)}{kT} \right] \\
 & \qquad \qquad \qquad {}_{sc}S_r(N,T)
 \end{aligned}$$

$$\begin{aligned}
 {}_{sc}C_{vol}(N,T) &= k \sum_{i=1}^{3N-6} \left\{ \frac{(h\nu_i/kT)^2 \exp(h\nu_i/kT)}{[\exp(h\nu_i/kT) - 1]^2} \right\} + 3k \\
 {}_{sc}C_{vol,v}(N,T) & \qquad \qquad \qquad {}_{sc}C_{vol,t}(N,T) + {}_{sc}C_{vol,r}(N,T) \qquad (5.12)
 \end{aligned}$$

Equations (5.9) to (5.12) are used in Chapter 6 to calculate single-configuration thermodynamic quantities.

5.3 The Multi-Configuration Approximation

The single-configuration approximation described in the previous section involves the interpretation of the partition function in equations (5.2) to (5.5) as corresponding to only one stable configuration of N atoms. However, for each value of N there is a multiplicity of stable configurations (McGinty (1971),(1972)), each of which provides contributions to the 'exact' cluster partition function from the region of phase space in the neighbourhood of each minimum in the potential energy function. Consequently a more realistic representation of the cluster partition function, and subsequently of allied thermodynamic properties, is provided by the multi-configuration approximation in which contributions from all phase space are summed to produce a multi-configuration partition function. Thus

$$Z_{mc}(N,T) = \sum_{i=1}^C Z_{sc}(N,T)^{(i)} \quad (5.13)$$

where the summation runs over all geometrically distinct stable minima for clusters of N atoms. Each stable configuration k has corresponding vibrational, rotational and translational sub-partition functions, which, in the case of a separable hamiltonian, may be written

$$Z_{sc}(N,T)^{(k)} = \tilde{Z}_{v,sc}(N,T)^{(k)} Z_{r,sc}(N,T)^{(k)} Z_{t,sc}(N,T)^{(k)} \quad (5.14)$$

In (5.14) the tilde on the vibrational partition function indicates the absorption of the exponential factor in equation (5.1). Substitution of (5.14) into (5.13) produces

$$Z_{mc}(N,T) = \sum_{i=1}^C \tilde{Z}_{v,sc}(N,T)^{(i)} Z_{r,sc}(N,T)^{(i)} Z_{t,sc}(N,T)^{(i)}$$

which reduces to

$$Z_{mc}(N,T) = Z_{t,sc}(N,T)^{(1)} \sum_{i=1}^C Z_{v,sc}(N,T)^{(i)} Z_{r,sc}(N,T)^{(i)} \quad (5.15)$$

since the translational partition function is configuration-independent. Equation (5.15) is the full MCPF: a vibrational MCPF is obtained in a similar fashion by summing over all vibrational partition functions,

$$Z_{v,mc}(N,T) = \sum_{i=1}^C \tilde{Z}_{v,sc}(N,T)^{(i)} \quad (5.16)$$

The vibrational multi-configuration thermodynamic functions used in Chapter 7 are contained in equations (5.17) to (5.20), which are obtained via equations (5.2) to (5.6) and (5.16). A useful check on the validity of equations (5.17) to (5.20) may be made by comparing thermodynamic quantities calculated by the use of these equations when only one configuration exists with those obtained on using the vibrational components of the single-configuration equations (5.9) to (5.12).

$${}_{mc}F_v(N,T) = -kT \ln \sum_{i=1}^C \prod_{j=1}^{3N-6} \left[\frac{e^{-h\nu_j/2kT}}{1-e^{-h\nu_j/kT}} \right]_i \exp \left[\frac{|E_{o,i}|}{kT} \right] \quad (5.17)$$

$${}_{mc}E_v(N,T) = kT^2 \frac{\sum_{i=1}^C \left[\prod_{j=1}^{3N-6} \left\{ \frac{\partial \alpha_j}{\partial T} \cdot \frac{1}{\alpha_j} \right\}_i - \frac{E_{o,i}}{kT^2} \right] \cdot \prod_{j=1}^{3N-6} \left[\frac{e^{-h\nu_j/2kT}}{1-e^{-h\nu_j/kT}} \right]_i \cdot \exp \left[\frac{|E_{o,i}|}{kT} \right]}{\sum_{i=1}^C \prod_{j=1}^{3N-6} \left[\frac{e^{-h\nu_j/2kT}}{1-e^{-h\nu_j/kT}} \right]_i \cdot \exp \left[\frac{|E_{o,i}|}{kT} \right]} \quad (5.18)$$

$${}_{mc}S_v(N,T) = \frac{{}_{mc}E_v(N,T) - {}_{mc}F_v(N,T)}{T} \quad (5.19)$$

$${}_{mc}C_{vol,v}(N,T) = \frac{2 {}_{mc}E_v(N,T)}{T} + kT^2 \frac{\left[\delta - \eta^2 \left\{ \sum_{i=1}^C \prod_{j=1}^{3N-6} \left[\frac{e^{-h\nu_j/2kT}}{1-e^{-h\nu_j/kT}} \right]_i \cdot \exp \left[\frac{|E_{o,i}|}{kT} \right] \right\} \right]}{\sum_{i=1}^C \prod_{j=1}^{3N-6} \left[\frac{e^{-h\nu_j/2kT}}{1-e^{-h\nu_j/kT}} \right]_i \cdot \exp \left[\frac{|E_{o,i}|}{kT} \right]} \quad (5.20)$$

where α_j , $\frac{\partial \alpha_j}{\partial T}$, and $\frac{\partial^2 \alpha_j}{\partial T^2}$ are given by:

$$\alpha_j = \frac{e^{-h\nu_j/2kT}}{1 - e^{-h\nu_j/kT}} \quad (5.21)$$

$$\frac{\partial \alpha_j}{\partial T} = \left(\frac{h\nu_j}{2kT^2} \right) \cdot \left(\frac{e^{-h\nu_j/2kT}}{1 - e^{-h\nu_j/kT}} \right) \cdot \left(1 + \frac{2e^{-h\nu_j/kT}}{1 - e^{-h\nu_j/kT}} \right) \quad (5.22)$$

$$\begin{aligned} \frac{\partial^2 \alpha_j}{\partial T^2} &= \left(\frac{h\nu_j}{2kT^4} \right) \cdot \left(\frac{e^{-h\nu_j/2kT}}{1 - e^{-h\nu_j/kT}} \right) \cdot \left(\frac{h\nu_j}{k} \cdot \frac{e^{-h\nu_j/kT}}{(1 - e^{-h\nu_j/kT})} + \frac{h\nu_j}{2k} - 2T \right) \\ &\quad \left(\frac{h\nu_j}{kT^4} \right) \cdot \left(\frac{e^{-h\nu_j/2kT}}{1 - e^{-h\nu_j/kT}} \right)^2 \cdot \left(e^{-h\nu_j/2kT} \right) \cdot \left(\frac{2h\nu_j}{k} \cdot \frac{e^{-h\nu_j/kT}}{(1 - e^{-h\nu_j/kT})} + \frac{3h\nu_j}{2k} - 2T \right) \end{aligned} \quad (5.23)$$

with

$$\begin{aligned} \delta &= \sum_{i=1}^C \left\{ \prod_{j=1}^{3N-6} \left(\frac{e^{-h\nu_j/2kT}}{1 - e^{-h\nu_j/kT}} \right)_i \times \left(\frac{E_{o,i}}{kT} + 2 \right) \left(\frac{E_{o,i}}{kT^3} \right) \exp \left(\frac{+|E_{o,i}|}{kT} \right) \right. \\ &+ \prod_{j=1}^{3N-6} \left(\frac{e^{-h\nu_j/2kT}}{1 - e^{-h\nu_j/kT}} \right)_i \exp \left(\frac{+|E_{o,i}|}{kT} \right) \left[\sum_{j=1}^{3N-6} \left(\frac{\partial^2 \alpha_j}{\partial T^2} \cdot \frac{1}{\alpha_j} - \left[\frac{\partial \alpha_j}{\partial T} \cdot \frac{1}{\alpha_j} \right]^2 \right)_i + \left(\sum_{j=1}^{3N-6} \left[\frac{\partial \alpha_j}{\partial T} \cdot \frac{1}{\alpha_j} \right]_i \right)^2 \right. \\ &\left. \left. - 2 \prod_{j=1}^{3N-6} \left(\frac{e^{-h\nu_j/2kT}}{1 - e^{-h\nu_j/kT}} \right)_i \sum_{j=1}^{3N-6} \left(\frac{\partial \alpha_j}{\partial T} \cdot \frac{1}{\alpha_j} \right)_i \cdot \frac{|E_{o,i}|}{kT^2} \cdot \exp \left(\frac{+|E_{o,i}|}{kT} \right) \right\} \end{aligned} \quad (5.24)$$

and

$$\eta = \sum_{i=1}^C \left\{ \prod_{j=1}^{3N-6} \left(\frac{e^{-h\nu_j/2kT}}{1 - e^{-h\nu_j/kT}} \right)_i \exp \left(\frac{+|E_{o,i}|}{kT} \right) \left[\sum_{j=1}^{3N-6} \left(\frac{\partial \alpha_j}{\partial T} \cdot \frac{1}{\alpha_j} \right)_i - \frac{|E_{o,i}|}{kT^2} \right] \right\} \quad (5.25)$$

$(\nu_j)_i$ is the j^{th} vibrational frequency of the i^{th} configuration.

$|E_{o,i}|$ is the absolute value of the i^{th} potential energy minimum.

Derivations of equations (5.17) to (5.20) are contained in Appendix B.

In subsequent chapters the subscripts sc and mc are inserted only when ambiguity may arise through their omission.

The immense problem of identifying the symmetry factor of each N-atom cluster necessitates the introduction of an approximation to the full MCPF. This approximation involves the use of only the most symmetric cluster, thereby removing the requirement that all cluster symmetry factors are known. Thus

$$Z_{mc}(N,T) \approx Z_{t,sc}(N,T)Z_{r,sc}(N,T) \prod_{i=1}^C \tilde{Z}_{v,sc}^{(i)}(N,T) \quad (5.26)$$

This is the form of the MCPF used in subsequent calculations of equilibrium concentrations, equilibrium constants and free energies of formation - it is seen to be related to the vibrational MCPF by a simple multiplication factor.

5.4 Equilibrium Constants and Relative Equilibrium Concentrations

The equilibrium constant $K(N,T)$ of an N-atom cluster in equilibrium with the monomeric vapour at temperature T may be expressed in terms of the cluster partition function by using the principle of detailed balance. The grand canonical partition function is written

$$\Xi(\mu, V, T) = \sum_{N=0}^{\infty} \left\{ \sum_{\Sigma} \exp \left[\frac{\mu(N,T)C(N,T)}{kT} \right] \frac{\hat{Z}(N,T)^{C(N,T)}}{C(N,T)!} \right\} \quad (5.27)$$

In equation (5.27)

- (i) the outer summation is over all 'phases' of the system,
- (ii) $C(N,T)$ is the number of clusters of size N at temperature T per unit volume,
- (iii) $\mu(N,T)$ is the chemical potential of the N^{th} phase at temperature T ($\mu(N,T) = N\mu(1,T)$),
- (iv) $\hat{Z}(N,T)$ is the N-atom cluster partition function per unit volume at temperature T (given by equation (5.26) divided by the volume V).

Let us now consider clusters of size N only and drop the explicit temperature dependence to simplify notation. The contribution to the grand canonical partition function from the N^{th} phase ($\Xi_{\text{phase } N}$) is the term in curly brackets in equation (5.27). The average population of N -atom clusters $\langle C(N) \rangle$ is given by (Hill (1956))

$$\langle C(N) \rangle = kT \frac{\partial \ln \Xi_{\text{phase } N}}{\partial \mu(N)} \quad (5.28)$$

From equation (5.27)

$$\begin{aligned} \Xi_{\text{phase } N} &= \sum_{C(N)} \frac{\left[\hat{Z}(N) \exp\left(\frac{\mu(N)}{kT}\right) \right]^{C(N)}}{C(N)!} = \\ &= \exp \left[\hat{Z}(N) \exp\left(\frac{\mu(N)}{kT}\right) \right] \end{aligned} \quad (5.29)$$

In equation (5.29) the relationship

$$\exp(Y) = \sum_{n=1}^{\infty} \frac{Y^n}{n!}$$

has been used.

Equations (5.28) and (5.29) lead to

$$\frac{\langle C(N) \rangle}{\hat{Z}(N)} = \exp \left[\frac{\mu(N)}{kT} \right] = \left[\frac{\langle C(1) \rangle}{\hat{Z}(1)} \right]^N, \quad (5.30)$$

or in a more familiar form

$$\frac{\langle C(N) \rangle}{\langle C(1) \rangle^N} = \frac{\hat{Z}(N)}{\hat{Z}(1)^N} = K(N) \quad (5.31)$$

The equilibrium constant of an N -atom cluster (at temperature T) may therefore be expressed in terms of the N -atom cluster partition function and the monomer partition function.

For two geometrically distinct N-atom clusters A and B, differing in free energy by $\Delta F = F(N,T)_A - F(N,T)_B$, the relative equilibrium concentration of cluster A to cluster B at temperature T is written

$$\frac{C(N,T)_A}{C(N,T)_B} = \exp \left[- \frac{\Delta F}{kT} \right], \quad (5.32)$$

in which the free energy of each cluster is calculated according to equation (5.2). Use of equations (5.1), (5.2) and (5.32) enables the relative equilibrium concentration of two N-atom clusters at temperature T to be written

$$\frac{C(N,T)_A}{C(N,T)_B} = \frac{Z(N,T)_A}{Z(N,T)_B} \quad (5.33)$$

The temperature dependence in equation (5.33) is suppressed in future references unless ambiguity may arise by this suppression.

Chapter 6

6.1 Introduction

The vibrational single-configuration thermodynamic properties of monatomic systems of rare gas clusters interacting through a Lennard-Jones 6-12 potential are presented in this chapter. Vibrational cluster frequencies are calculated as detailed in Chapter 4 and these frequencies used in equations (5.9) to (5.12). Graphs of free energies, entropies and heat capacities are plotted as a function of reduced temperature, and the T^3 dependence of the heat capacities at low temperatures ($\leq 5^\circ\text{A}$) investigated. Configurational thermodynamic properties for Lennard-Jones and Morse clusters are calculated and comparison is made of the relative contributions of vibrational and configurational components to cluster properties. Configurational heat capacities and entropies are found to be independent of the chemical species; it is suggested (Gibbs (1960), Adam and Gibbs (1965), Goldstein (1973a)) that configurational entropy is a major factor in precipitating the glass transition.

6.2 Vibrational Single-Configuration Internal Energies

Cluster internal energies are calculated using the vibrational component of equation (5.10). The internal energy may be naturally divided into thermal, zero-point ($E_{\text{zero}}(N)$) and potential ($V(N)$) contributions (respectively the first three terms in equation (5.4)). Thus to compare cluster stabilities even at absolute zero it is necessary to compare values of $E_{\text{zero}}(N) + V(N)$ rather than values of the classical potential energy $V(N)$. As the depth of the potential well increases the zero-point contribution decreases; for the heavier

krypton and xenon clusters the potential well supports very many more bound states (see Table 21) and zero-point energy effects become almost negligible. For cluster of neon and to a lesser extent argon such effects are no longer negligible. Zero-point energies are included in the thermodynamic calculations presented here - the zero temperature limits of the free energy curves in Figures 22 and 23 correspond to $V(N) + E_{\text{zero}}(N)$ rather than to the classical potential energy $V(N)$ (Table 6).

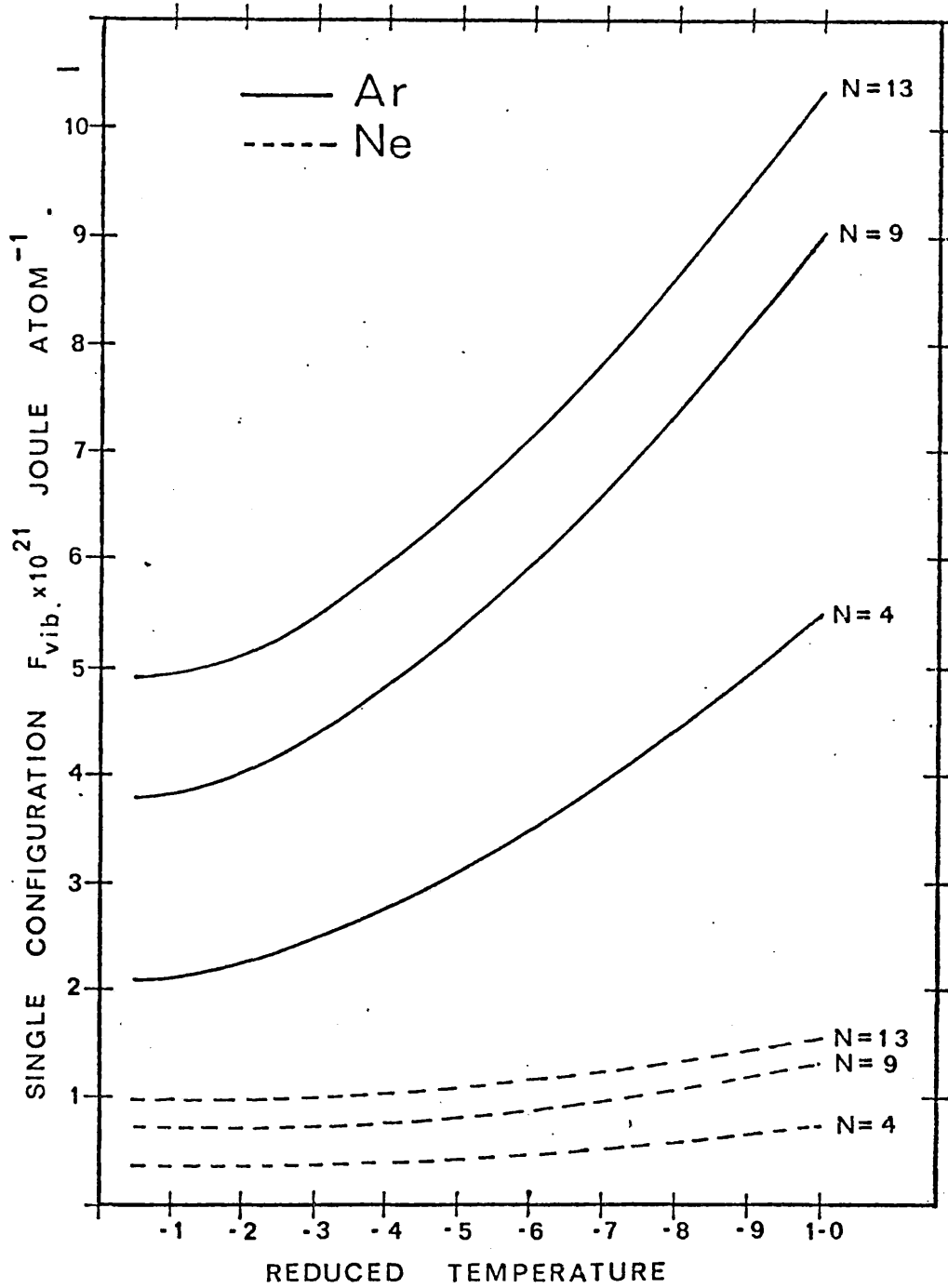
6.3 Vibrational Single-Configuration Free Energies

Use of the first term in equation (5.9) enables calculations of the vibrational single-configuration free energies of N-atom clusters to be made. This term may be written

$${}_{\text{sc}}F_v(N,T) = kT \sum_{i=1}^{3N-6} \frac{h\nu_i}{2kT} + kT \sum_{i=1}^{3N-6} \ln \left[1 - \exp \left(-\frac{h\nu_i}{kT} \right) \right] + V(N) \quad (6.1)$$

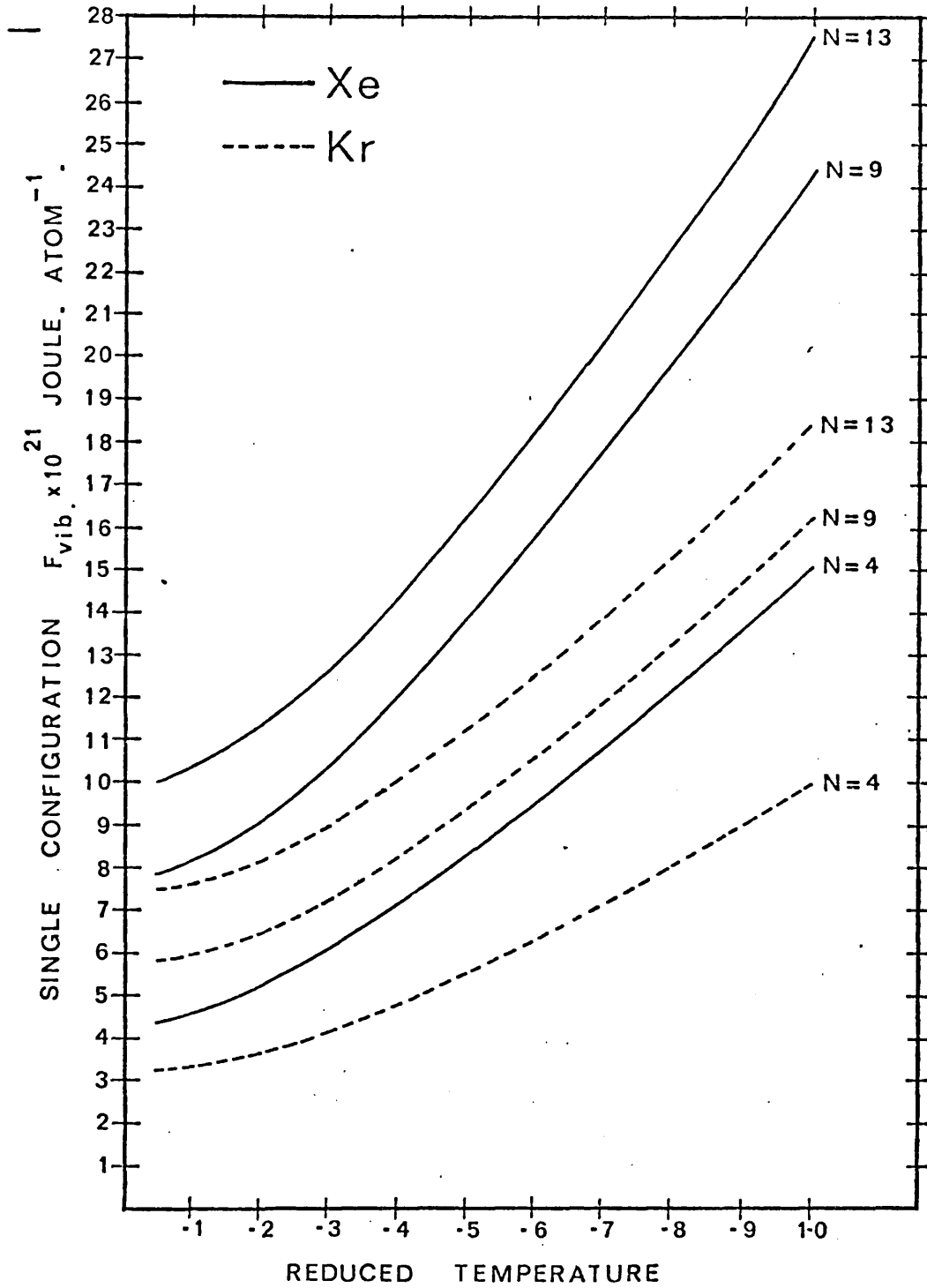
where the first contribution represents the zero-point energy for the $3N-6$ vibrations, the last contribution is the binding energy of the minimum about which vibration occurs, and the middle contribution reflects the entropic effects (see equation (6.2)). Equation (6.1) illustrates the conflict between energetic and entropic effects in cluster free energies. It is seen in Figure 22 that for values of $T^* \lesssim .3$ for neon clusters and $T^* \lesssim .1$ for argon clusters the cluster free energies per atom remain almost constant; i.e. entropic effects below $10-12^\circ\text{A}$ are negligible (McGinty (1971), Hoare and Pal (1972a,1975)). The curves in Figure 23 show a steady decrease in free energy per atom from the lowest reduced temperature plotted - since this reduced

Figure 22



Free Energy: Reduced Temperature

Figure 23



Free Energy: Reduced Temperature

temperature corresponds to an absolute temperature of $\sim 17^\circ$ for krypton and $\sim 22^\circ$ for xenon one may conclude that at these temperatures there are non-negligible entropic contributions to cluster free energies. Figures 22 and 23 indicate that the free energy per atom decreases virtually monotonically with both T^* and N ; no structure is seen in these curves. With increasing atomic mass the absolute free-energy per atom increases, as shown clearly in these figures.

The weak entropic contributions at temperatures below approximately 12°A reinforces the assumption that energy-minimized clusters are also thermodynamically favourable (Hoare and Pal (1972a,1975)). Equation (6.2) presents the energy-entropy competition in a more transparent manner.

$$\begin{aligned}
 F(N,T) &= E(N,T) - TS(N,T) \\
 &= \sum_{i=1}^{3N-6} \left[\frac{h\nu_i}{\exp(h\nu_i/kT)-1} + \frac{h\nu_i}{2} \right] - T \left[S(N,T) \right] + V(N)
 \end{aligned}
 \tag{6.2}$$

The free energy of formation of an N -atom cluster from the ideal monomer at specified temperature and pressure is calculated in Chapter 9 for $N \leq 13$. The free energies thus calculated are compared to those obtained by McGinty (1971) for crystalline structures to determine whether the potential energy advantage of microcrystallites over crystalline forms is maintained as a thermodynamic advantage in the rigid rotor/harmonic oscillator approximation (Chapter 9).

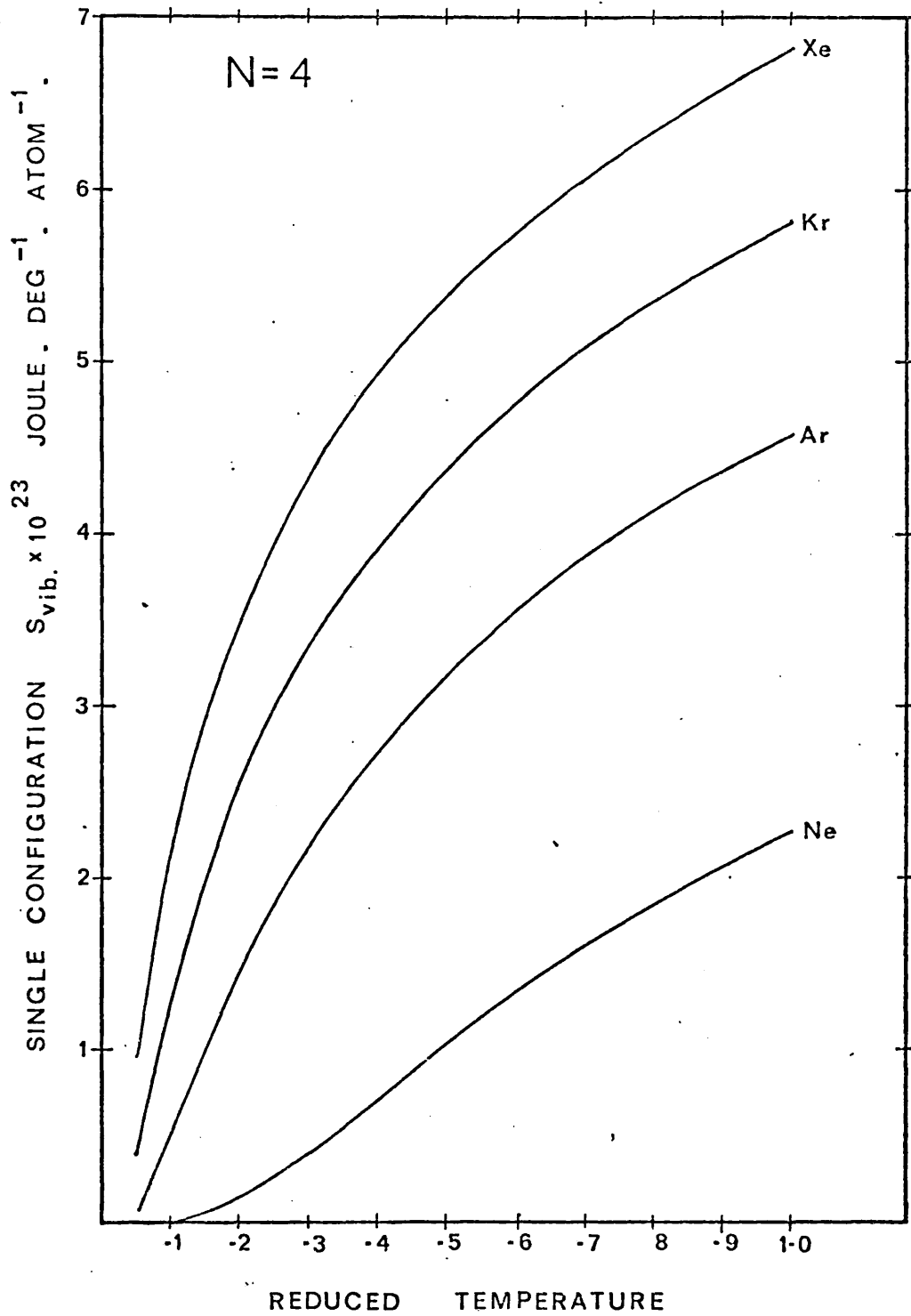
6.4 Vibrational Single-Configuration Entropies

Cluster entropies are calculated according to equation (5.11) and the entropy per atom $S(N,T)/N$ for the four rare gases are plotted in

Figures 24 to 27 . These curves show an increase in $S(N,T)/N$ with both T^* and atomic mass. No structure is seen on these curves nor any tendency for the entropy per atom to rise to a maximum and subsequently decrease (see Burton (1970a,1972b) who suggests an entropy 'peak' at $N=40$). With increasing N the entropy per atom approaches a limit - such behaviour is consistent with the conclusion of Hoare and Pal (1972a,1975) that $S(N,T)/N$ remains approximately constant for clusters containing more than 20 atoms. This tendency to remain constant implies that any change in the free energy per atom is due to energetic rather than entropic effects for clusters containing more than 20 atoms. It is possible that the constant entropy per atom (for $N>20$) is an artifact due to the harmonic oscillator approximation; computer calculations using exact equations of motion may be used to confirm or deny this hypothesis. The molecular dynamical calculations of Kristensen et al (1974) do not provide any systematic study of the variation of entropy with size, although they do simulate pre-melting phenomena in clusters containing between 55 and 429 atoms.

As is shown in equation (6.2), the existence of entropy sources indicates a tendency for a condensed nucleus to remain stable if the internal energy remains constant. A highly symmetric cluster has less high frequency modes (Table 17) and therefore possesses higher entropy (Burton (1972b), Kanamori (1960)); on the other hand a tightly packed cluster has less low frequency modes which results in an entropy decrease (Hoover et al (1972)). If a low saddle point is associated with a particular minimum in the potential energy space (i.e. the minimum has at least one large radius of curvature) more regions of phase space are accessible to the N -atom cluster and the entropy is

Figure 24



Entropy: Reduced Temperature

Figure 25

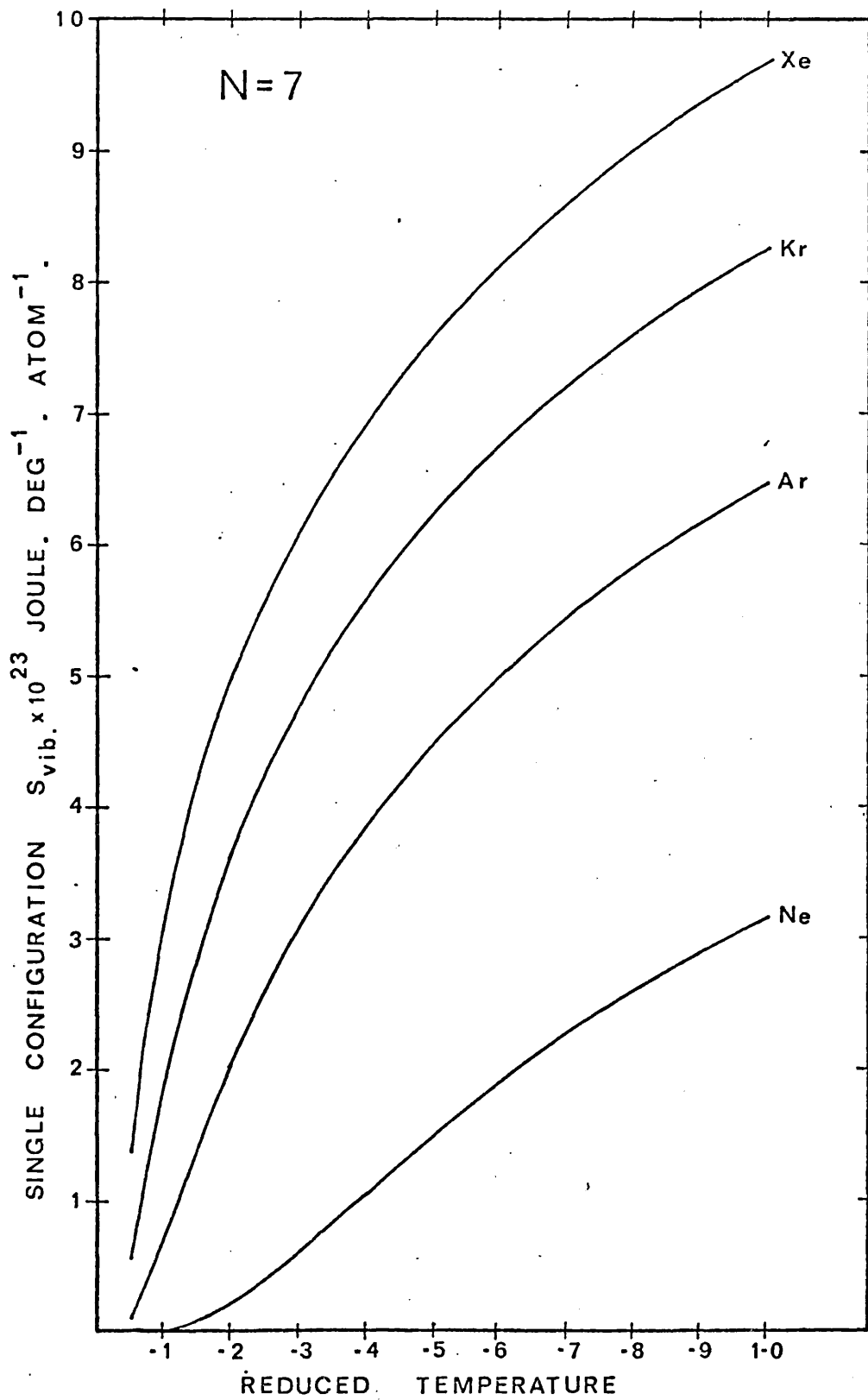


Figure 26

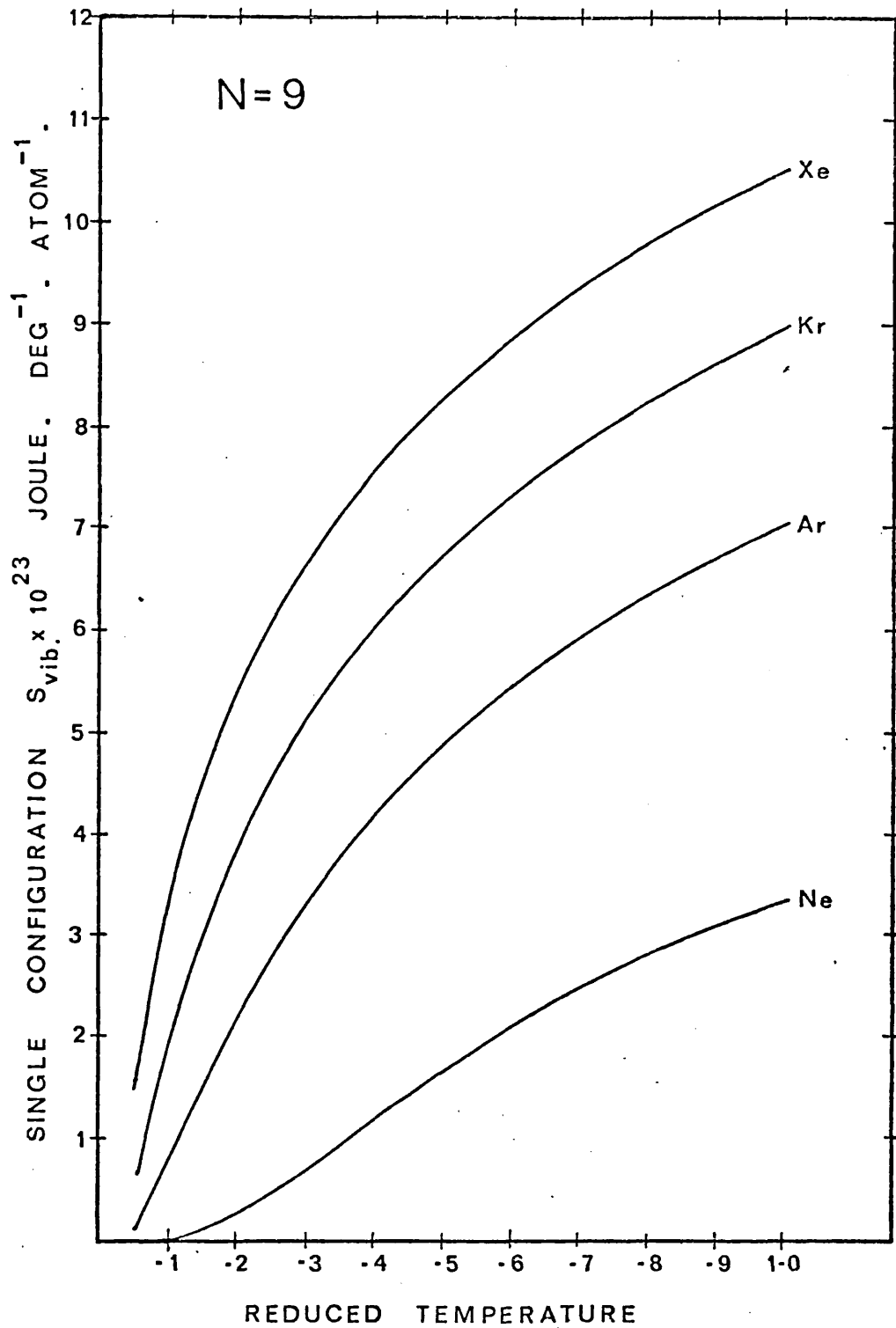
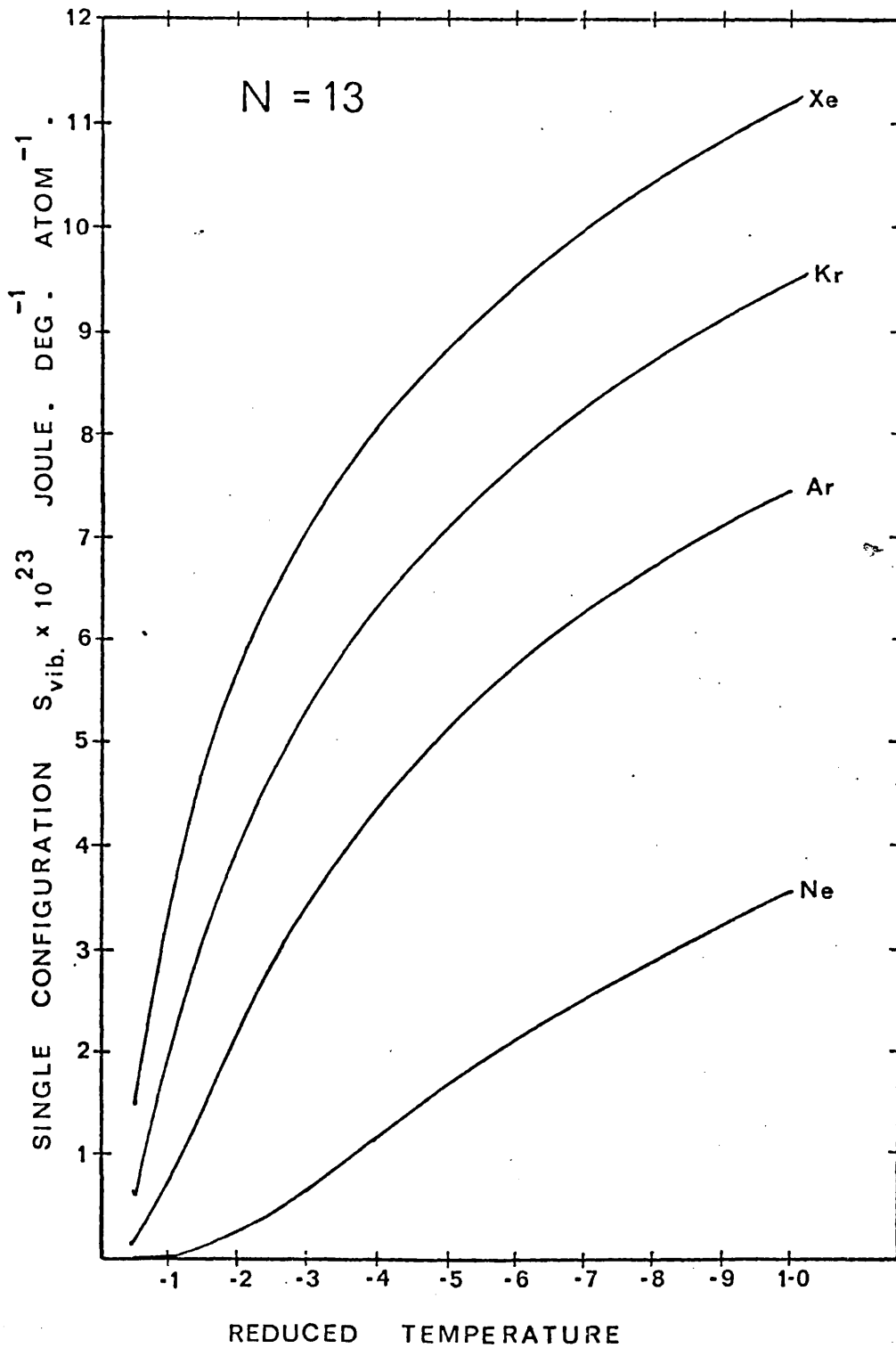


Figure 27



Entropy: Reduced Temperature

correspondingly higher. Related to the latter factor is the effect of isomer multiplicity; the greater the multiplicity the greater the entropy is since more minima exist in the potential energy space. As a further complication discrete clusters have low frequency edge vibrational modes which cause the generation of higher entropy (Burton (1972b)). Edge effects are particularly important for clusters of the size studied here - these clusters have high surface to volume ratios.

It is important not to underestimate entropic contributions to the free energy since the basic competition between internal energy and entropy (equation (6.2)) may cause clusters which are not minimal in binding energy to become minimal in free energy. Entropic effects at temperatures less than 10-12°A are very weak (Figures 22 and 23); at higher temperatures entropic contributions increase in importance with increasing N, although as N approaches 12 and 13 this increase appears to approach a limit.

The entropy excess per atom at $T^* = .7$ (approximately the melting temperature for the species), relative to the corresponding infinite crystalline solids, is calculated for various sized clusters of each gas (Table 23). Equation (6.3) (Pal (1972)) is used to approximate the entropy per atom for the infinite solid,

$$\frac{S}{k} = 3 \left[\frac{4}{3} - \ln \left(\frac{\theta}{T} \right) + \frac{1}{40} \left(\frac{\theta}{T} \right)^2 - \frac{1}{2240} \left(\frac{\theta}{T} \right)^4 + \dots \right] \text{ per atom} \quad (6.3)$$

in which θ is the Debye temperature.

Table 23

	$\theta^{\circ}\text{A}$	$T^{\circ}\text{A}$	$k\Delta S \text{ Joule deg}^{-1} \text{ atom}^{-1}\dagger$			
			<u>N=4</u>	<u>N=7</u>	<u>N=9</u>	<u>N=13</u>
Ne	75	24.92	-.106	.361	.511	.542
Ar	92	83.86	-1.020	.131	.479	.700
Kr	72	119.70	-1.863	-.330	.130	.471
Xe	64	154.7	-2.250	-.408	.144	.582

\dagger : k is Boltzmann's constant.

Entropy Excess per Rare Gas Atom

Table 23 shows that the entropy excess per atom increases with N for all gases. This excess implies that clusters containing less than 14 atoms may form nuclear 'seeds' under suitable conditions. Since the entropy excess per atom is increasing, albeit slowly, as N approaches 13 it seems that the larger clusters in the range considered here are more likely to form nuclear embryos than clusters containing 4-9 atoms. As N increases above 13 it is apparent that the entropic contribution to the free energy of formation of critical nuclei decreases in importance, indicating that energetic effects govern the formation of larger critical nuclei.

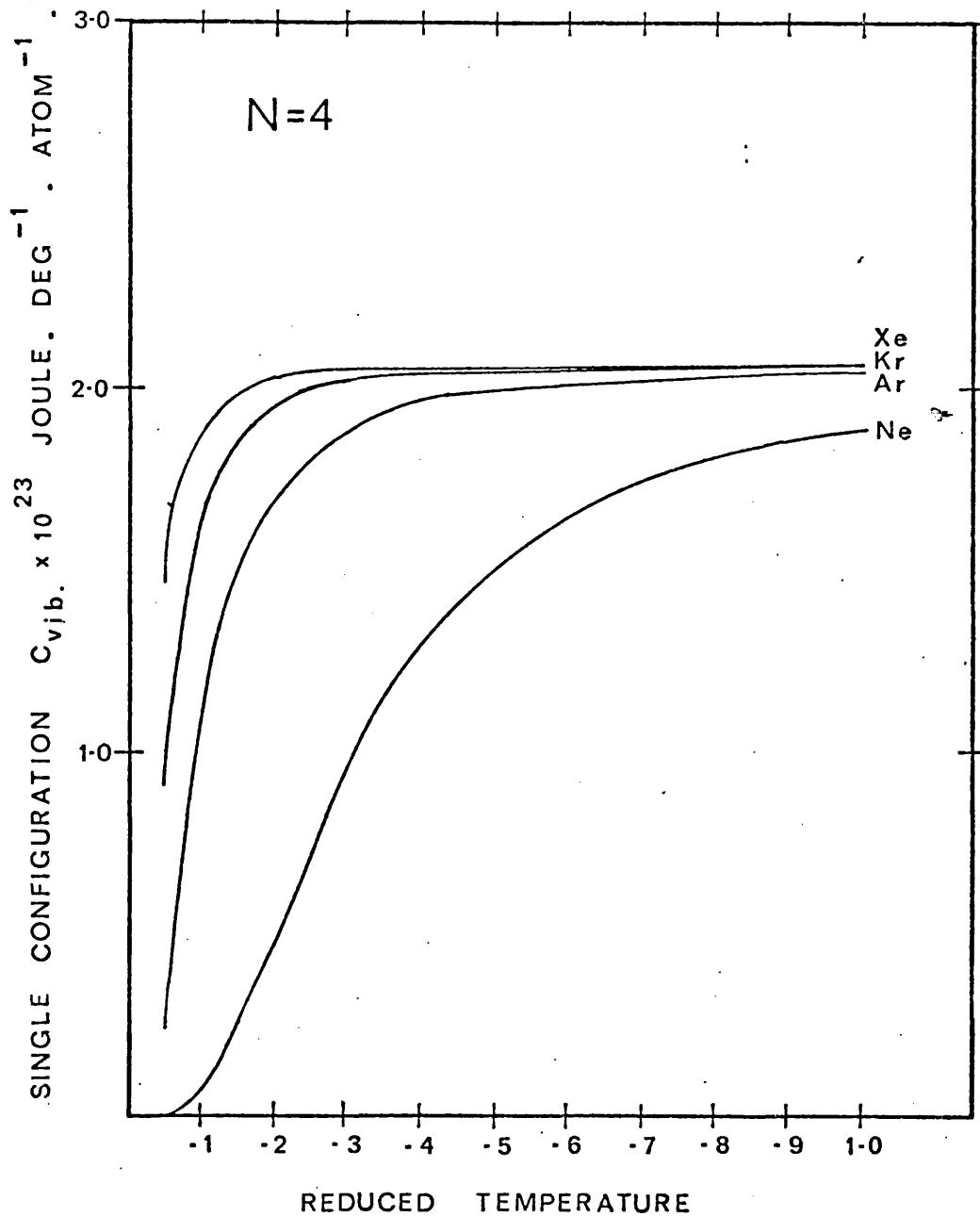
6.5 Vibrational Single-Configuration Heat Capacities

The vibrational S-C heat capacities ($C_{sc, vol, v}^{(N, T)}$) of small clusters of rare gases, calculated by use of equation (5.12), are plotted in Figures 28 to 31 as functions of reduced temperature T^* . These curves illustrate the following trends in cluster heat capacities:

- (i) $C_{sc\ vol, v}^{(N, T)}$ per atom increases with increasing N for all $T^* \leq 1$ (Figure 30);
- (ii) " " " per degree of freedom decreases with increasing N for all $T^* \leq 1$;
- (iii) " " " per atom increases as the mass of the cluster atoms increases for all $T^* \leq 1$ (Figures 28 and 29);
- (iv) as the cluster temperature approaches the appropriate Debye temperature θ ($\theta = h\omega/k$, where ω is the phonon spectrum cut-off frequency and k is Boltzmann's constant) the $C_{sc\ vol, v}^{(N, T)}$ per atom: T^* curves level out for argon, krypton and xenon clusters - the neon curves show no such behaviour since the Debye temperature for neon (75°A) corresponds to a reduced temperature of 2.1 (Figures 28 and 31);
- (v) no structure is seen in the $C_{sc\ vol, v}^{(N, T)}$ curves.

Attempts have been made by various authors (Jura and Pitzer (1952), Maradudin (1963), Burton (1969, 1970a, b), Hoare and Pal (1972a, 1975)) to explain the anomalous behaviour of the heat capacities exhibited by finite clusters. Nonnenmacher (1975) shows that such anomalous behaviour follows from a qualitative discussion of the asymptotic behaviour of the heat capacity formulae in the high and low temperature limits. The vibrational spectrum of the cluster governs the calculated heat capacity (equation (5.12)) - the spectrum is itself dependent on the cluster size and shape. As the cluster size decreases the vibrational spectrum contains fewer low frequency modes (Table 17 in Chapter 4); the low frequency vibrations provide larger contributions to the heat capacity than do higher frequency modes. The absence of these

Figure 28



Heat Capacity: Reduced Temperature

Figure 29

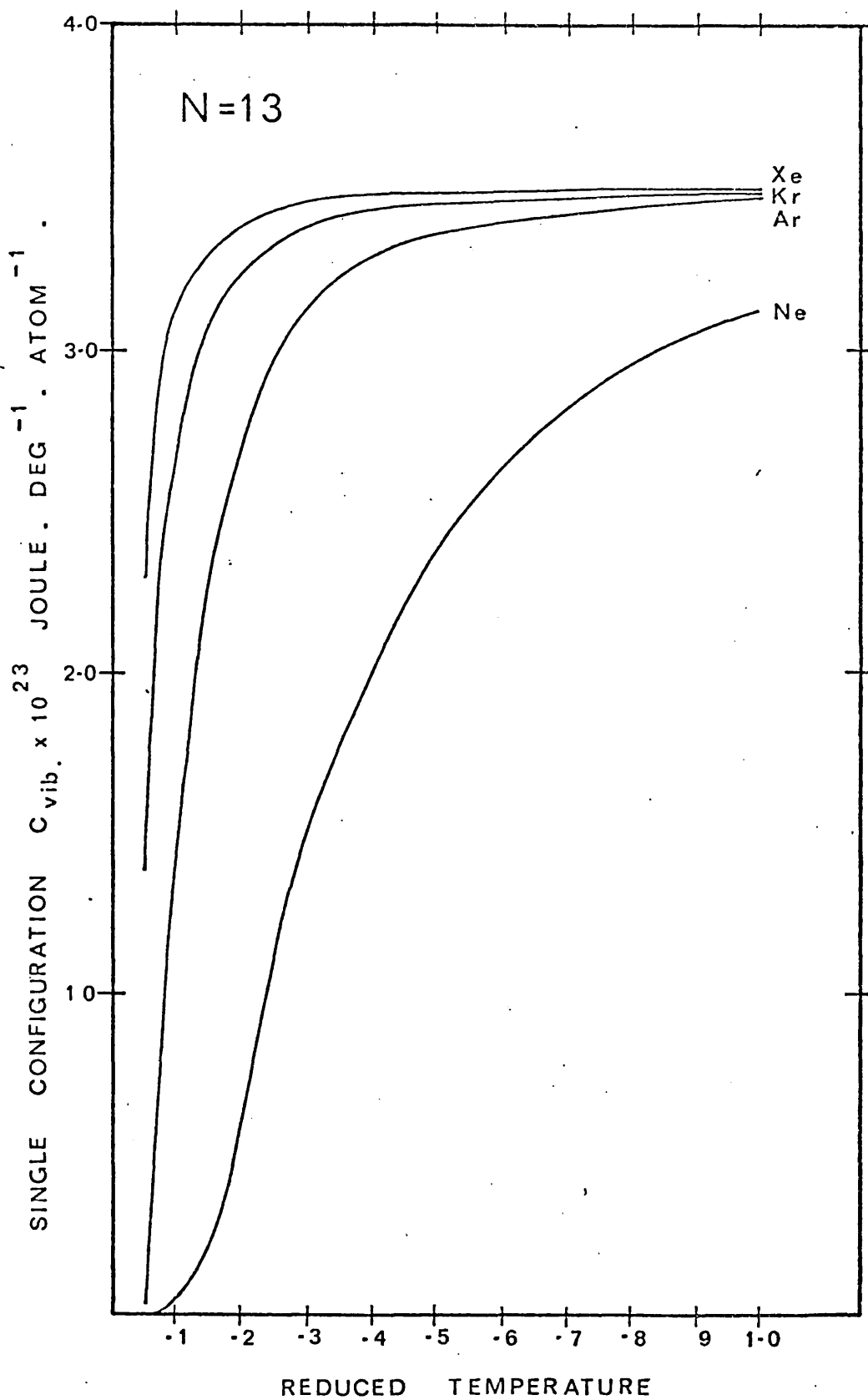
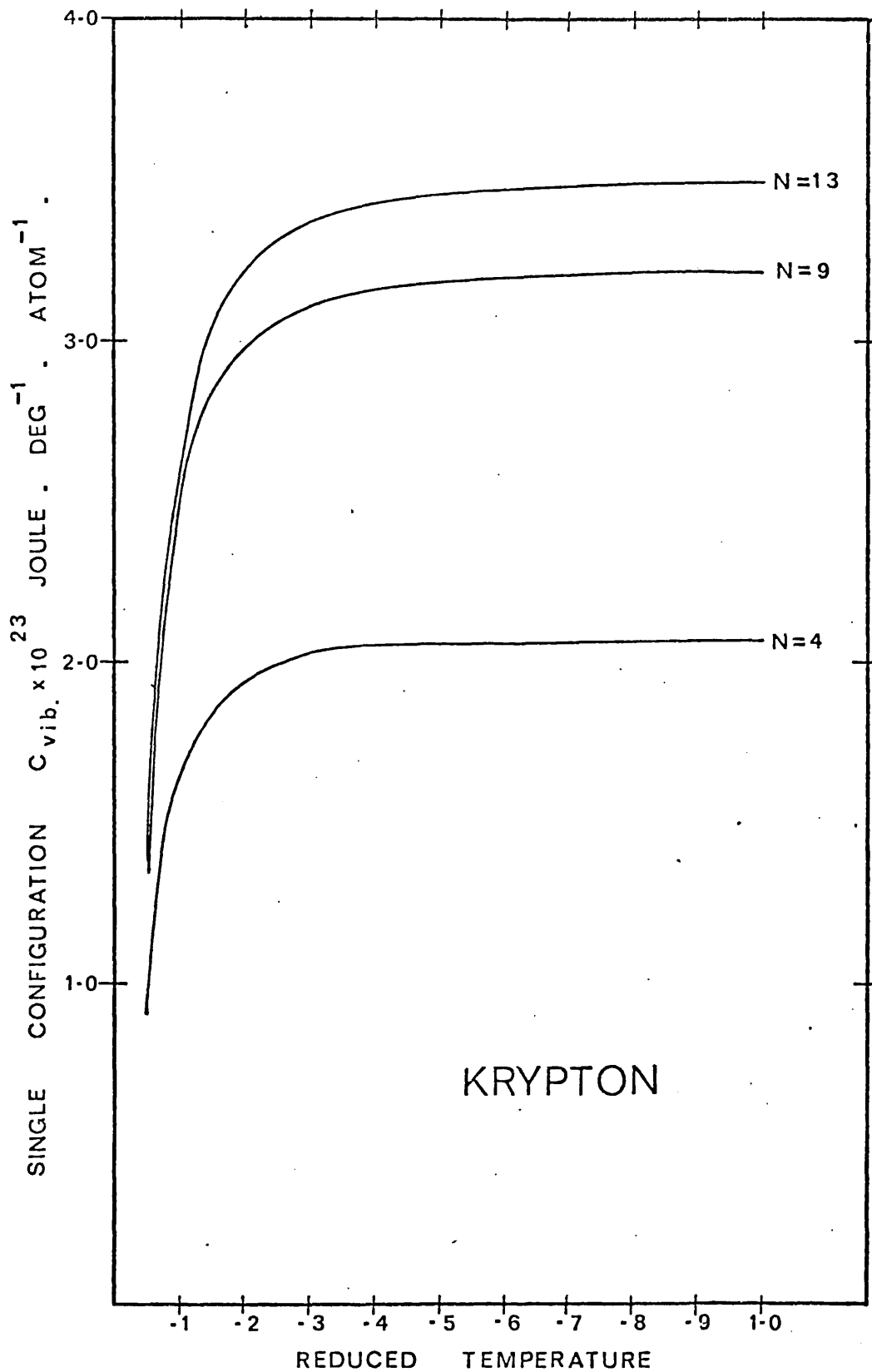
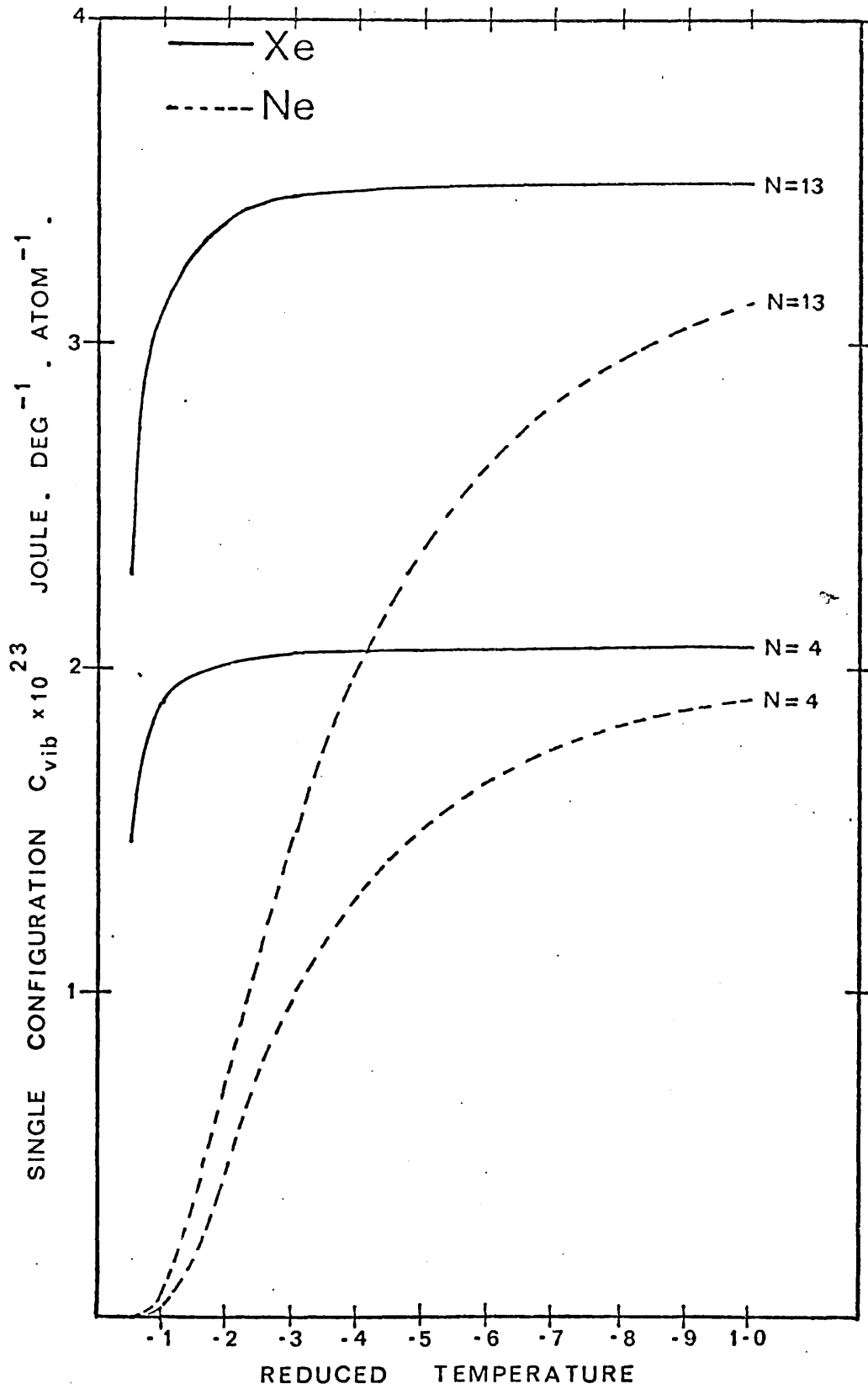


Figure 30



Heat Capacity: Reduced Temperature

Figure 31



Heat Capacity: Reduced Temperature

lower modes in small clusters therefore contributes comparatively little to the heat capacities of these clusters, leading to a decrease in heat capacity per atom as N decreases ((i) above). The deficiency of vibrational degrees of freedom as N decreases becomes more pronounced, as reflected in (ii) above.

Montroll (1950) derives the following equation (6.4) for the heat capacity per atom of a semi-infinite solid:

$$C_{\text{vol,vol}} = \frac{12\pi^4 k}{5} \left(\frac{T}{\theta}\right)^3 + \frac{9k\xi(3)}{4} (12\pi)^{1/3} \left(\frac{S}{V^{2/3}}\right) \frac{C_3^{2/3}}{C_2} \frac{1}{N^{1/3}} \left(\frac{T}{\theta}\right)^2 \quad (6.4)$$

per atom.

In equation (6.4) $\xi(3)$ is the Riemann zeta function, C_3 and C_2 are related to the velocities of propagation of longitudinal and transverse elastic waves in the crystal (c_l and c_t) by:

$$C_i^{-1} = c_l^{-1} + 2c_t^{-1} \quad (6.5),$$

and S and V are the crystal's surface area and volume respectively. Equation (6.4) presents two components of the vibrational heat capacity per atom; one proportional to T^3 (the Debye law) and the other proportional to T^2 . It is evident from equation (6.4) that for high surface to volume ratios the T^2 contribution to the heat capacity increases in importance (between .5 and 10 per cent of the total heat capacity at 1°A (Montroll (1950))). Jura and Pitzer (1952) indicate that changes in the shape of a cluster, leading to a greater surface area for the same volume, are important factors governing heat capacity increases. The computer simulations of Dickey and Paskin (1970) show the increasing importance of surface modes as the cluster size decreases; Fröhlich (1937) provides a discussion of the effect of cluster size on low temperature heat capacities.

The first term in equation (6.4) is used to calculate the heat capacity per atom of semi-infinite crystals of neon and argon at a reduced temperature of .05 and .1. These data are presented in Table 24, with the heat capacities per atom of 13-atom clusters calculated by use of equation (5.12). We see that the semi-infinite crystal has a lower heat capacity than the finite cluster at $T^* = .1$ but a higher value at $T^* = .05$. The reduction in Debye temperature at very low temperatures (Blackman (1937)) increases the heat capacities of finite clusters; on the other hand the heat capacities of finite clusters fall faster to zero than do those of the semi-infinite crystal as $T \rightarrow 0$. The latter effect is due to the lack of relatively low frequencies in finite clusters; the exponential term in equation (5.12)

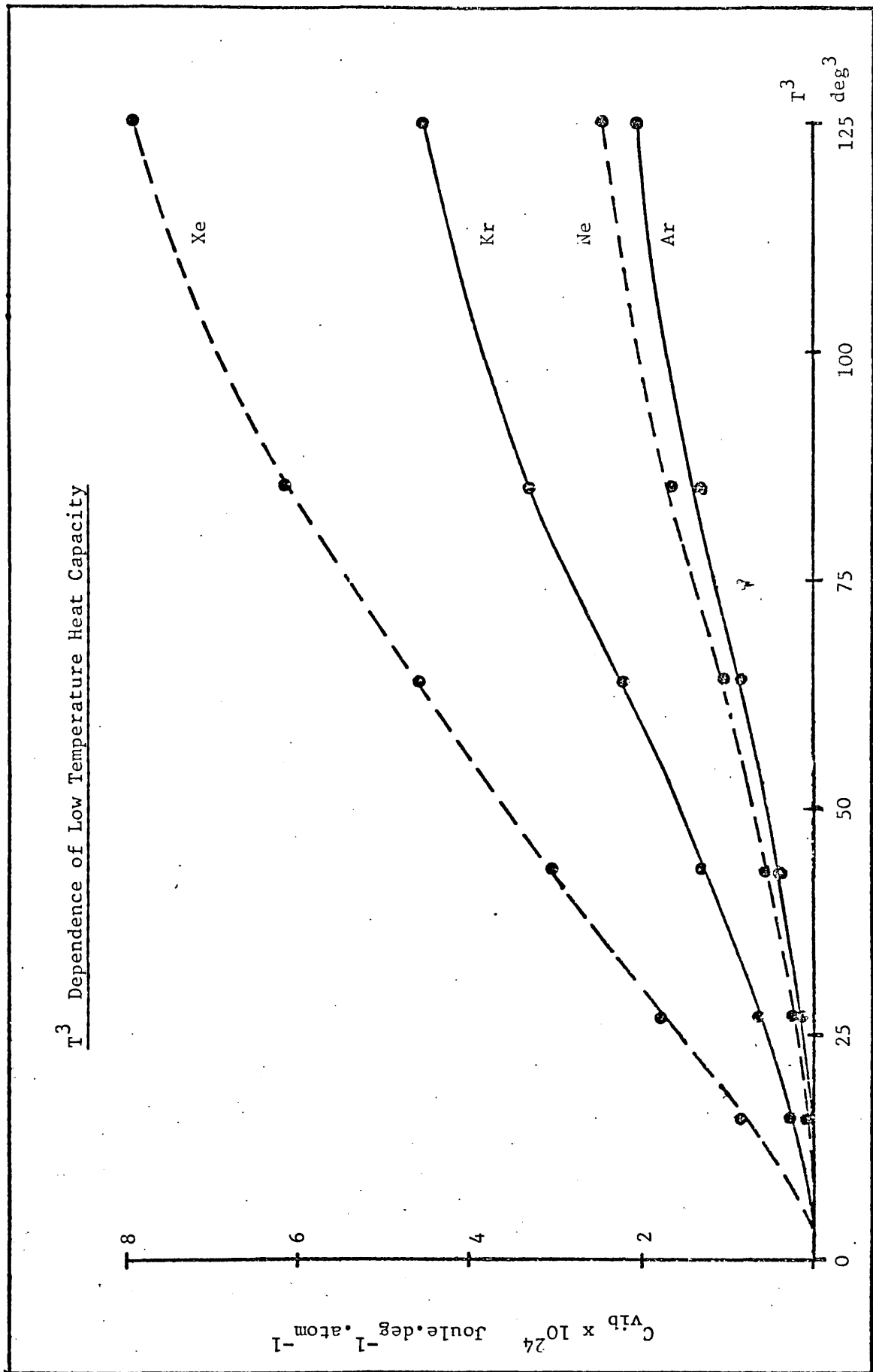
Table 24

		<u>Heat Capacity/Atom. Joule. deg⁻¹ x10²³</u>	
	T	Equation (5.12) finite clusters	Equation (6.4) Montroll (1950)
Ne	1.78	.00041	.00043
Ne	3.56	.0373	.0891
Ar	5.99	.060	.0345
Ar	11.98	1.558	.7123

Comparison of Cluster Heat Capacities/Atom and Semi-Infinite
Heat Capacities/Atom

reduces their heat capacities to zero faster than the T^3 term in equation (6.4) does. Figure 32 shows that cluster heat capacities at temperatures less than 5°A is not linear in T^3 . This anomalous effect is due to the surface effects of very small clusters and the

Figure 32



dependence of vibrational heat capacities on the cluster frequency spectrum as well as to the reduction in the Debye temperature.

Figure 29 indicates that once the Debye temperature of the relevant gas has been reached the heat capacity per atom remains approximately independent of temperature for specified N. Below the Debye temperature the heat capacity is dependent on both N and T^* in agreement with Pal (1972) who suggests that the heat capacity increases monotonically with N for $N < 20$. The heat capacity per xenon atom at the Debye temperature, calculated by use of equation (5.12) for a 13-atom cluster, is $\sim 2.53k$; calculated for a 4-atom xenon cluster it is $\sim 1.50k$. Classically, the heat capacity per atom in an infinite crystal is given by the high temperature approximation

$$C_{v,\infty}(N,T) = (3-6/N)k \left[1 - \frac{1}{20} \left(\frac{\theta}{T} \right)^2 + \frac{1}{560} \left(\frac{\theta}{T} \right)^4 \dots \right] \quad (6.6)$$

which is approximately equal to $2.95k$ at the Debye temperature.

The heat capacities of finite clusters at temperatures above the Debye temperature therefore show the same qualitative behaviour as those shown by infinite crystals.

Figure 32 presents the heat capacity/atom curves for 13-atom clusters of all gases at temperatures less than $5^\circ A$ - smaller clusters exhibit similar behaviour. As at higher temperatures the heat capacity per atom increases with increasing N whilst per degree of freedom it decreases. An interesting point to note is that for neon clusters the heat capacity curve lies above the argon curve - this is a trend not seen at higher temperatures (Figures 28 and 29) and is therefore more likely to be a consequence of quantum effects important in neon clusters at low temperatures than due to the scaling factors for

neon frequencies (Table 16). The Debye T^3 dependence is valid for temperatures $\lesssim .1\theta$ (Kittel (1969)); reference to Table 23 shows that

$$.1\theta_{\text{Ar}} > .1\theta_{\text{Ne}} > .1\theta_{\text{Kr}} > .1\theta_{\text{Xe}} > 5^{\circ}\text{A} \quad (6.7)$$

One would therefore expect the heat capacities in Figure 32 to show a linear dependence on T^3 . Deviation from the T^3 law is seen first for xenon clusters, followed by krypton, neon and argon clusters, in accord with the ordering of $\{.1\theta\}$ in (6.7) above. One may conclude that with increasing temperature on the range $0-5^{\circ}\text{A}$ clusters containing 13 or fewer atoms possess heat capacities which increase less rapidly than T^3 .

6.6 Configurational Thermodynamic Properties

The glass transition has been explained in terms of free volume effects by Williams et al (1955) and Turnbull and Cohen (1961), whilst other investigations (Gibbs (1960), Adam and Gibbs (1965), Goldstein (1973a)) attribute the transition to the effects of configurational entropy. Goldstein (1969) postulates that at low temperatures a glass is in or near a potential energy minimum; the relaxation of glass and the statistical mechanics of the glass transition are elaborated upon by Goldstein (1972,1973b). In this section the configurational thermodynamic properties of L-J and Morse 13-atom isomers are compared at two reduced temperatures (Table 25) in an attempt to decide whether or not the sets of minima discovered in Chapters 2 and 3 are able to model the glass transition.

If the exponential term in equation (5.1) is interpreted as a configurational partition function which may be separated from the

vibrational partition function as shown below

$$Z(N,T) = Z_r^*(N,T) Z_t(N,T) \prod_{i=1}^C Z_v(N,T)^{(i)} \prod_{i=1}^C \exp\left[\frac{-E_{o,i}^{(i)}}{kT}\right], \quad (6.8)$$

in which the * indicates the partition function of the most stable cluster and $E_{o,i}$ is the energy of the i^{th} potential energy minimum ($\equiv V(N)^{(i)}$), it becomes possible to calculate configurational thermodynamic properties for the rare gases. Such a separation is analogous to considering an Einstein model in which all the $3N-6$ vibrational frequencies of the cluster are assumed to be identical. Equations (5.2) to (5.5) indicate that configurational thermodynamic properties may be calculated if the 1st and 2nd derivatives of \ln (configurational partition function) are obtained. Thus,

$$\ln Z_{\text{config}}(N,T) = \ln \prod_{i=1}^C \exp\left[\frac{-E_{o,i}}{kT}\right], \quad (6.9)$$

$$\frac{\partial \ln Z_{\text{config}}(N,T)}{\partial T} = \left[\prod_{i=1}^C \frac{E_{o,i}}{kT} \cdot e^{-E_{o,i}/kT} \right] \left[\prod_{i=1}^C e^{-E_{o,i}/kT} \right]^{-1}, \quad (6.10)$$

$$\frac{\partial^2 \ln Z_{\text{config}}(N,T)}{\partial T^2} = \prod_{i=1}^C \frac{E_{o,i}}{kT^3} \left[\frac{E_{o,i}}{kT} - 2 \right] \cdot e^{-E_{o,i}/kT}$$

$$\left[\frac{\prod_{i=1}^C \frac{E_{o,i}}{kT^2} \cdot e^{-E_{o,i}/kT}}{\prod_{i=1}^C e^{-E_{o,i}/kT}} \right]^2, \quad (6.11)$$

Substitution of equations (6.9) to (6.11) into equations (5.2) to (5.5) produces configurational thermodynamic functions.

Table 25 contains the results of a comparison of Morse and L-J configurational properties of rare gas clusters. One sees from this table that the entropies and heat capacities are independent of the chemical species. This result is more easily understood when one remembers that these two properties are proportional to energy differences and not to absolute energies (equation (6.12)).

$$S = \frac{U - F}{T} \quad (6.12)$$

$$C_v = \frac{dU}{dT}, \quad \text{where the symbols have their usual meanings.}$$

Rapid decreases in configurational entropy and heat capacity with decreasing temperature are clearly seen in Table 25; Kauzmann (1948) indicates that the fall-off of configurational entropy with decreasing temperature is so rapid that it would become zero at a finite temperature. The decrease calculated in the present work is more pronounced for clusters interacting through the Lennard-Jones potential, probably due to the far greater number of minima in the Lennard-Jones potential space. The studies of Johari and Goldstein (1970,1971) reveal a uniformity of behaviour in glass-forming liquids which implies a dependence of these liquids on either configurational entropy or configurational heat capacity. Rosenstock (1972) shows that the low temperature heat capacity of disordered solids is linear in the temperature provided that the distribution of cavities in the solid is of inverse-cube nature. The atomistic model considered here confirms the uniform behaviour observed by Johari and Goldstein (1970,1971) and shows the rapid decrease in configurational entropy required for agreement with Kauzmann (1948).

Table 25

T*	Ne		Ar		Kr		Xe		T-D Property
	L-J	Morse	L-J	Morse	L-J	Morse	L-J	Morse	
.2	-.218	-.256	-.733	-.860	-1.046	-1.228	-1.352	-1.587	Free energy J x10 ¹⁹
.7	-.219	-.259	-.736	-.873	-1.051	-1.246	-1.358	-1.610	
.2	-.218	-.254	-.733	-.856	-1.046	-1.221	-1.352	-1.578	Internal Energy J x10 ¹⁹
.7	-.213	-.253	-.717	-.852	-1.023	-1.216	-1.322	-1.572	
.2	3.862 (-28)	1.915 (-23)							Entropy J. deg ⁻¹
.7	2.329 (-23)	2.465 (-23)	*	†	*	†	*	†	
.2	5.363 (-27)	1.289 (-25)							Heat Capacity J. deg ⁻¹
.7	1.089 (-22)	1.311 (-23)	*	†	*	†	*	†	

Comparison of Configurational Thermodynamic Properties of 13-atom L-J (6-12) and Morse ($\alpha=3$) Clusters[†]

* as L-J Ne; † as Morse Ne; ‡ numbers in brackets denote powers of 10.

In Table 26 configurational and vibrational free energies and internal entropies of 13-atom L-J clusters are shown to be within one order of magnitude of each other throughout the entire temperature range. Configurational heat capacities and entropies are approximately five orders of magnitude smaller than their vibrational counterparts at low reduced temperatures, with the difference decreasing to 1~2 orders at higher reduced temperatures. This behaviour illustrates the increasing

configurational disorder in the cluster as the temperature increases.

Vibrational properties have been calculated by use of equations

(5.9) to (5.12).

Table 26

T*	Thermodynamic Property	Configurational	Vibrational	Gas
.2	Entropy (Joule. deg ⁻¹)	3.862(-28)	0.276(-22)	Ne
			2.916(-22)	Ar
			5.277(-22)	Kr
			7.360(-22)	Xe
.7		2.329(-23)	0.472(-21)	Ne
			0.958(-21)	Ar
			1.230(-21)	Kr
			1.449(-21)	Xe
.2	Heat Capacity (Joule. deg ⁻¹)	5.363(-27)	0.884(-22)	Ne
			3.533(-22)	Ar
			4.191(-22)	Kr
			4.409(-22)	Xe
.7		1.089(-22)	4.314(-22)	Ne
			5.305(-22)	Ar
			5.401(-22)	Kr
			5.427(-22)	Xe
.2	Internal Energy (Joule)	-0.218(-19)	-0.126(-19)	Ne
			-0.733(-19)	Ar
			-1.046(-19)	Kr
			-1.352(-19)	Xe
.7		-0.213(-19)	-0.530(-20)	Ne
			-0.717(-19)	Ar
			-1.023(-19)	Kr
			-1.322(-19)	Xe
.2	Free Energy (Joule)	-0.218(-19)	-0.128(-19)	Ne
			-0.733(-19)	Ar
			-1.046(-19)	Kr
			-1.352(-19)	Xe
.7		-0.219(-19)	-0.171(-19)	Ne
			-0.736(-19)	Ar
			-1.051(-19)	Kr
			-1.358(-19)	Xe

Comparison of Configurational and Vibrational Thermodynamic Properties of
13-atom L-J (6-12) Clusters[†]

[†]: numbers in brackets denote powers of ten.

Chapter 77.1 Introduction to the Multi-Configuration Approach

The need to use a multi-configuration (MC) approach in the calculations of the thermodynamic properties of systems of the type considered here has been recognised by a number of authors: McGinty (1971,1972) and Burton (1970) remain in conflict over the interpretation of multi-configurational results. Bonissent and Mutaftschiev (1973) conclude that such an approach is not necessary for clusters containing less than 15 atoms. Kristensen et al (1974) note the limitations imposed by a single configuration (SC) approach and resort to molecular dynamical techniques in an investigation of cluster thermodynamic properties. Similar techniques are used by Briant and Burton (1973) in a study of the melting transition of a 55-atom cluster. The use of molecular dynamics enables anharmonic effects to be included in the calculations - which appear at low temperatures as perturbations on the energy levels - and in principle enable all phase space to be explored. Andres (1962) notes that the single occupancy model (equivalent to the SC approximation) underestimates the equilibrium concentrations because of the prevention of free interchange of the atoms. This chapter investigates how accurately the single-configuration partition function approximates the multi-configuration partition function for $N > 5$, and the resulting effect on the cluster thermodynamic properties*. In all cases the percentage difference between MC and SC results are calculated by use of equation (7.1) below.

$$\% \text{ diff} = \Delta = \frac{\text{MC}(\text{calc.}) - \text{SC}(\text{calc.})}{\text{SC}(\text{calc.})} \times 100 \quad (7.1)$$

*For $N < 6$ isomer multiplicity does not exist; in such cases MC calculations provide thermodynamic properties equal to those produced by SC calculations.

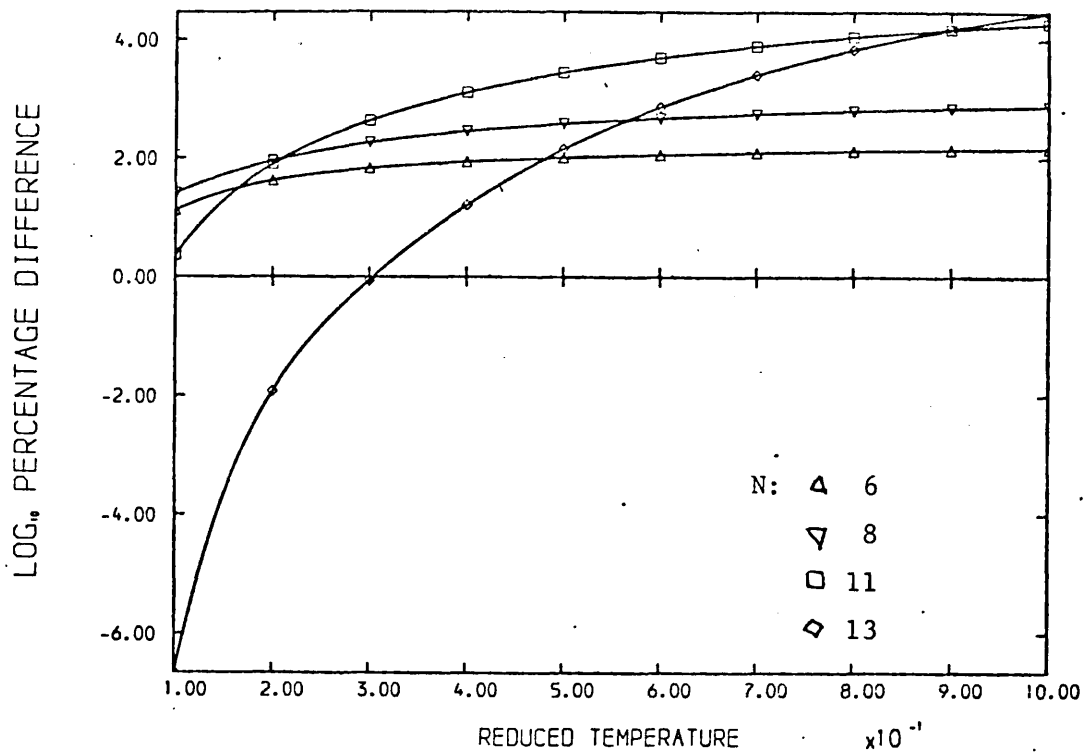
7.2 Vibrational Partition Functions

Tables 27 to 30, containing percentage differences between vibrational MCPFs and SCPFs, illustrate clearly two points:

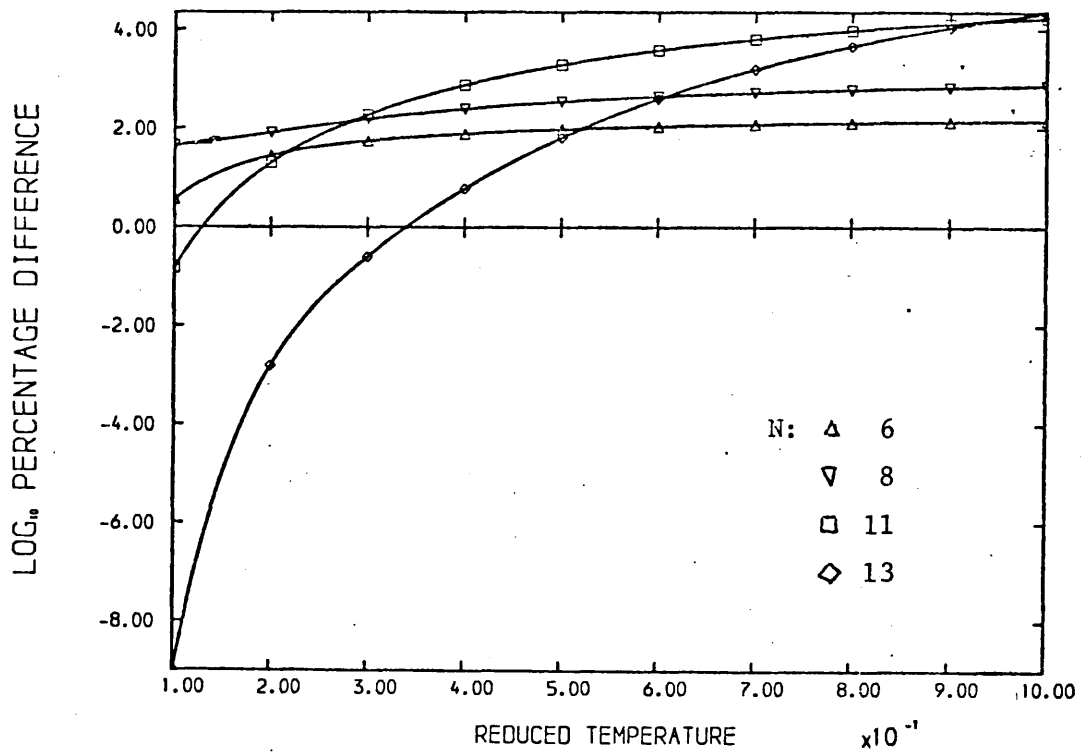
- (i) the increasing importance of the MCPF approximation with increasing temperature, and
- (ii) the decreasing importance of the MCPF approximation with increasing atomic mass.

Figure 33 indicates the dependence of Δ_{PF} on N - all four gases show the same qualitative behaviour. If the energy of the most stable configuration is widely separated, in terms of binding energy, from the energies of alternative stable configurations, the corresponding MCPF is dominated by the contribution from the region of phase space in the neighbourhood of this energy minimum. In this case the SCPF approximates closely the MCPF up to a reduced temperature of $\sim .4$ (see the 13-atom curve in Figure 33). At $T^* = .4$ Δ_{PF} for 13-atom argon clusters is only 6.6. On the other hand those sets of N -atom clusters in which the energy of the most stable configuration is comparatively close to the energies of the other structures lead to the production of a MCPF which does not possess any dominant contribution. In this case the MCPF depends on the number of contributing structures and is approximated rather less well by the SCPF (see, for example, the 11-atom curve in Figure 33). For 11-atom argon clusters at $T^* = .4$ Δ_{PF} is 782. 13-atom clusters of all gases at $T^* = .1$ have Δ_{PF} s $\lesssim 10^{-7}$ (Figure 33). This figure shows that the percentage difference between the MCPFs and the SCPFs remains almost constant at 2 orders of magnitude for 6- and 8-atom clusters. It is significant that for clusters of these sizes there is no particularly favourable configuration.

Figure 33



NEON : COMPARISON OF MC AND SC PARTITION FUNCTIONS



XENON : COMPARISON OF MC AND SC PARTITION FUNCTIONS

Table 27

$\frac{N}{T^*}$	6	7	8	9	10	11	12	13
.1	13.16	1.73	25.70	1.50	0.79	2.34	6.57×10^{-4}	2.15×10^{-7}
.2	41.91	24.25	89.26	52.91	36.18	78.81	1.14	1.18×10^{-2}
.3	66.66	66.23	180.79	210.79	210.78	421.40	26.90	0.87
.4	86.39	114.47	281.99	457.93	631.22	1260.10	197.75	16.06
.5	101.99	162.02	381.01	760.40	1333.33	2752.86	793.27	142.39
.6	114.46	206.16	472.88	1090.43	2290.01	4940.95	2200.26	730.61
.7	124.59	246.09	556.11	1429.03	3446.81	7776.96	4799.35	2558.25
.8	132.93	281.84	630.78	1764.26	4745.72	11166.44	8880.13	6866.69
.9	139.92	313.76	697.57	2089.07	6135.73	14998.97	14608.94	15241.88
1.0	145.84	342.28	757.33	2399.62	7575.91	19166.49	22035.09	29412.22

Percentage Differences for Neon Vibrational Partition Functions

Table 28

$\frac{N}{T^*}$	6	7	8	9	10	11	12	13
.1	4.26	0.62	40.91	0.26	0.18	0.20	9.29×10^{-5}	1.99×10^{-9}
.2	29.10	14.81	81.82	27.61	18.34	22.36	0.43	1.98×10^{-3}
.3	56.22	50.44	155.43	148.86	134.53	199.72	13.03	0.29
.4	78.43	96.69	249.59	367.05	460.11	782.16	113.16	6.61
.5	95.87	144.60	347.62	651.56	1058.44	1978.64	515.50	70.26
.6	109.65	190.01	441.12	972.62	1923.38	3874.80	1568.74	419.18
.7	120.72	231.49	526.93	1308.51	3008.94	6451.16	3661.18	1643.29
.8	129.77	268.77	604.37	1645.02	4257.70	9626.12	7122.20	4795.03
.9	137.28	302.09	673.80	1973.50	5615.89	13291.87	12168.98	11331.66
1.0	143.61	331.84	735.96	2289.03	7038.88	17337.19	18897.79	22940.31

Percentage Differences for Argon Vibrational Partition Functions

Table 29

N/T^*	6	7	8	9	10	11	12	13
.1	3.79	0.55	43.56	0.22	0.15	0.16	6.81×10^{-5}	1.068×10^{-9}
.2	28.26	14.16	81.53	26.00	17.09	20.47	0.38	1.62×10^{-3}
.3	55.50	49.29	153.60	144.55	129.30	189.00	12.08	0.26
.4	77.86	95.37	247.18	360.54	447.96	754.22	107.45	6.09
.5	95.42	143.29	345.11	643.64	1038.64	1928.84	496.48	66.07
.6	109.30	188.80	438.73	963.96	1896.68	3802.53	1524.76	400.01
.7	120.44	230.39	524.73	1299.59	2976.77	6358.45	3580.77	1584.48
.8	129.53	267.79	602.37	1636.15	4221.62	9516.24	6996.54	4657.61
.9	137.09	301.21	672.00	1964.86	5577.27	13168.44	11992.91	11066.10
1.0	143.45	331.05	734.34	2280.74	6998.83	17203.65	18669.83	22492.78

Percentage Differences for Krypton Vibrational Partition Functions

Table 30

N/T^*	6	7	8	9	10	11	12	13
.1	3.68	0.53	44.29	0.20	0.14	0.14	8.97×10^{-5}	8.746×10^{-10}
.2	28.04	13.98	81.45	25.57	16.76	19.99	0.37	1.530×10^{-3}
.3	55.31	48.99	153.12	143.41	127.79	186.27	11.83	0.25
.4	77.71	95.02	246.54	358.83	444.77	747.01	105.95	5.96
.5	95.30	142.95	344.45	641.56	1033.44	1915.88	491.50	64.99
.6	109.20	188.48	438.10	961.68	1889.65	3783.65	1513.24	395.04
.7	120.36	230.10	524.15	1297.24	2968.30	6334.16	3559.69	1569.19
.8	129.47	267.53	601.84	1633.81	4212.12	9487.42	6963.56	4621.79
.9	137.03	300.98	671.52	1962.59	5567.10	13136.02	11946.66	10996.73
1.0	143.40	330.84	733.91	2278.56	6988.29	17168.54	18609.88	22375.69

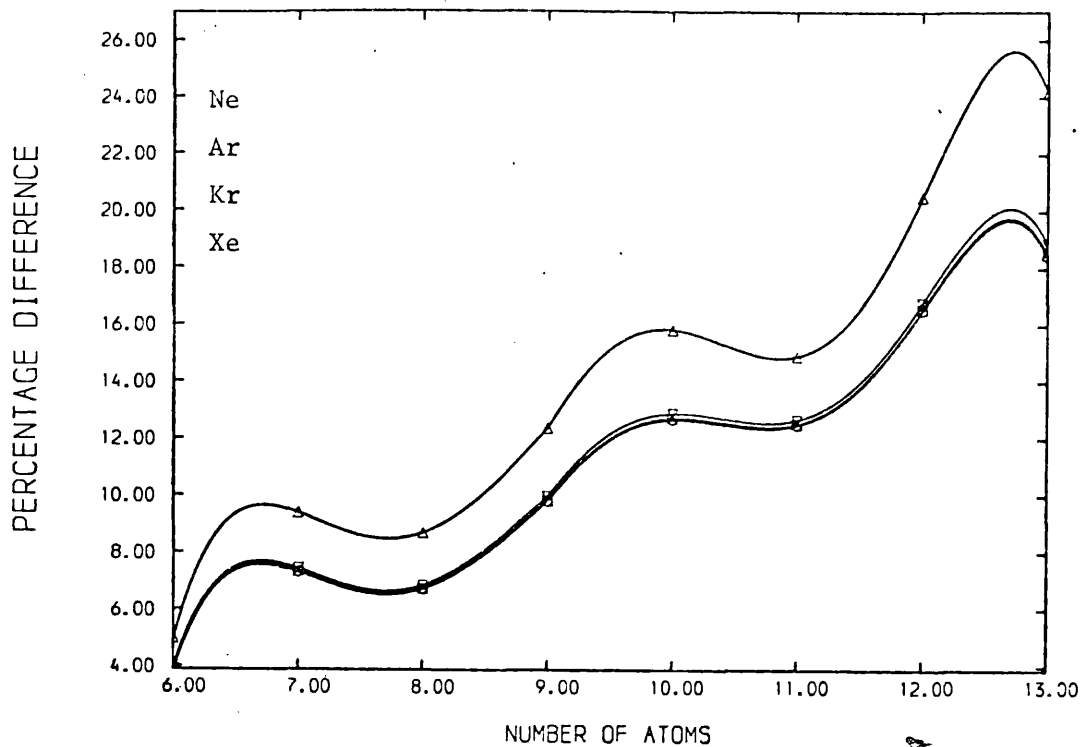
Percentage Differences for Xenon Vibrational Partition Functions

The decision as to whether or not one should use the MCPF hinges on the answer to the question: are the energies of the stable configurations evenly distributed over an energy range or is there one configuration possessing an energy widely separated from the others in that group? In the former case it appears to be necessary to use the MCPF, whilst if the latter situation exists one has some justification for using the SCPF. With increasing temperature the $\{\Delta_{PF}\}$ increase to ~ 4 orders of magnitude, although at reduced temperatures much above $.3 \sim .4$ anharmonic effects and fluid-like motions render the harmonic oscillator approximation strictly invalid, except as a general guide to the properties of the system. Near the boiling point ($T^* \approx .7$) of argon there is a percentage difference of ~ 2 orders of magnitude. The results in Tables 27 to 30 contradict the conclusion of Bonissent and Mutaftschiev (1973): ie. that the MCPFs for $N < 15$ differ only slightly from the SCPFs. This contradiction is probably due to the neglect by Bonissent and Mutaftschiev of some stable configurations.

7.3 Vibrational Free Energies

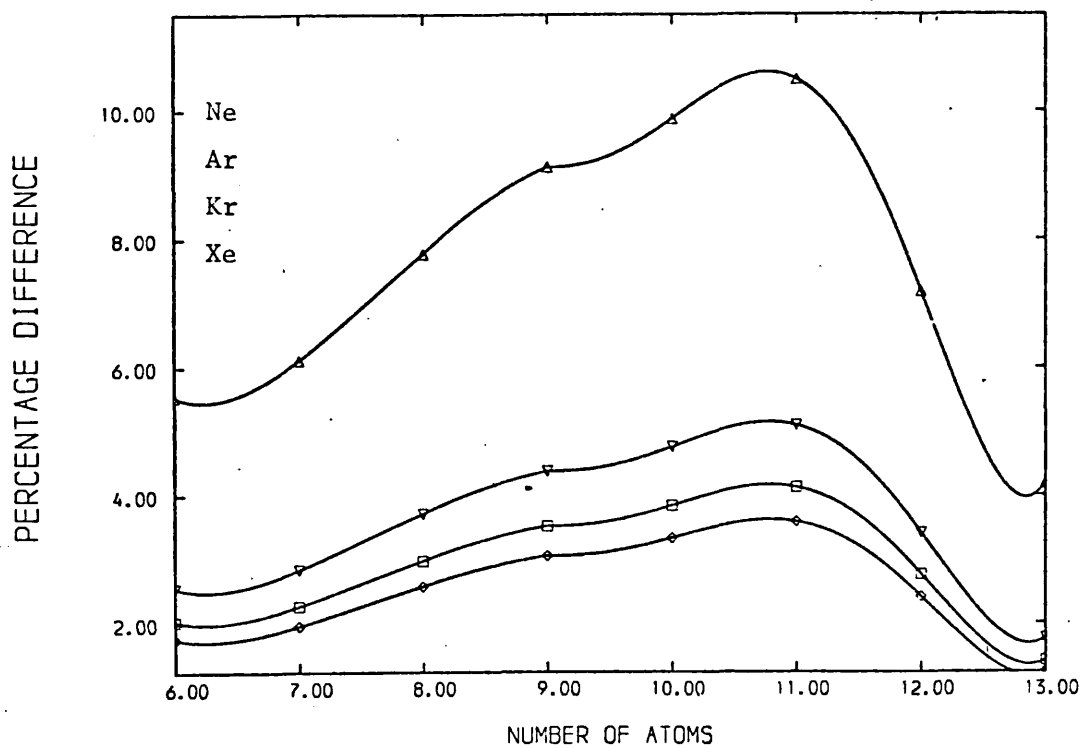
The free energy percentage differences $\{\Delta_{FE}\}$ in Table 31 follow the pattern shown by the $\{\Delta_{PF}\}$ with a maximum for 11-atom clusters. The maximum Δ_{FE} is just less than 17 - this percentage difference occurs for 11-atom neon clusters at $T^* = 1.0$. The overall minimum Δ_{FE} for neon clusters is 3 at $T^* = .3$; for argon clusters at the same temperature it is not greater than 1.5, whilst for the heavier krypton and xenon clusters at this temperature it is ~ 1 . Figure 35 shows the $\{\Delta_{FE}\}$ for neon clusters to be substantially greater than those for clusters of the heavier gases - this is probably due to quantum effects which become increasingly important with decreasing atomic mass. Near the boiling point of the gases all the percentage differences are ≤ 11 . With

Figure 34



$T^* = .6$: COMPARISON OF MC AND SC INTERNAL ENERGIES

Figure 35



$T^* = .6$: COMPARISON OF MC AND SC FREE ENERGIES

increasing temperature the percentage differences increase, shown quite clearly in Table 31.

For reduced temperatures $\leq .3$ the SC approximation to free energies appears to be valid. McGinty (1971) notes differences of up to 2% in the free energy/argon atom - his calculations use a simplified MC approach for clusters containing less than 100 atoms at temperatures up to 70°K. The present calculations produce differences of up to .5% in free energy/argon atoms at a reduced temperature of .6 (ie. $\sim 72^\circ\text{K}$). Even for the light neon clusters the maximum $\Delta_{\text{FE}}/\text{neon atom}$ at $T^* = .6$ is only ~ 1 .

Table 31

N	T^*	6	7	8	9	10	11	12	13
.3		2.26	1.68	2.80	2.51	2.10	2.61	3.20(-1)	9.87(-3)
.6		5.54	6.12	7.78	9.13	9.88	10.49	7.18	4.19
1.0		7.27	9.20	10.81	13.67	15.75	16.58	14.81	13.85
<u>Neon</u>									
N	T^*	6	7	8	9	10	11	12	13
.3		1.08	7.56(-1)	1.44	1.16	9.19(-1)	1.03	9.90(-2)	2.02(-3)
.6		2.55	2.84	3.72	4.39	4.77	5.10	3.41	1.76
1.0		3.32	4.27	5.11	6.49	7.55	8.01	7.20	6.70
<u>Argon</u>									
N	T^*	6	7	8	9	10	11	12	13
.3		8.98(-1)	6.30(-1)	1.21	9.69(-1)	7.67(-1)	8.54(-1)	7.97(-2)	1.57(-3)
.6		2.03	2.27	2.98	3.53	3.85	4.13	2.76	1.41
1.0		2.61	3.37	4.04	5.14	5.99	6.38	5.75	5.35
<u>Krypton</u>									
N	T^*	6	7	8	9	10	11	12	13
.3		8.00(-1)	5.62(-1)	1.08	8.66(-1)	6.86(-1)	7.64(-1)	7.08(-2)	1.39(-3)
.6		1.75	1.06	2.58	3.06	3.34	3.59	2.41	1.23
1.0		2.23	2.89	3.47	4.41	5.15	5.49	4.96	4.62
<u>Xenon</u>									

Percentage Differences in Vibrational Free Energies for the Rare Gases

Numbers in parenthesis denote powers of 10.

7.4 Vibrational Internal Energies

The percentage differences in internal energies $\{\Delta_{IE}\}$ are presented in Table 32. The most obvious feature of this table is that all except one of the percentage differences are negative (the exception being for 6-atom neon clusters at the top of the potential well). This feature shows that the internal energies increase when the MC approximation is used. For 6-atom neon clusters at $T^* = 1.0$ the internal energy is positive for both MC and SC approximations, being greater in the MC calculations. This increase is in accord with the behaviour shown by clusters of different sizes for the other rare gases. The very large percentage differences possessed by 7, 8 and 9-atom neon clusters (e.g. -550 for 7-atom neon clusters) become acceptable when one realizes that the internal energies are increasing from a negative value, through zero, to positive values. As the SC internal energies pass through the immediate vicinity of zero the percentage differences obtained via equation (7.1) become very large.

The maximum Δ_{IE} (~ -6) at $T^* = .3$ occurs for neon 10-atom clusters: for argon, krypton and xenon clusters at the same reduced temperature the Δ_{IE} is $\lesssim -4$. The SC approach may be used with some confidence at or below this temperature. At the top of the potential well 6-atom xenon clusters show the least sensitivity to the different approximations, as expected because of their mass. Figure 34 illustrates the marked difference between the $\{\Delta_{IE}\}$ for neon clusters and those for clusters of the other gases. The same figure shows the tendency for the $\{\Delta_{IE}\}$ to increase with N ; this result contrasts with the behaviour at $T^* = .3$. In the latter case the percentage differences reach a maximum for clusters containing 10 \sim 11 atoms, and fall rapidly for larger sized clusters. The maximum Δ_{IE} of ~ -550 occurs for 7-atom neon clusters at a reduced temperature of 1.; for the other gases

at this temperature the average Δ_{IE} is -40. With increasing temperature the $\{\Delta_{IE}\}$ increase.

Table 32

N	T^*	6	7	8	9	10	11	12	13
.3		-1.96	-3.10	-3.23	-4.92	-5.60	-5.56	-2.26	-1.06(-1)
.6		-4.97	-9.38	-8.69	-12.35	-15.80	-14.87	-20.51	-24.20
1.0		+60.16	-550.08	-472.44	-114.02	-94.98	-75.40	-79.31	-79.45

Neon

N	T^*	6	7	8	9	10	11	12	13
.3		-1.64	-2.22	-2.22	-3.67	-3.83	-4.25	-9.73(-1)	-2.87(-2)
.6		-3.96	-7.43	-6.84	-9.96	-12.86	-12.64	-16.78	-18.88
1.0		-39.61	-47.66	-42.56	-44.35	-48.37	-43.93	-52.21	-58.41

Argon

N	T^*	6	7	8	9	10	11	12	13
.3		-1.61	-2.16	-2.15	-3.58	-3.71	-4.12	-8.97(-1)	-2.54(-2)
.6		-3.90	-7.32	-6.73	-9.81	-12.69	-12.49	-16.55	-18.51
1.0		-35.38	-44.70	-39.91	-42.45	-46.71	-42.64	-50.94	-57.30

Krypton

N	T^*	6	7	8	9	10	11	12	13
.3		-1.60	-2.15	-2.13	-3.56	-3.68	-4.09	-8.77(-1)	-2.46(-2)
.6		-3.88	-7.29	-6.71	-9.78	-12.64	-12.45	-16.49	-18.41
1.0		-34.42	-43.98	-39.27	-41.98	-46.29	-42.31	-50.61	-57.02

Xenon

Percentage Differences in Vibrational Internal Energies for the Rare Gases

Numbers in parenthesis denote powers of 10.

7.5 Vibrational Entropies

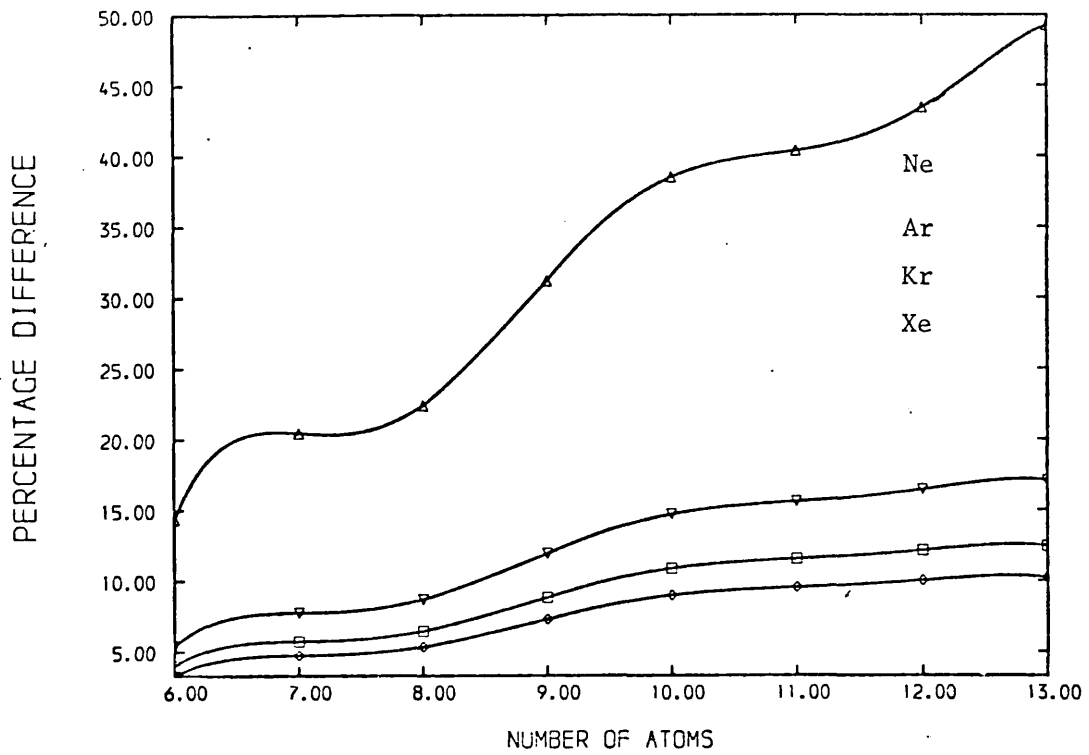
All the gases show the same qualitative behaviour for the variation of percentage differences in entropy $\{\Delta_E\}$ with N . At reduced temperatures $\lesssim .3$ the $\{\Delta_E\}$ rise to a maximum at $N = 11$, and then fall rapidly for 12- and 13-atom clusters. At higher temperatures the $\{\Delta_E\}$ increase steadily with N over the entire N range (see Figure 36). As in Figures 34 and 35 the neon curve is widely separated from the other curves. The variation of the $\{\Delta_E\}$ with temperature is rather more complicated - for most clusters containing less than 12 neon or argon atoms the percentage difference in entropy decreases as the temperature increases. On the other hand $\Delta_E(T^*)$ rises to a maximum value at $T^* = .5 \sim .7$ (i.e. near the boiling point of the gases) for most clusters of the heavier gases. This behaviour of the $\{\Delta_E(T^*)\}$ is also exhibited by 12- and 13-atom clusters of neon and argon.

The SC approximation introduces quite serious errors in the vibrational entropy at $T^* = .3$ (e.g. for neon 11-atom clusters $\Delta_E \approx 85$; for xenon 11-atom clusters $\Delta_E \approx 8$). The $\{\Delta_E\}$ for clusters containing more than 11-atoms drop rapidly at $T^* = .3$, to a value of ~ 0.05 for 13-atom xenon clusters. The comparatively mild decrease from the $\{\Delta_E(N=11)\}$ to the $\{\Delta_E(N=12)\}$ at this temperature is probably due more to the combined effects of a large multiplicity of isomers and an appropriate energy distribution rather than to just one of these factors. Conversely, the very low percentage differences for 13-atom clusters is almost certainly a direct consequence of the dominance of the icosahedron in the 13-atom set. At the top of the potential well the 6-atom clusters are least affected by the SC approximation, with Δ_E s ranging from 9(Ne) to 3(Xe). At $T^* = .3$ percentage entropy differences lie in the following ranges

neon 2 - 85; argon .1 - 16; krypton 0 - 10; xenon 0 - 8.

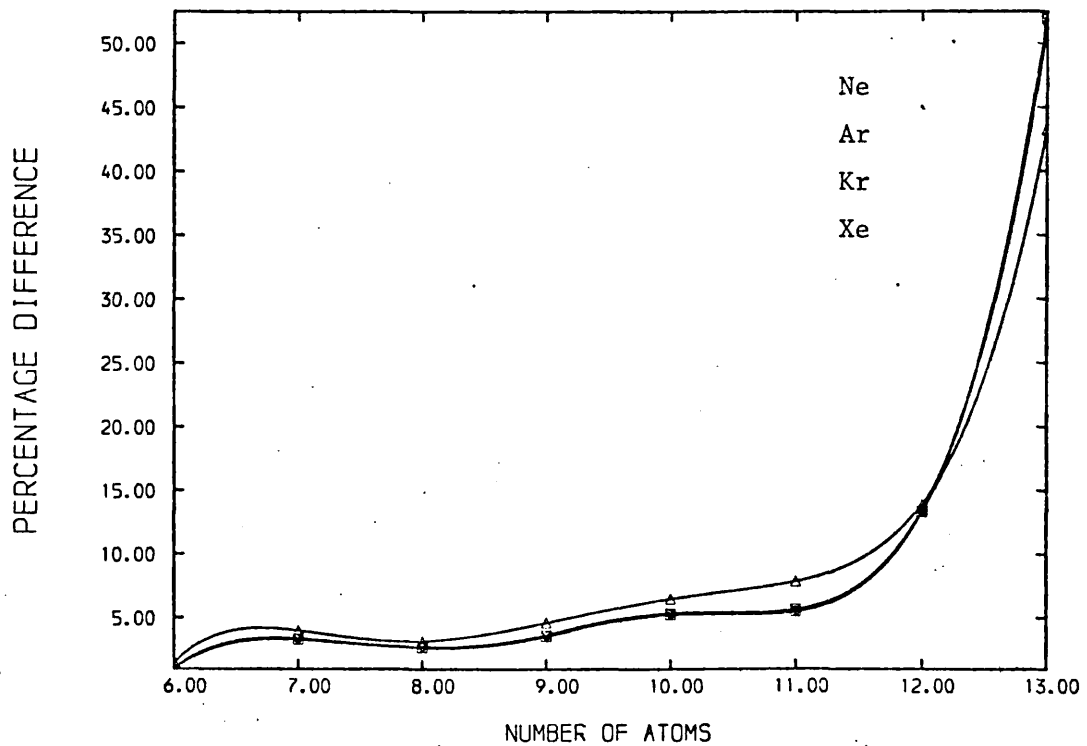
From these data the SC approximation appears to be definitely invalid at

Figure 36



$T^* = .6$: COMPARISON OF MC AND SC ENTROPIES

Figure 37



$T^* = .6$: COMPARISON OF MC AND SC HEAT CAPACITIES

reduced temperatures less than $\sim .3$, with $N < 12$. For larger clusters of the heavier gases the SC approximation may be used at these temperatures. McGinty (1971) notes an 8% difference in entropy/argon atom between SC and MC calculations; this difference is about 5 times greater than the difference predicted in the present work. At $T^* = 1.0$ the percentage differences range from ~ 3 (6-atom xenon clusters) to ~ 35 (13-atom neon clusters). These differences call into question the use of the SC approximation even at higher temperatures.

Table 33

N	T^*	6	7	8	9	10	11	12	13
.3		39.75	44.63	51.47	71.45	77.72	84.64	28.48	1.61
.6		14.37	20.45	22.41	31.20	38.53	40.38	43.44	49.25
1.0		8.80	13.06	14.22	19.70	24.40	26.04	28.76	34.78

Neon

N	T^*	6	7	8	9	10	11	12	13
.3		7.51	8.16	10.30	13.87	14.05	16.08	3.35	1.07(-1)
.6		5.41	7.76	8.70	11.93	14.70	15.59	16.44	17.07
1.0		4.31	6.43	7.08	9.70	12.01	12.85	14.17	16.85

Argon

N	T^*	6	7	8	9	10	11	12	13
.3		4.83	5.23	6.66	8.91	8.96	10.25	2.04	6.18(-2)
.6		4.00	5.74	6.46	8.83	10.87	11.54	12.14	12.44
1.0		3.38	5.05	5.58	7.62	9.42	10.08	11.11	13.16

Krypton

N	T^*	6	7	8	9	10	11	12	13
.3		3.72	4.03	5.15	6.87	6.89	7.89	1.55	4.61(-2)
.6		3.30	4.75	5.35	7.29	8.98	9.53	10.02	10.22
1.0		2.88	4.31	4.76	5.40	8.03	8.60	9.47	11.19

XenonPercentage Differences in Vibrational Entropies for the Rare Gases

Numbers in parenthesis denote powers of 10.

7.6 Vibrational Heat Capacities

The heat capacity percentage differences $\{\Delta_{\text{HC}}\}$ in Table 34 show that except for 13-atom clusters of all gases, the SC approximation introduces larger deviations to the heat capacities at low temperatures than it does at higher temperatures. This behaviour is possibly due to the dependence of heat capacity on the first and second derivatives with respect to temperature of \ln (partition function). As in the previous section the $\{\Delta_{\text{HC}}(N)\}$ at $T^* \lesssim .3$ rise to a maximum at $N = 10 \sim 11$ and then decrease, whilst at higher temperatures they increase constantly over the full range of N . The structure shown in Table 33 is lost in Table 34, due in some measure to the compensating effect of the second derivative. For 13-atom clusters, dominated by the icosahedron, the $\{\Delta_{\text{HC}}(T^*)\}$ increase with $T^* = .5 \sim .6$, and then decrease rapidly. For $5 < N < 13$ at $T^* = .3$ the percentage differences range from 7 to 77 for neon, and from 4 to 32 for argon, krypton and xenon. The neon clusters are, as before, the most seriously affected by the SC approximation, although the discrepancy between the neon heat capacity curves and those curves for the other gases is much less than for the other thermodynamic properties (see Figure 37). At $T^* = 1.0$ the maximum Δ_{HC} is ~ 5 (13-atom neon clusters) with a minimum at this temperature of $\sim .3$ (6-atom xenon clusters).

For $N < 12$ and $T^* \lesssim .3$, the SC approximation is invalid. As is the case for the vibrational entropies, the SC approximation may be used for larger clusters at reduced temperatures less than .3 if the MCPF for these clusters possesses a dominant term. At $T^* = 1.0$ the maximum Δ_{HC} is $\lesssim 6$, implying that, once one approaches the boiling point of the gases, the use of the SCPF gains validity with increasing temperature. This conclusion remains questionable due to the breakdown of the harmonic oscillator approximation at these temperatures.

Table 34

N	T^*	6	7	8	9	10	11	12	13
.3		6.93	19.60	15.97	28.40	50.97	41.95	77.02	7.14
.6		1.45	3.99	3.15	4.64	6.50	7.88	13.93	43.25
1.0		4.97(-1)	1.27	1.01	1.61	2.02	2.92	3.77	5.38
<u>Neon</u>									
N	T^*	6	7	8	9	10	11	12	13
.3		3.85	11.71	10.50	17.88	30.85	31.97	25.94	1.28
.6		1.01	3.36	2.71	3.66	5.37	5.69	13.42	51.34
1.0		3.52(-1)	1.02	8.01(-1)	1.27	1.55	2.24	3.13	4.41
<u>Argon</u>									
N	T^*	6	7	8	9	10	11	12	13
.3		3.64	11.10	10.02	16.98	29.15	30.57	23.08	1.08
.6		9.80(-1)	3.30	2.68	3.58	5.28	5.55	13.35	51.97
1.0		3.42(-1)	1.01	7.86(-1)	1.24	1.51	2.19	3.07	4.33
<u>Krypton</u>									
N	T^*	6	7	8	9	10	11	12	13
.3		3.59	10.93	8.89	16.74	28.69	30.18	22.34	1.03
.6		9.70(-1)	3.28	2.67	3.56	5.25	5.51	13.33	52.14
1.0		3.39(-1)	1.00	7.82(-1)	1.24	1.50	2.18	3.05	4.30
<u>Xenon</u>									

Percentage Differences in Vibrational Heat Capacities for the Rare Gases

Numbers in parentheses denote powers of 10.

7.7 Conclusion

The overall conclusions of this work disagree with the suggestion of Bonissent and Mutaftschiev (1973) that the MCPF differs only slightly from the SCPF at all temperatures. Whilst this suggestion may be true at reduced temperatures less than .1 it is certainly not substantiated at

higher reduced temperatures. The percentage differences in thermodynamic properties decrease with increasing atomic mass, as shown in Figures 34 to 37. They also depend strongly upon the energy distribution of the clusters and less strongly upon the number of these clusters. It should be noted that the harmonic oscillator approximation is not valid for reduced temperatures much greater than $\sim .3$.

Burton (1972c), McGinty (1971,1972) and Nishioka et al (1971) all suggest, as is suggested in this present work, large corrections to cluster free energies calculated using the SC approximation. McGinty (1972) indicates that at low temperatures the SCPF yields free energies very close to the 'exact' MCPF free energies if the most stable configuration is used in the SC calculations. This indication is confirmed by the present work. It appears essential to use a full MC treatment in the calculation of vibrational entropies and specific heats at reduced temperatures $\lesssim .3$. Any fine structure seen on entropy and specific heat curves is more likely to be due to the SC approximation than to possess any physical significance (in agreement with McGinty (1972) and Abraham and Dave (1971a)). On the other hand the comparatively small percentage differences in free and internal energies introduced by the SC approximation are unlikely to cause much fine structure for $N < 14$. In these cases fine structure may possess physical significance (Burton (1970a)). As the cluster size increases the number of possible configurations rises exponentially, so it is probable that for $N > 13$ the fine structure seen on any graph of thermodynamic properties is due to the SC approximation.

Chapter 8

8.1 Introduction

The development of statistical mechanical techniques in Chapter 5 produces equation (5.31) for the equilibrium constant of an N -atom cluster and equation (5.33) for the relative equilibrium concentrations of two different isomers containing the same number of atoms. Bearing in mind that according to classical nucleation theory (Zettlemoyer (1969)) clusters containing less than a certain critical number N^* of atoms may be metastable with respect to both the vapour and smaller clusters, equations (5.31) and (5.33) are used, in conjunction with the MCPF for $6 \leq N \leq 13$ and the SCPF for $2 \leq N \leq 5$, to calculate equilibrium constants and relative equilibrium concentrations at various temperatures for the four rare gases considered. Comparison is made in the case of equilibrium constants with data obtained by use of Andres' (1965) model, which is described in section 2 of this Chapter.

8.2 Equilibrium Constants

Equilibrium constants for the four rare gases with $2 \leq N \leq 13$ over the entire reduced temperature range are calculated by use of equation (5.31). Tables 35 to 38 present the \log_{10} of these constants, with the \log_{10} of the equilibrium constants calculated by the simplified model of Andres (1965), equations (8.1) and (8.2), included for comparison. Following the example set by Reed (1952), who estimated the equilibrium constants of clusters with $2 \leq N \leq 8$ by considering the clusters as polymers with an equilibrium configuration of lowest energy and greatest symmetry, and assuming $3N-6$ harmonic dimer modes, Andres has obtained expressions for the equilibrium constants of

clusters with $2 \leq N \leq 12$. Andres makes the further assumptions (i) regular tetrahedral growth and (ii) only nearest neighbour bonds contribute to the cluster's binding energy. The equilibrium constant of a dimer based on such a model is represented by

$$K(2) = 2\pi\sigma^2 \left[\frac{2\pi kT}{V''(\sigma)} \right]^{\frac{1}{2}} \exp(\epsilon/kT), \quad (8.1)$$

and for $2 < N \leq 12$

$$K(N) = \chi^{-1} (8\pi^2 \sigma^3)^{2(N-3)/2} \left[\frac{2\pi kT}{V''(\sigma)} \right]^{3(N-2)/2} \exp\left\{ \frac{(3N-6)\epsilon}{kT} \right\} \quad (8.2)$$

where σ is the equilibrium separation of 2 atoms,

$V''(\sigma)$ the 2nd derivative of the intermolecular potential at that separation,

ϵ is the depth of the potential energy well and

χ is the rotational symmetry number.

8.3 Discussion of Tables 35 to 38

Andres' model for the equilibrium constant with $N > 2$ is valid only for $N \leq 12$. However Tables 35 to 38 contain the \log_{10} of the equilibrium constants for $N=13$ obtained by equation (5.31) to test the validity of equation (8.2) for $N > 12$. Before a detailed analysis of Tables 35 to 38 is made 3 points should be noted:

(i) the assignment of dimer modes to represent the frequency spectrum overestimates the zero point energy,

(ii) consideration of only nearest neighbour bonds to represent the binding energy underestimates the cluster potential energy,

(iii) owing to the importance of non-nearest neighbour bonds the overall energy of an optimized cluster is higher. As N increases so does the contribution due to non-nearest neighbour bonds, leading to a decrease in $K(N)$.

The equilibrium constant $K(N)$, as defined by equation (5.31),

is expressed in terms of partition functions per unit volume. Consequently it is not dimensionless, having dimensions $L^{3(N-1)}$ where N is the number of atoms in the cluster under consideration. Care has to be taken when comparing equilibrium constants expressed in this form. The equilibrium constants presented in Tables 35 to 38 are calculated in S.I. units, ie. their dimensions are $\text{metre}^{3(N-1)}$.

A single-configuration partition function underestimates the 'exact' partition function of a system, so one would expect the multi-configuration partition functions used in equation (5.31) for $K(N)$ to produce equilibrium constants higher than those produced by single-configuration partition functions or by Andres' simplified model. Tables 36 to 38 for argon, krypton and xenon respectively show that the equilibrium constants calculated by use of equation (5.31) and the SCPF ($2 \leq N \leq 5$) or the MCPF ($6 \leq N \leq 13$) are either extremely close to Andres' figures or are higher than his figures (ie. are less negative). The differences between the calculations of this work and of Andres are greater at lower than at higher temperatures. For argon, krypton and xenon clusters with $N \geq 6$ the values of $K(N)$ obtained from equation (5.31) are all greater than Andres' values. It is worth noticing that for $N \geq 6$ the MCPF approximation has been used. For $N < 6$ at $T^* = .1$ for the three gases mentioned above the % by which Andres calculations exceed these in this work is less than 1, for argon, decreasing with increasing atomic weight to less than .1 for xenon. These % differences fall easily into the range of fluctuation produced by cumulative rounding errors in computation.

Table 35 shows that there are larger discrepancies between this work and that of Andres for neon than for the other rare gases. For $2 \leq N \leq 5$ Andres' figures exceed this work's figures by just under 5% for $N=2$, increasing to 12% for $N=5$ at a reduced temperature of .1. For $6 \leq N \leq 13$ at the same temperature the % difference drops to less than .5% at $N=13$. This turning point in % differences at $N=5$ is again an indication of the validity of the MC approximation in calculating these equilibrium constants. With increasing temperature the %s by which Andres' figures exceed those of this work drop to a maximum of .13% (for 5-atom clusters), at the top of the potential energy well, and to a minimum of .03% (for 6-atom clusters), at the same temperature. As the temperature increases from $T^* = .1$ to $T^* = .2$ Andres' excess rises from 1.5% to just over 3% in the range $2 \leq N \leq 5$, and drops to <.7% at $N=11$. For $11 < N \leq 13$ Andres' figures are less than those for this work ($T^* > .1$).

It seems reasonable to conclude that use of the multi-configuration approximation produces equilibrium constants which are greater than those produced by Andres' simple model over the entire temperature range for argon, krypton and xenon. Extension of Andres' model to include the equilibrium constants of 13-atom clusters appears to be valid on examination of the data in Tables 35 to 38. The equilibrium constants obtained via the multi-configuration approximation imply the existence in equilibrium of a set of different isomeric forms for a specific N . With $T^* \gtrsim .1$ the MC approximation is also valid for neon clusters. With $T^* \lesssim .1$ it seems probable that important quantum effects need to be considered in the case of neon, and that the use of the classical rotational partition function in equation (5.26) is no longer permissible. The Lennard-Jones

Table 35
 $\log_{10} K(N, T^*)$

T^*	$N=2$		$N=3$		$N=4$		$N=5$		$N=6$		$N=7$	
	(a)	(b)	(a)	(b)	(a)	(b)	(a)	(b)	(a)	(b)	(a)	(b)
1	-25.71	-24.52	-49.52	-46.00	-71.66	-64.75	-92.85	-82.89	-113.88	-101.93	-132.67	-119.99
2	-26.93	-26.54	-53.23	-52.07	-79.16	-76.87	-104.35	-101.08	-129.87	-126.18	-153.91	-150.31
3	-27.36	-27.18	-54.54	-53.97	-81.80	-80.69	-108.38	-106.80	-135.45	-133.81	-161.23	-159.84
4	-27.59	-27.48	-55.20	-54.87	-83.14	-82.48	-110.41	-109.49	-138.26	-137.40	-164.89	-164.33
5	-27.72	-27.65	-55.59	-55.38	-83.92	-83.50	-111.61	-111.01	-139.14	-139.43	-167.04	-166.86
6	-27.80	-27.75	-55.85	-55.69	-84.43	-84.13	-112.37	-111.96	-140.63	-140.69	-168.42	-168.44
7	-27.86	-27.82	-56.02	-55.90	-84.77	-84.55	-112.90	-112.59	-141.71	-141.53	-169.35	-169.49
8	-27.90	-27.87	-56.14	-56.05	-85.01	-84.84	-113.26	-113.02	-142.22	-142.11	-170.01	-170.22
9	-27.93	-27.90	-56.22	-56.15	-85.18	-85.05	-113.53	-113.37	-142.59	-142.53	-170.49	-170.74
1.0	-27.95	-27.93	-56.29	-56.23	-85.31	-85.20	-113.72	-113.57	-142.87	-142.83	-170.85	-171.12

T^*	$N=8$		$N=9$		$N=10$		$N=11$		$N=12$		$N=13$	
	(a)	(b)	(a)	(b)	(a)	(b)	(a)	(b)	(a)	(b)	(a)	(b)
1	-152.29	-137.43	-170.61	-156.18	-188.39	-174.79	-205.56	-193.06	-220.22	-211.90	-232.37	-231.42
2	-177.86	-173.81	-202.10	-198.62	-226.00	-223.30	-249.24	-247.62	-271.92	-272.53	-293.51	-298.11
3	-186.66	-185.25	-212.83	-211.97	-238.76	-238.55	-264.03	-264.79	-289.73	-291.60	-314.70	-319.09
4	-191.06	-190.64	-218.15	-218.26	-245.03	-245.74	-271.32	-272.88	-298.41	-300.58	-325.36	-328.97
5	-193.64	-193.68	-221.27	-221.80	-248.68	-249.79	-275.58	-277.43	-303.32	-305.64	-331.44	-334.54
6	-195.30	-195.57	-223.28	-224.01	-251.01	-252.31	-278.31	-280.27	-306.41	-308.80	-335.08	-338.01
7	-196.43	-196.83	-224.64	-225.47	-252.60	-253.99	-280.17	-282.16	-308.51	-310.90	-337.48	-340.32
8	-197.23	-197.71	-225.61	-226.49	-253.73	-255.16	-281.48	-283.47	-309.99	-312.35	-339.15	-341.92
9	-197.80	-198.33	-226.31	-227.22	-254.55	-255.99	-282.45	-284.41	-311.07	-313.40	-340.37	-343.07
1.0	-198.23	-198.79	-226.83	-227.76	-255.16	-256.60	-283.16	-285.09	-311.87	-314.16	-341.28	-343.90

Equilibrium Constants: Neon

(a) *This work*

(b) *Andres*

Table 36
 $\log_{10} K(N, T^*)$

T^*	N=2		N=3		N=4		N=5		N=6		N=7	
	(a)	(b)	(a)	(b)	(a)	(b)	(a)	(b)	(a)	(b)	(a)	(b)
1	-24.41	-24.24	-45.95	-45.45	-64.90	-63.91	-82.86	-81.77	-100.06	-100.54	-115.23	-118.32
2	-26.31	-26.26	-51.64	-51.51	-76.30	-76.04	-100.17	-99.96	-124.20	-124.79	-146.76	-148.63
3	-26.92	-26.90	-53.48	-53.42	-79.97	-79.85	-105.75	-105.68	-131.94	-132.42	-156.86	-158.17
4	-27.21	-27.20	-54.35	-54.32	-81.72	-81.65	-108.40	-108.38	-135.63	-136.01	-161.64	-162.66
5	-27.37	-27.37	-54.84	-54.82	-82.70	-82.66	-109.91	-109.90	-137.71	-138.03	-164.33	-165.19
6	-27.48	-27.47	-55.15	-55.15	-83.32	-83.29	-110.85	-110.84	-139.02	-139.30	-166.02	-166.77
7	-27.54	-27.54	-55.35	-55.35	-83.73	-83.71	-111.48	-111.47	-139.89	-140.14	-167.14	-167.82
8	-27.60	-27.59	-55.50	-55.49	-84.02	-84.00	-111.91	-111.91	-140.50	-140.72	-167.93	-168.55
9	-27.63	-27.63	-55.60	-55.60	-84.22	-84.21	-112.22	-112.22	-140.94	-141.14	-168.49	-169.07
1.0	-27.65	-27.65	-55.68	-55.67	-84.37	-84.36	-112.46	-112.46	-141.26	-141.44	-168.91	-169.45

	N=8		N=9		N=10		N=11		N=12		N=13	
	(a)	(b)	(a)	(b)	(a)	(b)	(a)	(b)	(a)	(b)	(a)	(b)
1	-131.51	-135.48	-145.80	-153.94	-159.61	-172.28	-172.88	-190.27	-183.26	-208.83	-190.03	-228.07
2	-169.33	-171.86	-191.98	-196.38	-214.22	-220.79	-235.95	-244.84	-256.68	-269.46	-276.10	-294.76
3	-181.46	-183.30	-206.70	-209.74	-231.68	-236.05	-256.09	-262.00	-280.53	-288.53	-304.19	-315.74
4	-187.20	-188.69	-213.63	-216.02	-239.84	-243.23	-265.50	-270.09	-291.78	-297.52	-317.74	-325.63
5	-190.44	-191.73	-217.54	-219.57	-244.42	-247.28	-270.80	-274.64	-297.95	-302.58	-325.38	-331.19
6	-192.47	-193.62	-219.99	-221.78	-247.19	-249.80	-274.12	-277.48	-301.74	-305.73	-329.91	-334.66
7	-193.83	-194.88	-221.63	-223.24	-249.52	-251.48	-276.34	-279.37	-304.26	-307.83	-332.80	-336.97
8	-194.77	-195.75	-222.78	-224.26	-250.75	-252.65	-277.90	-280.68	-306.02	-309.29	-334.79	-338.57
9	-195.46	-196.38	-223.60	-224.99	-251.49	-253.48	-279.02	-281.62	-307.28	-310.33	-336.22	-339.72
1.0	-195.96	-196.84	-224.21	-225.53	-252.20	-254.09	-279.86	-282.30	-308.22	-311.09	-337.28	-340.58

Equilibrium Constants: Argon

(a) *This work*
 (b) *Andres*

Table 37
 $\log_{10} K(N, T^*)$

T^*	$N=2$		$N=3$		$N=4$		$N=5$		$N=6$		$N=7$	
	(a)	(b)	(a)	(b)	(a)	(b)	(a)	(b)	(a)	(b)	(a)	(b)
.1	-24.22	-24.17	-45.46	-45.30	-64.01	-63.69	-81.55	-81.48	-98.24	-100.17	-112.94	-117.88
.2	-26.20	-26.19	-51.41	-51.36	-75.90	-75.82	-99.60	-99.67	-123.44	-124.43	-145.81	-148.20
.3	-26.83	-26.83	-53.29	-53.27	-79.67	-79.63	-105.33	-105.39	-131.41	-132.05	-156.20	-157.73
.4	-27.13	-27.13	-54.18	-54.17	-81.45	-81.43	-108.04	-108.09	-135.17	-135.65	-161.07	-162.23
.5	-27.29	-27.29	-54.68	-54.68	-82.46	-82.44	-109.57	-109.61	-137.29	-137.67	-163.82	-164.76
.6	-27.40	-27.40	-54.99	-54.99	-83.08	-83.07	-110.53	-110.55	-138.61	-138.93	-165.53	-166.33
.7	-27.47	-27.47	-55.20	-55.20	-83.50	-83.49	-111.16	-111.18	-139.50	-139.77	-166.67	-167.38
.8	-27.52	-27.52	-55.35	-55.35	-83.79	-83.78	-111.61	-111.62	-140.15	-140.36	-167.46	-168.11
.9	-27.55	-27.55	-55.45	-55.45	-84.00	-83.99	-111.92	-111.93	-140.56	-140.77	-168.03	-168.63
1.0	-27.58	-27.58	-55.53	-55.53	-84.15	-84.14	-112.15	-112.16	-140.89	-141.08	-168.45	-169.01

	$N=8$		$N=9$		$N=10$		$N=11$		$N=12$		$N=13$	
	(a)	(b)	(a)	(b)	(a)	(b)	(a)	(b)	(a)	(b)	(a)	(b)
.1	-128.76	-134.97	-142.50	-153.36	-155.78	-171.63	-168.50	-189.54	-178.27	-208.03	-184.31	-227.20
.2	-168.21	-171.35	-190.65	-195.80	-212.68	-220.13	-234.20	-244.11	-254.69	-268.66	-273.84	-293.89
.3	-180.67	-182.79	-205.78	-209.16	-230.64	-235.39	-254.91	-261.28	-279.19	-287.73	-302.68	-314.87
.4	-186.53	-188.18	-212.86	-215.44	-238.97	-242.58	-264.52	-269.36	-290.68	-296.72	-316.51	-324.76
.5	-189.83	-191.22	-216.84	-218.99	-243.62	-246.63	-269.91	-273.92	-296.97	-301.78	-324.29	-330.32
.6	-191.89	-193.11	-219.33	-221.20	-246.53	-249.15	-273.28	-276.76	-300.82	-304.93	-328.89	-333.79
.7	-193.27	-194.37	-220.99	-222.66	-248.46	-250.83	-275.53	-278.64	-303.37	-307.03	-331.82	-336.10
.8	-194.23	-195.25	-222.15	-223.68	-249.81	-251.99	-277.11	-279.95	-305.15	-308.49	-333.84	-337.70
.9	-194.92	-195.87	-222.99	-224.41	-250.79	-252.83	-278.25	-280.89	-306.43	-309.53	-335.29	-338.85
1.0	-195.43	-196.33	-223.60	-224.95	-251.51	-253.44	-279.09	-281.58	-307.38	-310.29	-336.36	-339.69

Equilibrium Constants: Krypton

(a) *This work*

(b) *Andres*

Table 38
 $\log_{10}K(N, T^*)$

T^*	$N=2$		$N=3$		$N=4$		$N=5$		$N=6$		$N=7$	
	(a)	(b)	(a)	(b)	(a)	(b)	(a)	(b)	(a)	(b)	(a)	(b)
.1	-24.02	-24.00	-45.02	-44.96	-63.31	-63.18	-80.57	-80.80	-96.98	-99.33	-111.38	-116.87
.2	126.03	-26.02	-51.04	-51.03	-75.34	-75.31	-98.85	-98.99	-122.49	-123.58	-144.66	-147.18
.3	-26.66	-26.66	-52.94	-52.93	-79.14	-79.12	-104.62	-104.71	-130.51	-131.21	-155.12	-156.72
.4	-26.96	-26.96	-53.84	-53.83	-80.93	-80.92	-107.34	-107.41	-134.29	-134.80	-160.02	-161.21
.5	-27.12	-27.12	-54.34	-54.34	-81.94	-81.93	-108.88	-108.93	-136.42	-136.82	-162.78	-163.74
.6	-27.23	-27.23	-54.65	-54.65	-82.57	-82.56	-109.84	-109.87	-137.76	-138.09	-164.49	-165.32
.7	-27.30	-27.30	-54.86	-54.86	-82.98	-82.98	-110.48	-110.50	-138.64	-138.93	-165.64	-166.37
.8	-27.35	-27.35	-55.01	-55.01	-83.28	-83.28	-110.92	-110.94	-139.26	-139.51	-166.43	-167.09
.9	-27.38	-27.38	-55.11	-55.11	-83.48	-83.48	-111.24	-111.25	-139.71	-139.93	-167.01	-167.62
1.0	-27.41	-27.41	-55.18	-55.19	-83.64	-83.64	-111.47	-111.48	-140.03	-140.23	-167.43	-167.99

	$N=8$		$N=9$		$N=10$		$N=11$		$N=12$		$N=13$	
	(a)	(b)	(a)	(b)	(a)	(b)	(a)	(b)	(a)	(b)	(a)	(b)
.1	-126.93	-133.79	-140.36	-152.01	-153.32	-170.11	-165.74	-187.85	-175.17	-206.17	-180.84	-225.17
.2	-166.85	-170.16	-189.09	-194.45	-210.92	-218.61	-232.23	-242.42	-252.50	-266.80	-271.43	-291.86
.3	-179.41	-181.61	-204.34	-207.80	-229.01	-233.87	-253.10	-259.58	-277.18	-285.87	-300.47	-312.84
.4	-185.31	-186.99	-211.45	-214.09	-237.38	-241.05	-262.76	-267.67	-288.74	-294.85	-314.38	-322.72
.5	-188.62	-190.04	-215.45	-217.63	-242.06	-245.10	-268.18	-272.22	-295.06	-299.91	-322.20	-328.29
.6	-190.69	-191.93	-217.95	-219.84	-244.97	-247.63	-271.56	-275.06	-298.92	-303.07	-326.82	-331.76
.7	-192.07	-193.19	-219.62	-221.31	-246.92	-249.30	-273.82	-276.95	-301.48	-305.17	-329.76	-334.07
.8	-193.03	-194.06	-220.78	-222.33	-248.28	-250.47	-275.40	-278.26	-303.26	-306.62	-331.79	-335.67
.9	-193.72	-194.69	-221.62	-223.06	-249.25	-251.30	-276.54	-279.20	-304.55	-307.67	-333.24	-336.82
1.0	-194.23	-195.14	-222.24	-223.59	-249.98	-251.91	-277.39	-279.88	-305.50	-308.43	-334.32	-337.65

Equilibrium Constants: Xenon

(a) This work
 (b) Andres

parameters used for neon in these calculations are contained in Table 11; use of different parameters (e.g. p.1110 in Hirschfelder, Curtiss and Bird (1954)) in conjunction with a full quantum mechanical treatment may yield equilibrium constants at very low temperatures more in accord with those provided by Andres.

8.4 Relative Equilibrium Concentrations

Any model which is designed to investigate the thermodynamic properties of a system needs to incorporate the existence of very many stable and distinct isomeric forms for specified N . Modification of the single configuration model becomes necessary to take account of these isomeric forms. The relative concentration of one isomer over another in a heat bath depends on the thermodynamic advantage of one over the other: relative equilibrium concentrations for the most stable and least stable configurations for $6 \leq N \leq 13$, calculated by use of equation (5.33), for the 4 gases under consideration over the entire temperature range are presented in Tables 39 to 42. Figures 38 to 41 illustrate the behaviour of these equilibrium concentrations. Except for $N=6$, in which case the most stable isomer possesses octahedral symmetry, both the most and least stable isomers for all N are grown on the tetrahedral growth scheme. This growth scheme is therefore capable of producing both very compact structures and elongated structures. Metastable configurations are not used in the calculation of these equilibrium concentrations; these configurations are considered to reform extremely rapidly to a previously identified stable configuration and do not therefore contribute to the overall concentration for that size cluster.

Figure 38

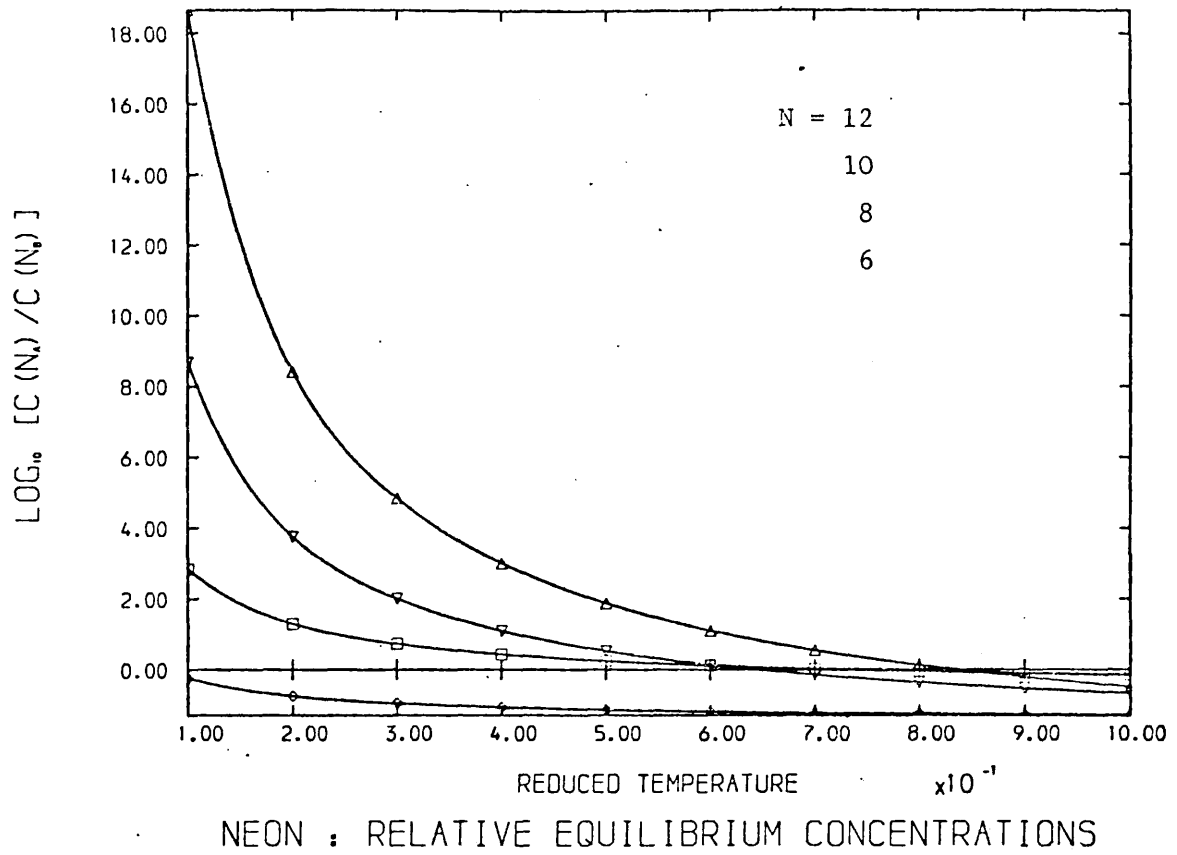


Figure 39

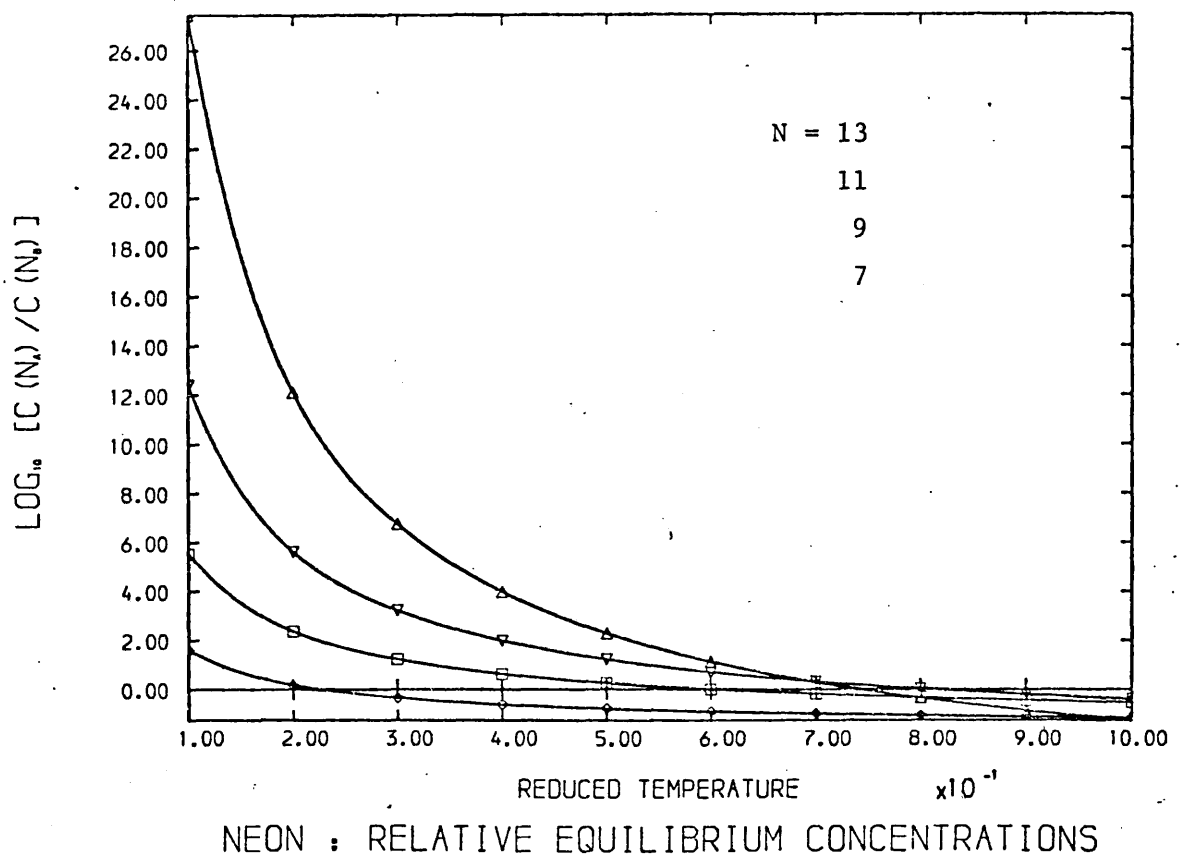
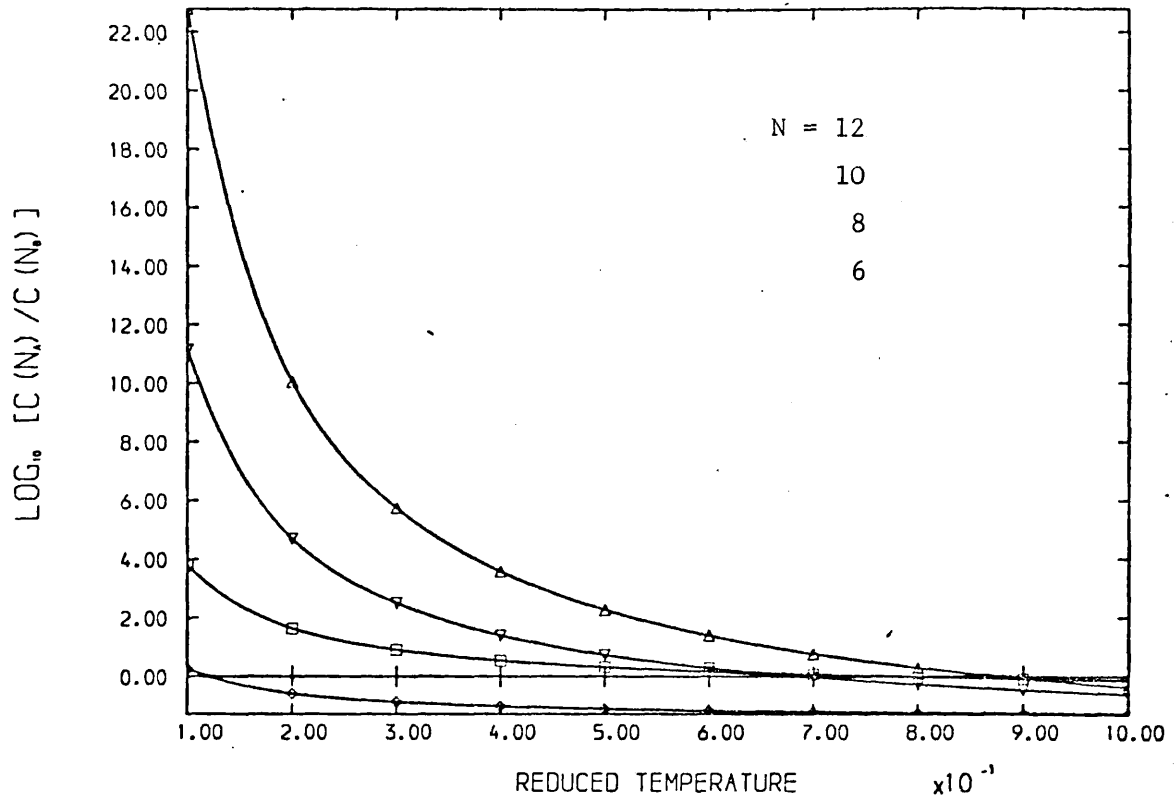
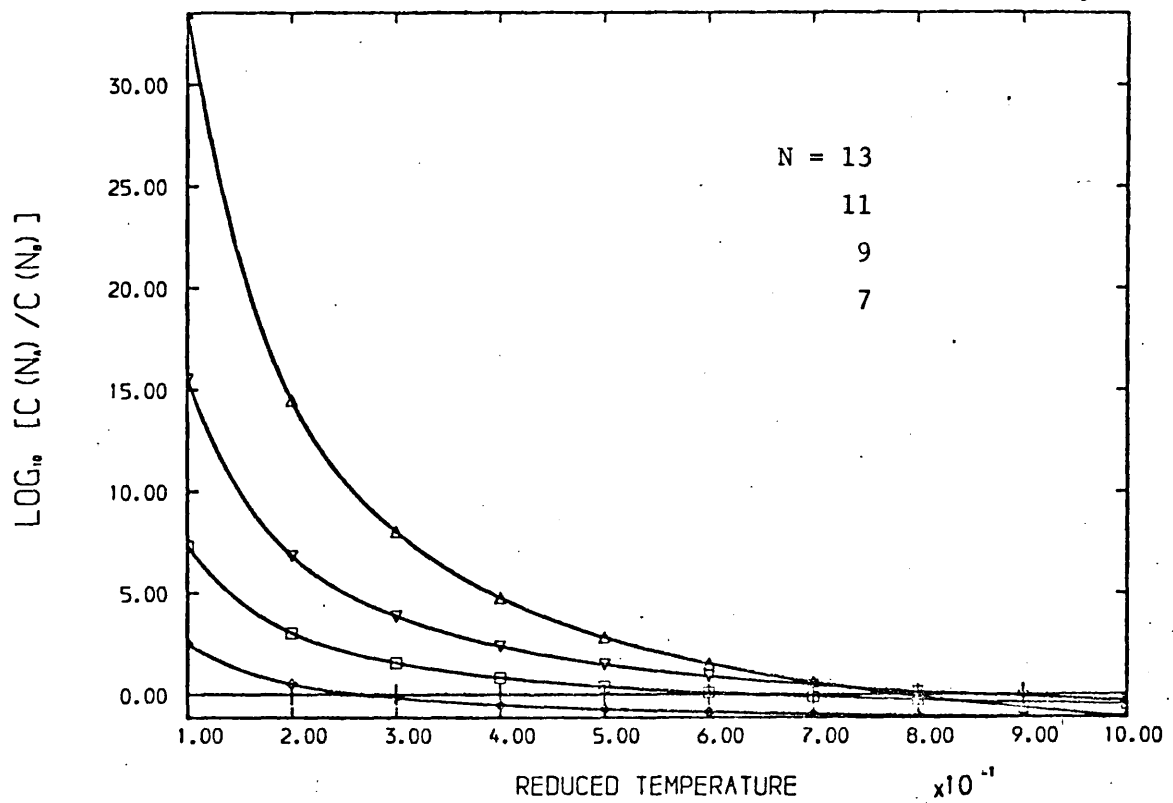


Figure 40



ARGON : RELATIVE EQUILIBRIUM CONCENTRATIONS

Figure 41



ARGON : RELATIVE EQUILIBRIUM CONCENTRATIONS

Writing equation (5.33) for the concentration of isomer A over isomer B explicitly, with an implicit temperature dependence, produces

$$\frac{C(N)_A}{C(N)_B} = \frac{\chi_B (I_A I_B I_C)_A^{\frac{1}{2}}}{\chi_A (I_A I_B I_C)_B^{\frac{1}{2}}} \frac{\prod_{i=1}^{3N-6} \{\exp(-h\nu_i/2kT) [1 - \exp(-h\nu_i/kT)]^{-1}\}_A}{\prod_{i=1}^{3N-6} \{\exp(-h\nu_i/2kT) [1 - \exp(-h\nu_i/kT)]^{-1}\}_B} \times \exp\{[-V(N)_A + V(N)_B]/kT\} \quad (8.3)$$

where $V(N)_A$ is the potential energy of the A^{th} N-atom cluster.

This equation illustrates the competition between the vibrational and rotational partition functions: the most stable configuration with the largest vibrational partition function is likely to possess a high order of symmetry

(e.g. N=6, regular octahedron, symmetry group O_h , $\chi=24$;

N=7, pentagonal bipyramid, symmetry group D_{5h} , $\chi=10$;

N=13, regular icosahedron, symmetry group I_h , $\chi=60$)

with a correspondingly large symmetry number χ . Since the rotational partition function varies inversely with χ the competition between rotational and vibrational contributions to equation (8.3) is clearly seen. In the size range studied here the more compact structures (ie. higher binding energies) are also highly symmetric; these mutually compensating effects reduce the relative equilibrium concentrations for most and least stable configurations. Consequently in this size range symmetry effects are extremely important, since the compensating contribution due to binding energy is small for small clusters. With increasing N symmetry considerations become less important and the relative concentration of two isomers depends predominantly on potential energy contributions. Because of the minute size of the clusters any possibility of a sharp transition between differing isomeric forms or between liquid and solid

behaviour is removed. Fluctuations between different forms become important for microclusters of these dimensions in the determination of the Gibbs free energy of formation; consequently a multi-configurational approximation should be used in any search for critical nuclear sizes from the stationary values of the free energy of formation curves at different pressures.

8.5 Discussion of Relative Equilibrium Concentrations

The immediate impression gained from Tables 39 to 42, or from Figures 38 to 41, is that with increasing temperature the relative concentrations of most to least stable configurations decrease. It is interesting to note the temperature at which the relative concentrations pass through unity. For neon 6-atom clusters the relative concentrations are always less than 1 in the temperature range studied ($T^* = .1 \rightarrow 1.0$), but for larger neon clusters we see that there is a preponderance of the more stable configurations over the less stable configurations up to $T^* \sim .2$ for $N=7$, $T^* \sim .6-.7$ for $N=8,9,10$ and $T^* \sim .8$ for $N=11,12$ and 13. The interpretation of these temperatures is that for larger clusters (in the size range studied) the most stable configuration takes precedence over the least stable up to a temperature which is approximately the bulk melting point, whilst for smaller clusters, with correspondingly smaller energy differences between most and least stable configurations, thermal fluctuations are sufficient to cause the formation of less ordered structures at very low reduced temperatures. One sees that for neon 6-atom clusters the thermal disorder in the system is sufficient at $T^* = .1$ to cause an excess of the least stable isomers over the most stable. Tables 40, 41 and 42 for argon, krypton and xenon respectively show the same qualitative behaviour

as Table 39 does for neon; this is perhaps illustrated more clearly by Figures 38 and 40. For the heavier rare gases the relative concentrations increase, although the concentrations for all gases, for the same N , pass through unity at approximately the same reduced temperature. The largest concentration is for 13-atom neon clusters, at a reduced temperature of .1, with a \log_{10} of ~ 27.5 . The smallest concentration is for 6-atom clusters of the same gas at a reduced temperature of 1.0 with a \log_{10} of ~ 1.3 . Figures 38 to 41 show an almost exponential decrease, suggesting at lower temperatures the most stable configuration is strongly dominant. With increasing temperature the advantage possessed by the most stable configuration is diminished by increasing disorder in the system, until the concentration ratio passes through 1 and the least stable configuration becomes dominant. However, the dominance of the least stable configuration is weak; see Figures 38 to 41, which show that \log_{10} of the equilibrium concentration slows almost asymptotically. Such behaviour may be deduced from the form of equation (8.3), which shows the relative concentrations to be dominated by the interatomic potential of the most stable configuration. With increasing temperature the effect of this potential is strongly reduced. Once the concentration ratio has passed through 1 (from above) temperature increases do not significantly alter the proportion of number of most stable configurations to number of least stable configurations.

Table 39

T*	$\log_{10} C_A(N, T^*) / C_B(N, T^*)$												
	N	6	7	8	9	10	11	12	13				
.1		-0.2478	1.5910	2.8384	5.5405	8.6762	12.5059	18.6470	27.4556				
.2		-0.7509	+0.1805	1.2936	2.3763	3.7590	5.6222	8.4153	12.1189				
.3		-0.9525	-0.3376	.7321	1.2372	2.0106	3.2336	4.8480	6.7600				
.4		-1.0651	-0.6152	.4332	.6354	1.0951	1.9910	3.0007	3.9881				
.5		-1.1372	-0.7898	.2458	.2598	.5268	1.2227	1.8755	2.2832				
.6		-1.1873	-0.9100	.1169	+0.0021	+0.1381	.6984	1.1061	1.1244				
.7		-1.2241	-0.9979	+0.0227	-0.1860	-0.1452	.3168	.5474	+0.2835				
.8		-1.2522	-1.0650	-0.0491	-0.3294	-0.3611	+0.0263	+0.1227	-0.3553				
.9		-1.2745	-1.1179	-0.1058	-0.4425	-0.5311	-0.2025	-0.2114	-0.8575				
1.0		-1.2925	-1.1607	-0.1516	-0.5339	-0.6685	-0.3873	-0.4813	-1.2629				

Relative Equilibrium Concentrations: Neon

Table 40

T*	$\log_{10} C_A(N, T^*) / C_B(N, T^*)$												
	N	6	7	8	9	10	11	12	13				
.1		+0.2416	2.4972	3.7734	7.3046	11.1408	15.5189	22.7788	33.5364				
.2		-0.5925	+0.5032	1.6334	3.0281	4.6928	6.8285	10.0562	14.4895				
.3		-0.8785	-0.1769	.9039	1.5724	2.5019	3.8800	5.7493	8.0440				
.4		-1.0231	-0.5203	.5355	.8375	1.3961	2.3918	3.5771	4.7947				
.5		-1.1103	-0.7276	.3133	.3941	.7989	1.4941	2.2667	2.8353				
.6		-1.1169	-0.8662	.1646	+0.0975	+0.2826	.8936	1.3901	1.5247				
.7		-1.2104	-0.9654	.0581	-0.1149	-0.0370	.4635	.7624	+0.5863				
.8		-1.2418	-1.0400	-0.0218	-0.2745	-0.2771	+0.1404	+0.2907	-0.1188				
.9		-1.2662	-1.0981	-0.0841	-0.3988	-0.4642	-0.1113	-0.0767	-0.6679				
1.0		-1.2858	-1.1446	-0.1340	-0.4983	-0.6139	-0.3129	-0.3710	-1.1076				

Relative Equilibrium Concentrations: Argon

Table 41

T*	$\log_{10} C(N, T^*) / C_B(N, T^*)$												
	N	6	7	8	9	10	11	12	13				
.1		+2.2923	2.6065	3.8900	7.5314	11.4717	15.9525	23.3796	34.3936				
.2		-5.798	+5.332	1.6660	3.0932	4.7914	6.9614	10.2492	14.7616				
.3		-8.729	-1.634	.9187	1.6023	2.5477	3.9421	5.8412	8.1735				
.4		-1.0200	-5.127	.5439	.8545	1.4223	2.4276	3.6302	4.8695				
.5		-1.1083	-7.226	.3187	.4051	.7458	1.5172	2.3012	2.8838				
.6		-1.1672	-8.628	.1684	+1.1051	+2.2944	.9097	1.4142	1.5586				
.7		-1.2093	-9.629	+0.0610	-1.1093	-0.283	.4754	.7801	+6.113				
.8		-1.2410	-1.0381	-0.0197	-2.2702	-2.705	+1.1495	+3.3043	-0.0995				
.9		-1.2656	-1.0966	-0.0824	-3.954	-4.589	-1.041	-0.659	-6.526				
1.0		-1.2853	-1.1433	-1.1326	-4.955	-6.097	-3.070	-3.622	-1.0953				

Relative Equilibrium Concentrations: Krypton

T*	$\log_{10} C(N, T^*) / C_B(N, T^*)$												
	N	6	7	8	9	10	11	12	13				
.1		+3.058	2.6378	3.9240	7.5991	11.5737	16.0894	23.5772	34.6722				
.2		-5.764	+5.413	1.6748	3.1111	4.8188	6.9989	10.3048	14.8392				
.3		-8.714	-1.597	.9227	1.6103	2.5601	3.9590	5.8665	8.2091				
.4		-1.0191	-5.107	.5462	.8591	1.4293	2.4372	3.6446	4.8897				
.5		-1.1077	-7.213	.3202	.4080	.7503	1.5234	2.3104	2.8968				
.6		-1.1669	-8.619	.1694	+1.1072	+2.2975	.9140	1.4206	1.5677				
.7		-1.2091	-9.622	+0.0617	-1.1078	-0.260	.4786	.7849	+6.180				
.8		-1.2408	-1.0376	-0.0191	-2.2690	-2.687	+1.1519	+3.3079	-0.0944				
.9		-1.2655	-1.0961	-0.0820	-3.945	-4.575	-1.022	-0.631	-6.486				
1.0		-1.2852	-1.1430	-1.1323	-4.948	-6.086	-3.055	-3.599	-1.0920				

Relative Equilibrium Concentrations: Xenon

Chapter 9

9.1 An Introduction to Nucleation Theory

Gibbs (1906) and Thomson (1870) were the first to treat quantitatively the stability of a phase by considering the work required to form a spherical droplet of radius $r(N)$. The ideas of Gibbs were developed by Volmer and Weber (1926), Farkas (1927), Volmer and Flood (1934), Becker and Döring (1935), and Zeldovich (1942,1943), and culminated in the classical liquid-drop theory of nucleation. Feder et al (1966) provide a general review of steady state nucleation theory. In the liquid-drop theory the free energy of formation of a spherical drop of radius $r(N)$ in the centre of a large volume of vapour is calculated by use of equation (9.1).

$$\Delta G(N) = 4\pi r(N)^2 \eta + \frac{4\pi r(N)^3}{3} \Delta G_v \quad (9.1)$$

In equation (9.1) η is the surface free energy,

$$\Delta G_v = \frac{-kT}{v_1} \ln \left(\frac{P}{P_o} \right),$$

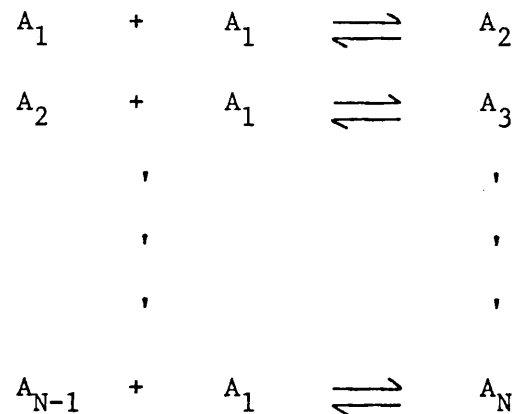
v_1 is the molecular volume of the liquid,

P is the partial pressure of the vapour,

P_o is the equilibrium vapour pressure.

ΔG_v is the free energy change per unit volume of the stable condensed phase. This equation has a maximum at the critical radius $r^*(N^*)$; clusters containing fewer than N^* atoms are unstable whilst larger clusters form stable, growing nuclei. The formation of the condensed

phase is by the growth of small clusters into droplets by the addition of monomers. The supersaturated vapour is considered as a gaseous mixture of these clusters and the monomers (Frenkel (1946)); growth and decay is limited to the gain or loss of a single atom. Thus the growth mechanism may be represented as follows:



Interactions between clusters are ignored, since these are considered to be highly improbable (Volmer and Weber (1925)). The equilibrium concentration of an N-atom critical nucleus at temperature T is given by equation (9.2); this equation is valid only for the critical nucleus since other clusters are not in equilibrium with the monomeric vapour. A lower limit to

$$\frac{C(N)}{C(1)} = \exp \left[- \frac{G(N)}{kT} \right] \quad (9.2)$$

the applicability of equation (9.2) is suggested by Courtney (1962) to be for clusters containing 19 atoms; Frisch (1957) advocates a lower limit for clusters containing only 2 atoms.

Kirkwood and Buff (1945), Benson and Shuttleworth (1951) and Plesnes (1964) have attempted to extend classical nucleation theory so that the behaviour of very small finite clusters may be investigated. These authors have considered modifications to the surface energy term

in equation (9.1); Dunning (1969) has questioned the propriety of such modifications. Rather than any extrapolation of the classical theory one would prefer an atomistic theory (Walton (1962)), based on intermolecular forces rather than on assumed macroscopic quantities such as surface energy. Hirth (1963) has pointed out that the classical model may not be used in calculations of the thermodynamic properties of very small clusters - Benson and Shuttleworth (1951) have established differences between the potential energies of finite clusters and larger clusters. Classical nucleation theory neglects the translational and rotational motion of a free cluster (Lothe and Pound (1962)) - a finite N-atom cluster has only $3N-6$ degrees of freedom. This neglect may lead to differences of $\sim 10^{15}$ between experimental and classical nucleation rates, and has been discussed by Abraham and Pound (1968) and Abraham and Canosa (1969). A number of experimental studies involving nucleation processes have been undertaken (Milne and Green (1967), Stein and Wegener (1967), Milne, Vandegrift and Greene (1970), Farges et al (1973)); agreement with classical nucleation rates is in general good (Volmer and Flood (1934), Katz (1970)). However, the classical theory should not be applied to very small clusters because of basic incompatibilities between this theory and its extension to finite clusters. Refinements of the classical theory by Lee et al (1973), and Abraham and Dave (1971a), who use Einstein model to introduce the six degrees of freedom that a microcluster lacks, have produced closer agreement with experimental data. Nishioka et al (1971) and Burton (1971b) have argued that such modifications are necessary; these authors are opposed by Bonissent and Mutaftschiev (1973) who have provided evidence in favour of the original Gibbs-Thomson formulation. The validity of the Einstein model has been established through

the molecular dynamical experiments of Dickey and Paskin (1970) and by Burton (1970b). Burton (1971b) has stated that the combination of the Lothe-Pound replacement factor (i.e. the inclusion of six Einstein oscillators) and the statistical thermodynamical results produces nucleation rates in agreement with those predicted by the classical theory. Thus an indication is provided as to why the liquid-drop model often produces results compatible with experimental observations.

In recent years several investigations of the morphological and thermodynamic properties of small clusters (Burton (1969,1970a,b,1971b, 1972a,b,c,1973), McGinty (1971,1972,1973), Hoare and Pal (1971a,b, 1972a,b,1975)) have been undertaken, with a view to using an atomistic model in subsequent calculations of nucleation properties. These investigations have shown that general Gibbsian behaviour may be reproduced by an atomistic model.

The detailed balance equation in Chapter 5 (equation (5.31)) is used to express the ratio of N-atom concentration to monomer concentration $\frac{C(N,T)}{C(1,T)}$ in terms of the cluster partition functions in the following fashion:

$$\frac{\hat{Z}(N,T) \cdot C(1,T)^{N-1}}{\hat{Z}(1,T)^N} = \frac{C(N,T)}{C(1,T)} = \frac{\hat{Z}(N,T)}{\hat{Z}(1,T)^N} \left(\frac{kT}{P}\right)^{1-N} \quad (9.3)$$

In equation (9.3) the partition functions are reduced for unit volume, and the monomer pressure is approximated by the total pressure. Equation (9.3) may now be used to express the Gibbs free energy of formation of an N-atom cluster at temperature T and pressure P in terms of the cluster partition function.

9.2 Free Energies of Formation of Atomic Clusters

McGinty (1971) and Hoare and Pal (1975) have prepared extensive tables of the standard Gibbs free energy of formation of argon micro-clusters; the former author has constructed both 'spherical' and lattice-based structures whilst Hoare and Pal have relied upon their knowledge of the morphology of microclusters (1971a,b,1972a,b) to locate minimal energy configurations. In the present work the necessity of using clusters minimal in potential energy is removed; an 'effective' partition function (the multi-configuration partition function described in Chapter 5) is used in subsequent calculations of free energies. The dependence of the free energy of formation on size is examined to determine the critical nuclear size at specified temperature and pressure. Since the identity of the critical nucleus is by no means well-defined in atomistic terms (Hoare and Pal (1975)) the use of an 'effective' partition function is particularly appropriate. When the number of nuclei is greater than ~ 13 a single-configuration approximation (Zeldovich (1942)) is probably inescapable due to the rapid increase in isomer multiplicity.

Following the example of McGinty (1971) and Hoare and Pal (1975) the cluster partition functions (see Chapter 5) are used in equations (9.2) and (9.3) to calculate the cluster free energies of formations. Equations (9.2) and (9.3) may be combined to yield the following equation for the Gibbs free energy of formation $\Delta G_f(N,T,P)$ of an N-atom cluster as a function of temperature and pressure:

$$\Delta G_f(N,T,P) = -kT \left[\ln \hat{Z}(N,T) - N \ln \hat{Z}(1,T) + (1-N) \ln \left(\frac{kT}{P} \right) \right] \quad (9.4)$$

In equation (9.4) $\hat{Z}(N,T)$ is the partition function defined in equation

(5.1), reduced for unit volume. The standard free energy of formation $\Delta G_f^{\circ}(N,T,1)$ is obtained from equation (9.4) by introducing a pressure of one atmosphere (in the appropriate units), and is related to $\Delta G_f(N,T,P)$ in the following fashion,

$$\Delta G_f^{\circ}(N,T,1) = \Delta G_f(N,T,P) - kT(1-N)\ln P \quad (9.5)$$

Equations (9.4) and (9.5) illustrate the connection between the partition functions and experimentally determined parameters such as temperature and pressure.

Extensive tables of $\Delta G_f^{\circ}(N,T,1)$ for neon, argon, krypton and xenon have been prepared (Appendix D) by using an appropriate partition function in equation (9.4). For $N > 5$ the MCPF (equations (5.26), (5.6) to (5.8)) is used; when $N < 6$ the single-configuration partition function is relevant (equations (5.6) to (5.8) directly inserted into equation (5.1)). Reference to the tables in Appendix D confirms that $\Delta G_f^{\circ}(N,T,1)$ reaches a maximum at a critical value N^* , and that with increasing temperature $\Delta G_d^{\circ}(N,T,1)$ increases. From these tables it is possible to calculate $\Delta G_f(N,T,P)$ at any pressure by use of equation (9.5).

Table 43 contains the $\{\Delta G_f^{\circ}(N,T,1)\}$ of argon microclusters computed via equation (9.4) and the $\{\Delta G_f^{\circ}(N,T,1)\}$ of lattice-grown argon structures calculated by McGinty (1971). Comparison of these data is not easy due to the calculation of $\{\Delta G_f^{\circ}(N,T,1)\}$ at slightly different temperatures. However it appears that at a reduced temperature of .4 non-crystalline clusters possess a distinct thermodynamic advantage over the lattice-based structures. At higher temperatures the MCPF approximation yields standard free energies of formation which imply that the non-crystalline microclusters are thermodynamically favourable;

however the literal validity of the harmonic oscillator approximation is lost at reduced temperatures greater than .3~.4.

Table 43

<u>N</u>	<u>$\Delta G_f^0(N,T,1)$.Joules $\times 10^{21}$</u>			
	<u>a</u>	<u>b</u>	<u>c</u>	<u>d</u>
2	1.561	1.575	3.361	2.993
3	3.012	3.425	7.156	6.847
4	4.820	5.539	12.093	11.54
5	5.574	6.565	15.568	14.79
6	7.166	8.121	20.506	19.10
7	6.899	8.965	22.770	22.54
8	5.947	9.810	23.777	25.64
9	6.320	9.152	27.230	26.60
10	6.357	10.30	29.951	30.74
11	5.557	10.94	32.055	33.96
12	5.702	11.00	35.736	36.78
13	5.359	9.264	40.673	37.93

Comparison of Standard Gibbs Free Energy of Formation
of Argon Clusters

- a) *this work at $T = 47.92^\circ A$*
- b) *McGinty (1971) at $T = 50.3^\circ A$*
- c) *this work at $T = 71.88^\circ A$*
- d) *McGinty (1971) at $T = 70.1^\circ A$*

Equation (9.5) and the data in Appendix D are used to calculate free energies of formation of N-atom clusters at pressures of .01, .1

and 1.00 atmospheres. Figures 46 to 49 illustrate the behaviour of $\Delta G_f(N,T,P)$ as a function of temperature and chemical species. These figures, in agreement with those of McGinty (1971) and Hoare and Pal (1975), show broad maxima at critical values of N , thereby confirming the validity of the atomistic approach. With increasing atomic mass the free energy of formation of an N -atom cluster increases (see Appendix D and Figures 42 to 49).

9.3 Critical Nuclear Sizes

From Figures 46 to 49, equation (9.5) and the data in Appendix D the critical nuclear sizes of rare gas clusters as a function of pressure may be calculated. Table 44 contains representative results at a reduced temperature of .3. The number of nuclei in the critical nucleus is seen to remain constant (at 4) for all four gases at a pressure of one atmosphere, although more energy is required to form the nucleus as the atomic mass increases. With reducing pressure the size of the critical nucleus increases, until at a pressure of .01 atmosphere no critical nucleus is predicted for neon clusters containing less than 14 atoms. The critical nuclei predicted by McGinty (1971),

Table 44

$\Delta G_f(N^*, T^*=.3, P)$ Joules $\times 10^{21}$

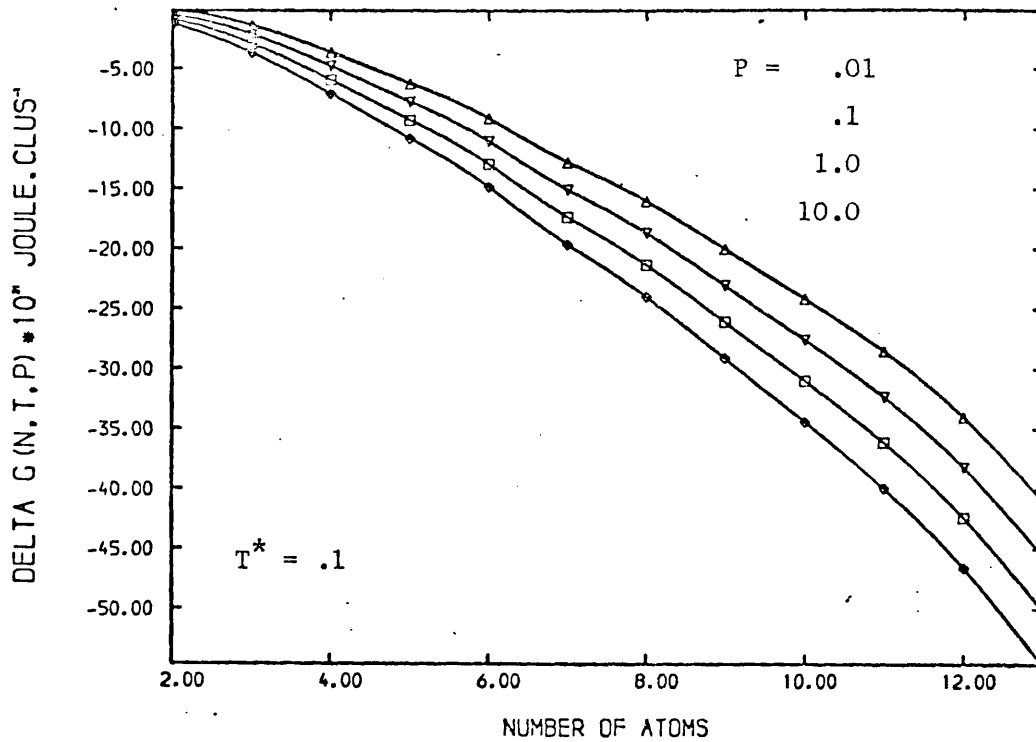
<u>P</u> <u>atmos.</u>	<u>Ne</u>	<u>(N*)</u>	<u>Ar</u>	<u>(N*)</u>	<u>Kr</u>	<u>(N*)</u>	<u>Xe</u>	<u>(N*)</u>
.01	*		14.987	(12)	21.980	(12)	26.753	(12)
.10	2.127	(6)	6.157	(6)	9.761	(7)	11.147	(6)
1.00	0.438	(4)	1.188	(4)	1.962	(4)	2.123	(4)

Critical Nuclear Sizes and Corresponding Free Energies of Formation

*: *no turning point for $N < 14$.*

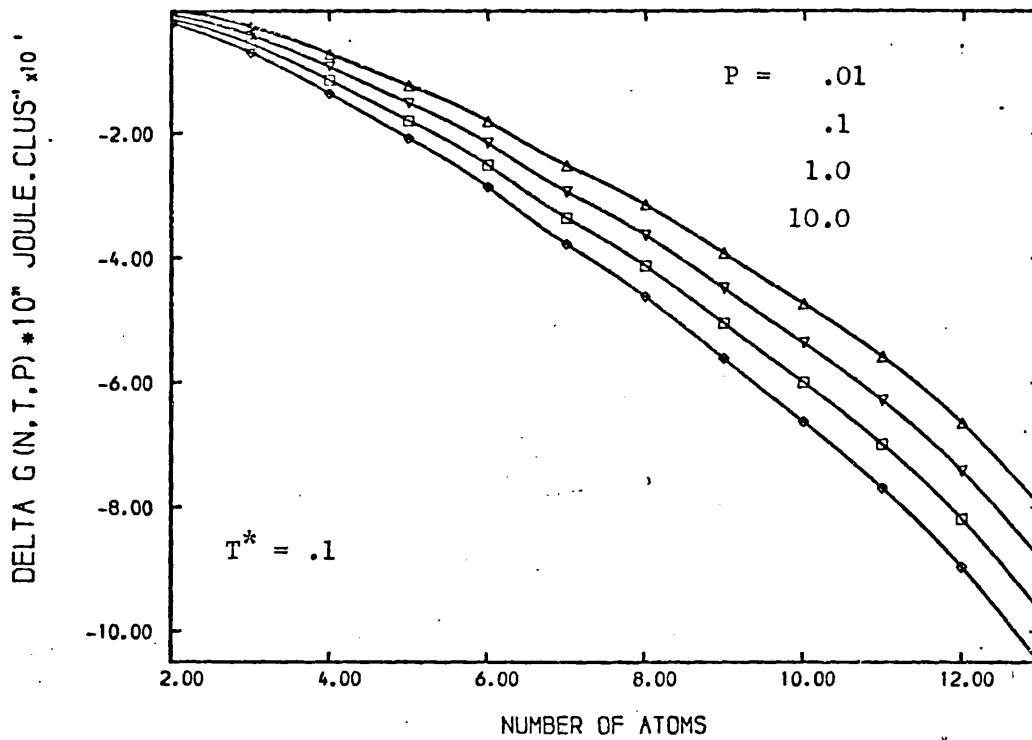
Burton (1971b), and Hoare and Pal (1975) all contain at least 10 atoms more than do the nuclei estimated in the present work.

Figure 42



ARGON : GIBBS FREE ENERGY OF FORMATION

Figure 43



XENON : GIBBS FREE ENERGY OF FORMATION

Figure 44

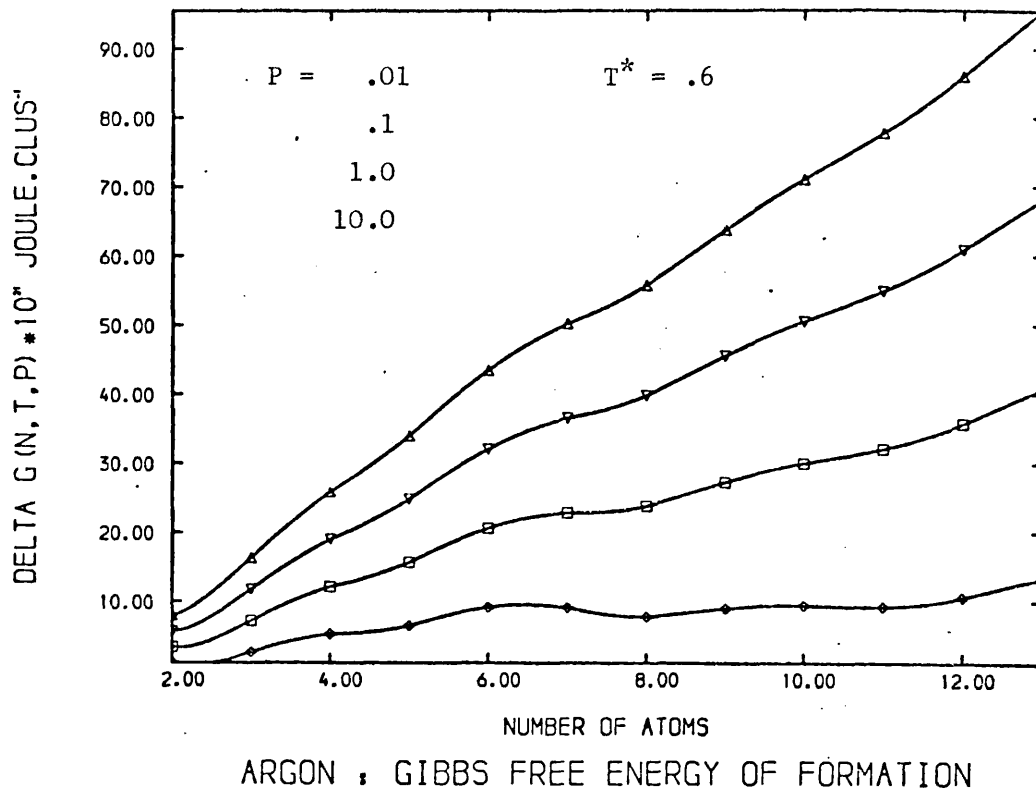


Figure 45

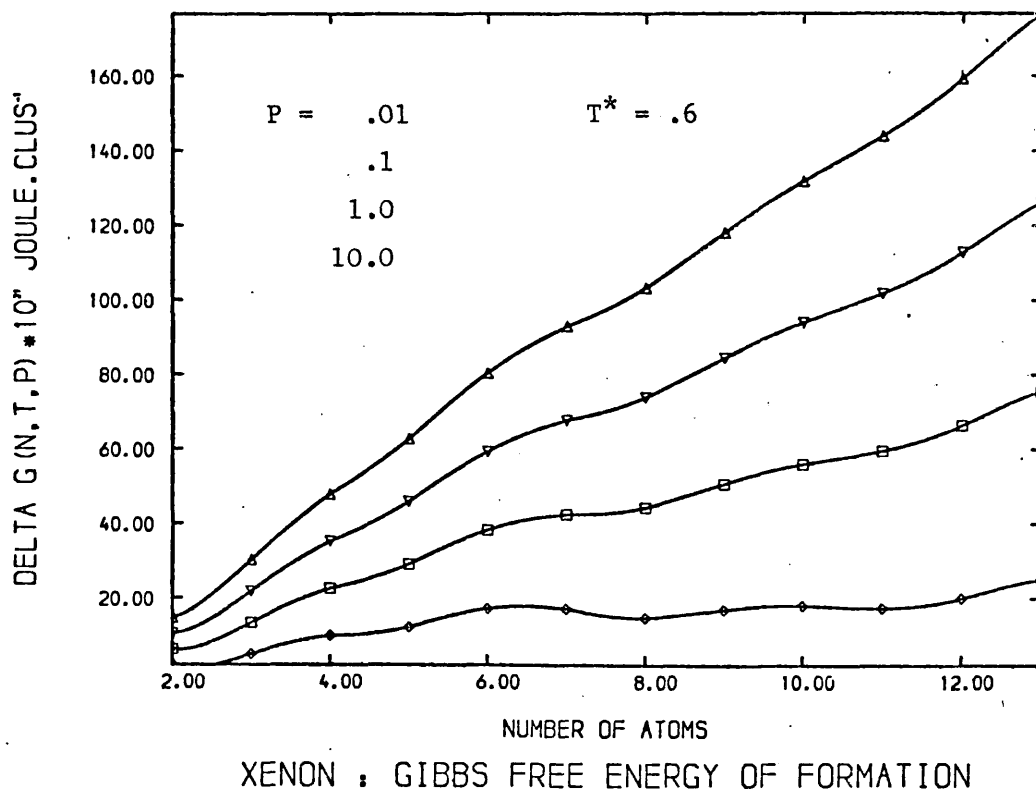


Figure 46

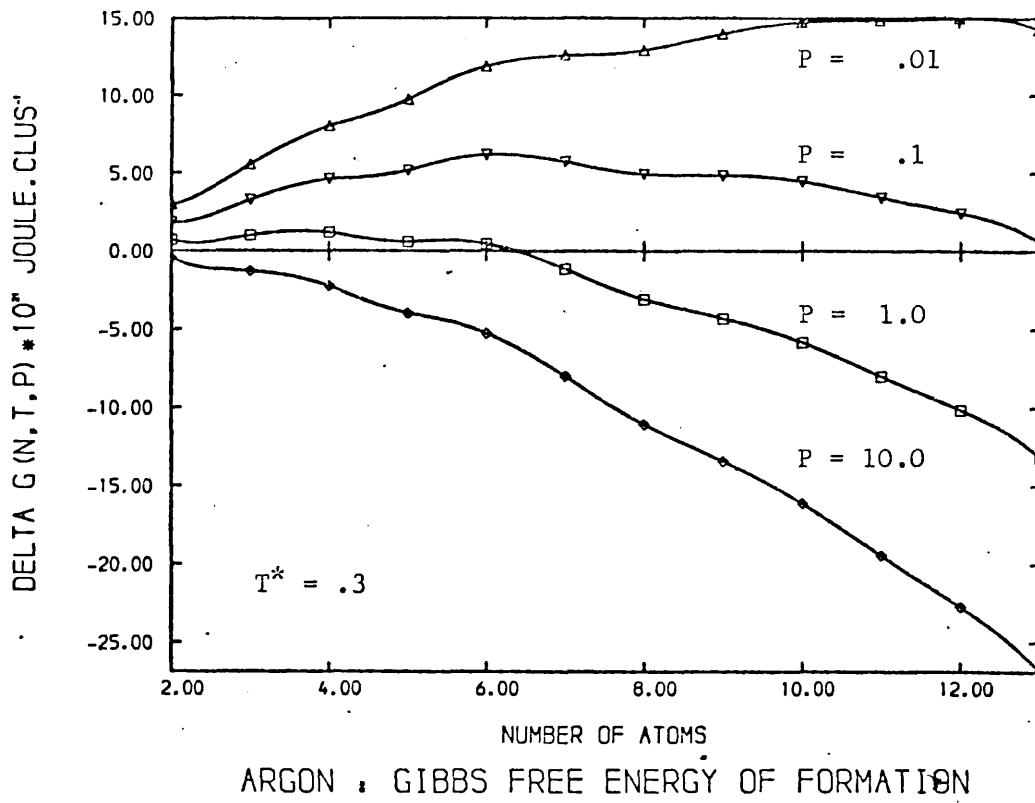


Figure 47

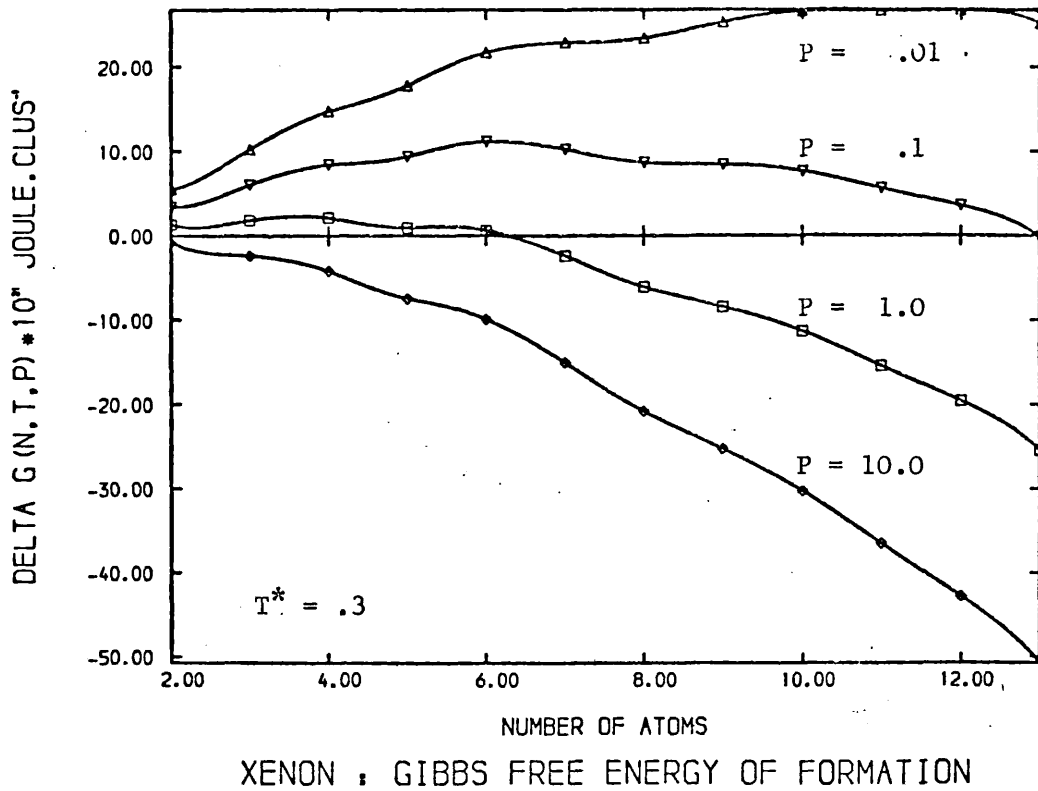
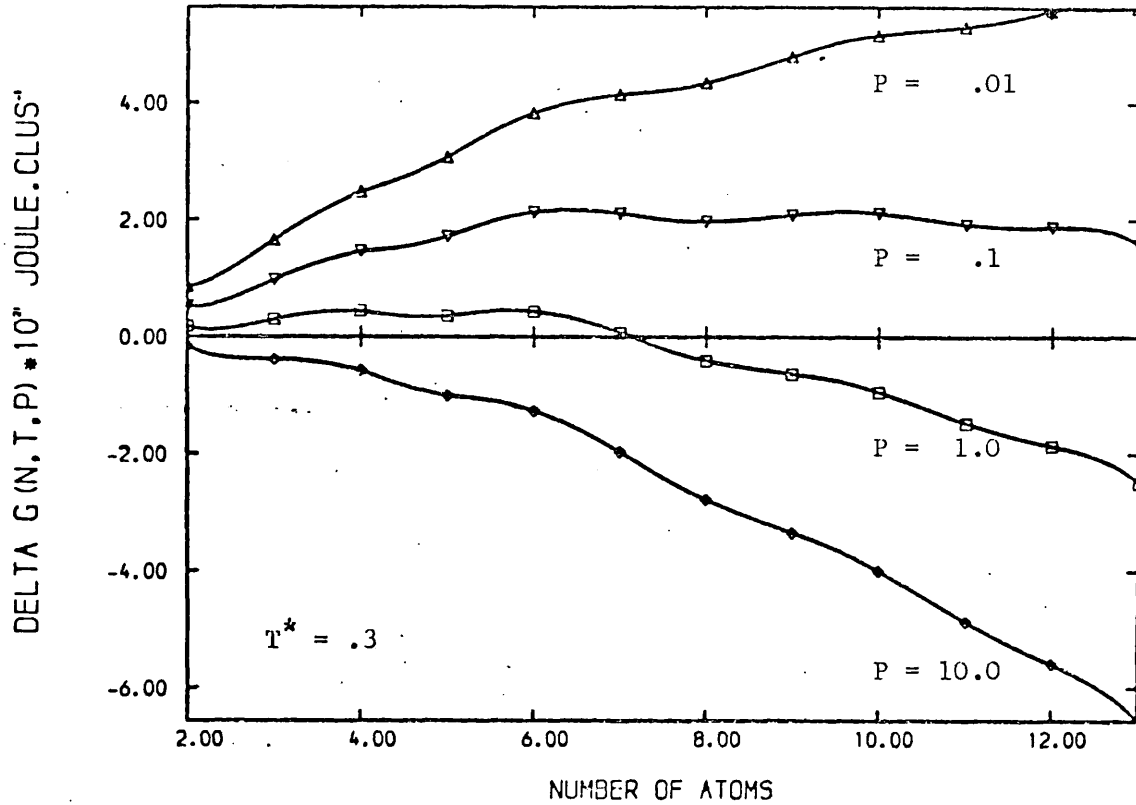
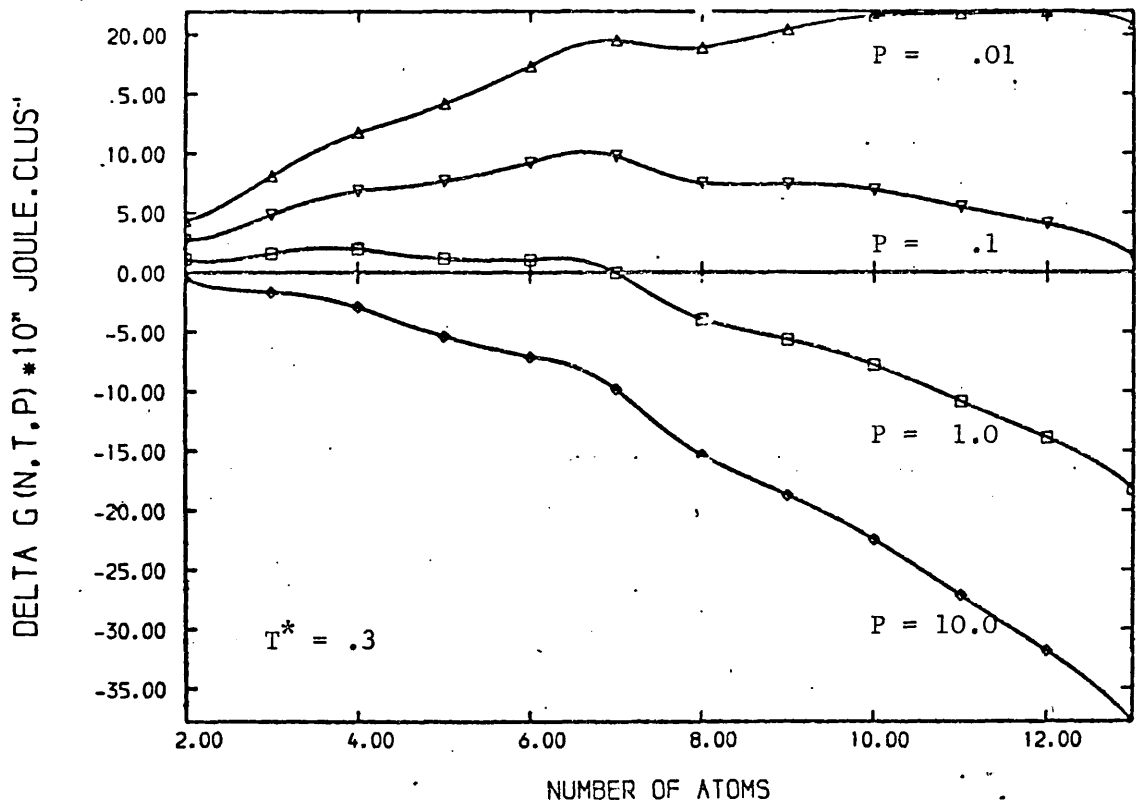


Figure 48



NEON : GIBBS FREE ENERGY OF FORMATION

Figure 49



KRYPTON : GIBBS FREE ENERGY OF FORMATION

Chapter 10

10.1 Introduction

The canonical partition function for a single-component system of N structureless particles may be written (see for example Hill (1956)).

$$Q_N = \frac{\int d^{3N}r \exp\left[-\frac{1}{kT} \left(\sum_{i<j} u_{ij} \right)\right]}{N! \Lambda^{3N}} \quad (10.1)$$

where $\Lambda = \left(\frac{h^2}{2\pi m kT} \right)^{\frac{1}{2}}$, u_{ij} is the potential energy of interaction between the i^{th} and j^{th} particles, and the integral in (10.1) is the configuration integral q_N . The grand canonical partition function is given by

$$\Xi(\mu, V, T) = \sum_{N=0}^{\infty} Q_N \exp(\mu N/kT) = 1 + \sum_{N=1}^{\infty} \frac{q_N \lambda^N}{N!} \quad (10.2)$$

where μ = chemical potential,

$$\lambda = \frac{\exp(\mu/kT)}{\Lambda^3} = \text{activity.}$$

Since $\Xi = \exp\left(\frac{pV}{kT}\right)$ the pressure may be expressed as a power series in the activity

$$\frac{P}{kT} = \frac{1}{V} \ln \left[1 + \sum_{N=1}^{\infty} \frac{q_N \lambda^N}{N!} \right] \quad (10.3)$$

Use of the expansion

$$\ln(1+x) = - \sum_{n=1}^{\infty} \frac{(-x)^n}{n}$$

in (10.3) leads directly to

$$\frac{P}{kT} = \frac{1}{V} \ln \Xi = \sum_{\ell=1}^{\infty} b_{\ell} \lambda^{\ell} \quad (10.4),$$

where the coefficients $\{b\}$ are the Mayer cluster integrals.

Expressions for $\ell!Vb_\ell$ are known as the semi-invariants of Thiele and are tabulated for $\ell \leq 10$ by Kendall and Stuart (1969).

Since the mean number of particles $\bar{N} = \lambda \left(\frac{\partial \ln \Xi}{\partial \lambda} \right)$, equation (10.4) may be used to produce

$$\frac{\bar{N}}{V} = \lambda \frac{\partial}{\partial \lambda} \left[\sum_{\ell=1}^{\infty} b_\ell \lambda^\ell \right] = \sum_{\ell=1}^{\infty} \ell b_\ell \lambda^{\ell-1} \quad (10.5)$$

Inversion of (10.5) to obtain λ as a power series in $\frac{\bar{N}}{V}$ enables the substitution of λ into (10.4) thus producing the virial expansion

$$\frac{P}{kT} = \sum_{i=1}^{\infty} B_i \left(\frac{\bar{N}}{V} \right)^i \quad (10.6)$$

The coefficients $\{B\}$ in (10.6) are the virial coefficients expressed in terms of the cluster integrals $\{b\}$: $\{B\}_i$, $i=2,5$, are tabulated below.

$$\begin{aligned} B_2 &= -b_2^2; & B_3 &= -2b_3 + 4b_2^2; & B_4 &= -3b_4 + 18b_2b_3 - 20b_2^3, \\ B_5 &= -4b_5 + 18b_3^2 + 24b_2b_4 - 84b_2^2b_3 + 32b_2^4 \end{aligned} \quad (10.7)$$

Equations (10.4) and (10.5) are the Mayer Cluster Expansions (Mayer 1940) by means of which the configuration integral has been factorized into a set of 'mathematical', ie. non-physical, clusters. Such a factorization is rigorous only when the gaseous phase alone is present. The following sections investigate a connection between the mathematical cluster integrals of Mayer and physical cluster partition functions.

10.2 Virial Coefficients

Since the physical clusters constructed in this thesis exhibit Van der Waals forces it is reasonable to expect deviations from ideal

gas behaviour. Such deviations of an imperfect gas may be investigated by considering the gas as a perfect-gas mixture of different species, each species corresponding to a set of the same size 'mathematical' clusters. Frenkel (1939) and Band (1939) indicate that approximate results may be obtained via a theory based on the equilibrium constants of physical clusters. The n^{th} virial coefficient is then a measure of the degree of interaction between physical n -clusters.

The cluster concentration C_T of all clusters in thermodynamic equilibrium in a volume V is

$$C_T = \frac{N_T}{V} = \sum_N N C(N,T) \quad (10.8)$$

The principle of detailed balance i.e.

$$\frac{C(N,T)}{C(1,T)^N} = \frac{Z(N,T)}{Z(1,T)^N} \cdot \frac{V^N}{V}$$

may be used in (10.8) to obtain

$$C_T = \sum_N N \alpha(N,T) \beta(T)^N \quad (10.9)$$

where $\alpha(N,T) = \hat{Z}(N,T) = \frac{Z(N,T)}{V}$, $\beta(T) = \frac{C(1,T)V}{Z(1,T)} = \frac{C(1,T)}{\alpha(1,T)}$, and $Z(N,T)$ and $C(N,T)$ are the cluster partition function and cluster concentration respectively. To simplify notation the explicit temperature dependence will now be dropped.

When the gas is sufficiently dilute there is no interaction between clusters and $\beta = \frac{C_T}{\alpha(1)}$. As the gas becomes, less dilute deviations from ideal gas behaviour may be included by expanding β as a power series in the concentration C_T i.e.

$$\beta = \sum_i \gamma_i C_T^i \quad (10.10)$$

Inserting (10.10) into (10.9) yields

$$C_T = \frac{\sum_N \alpha(N)}{N} \left[\sum_i \gamma_i C_T^i \right]^N \quad (10.11)$$

For a 5th order approximation the $\{\gamma\}_i$, $i=1,5$, are obtained by equating the coefficients of C_T^i , $i=1,5$, in (10.11). Explicitly

$$\begin{aligned} \gamma_1 &= \frac{1}{\alpha(1)} ; \quad \gamma_2 = \frac{-2\alpha(2)}{\alpha(1)^3} ; \quad \gamma_3 = \frac{-3\alpha(3)}{\alpha(1)^4} + \frac{8\alpha(2)^2}{\alpha(1)^5} \\ \gamma_4 &= \frac{-4\alpha(4)}{\alpha(1)^5} + \frac{30\alpha(2)\alpha(3)}{\alpha(1)^6} - \frac{40\alpha(2)^3}{\alpha(1)^7} \\ \gamma_5 &= \frac{-5\alpha(5)}{\alpha(1)^6} + \frac{48\alpha(2)\alpha(4)}{\alpha(1)^7} - \frac{228\alpha(2)^2\alpha(3)}{\alpha(1)^8} + \frac{224\alpha(2)^4}{\alpha(1)^5} + \frac{18\alpha(3)^2}{\alpha(1)^7} \end{aligned} \quad (10.12)$$

A comparison of equations (10.9) and (10.5) enables an identification of $\alpha(N)$ with b_ρ and β^N with λ^ρ to be made - thus

$$\frac{P}{kT} = \alpha(1)\beta + \alpha(2)\beta^2 + \alpha(3)\beta^3 + \dots \quad (10.13)$$

Using the $\{\gamma\}$ from (10.12) in (10.13) and collecting terms in powers of C_T enables the first 5 coefficients, equal to the n^{th} virial coefficient divided by \tilde{N}^{n-1} , where \tilde{N} is Avogadro's number and $n=1$ to 5, to be written:

$$\begin{aligned} A &= 1; \quad B = \frac{-\alpha(2)}{\alpha(1)^2} ; \quad C = \frac{-2\alpha(3)}{\alpha(1)^3} + \frac{4\alpha(2)^2}{\alpha(1)^4} ; \\ D &= \frac{-3\alpha(4)}{\alpha(1)^4} + \frac{18\alpha(2)\alpha(3)}{\alpha(1)^5} - \frac{20\alpha(2)^3}{\alpha(1)^6} \\ E &= \frac{-4\alpha(5)}{\alpha(1)^5} + \frac{18\alpha(3)^2}{\alpha(1)^6} + \frac{24\alpha(2)\alpha(4)}{\alpha(1)^6} - \frac{84\alpha(2)^2\alpha(3)}{\alpha(1)^7} + \frac{32\alpha(2)^4}{\alpha(1)^8} \end{aligned} \quad (10.14)$$

The functions of $\alpha(N)$ in (10.14) are related to the equilibrium constants $K(N)$ by

$$K(N) = \frac{\alpha(N)}{\alpha(1)^N} = \frac{\hat{Z}(N)}{\hat{Z}(1)^N} \quad (10.15)$$

The reduced virial coefficients in terms of the equilibrium constants are

$$\begin{aligned} B^* &= \frac{-K(2)}{b_o} ; \quad C^* = \frac{-2}{b_o^2} [K(3) - 2K(2)^2] \\ D^* &= \frac{-1}{b_o^3} [3K(4) - 18K(2)K(3) + 20K(2)^3] \\ E^* &= \frac{-1}{b_o^4} [4K(5) - 32K(2)K(4) + 120K(2)^2K(3) - 9K(3)^2 - 112K(2)^4] \end{aligned} \quad (10.16)$$

where $b_o = \frac{2\pi\sigma^3}{3}$, with the appropriate choice of σ from Table 11. Woolley (1953), Leckenby and Robbins (1968) and Spurling and Mason (1969) have investigated the relationships between virial coefficients and equilibrium constants with similar results. The coefficients of the equilibrium constants in Woolley's (1953) expression for the fifth virial coefficient differ from those presented here; Woolley's coefficients may be reconstructed by omitting the coefficient of C_T^5 in the expansion of β^3 (equation (10.13)). Hirschfelder et al (1942) and Epstein (1952) also relate the second virial coefficient with the dimer equilibrium constant $K(2)$.

10.3 Results and Discussion

Tables 45 to 47 contain the second to fifth reduced virial coefficients, based on an harmonic partition function. Hirschfelder

et al (1954) provides comparative data for B^* and C^* , whilst the expansion coefficients of Kihara (1951) enable the computation of C^* for further comparison. Barker et al (1966) present data for the exact D^* and E^* but their temperature range permits comparison only at $T^* = .8$ and 1.0 .

The harmonic partition function differs on two points from the exact partition function. Firstly, due to the flattening of the potential energy curve at large displacements from the minimum the harmonic partition function is lower than the exact partition function. Secondly, only bound clusters are considered in the harmonic approximation, whilst the exact partition function takes into account the effect of non-bound clusters; i.e. those with a positive relative energy. This second effect reduces the exact partition function due to the exclusion of a region of space for the molecules' passage. These effects are unfortunately not separated, although increasing temperature accentuates the latter condition.

T^*	Table 45	
	$\log_{10} B^*(T^*)$	
	(a)	(b)
.1	3.673	-
.2	1.773	-
.3	1.163	1.445
.4	0.873	1.140
.5	0.713	0.941
.6	0.603	0.792
.7	0.543	0.673
.8	0.483	0.572
.9	0.453	0.484
1.0	0.433	0.405

The Second Reduced Virial Coefficients

(a) *This work*

(b) *Data from Hirschfelder et al (1954)*

All coefficients are negative.

Table 46

T*	$\log_{10} C^*(T^*)$		
	(a)	(b)	(c)
.1	10.515	-	6.920
.2	4.724	-	4.458
.3	2.090	-	3.130
.4	1.963	-	2.251
.5	1.807	-	1.595
.6	1.638	-	1.049
.7	1.551	0.528	0.537
.8	1.442	-0.071	-0.057
.9	1.366	-1.116	-1.182
1.0	1.366	-0.367	-0.371

The Third Reduced Virial Coefficients

(a) *This work*

(b) *Data from Hirschfelder et al (1954)*

(c) *Calculated from Kihara's expansion coefficients, Kihara (1951)*

Coefficients below the dotted line are positive.

Table 47

T*	$\log_{10} D^*(T^*)$		$\log_{10} E^*(T^*)$	
	(a)	(b)	(a)	(b)
.8	2.492	0.973	3.678	1.892
1.0	2.398	-0.558	3.541	0.456

The Fourth and Fifth Reduced Virial Coefficients

(a) *This work*

(b) *Data from Barker et al (1966)*

Coefficients below the dotted line are positive.

The second virial coefficient based on the harmonic partition function overestimates the effect of collisions involving dimers by approximately 48% at $T^* = .3$, falling to approximately 7% at $T^* = .9$. It underestimates by nearly 7% the same effect at $T^* = 1.0$. The overestimate of B_{harmonic}^* , corresponding to an underestimate of $K(2)$, may be explained by the results of Leckenby and Robbins (1966) which indicate that more bound dimers are detected. This excess of dimers increases the value of $K(2)$ which consequently reduces the coefficient B^* ($B^* = -K(2)$). The excess dimer contribution decreases as the temperature increases, leading to the closer agreement between B_{exact}^* and B_{harmonic}^* presented above. Stogryn and Hirschfelder (1959) indicate that contributions to the second virial coefficient due to (i) collisions between free monomers and (ii) the existence of metastable dimers remain non-negligible even at the boiling point of the rare gases ($T^* = .7$). This fact is noted by Milne and Greene (1969) and is substantiated by the data in Table 45.

The third virial coefficient is overestimated by almost 90% at $T^* = .3$, rising to an overestimate of nearly two orders of magnitude at $T^* = .9$. This overestimate falls to one order of magnitude at $T^* = 1.0$. At reduced temperatures below .3 C_{harmonic}^* is less than C_{exact}^* . One may conclude that the overestimate in the third virial coefficient is due to an underestimate in the equilibrium constant $K(3)$, ie that more bound trimers exist than predicted in the harmonic approximation. Such behaviour is reported by Reed (1952) with respect to Lennard-Jones nitrogen clusters. Graphs of the third reduced virial coefficients (Bird et al (1950)) show extremely steep gradients in the reduced temperature range $T^* \leq 1.0$. It is therefore reasonable to expect the difference between the calculated third virial coefficients to be large.

The data of Barker et al (1966) show the overestimate of the fourth virial coefficient to be one order of magnitude at $T^* = .8$ and two orders at $T^* = 1.0$. The same data present evidence of a similar order of magnitude overestimate of the fifth virial coefficient at $T^* = .8$, with a three order of magnitude overestimate for this coefficient at $T^* = 1.0$. Such large overestimates of the fourth and fifth virial coefficients imply the existence of higher concentrations of four and five atom clusters than is predicted. This statement is not unequivocal however due to the dependence of the virial coefficients on lower order equilibrium constants.

The estimation of higher order virial coefficients becomes increasingly hazardous due to the dependence of these coefficients on equilibrium constants which in general underestimate actual concentrations.

10.4 Mayer Cluster Integrals

The coefficients $\{B\}$ in (10.7) may be seen to bear a remarkable resemblance to the coefficients B to E in (10.14). One may identify $\{b\}$ in the former equation with the $\{\alpha(N)\}$ in the latter -

$$b_N \propto \frac{\alpha(N)}{\alpha(1)^N} = K(N) \quad (10.17)$$

where $K(N)$ is expressed in terms of partition functions in (10.15). Thus a formal relationship between the Mayer cluster integrals, which are based on the concept of mathematical clusters, and the equilibrium constants of physical clusters is presented. This relationship illustrates the connection between the Mayer theory of imperfect gases and the Frenkel-Band approximate theory.

Chapter 11

11.1 The Uses of Graph Theory in Isomer Enumeration

In this chapter a completely different approach to the problem of isomer enumeration is investigated; an approach used extensively in theoretical chemistry (Gutman et al (1975) and references therein), developed by, amongst others, Essam and Fisher (1970). The technique involves the construction of various graphs (Harary (1967)), corresponding to differing molecular arrangements, and their associated adjacency matrices, with the adjacency matrices being defined by

$$a_{ij} = \begin{cases} 1 & \text{for adjacent vertices (atoms)} \\ 0 & \text{otherwise} \end{cases} \quad (11.1)$$

Once these matrices have been generated the identity of any two or more graphs may be established by a procedure described by Randić (1974). Thus the problem of isomer enumeration reduces to one of counting graphs. Nevertheless this problem is in itself not trivial, since it involves the recognition of identical graphs from different adjacency matrices. One is also confronted with the fact that the theory is not restricted to the enumeration of isomers in 3-dimensional coordinate space; once the abstract concept of an adjacency matrix is left and attempts made to relate such a matrix to a physical 3-dimensional cluster, complications arise. It becomes necessary to reject those matrices, which, although corresponding to perfectly acceptable distinct graphs, have no place in the 3-dimensional world.

Graph theory is used in two stages to assist with isomer enumeration: (i) a complete set of anisomorphic graphs on a given

number of vertices may be listed, with the rejection of those graphs corresponding to physically non-realisable clusters, and (ii) having constructed a number of physical clusters in some alternative fashion, the isomorphism of these clusters may be tested by the construction of the relevant adjacency matrices.

11.2 Adjacency Matrices: their Classification and Ordering

For an N-atom cluster the symmetric adjacency matrix as defined by equation (11.1) may be constructed. It is apparent that different numberings of atoms lead to different adjacency matrices: in general for a graph on N vertices there exist N! adjacency matrices (some of which may be identical). The adjacency matrix for the 4-atom tetrahedron is

$${}_{4-1}A = \begin{bmatrix} 0 & 1 & 1 & 1 \\ 1 & 0 & 1 & 1 \\ 1 & 1 & 0 & 1 \\ 1 & 1 & 1 & 0 \end{bmatrix} \quad {}_{4}G_1 : \quad \begin{array}{c} 4 \qquad 3 \\ \bullet \qquad \bullet \\ \diagdown \quad \diagup \\ \bullet \qquad \bullet \\ 1 \qquad 2 \end{array}$$

with ${}_{4}G_1$ being the associated graph. The pre-subscripts refer to the number of atoms whilst the post-subscripts identify the particular structure within this set. Matrices ${}_{5-1}A$ and ${}_{5-2}A$ illustrate the possibility of the existence of more than one adjacency matrix for graphs which differ only in their labelling.

$${}_{5-1}A = \begin{bmatrix} 0 & 0 & 1 & 1 & 1 \\ 0 & 0 & 1 & 1 & 1 \\ 1 & 1 & 0 & 1 & 1 \\ 1 & 1 & 1 & 0 & 1 \\ 1 & 1 & 1 & 1 & 0 \end{bmatrix} \quad {}_{5-2}A = \begin{bmatrix} 0 & 1 & 1 & 1 & 1 \\ 1 & 0 & 1 & 1 & 1 \\ 1 & 1 & 0 & 1 & 0 \\ 1 & 1 & 1 & 0 & 1 \\ 1 & 1 & 0 & 1 & 0 \end{bmatrix}$$

$${}_{5}G_1 : \quad \begin{array}{c} 1 \qquad 5 \qquad 2 \\ \bullet \qquad \bullet \qquad \bullet \\ \diagdown \quad \diagup \quad \diagdown \quad \diagup \\ \bullet \qquad \bullet \\ 3 \qquad 4 \end{array} \quad {}_{5}G_2 : \quad \begin{array}{c} 3 \qquad 4 \qquad 5 \\ \bullet \qquad \bullet \qquad \bullet \\ \diagdown \quad \diagup \quad \diagdown \quad \diagup \\ \bullet \qquad \bullet \\ 1 \qquad 2 \end{array}$$

Some unique numbering convention for the constituent atoms within a cluster is required: once this convention exists graphs may be renumbered and the newly constructed adjacency matrices compared against a standard adjacency matrix. Read (1972) discusses various coding algorithms, whilst Silk (1964) and Penny (1965) consider numbering systems specifically related to chemical nomenclature.

By writing the rows of an adjacency matrix as a sequence of end-to-end segments, and considering the 0s and 1s as digits in a binary code, one may represent the matrix by a single number M . No two matrices will have the same M unless they differ only in the labelling of equivalent atoms. From all the different matrices associated with the same graph it is necessary to choose one matrix to represent that graph - one particular choice involves the interpretation of each row of the matrix as a binary number n_i , $1 \leq i \leq M$. The matrix is thus represented by a string of such numbers $\{n_i\}$. Rows and columns are then interchanged in the matrix until the members of the set $\{n_i\}$ combine to yield the smallest possible M -value. This requires an ordering such that

$$n_1 \leq n_2 \leq n_3 \leq \dots \leq n_M.$$

A matrix with rows ordered in such a fashion is known as an arranged matrix. Such a matrix is not necessarily unique, i.e. a number of ordered sets may arise from the same matrix. Additional permutations of rows and columns are required to establish whether or not the smallest M -value has been obtained. Each number n_i is examined in an attempt to reduce the current n_i value; if at any stage a disarranged matrix results, further arrangement is required.

An alternative method of choosing a representative matrix uses a numbering scheme which produces the largest possible M-value - however this method removes the possibility of ordering the set $\{n_i\}$ due to zeros on the principal diagonal.

11.3 Adjacency Matrices of Some Specific Structures

Arranged adjacency matrices for some structures of interest are constructed in this section. The complete graph on N vertices is defined as that graph with all vertices mutually connected: an unconnected graph is one in which free vertices exist. Only connected graphs are considered here.

11.3.1 The Dimer

$${}^2A_1 = \begin{bmatrix} 0 & 1 \\ 1 & 0 \end{bmatrix} \quad {}^2G_1 : \begin{array}{c} \text{---} \\ 1 \quad 2 \end{array}$$

Only one connected graph on 2 vertices exists.

11.3.2 The Equilateral Triangle and Linear Chain

$${}^3A_1 = \begin{bmatrix} 0 & 1 & 1 \\ 1 & 0 & 1 \\ 1 & 1 & 0 \end{bmatrix} \quad {}^3A_2 = \begin{bmatrix} 0 & 1 & 0 \\ 1 & 0 & 1 \\ 0 & 1 & 0 \end{bmatrix} \quad {}^3A_3 = \begin{bmatrix} 0 & 0 & 1 \\ 0 & 0 & 1 \\ 1 & 1 & 0 \end{bmatrix}$$

$${}^3G_1 : \begin{array}{c} 3 \\ \triangle \\ 1 \quad 2 \end{array} \quad {}^3G_2 : \begin{array}{c} \text{---} \\ 1 \quad 2 \quad 3 \end{array} \quad {}^3G_3 : \begin{array}{c} \text{---} \\ 1 \quad 3 \quad 2 \end{array}$$

3A_2 is not arranged: it may be arranged by interchanging rows (and columns) 2 and 3. This interchange reduces 3A_2 to 3A_3 - these two matrices represent the same graph. Consequently there

are only 2 connected graphs for $N = 3$, relating to the equilateral triangle and the linear chain.

11.3.3 The Tetrahedron

The tetrahedron corresponds to the complete graph on 4 vertices: this graph with its associated matrix is presented in Section 11.2. If one constrains each vertex to be connected to at least three others ${}_{4-1}A_1$ is the only $N = 4$ matrix which exists. Removing such a constraint permits the existence of linear chains and other planar configurations.

11.3.4 Some 5-Vertex Structures;

${}_{5-1}A_1$ and ${}_{5-2}A_2$ in Section 11.2 both correspond to the double tetrahedron. ${}_{5-2}A_2$ is not arranged: interchanging rows and columns 4 and 5 produces ${}_{5-2}A'_2$,

$${}_{5-2}A'_2 = \begin{bmatrix} 0 & 1 & 1 & 1 & 1 \\ 1 & 0 & 1 & 1 & 1 \\ 1 & 1 & 0 & 0 & 1 \\ 1 & 1 & 0 & 0 & 1 \\ 1 & 1 & 1 & 1 & 0 \end{bmatrix}$$

The base of the double tetrahedron is labelled 3-4-5 for ${}_{5-1}A_1$, and 1-2-5 for ${}_{5-2}A'_2$. One point to note is that neither of these matrices represent the complete graph on 5 vertices. The complete graph possesses 20 non-zero elements - since a parallel may be drawn between non-zero elements and nearest neighbour bonds it is apparent that the matrix corresponding to the double tetrahedron requires only 18 (i.e. $2x(3N-6)$, multiplied by 2 because of matrix symmetry) non-zero elements.

Consider all those clusters which may be grown from a 4-atom tetrahedron with atoms labelled 1-2-3-4. The faces on which a 5th atom may be added are 1-2-3, 1-2-4, 1-3-4, and 2-3-4. These four new structures produce matrices

$$\begin{array}{cccc}
 \text{(i)} & \begin{bmatrix} 0 & 1 & 1 & 1 & 1 \\ 1 & 0 & 1 & 1 & 1 \\ \text{face} & 1 & 1 & 0 & 1 & 1 \\ 1-2-3 & 1 & 1 & 1 & 0 & 0 \\ & 1 & 1 & 1 & 0 & 0 \end{bmatrix} & \text{(ii)} & \begin{bmatrix} 0 & 1 & 1 & 1 & 1 \\ 1 & 0 & 1 & 1 & 1 \\ \text{face} & 1 & 1 & 0 & 1 & 0 \\ 1-2-4 & 1 & 1 & 1 & 0 & 1 \\ & 1 & 1 & 0 & 1 & 0 \end{bmatrix} & \text{(iii)} & \begin{bmatrix} 0 & 1 & 1 & 1 & 1 \\ 1 & 0 & 1 & 1 & 0 \\ \text{face} & 1 & 1 & 0 & 1 & 1 \\ 1-3-4 & 1 & 1 & 1 & 0 & 1 \\ & 1 & 0 & 1 & 1 & 0 \end{bmatrix} & \text{(iv)} & \begin{bmatrix} 0 & 1 & 1 & 1 & 0 \\ 1 & 0 & 1 & 1 & 1 \\ \text{face} & 1 & 1 & 0 & 1 & 1 \\ 2-3-4 & 1 & 1 & 1 & 0 & 1 \\ & 0 & 1 & 1 & 1 & 0 \end{bmatrix}
 \end{array}$$

It is now necessary (a) to reduce if possible matrices (i)-(iv) to one single arranged matrix, and (b) to investigate whether further permutations lead to a lower M-value. Matrix (i) is already ordered and matrix (ii) is merely $\underline{5A}_2$, which itself has been arranged to form $\underline{5A}'_2$. Furthermore, interchanging rows and columns 3 and 4 followed by 4 and 5 in (i) again produces $\underline{5A}'_2$; i.e. (i) and (ii) represent the same structure with different labellings. Matrix (iii) may be arranged by interchanging rows and columns 4 and 5 followed by 3 and 4 - this produces

$$\underline{5A}_3 = \begin{bmatrix} 0 & 1 & 1 & 1 & 1 \\ 1 & 0 & 0 & 1 & 1 \\ 1 & 0 & 0 & 1 & 1 \\ 1 & 1 & 1 & 0 & 1 \\ 1 & 1 & 1 & 1 & 0 \end{bmatrix}$$

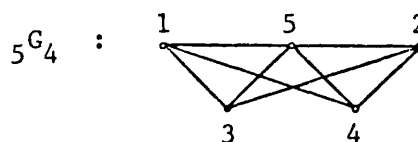
Is it now possible to reduce $\underline{5A}'_2$ to $\underline{5A}_3$? This is achieved by interchanging rows and columns 2 and 4. In the case of (iv) interchange of rows and columns 2 and 5 produces $\underline{5A}_1$. This latter matrix produces the lowest possible M-value for a graph with a minimum of 3 edges at each vertex, so finally the question is raised as to

whether ${}_{5-3}A_3$ may be reduced to ${}_{5-1}A_1$. This reduction is possible by the interchange of rows and columns 1 and 3 in ${}_{5-3}A_3$. The final arranged matrix ${}_{5-1}A_1$ corresponds to a double tetrahedral structure with atoms 3-4-5 forming the common face. Thus

- (a) matrices (i)-(iv) are isomorphic
- (b) the matrix with the lowest M-value requires the common face to have the highest possible atomic numbering.

The half octahedron possesses an adjacency matrix with 16 non-zero elements as opposed to the 18 in the case of the double tetrahedron due to its 8 nearest neighbour bonds. As ${}_{5-4}A_4$ shows the base is formed by atoms labelled 1-2-3-4.

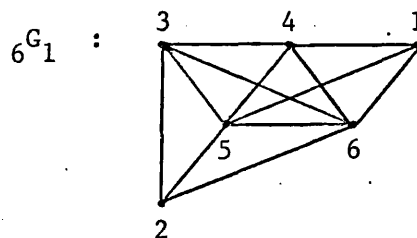
$${}_{5-4}A_4 = \begin{bmatrix} 0 & 0 & 1 & 1 & 1 \\ 0 & 0 & 1 & 1 & 1 \\ 1 & 1 & 0 & 0 & 1 \\ 1 & 1 & 0 & 0 & 1 \\ 1 & 1 & 1 & 1 & 0 \end{bmatrix}$$



11.3.5 Some 6-Vertex Structures

The arranged adjacency matrix with the lowest M-value corresponding to the trigonal prism is, with corresponding graph,

$${}_{6-1}A_1 = \begin{bmatrix} 0 & 0 & 0 & 1 & 1 & 1 \\ 0 & 0 & 1 & 0 & 1 & 1 \\ 0 & 1 & 0 & 1 & 1 & 1 \\ 1 & 0 & 1 & 0 & 1 & 1 \\ 1 & 1 & 1 & 1 & 0 & 1 \\ 1 & 1 & 1 & 1 & 1 & 0 \end{bmatrix}$$

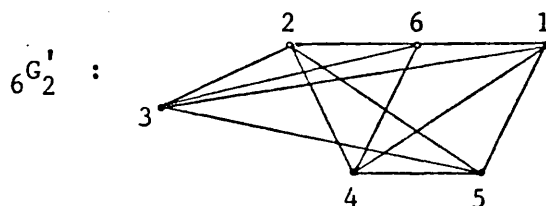


The structure corresponding to this graph is the double tetrahedron on a base labelled 4-5-6 with the final atom added on face 3-5-6.

The full octahedron with a base defined by labels 1-2-3-4 produces ${}_{6-2}A_2$.

$${}_{6-2}A_2 = \begin{bmatrix} 0 & 1 & 0 & 1 & 1 & 1 \\ 1 & 0 & 1 & 0 & 1 & 1 \\ 0 & 1 & 0 & 1 & 1 & 1 \\ 1 & 0 & 1 & 0 & 1 & 1 \\ 1 & 1 & 1 & 1 & 0 & 0 \\ 1 & 1 & 1 & 1 & 0 & 0 \end{bmatrix} \quad {}_{6-2}A'_2 = \begin{bmatrix} 0 & 0 & 1 & 1 & 1 & 1 \\ 0 & 0 & 1 & 1 & 1 & 1 \\ 1 & 1 & 0 & 0 & 1 & 1 \\ 1 & 1 & 0 & 0 & 1 & 1 \\ 1 & 1 & 1 & 1 & 0 & 0 \\ 1 & 1 & 1 & 1 & 0 & 0 \end{bmatrix}$$

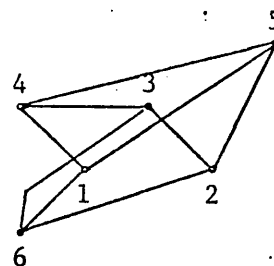
Permutations of rows and columns results in the arranged matrix ${}_{6-2}A'_2$, which corresponds to a structure with the base atoms labelled 3-5-4-6. The graph for this matrix is



The trigonal bipyramid is represented by

$${}_{6-3}A_3 = \begin{bmatrix} 0 & 0 & 0 & 1 & 1 & 1 \\ 0 & 0 & 1 & 0 & 1 & 1 \\ 0 & 1 & 0 & 1 & 0 & 1 \\ 1 & 0 & 1 & 0 & 1 & 0 \\ 1 & 1 & 0 & 1 & 0 & 0 \\ 1 & 1 & 1 & 0 & 0 & 0 \end{bmatrix}$$

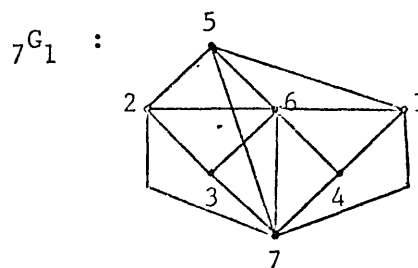
with graph ${}_{6-3}G_3$:



11.3.6 The Distorted Pentagonal Bipyramid

An arranged adjacency matrix for the distorted 7-atom pentagonal bipyramid formed by hard-sphere packings is

$${}^7A_1 = \begin{bmatrix} 0 & 0 & 0 & 1 & 1 & 1 & 1 \\ 0 & 0 & 1 & 0 & 1 & 1 & 1 \\ 0 & 1 & 0 & 0 & 0 & 1 & 1 \\ 1 & 0 & 0 & 0 & 0 & 1 & 1 \\ 1 & 1 & 0 & 0 & 0 & 1 & 1 \\ 1 & 1 & 1 & 1 & 1 & 0 & 1 \\ 1 & 1 & 1 & 1 & 1 & 1 & 0 \end{bmatrix}$$

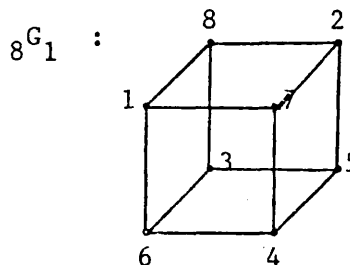


This structure has a clearance gap between atoms 3 and 4. The 5-membered ring defined by the plane containing atoms 3-2-5-1-4 is distorted by this gap and does not possess perfect 5-fold symmetry.

11.3.7 The Cube

The regular cube has an adjacency matrix associated with it as shown in 8A_1 .

$${}^8A_1 = \begin{bmatrix} 0 & 0 & 0 & 0 & 0 & 1 & 1 & 1 \\ 0 & 0 & 0 & 0 & 1 & 0 & 1 & 1 \\ 0 & 0 & 0 & 0 & 1 & 1 & 0 & 1 \\ 0 & 0 & 0 & 0 & 1 & 1 & 1 & 0 \\ 0 & 1 & 1 & 1 & 1 & 0 & 0 & 0 \\ 1 & 0 & 1 & 1 & 1 & 0 & 0 & 0 \\ 1 & 1 & 0 & 1 & 1 & 0 & 0 & 0 \\ 1 & 1 & 1 & 0 & 0 & 0 & 0 & 0 \end{bmatrix}$$



This structure has 12 nearest neighbour bonds.

11.3.8 The Icosahedron

Using data from the growth program the following adjacency matrix for the 13-atom icosahedron may be produced

$${}^{13}A_1 = \begin{bmatrix} 0 & 1 & 1 & 1 & 1 & 1 & 1 & 1 & 1 & 1 & 1 & 1 & 1 \\ 1 & 0 & 1 & 1 & 1 & 1 & 1 & 0 & 0 & 0 & 0 & 0 & 0 \\ 1 & 1 & 0 & 1 & 1 & 0 & 0 & 1 & 1 & 0 & 0 & 0 & 0 \\ 1 & 1 & 1 & 0 & 0 & 1 & 0 & 1 & 0 & 1 & 0 & 0 & 0 \\ 1 & 1 & 1 & 0 & 0 & 0 & 1 & 0 & 1 & 0 & 1 & 0 & 0 \\ 0 & 0 & 0 & 0 & 0 & 0 & 0 & 1 & 0 & 1 & 0 & 1 & 0 \end{bmatrix}$$

Continued

$$\begin{bmatrix} 1 & 1 & 0 & 1 & 0 & 0 & 0 & 0 & 0 & 1 & 0 & 1 & 0 \\ 1 & 1 & 0 & 0 & 1 & 0 & 0 & 0 & 0 & 0 & 1 & 1 & 0 \\ 1 & 0 & 1 & 1 & 1 & 0 & 0 & 0 & 0 & 0 & 0 & 0 & 1 \\ 1 & 0 & 1 & 0 & 1 & 0 & 0 & 0 & 0 & 0 & 0 & 0 & 1 \\ 1 & 0 & 0 & 1 & 0 & 1 & 0 & 0 & 0 & 0 & 0 & 0 & 0 \\ \\ 1 & 0 & 0 & 0 & 0 & 1 & 0 & 1 & 0 & 0 & 0 & 0 & 0 \\ 1 & 0 & 0 & 0 & 0 & 1 & 1 & 0 & 0 & 0 & 0 & 0 & 0 \\ 1 & 0 & 0 & 0 & 0 & 0 & 0 & 1 & 1 & 0 & 0 & 0 & 0 \end{bmatrix}$$

The following permutations of rows and columns are required to arrange

${}_{13}A_1$:

2 \leftrightarrow 13; 8 \leftrightarrow 13; 3 \leftrightarrow 4; 9 \leftrightarrow 12; 8 \leftrightarrow 11; 4 \leftrightarrow 5;
 5 \leftrightarrow 9; 6 \leftrightarrow 8; 9 \leftrightarrow 10; 4 \leftrightarrow 5; 8 \leftrightarrow 9; 9 \leftrightarrow 10;
 10 \leftrightarrow 11.

Such rearrangements lead to an arranged adjacency matrix ${}_{13}A_1'$ for a graph on 13 vertices.

$${}_{13}A_1' = \begin{bmatrix} 0 & 1 & 1 & 1 & 1 & 1 & 1 & 1 & 1 & 1 & 1 & 1 & 1 \\ 1 & 0 & 0 & 0 & 0 & 0 & 0 & 0 & 0 & 0 & 0 & 1 & 1 \\ 1 & 0 & 0 & 0 & 0 & 0 & 0 & 1 & 1 & 1 & 1 & 1 & 0 \\ 1 & 0 & 0 & 0 & 0 & 0 & 0 & 1 & 0 & 0 & 0 & 1 & 0 \\ 1 & 0 & 0 & 0 & 0 & 0 & 1 & 1 & 0 & 1 & 1 & 0 & 1 \\ \\ 1 & 0 & 0 & 0 & 1 & 0 & 1 & 0 & 0 & 0 & 0 & 0 & 0 \\ 1 & 0 & 0 & 1 & 1 & 1 & 0 & 0 & 0 & 1 & 0 & 0 & 0 \\ 1 & 0 & 1 & 0 & 0 & 0 & 0 & 0 & 0 & 0 & 0 & 1 & 0 \\ 1 & 0 & 1 & 0 & 1 & 0 & 0 & 0 & 0 & 0 & 1 & 0 & 1 \\ 1 & 0 & 1 & 0 & 1 & 0 & 0 & 1 & 0 & 1 & 0 & 1 & 0 \\ \\ 1 & 0 & 1 & 1 & 0 & 0 & 0 & 1 & 0 & 1 & 0 & 0 & 0 \\ 1 & 1 & 0 & 0 & 1 & 0 & 0 & 0 & 0 & 1 & 0 & 0 & 0 \\ 1 & 1 & 1 & 0 & 0 & 0 & 0 & 1 & 0 & 0 & 0 & 0 & 0 \end{bmatrix}$$

From this matrix it is seen that the central enclosed atom is labelled number 1.

11.4 The Generation of the Complete Set of Anisomorphic Graphs on a Given Number of Vertices

If all the arranged adjacency matrices on a given number of vertices are constructed and those matrices which are isomorphic are eliminated, all anisomorphic graphs on that number of vertices are, by necessity, found. From these graphs the various molecular configurations may be recognised. Cvetković (1974) suggests that permutations of the molecular graph are related to the various Kekulé structures whilst Gutman et al in a series of papers (1972-1975) apply graph theory to chemical problems. A systematic approach to the generation of all graphs involves starting from the complete $N \times N$ matrix and proceeding to first generation matrices by replacing a particular 1 by a 0. Resulting matrices must be arranged, thereby limiting the number of acceptable matrices. As further 1s are replaced by 0s second and higher generation matrices are produced, until the matrix corresponding to the connected graph with the minimum number of edges is generated. Subsequent operations lead to subgraphs with unconnected vertices which are of no interest here. For a graph on N vertices $(N-1)$ arranged matrices need to be considered (not all of which correspond to physically possible structures). All first generation graphs are isomorphic due to the equivalence of all edges in the complete graph. Harary (1959) and Spialter (1964) have shown that for $N=4$ and $N=5$ only non-isomorphic graphs are required for the determination of all possible graphs associated with the ordering of the vertices, corresponding to the lowest M -value; this has not been proved for $N>5$.

To apply this technique to the problem of isomer growth from various seed-structures some restrictions on the number and distribution of non-zero matrix elements are required. These restrictions are:

(i) the total number of non-zero matrix elements must equal

$2x(3N-6)$ tetrahedral, octahedral, square antiprism plus 2 caps, trigonal bipyramids plus 3 caps groups.

$2x(3N-7)$ square antiprism plus one cap, trigonal bipyramid plus 2 caps groups.

$2x(3N-8)$ square antiprism, trigonal bipyramid plus 1 cap groups.

$2x(3N-9)$ Trigonal bipyramid group.

(ii) there must be at least 3 non-zero elements per row. Restriction

(i) arises because of the choice of seed-structure and the condition that atoms are added to triangular facets. For example the arranged adjacency matrix A_{6-2} corresponding to the octahedral seed has 24 non-zero elements. Due to the symmetry of the matrix this represents only 12 edges - i.e. the octahedral seed has 12 nearest neighbour bonds. The addition of a single atom to a triangular facet increases the number of nearest neighbour bonds to $12 + 3(N-6) = 3N-6$. In the language of graph theory this condition states that each additional vertex contributes 3 edges to the graph. Similar arguments may be carried through for the other seed structures considered. The second restriction ensures that every atom touches at least three others, enabling several matrices to be immediately rejected. Those matrices not rejected correspond to structures which include the polytopes, described by Coxeter (1963), in 4 and higher dimensional spaces.

Two major points need to be noted when applying graph-theoretic methods to isomer enumeration problems; firstly that restriction (i) above leads to the generation of hard-sphere isomers, and secondly that although the adjacency matrix contains information as to which atoms are in mutual contact it does not contain information concerning the possible obstruction of a new site by neighbouring atoms. The

former point is a direct consequence of equation (11.1) - once one admits the existence of soft-sphere structures the question of whether two atoms 'touch' becomes problematic. The latter point allows the construction of matrices corresponding to physically non-realizable structures. The distance matrix \underline{D} contains the information necessary to decide whether a new matrix corresponds to a physical cluster - however the \underline{D} matrix requires the introduction of a coordinate system. Indiscriminate use of graph theory may lead to the prediction of various isomeric forms which although possessing the correct number of bonds are unable to exist in 3-dimensional space. Matrix ${}_{6-4}A$ illustrates this point.

$${}_{6-4}A = \begin{bmatrix} 0 & 0 & 0 & 1 & 1 & 1 \\ 0 & 0 & 0 & 1 & 1 & 1 \\ 0 & 0 & 0 & 1 & 1 & 1 \\ 1 & 1 & 1 & 0 & 1 & 1 \\ 1 & 1 & 1 & 1 & 0 & 1 \\ 1 & 1 & 1 & 1 & 1 & 0 \end{bmatrix}$$

At first sight ${}_{6-4}A$ appears to represent a perfectly reasonable physical cluster. Closer examination shows the first three rows to be identical. This implies that there are more than two atoms on the same triangular base (4-5-6); since any plane such as that defined by the base atoms (4-5-6) has only two faces the cluster associated with ${}_{6-4}A$ is not physically realizable. The identification of such clusters from their arranged adjacency matrices remains a formidable task, increasing in complexity as the number of vertices increases.

References and Bibliography

- Abraham F.F., Appl.Phys. Letts. 13 (1968) 208.
- Abraham F.F. and Canosa J., J.Chem.Phys. 50 (1969) 1303.
- Abraham F.F. and Dave J.V., J.Chem.Phys. 55 (1971a) 1587, 4817;
Chem.Phys.Letts. 8 (1971b) 351.
- Abraham F.F. and Pound G.M., J.Chem.Phys. 48 (1968) 732.
- Adam G. and Gibbs J.H., J.Chem.Phys. 43 (1965) 139.
- Adams D.J. and Matheson A.J., J.Chem.Phys. 56 (1972) 1989.
- Alfrey T.A., Goldfinger G. and Mark H., J.Appl.Phys. 14 (1943) 700.
- Allen H.C. and Cross P.C., 'Molecular Vib-Rotors' (1963) Wiley, N.Y.
- Allpress J.G. and Sanders J.V., Surf.Sci. 7 (1967) 1;
Aust.J.Phys. 23 (1970) 23.
- Andres R.P., Ind.Eng.Chem. 57 (1965) 24.
- Andres R.P. and Boudart M., J.Chem.Phys. 42 (1965) 2057.
- Audit P., J.Physique 30 (1969) 192.
- Bagley B.G., Nature 208 (1965) 674;
Nature 225 (1970) 1040.
- Band W., J.Chem.Phys. 7 (1939) 324, 927.
- Barker J.A., J.Chem.Phys. 63 (1975) 2767.
- Barker J.A., Hoare M.R. and Finney J.L., Nature 257 (1975) 120.
- Barker J.A., Leonard P.J. and Pompe A., J.Chem.Phys. 44 (1966) 4206.
- Becker E.W., Bier K. and Henkes W., Z.Phys. 146 (1956) 333.
- Becker E.W., Klingelhöfer R. and Lohse P., Z.Naturforschung 17A
(1962) 342.
- Becker R. and Döring W., Ann.Phys. 24 (1935) 719.

- Beckman F.S., in 'Mathematical Methods for Digital Computers' (1960)
J.Wiley & Sons, editors Ralston A. and Wilf H.S.
- Bennett C.H., J.Appl.Phys. 43 (1972) 2727.
- Bennett C.H., Polk D.E. and Turnbull D., Acta Met. 19 (1971) 1295.
- Benson G.C. and Shuttleworth R., J.Chem.Phys. 19 (1951) 130.
- Bernal J.D., Nature 183 (1959) 141;
Nature 185 (1960) 68;
in 'Liquids: Structures, Properties, Solid Interactions'
(1965) Elsevier, Amsterdam;
Proc.Roy.Soc. 280A (1964) 299.
- Bernal J.D. and Mason J., Nature 188 (1960) 910.
- Bird R.B., Spatz E.L. and Hirschfelder J.O., J.Chem.Phys. 18 (1950) 1395.
- Blackman M., Repts.Prog.Phys. 8 (1941);
Proc.Roy.Soc. A148 (1935) 384;
Proc.Roy.Soc. A159 (1937) 416.
- Blackman M. and Sambles J.R., Nature 226 (1970) 938.
- Boerdijk A.H., Philips Res.Repts. 7 (1952) 303.
- Bonissent A., Thesis: Equilibre et Structure des Phases de tres petits
dimensions (1971) Universite de Provence.
- Bonissent A. and Mutaftschiev B., J.Chem.Phys. 58 (1973) 3727.
- Briant C.L. and Burton J.J., Nat.Phys.Sci. 243 (1973) 100.
- Buckle E.R., Trans.Farad.Soc. 65 (1969) 1257.

- Burton J.J., Chem.Phys.Letts. B (1969) 594
J.Chem.Phys. 52 (1970a) 345
Chem.Phys.Letts. 7 (1970b) 567
Nature 229 (1971a) 335
Surf.Sci. 26 (1971b) 1
J.Chem.Phys. 56 (1972a) 3133
J.Phys.Chem.Sol. 33 (1972b) 589
Acta.Met. 21 (1973) 1225
Chem.Phys.Letts. 17 (1972c) 199
- Cargill G.S., J.Appl.Phys. 41 (1970a) 12
J.Appl.Phys. 41 (1970b) 2248.
- Cohen M.H. and Turnbull D., Nature 189 (1961) 131
Nature 203 (1964) 964
- Collins R., in 'Phase Transitions and Critical Phenomena' (1972) Vol.II
Chapter 7, Academic Press, N.Y. Editors Domb C. and Green M.S.
- Courant R. and Hilbert D., in 'Methods of Mathematical Physics' (1953)
Vol.I, pp.282-283, Interscience, N.Y.
- Courtney W.G., J.Chem.Phys. 35 (1961) 2249
J.Chem.Phys. 36 (1962) 2009.
- Coxeter H.S.M., 'Introduction to Geometry' (1961), J.Wiley & Sons, N.Y.
'Regular Polytopes' (1963), Collier-Macmillan, N.Y.
- Critchlow K., 'Order in Space' (1969), Thames and Hudson, London.
- Cundy H.M., Math.Gaz. 36 (1952) 263.
- Cundy H.M. and Rollett A.P., 'Mathematical Models' (1961), O.U.P., Oxford.
- Cvetković D., Gutman I. and Trinajstić N., J.Chem.Phys. 61 (1974) 2700.
- Davidon W.C., AEC Res. and Devel.Rep. ANL-5990, (1959).

- Derjaguin B.V., J.Chem.Phys. 61 (1974) 3665.
- Dickey J.M. and Paskin A., Phys.Rev.Letts. 21 (1968) 1441
Phys.Rev. B1 (1970) 851
- Drechsler M. and Nicholas J.F., J.Phys.Chem.Sol. 28 (1967) 2609.
- Dunning W.J., in 'Nucleation' (1969), Dekker, N.Y. Editor Zettlemoyer A.C.
- Epstein L.F., J.Chem.Phys. 20 (1952) 1670.
- Essam J.W. and Fisher M.E., Rev.Mod.Phys. 42 (1970) 272.
- Etters R.D. and Kaelberer Jaya., Phys.Rev.A 11 (1975) 1068.
- Farges J., J.Cryst.Growth 31 (1975) 79.
- Farges J., Raoult B. and Torchet G., J.Chem.Phys. 59 (1973) 3454.
- Farkas L., Z.Phys.Chem. A125 (1927) 236.
- Feder J., Russell K.C., Lothe J. and Pound G.M., Adv.Phys. 15 (1966)
111.
- Fejes T., 'Regular Figures' (1964), Macmillan, N.Y.
- Finney J.L., Proc.Roy.Soc. A319 (1970) 479, 495.
- Fletcher R., Comp.J. 13 (1970) 317
AERE Rept. TP.454 (1971)
AERE Rept. R7073 (1972)
- Fletcher R. and Reeves C.M., Comp.J. 7 (1964) 149.
- Fletcher R. and Powell M.J.D., Comp.J. 6 (1963) 163.
- Foster P.J., Leckenbury R.E. and Robbins E.J., J.Phys.B 2 (1969) 478.

- Frank F.C. and Kasper J.S., *Acta Cryst.* 11 (1958) 184
Acta Cryst. 12 (1959) 483
- Frenkel J., *J.Chem.Phys.* 7 (1939) 200
'Kinetic Theory of Liquids' (1955), Dover Publications,
N.Y.
- Frisch H.L., *J.Chem.Phys.* 2 (1957) 90; *J.Chem.Phys.* 36 (1962) 510.
- Fröhlich H., *Physica* 4 (1937) 406.
- Fukano Y. and Wayman C.M., *J.Appl.Phys.* 40 (1969) 1656.
- Garg P.K. and Gupta N.P., *Solid St.Comm.* 17 (1975) 89.
- Gibbs J.W., 'Scientific Papers Vol.I' (1906) Longman Green, London.
- Gillet E. and Gillet M., *Thin Sol.Films* 15 (1973) 249.
- Gingrich N.S., *Rev.Mod.Phys.* 15 (1943) 90.
- Girifalco L.A. and Weizer V.G., *Phys.Rev.* 114 (1959) 687.
- Goldstein H., *J.Chem.Phys.* 51 (1969) 3728
Farad.Symp.Chem.Soc. 6 (1972) 7
J.Phys,Chem. (U.S.A.) 77 (1973a) 667
Proc.Conf. on Phase Transitions and their Applications
(1973b) 263, Pergamon, N.Y.
- Greene F.T. and Milne T.A., *J.Chem.Phys.* 47 (1967) 4095.
- Gutman I., Rušćić B., Trinajstić N. and Wilcox C.F., *J.Chem.Phys.*
62 (1975) 3399.
- Gutman I. and Trinajstić N., *Fortschr.Chem.Forsch.* 42 (1973) 49.
- Gwinn W.D., *J.Chem.Phys.* 55 (1971) 477.

- Hagena O.F. and Obert W., J.Chem.Phys. 56 (1972) 1793.
- Harary F., J.Math.Phys. 38 (1959) 104.
- 'Graph Theory and Theoretical Physics' (1967), Academic Press, N.Y.
- 'Graph Theory' (1969), Addison-Wesley, Reading, Mass.
- van Hardeveld R. and Hartog F., Surf.Sci. 15 (1969) 189.
- Herschbach D.R., Johnston H.S. and Rapp D., J.Chem.Phys. 31 (1959) 1652.
- Herzberg G., 'Infrared and Raman Spectra of Polyatomic Molecules' (1945), van Nostrand, Lancaster, PA.
- Hill T.L., 'Statistical Mechanics' (1956), McGraw-Hill, N.Y.
- 'An Introduction to Statistical Thermodynamics' (1960), Addison-Wesley, Reading, Mass.
- Hirschfelder J.O., Curtiss C.F. and Bird R.B., 'Molecular Theory of Gases and Liquids' (1954), Wiley, N.Y.
- Hirschfelder J.O., McClure F.T. and Weeks I.F., J.Chem.Phys. 10 (1942) 201.
- Hirth J.P., Ann. N.Y. Acad.Sci. 101 (1963) 805.
- Hirth J.P. and Pound G.M., 'Condensation and Evaporation' (1963), Pergamon, Oxford.
- Hirth J.P. and Pound G.M., 'Progress in Material Science Vol.II', (1963) Pergamon, London.
- Hoare M.R., Ann. N.Y. Acad.Sci. (in press).
- Hoare M.R. and McInnes J.A., Farad.Disc.Chem.Soc. 61 (1976) (in press).

- Hoare M.R. and Pal P., Adv.Phys. 20 (1971a) 161
Nature 230 (1971b) 5
J.Cryst.Growth 17 (1972a) 77
Nature 236 (1972b) 35
Adv.Phys. 24 (1975) 645
- Hoover W.G., Young D.A. and Grover R., J.Chem.Phys. 56 (1972) 2207.
- Householder A.S. 'Principles of Numerical Analysis' (1953),
McGraw-Hill, N.Y.
- Ino S., J.Phys.Soc.Japan 21 (1966) 346.
- Johari G.P. and Goldstein M., J.Chem.Phys. 53 (1970) 2372.
J.Chem.Phys. 55 (1971) 4245.
- Jones H., Repts.Prog.Phys. 36 (1973) 1425.
- Jura G. and Pitzer K.S., J.Amer.Chem.Soc. 74 (1952) 6030.
- Katz J.L., J.Chem.Phys. 52 (1970) 4733.
- Kauzmann W., Chem.Revs. 43 (1948) 219.
- Kanamori J., J.Appl.Phys. 31 (1960) 5.
- Kendall M.G. and Stuart A., 'The Advanced Theory of Statistics Vol.I',
(1969), Griffin, London.
- Kihara T., J.Phys.Soc.Japan 3 (1948) 265
J.Phys.Soc.Japan 6 (1951) 184.
- Kihara T. and Koba S., J.Phys.Soc.Japan 7 (1952) 348.
- Kimoto K. and Nishida I., J.Phys.Soc.Japan 7 (1967) 940.
- Kittel C., 'Thermal Physics' (1969), Wiley, N.Y.

- Kirkwood J.G. and Buff F.P., *J.Chem.Phys.* 17 (1949) 338.
- Komoda T., *Jap.J.Appl.Phys.* 7 (1968) 27.
- Kristensen W.D., Jensen E.J. and Cotterill R.M.J., *J.Chem.Phys.* 60
(1974) 4161.
- Landau L.D. and Lifschitz E.M., 'Mechanics' (1969), Pergamon, Oxford.
- Law M.L. and Fitts D.D., *Mol.Phys.* 29 (1975) 1933.
- Leadbetter A.J., *Phys.Chem.Glasses* 9 (1968) 1.
- Leckenby R.E. and Robbins E.J., *Proc.Roy.Soc.* 291A (1966) 389.
J.Phys. B2 1 (1968) 441.
- Lee J.K., Abraham F.F. and Pound G.M., *Suf.Sci.* 34 (1973) 745.
- Leung P.K. and Wright J.G., *Phil.Mag.* 30 (1974a) 185,
Phil.Mag. 30 (1974b) 995.
- Lotne J. and Pound G.M., *J.Chem.Phys.* 36 (1962) 2080; *J.Chem.Phys.*
45 (1966) 630; *Phys.Rev.* 182 (1969) 339.
- Mackay A.L., *Acta Cryst.* 15 (1962) 916.
- Mackenzie J.D., editor of 'Modern aspects of the Vitreous State' Vols.
I-III (1960-1964), Butterworths, London.
- Maradudin A.A., Montroll E.W. and Weiss G.H., 'Solid St.Phys.Suppl.3'
(1963), Academic Press, N.Y.
- Mayer J.E., *J.Chem.Phys.* 5 (1937) 67.
- Mayer J.E. and Mayer M.G., 'Statistical Mechanics' (1940), Wiley, N.Y.
- McGinty D.J., *J.Chem.Phys.* 55 (1971) 580
Chem.Phys.Letts. 13 (1972) 525
J.Chem.Phys. 58 (1973) 4733.

- Mills I.M., in 'Infrared Spectroscopy and Molecular Structure' (1963),
Elsevier, Amsterdam. Editor Davies M.
- Milne T.A. and Greene F.T., J.Chem.Phys. 47 (1967) 4095.
J.Chem.Phys. 51 (1969) 1685.
- Milne T.A., Vandegrift A.E. and Greene F.T., J.Chem.Phys. 52 (1970) 1552.
- Montroll E.W., J.Chem.Phys. 15 (1947) 575
J.Chem.Phys. 18 (1950) 183.
- Morimoto H. and Sakata H., J.Phys.Soc.Japan 17 (1962) 136.
- Newell G.F., J.Chem.Phys. 21 (1953) 1877.
- Nicholas J.F., Aust.J.Phys. 21 (1968) 21.
- Nishioka K., Shawyer R., Bienenstock A. and Pound G.M., J.Chem.Phys.
55 (1971) 5082.
- Nonnemacher Th.F., Phys.Letts.(Netherlands) 51A (1975) 213.
- Pal P., Ph.D. Thesis (1972), Univ. of London, London, U.K.
- Penney R.H., J.Chem.Doc. 5 (1965) 113.
- Perelson A.S. and de Fisi C., J.Chem.Phys. 62 (1975) 4053.
- Plesner I.W., J.Chem.Phys. 40 (1964) 1510.
- Plummer P.L.M. and Hale B.N., J.Chem.Phys. 56 (1972) 4329.
- Polk D.E., Scripta Met. 4 (1970) 117
J.Non.Cryst.Sol. 5 (1971) 365
Acta Met. 20 (1972) 485.
- Polk D.E. and Boudreaux D.S., Phys.Rev.Letts.(U.S.A.) 31 (1973) 92.

- Powell C.F., Proc.Roy.Soc. A119 (1928) 553.
- Randić M., J.Chem.Phys. 60 (1974) 3920.
- Raoult B. and Farges J., Rev.Sci.Instr. 44 (1973) 430.
- Read R.C., 'Graph Theory and Computing' (1972), Academic Press, N.Y.
- Reed S.G., J.Chem.Phys. 20 (1952) 208.
- Reiss H. and Katz J.L., J.Chem.Phys. 46 (1967) 7, 2496.
- Romanowski W., Surf.Sci. 18 (1969) 373.
- Rosenbrock H.H., Comp.J. 3 (1960) 175.
- Rosenstock H.B., J.Non-Cryst.Sol. 7 (1972) 123.
- Rouvray D.H., Endeavour XXXIV, 121 (1975) 28.
- Sadoc J.F., Dixmier J. and Guinier A., J.Non-Cryst.Sol. 12 (1973) 46.
- Scott G.D. and Kilgour D.M., Brit.J.Appl.Phys. 2 (1969) 863.
- Silk J.A., J.Chem.Doc. 4 (1964) 189.
- Sinclair J.E. and Pollard H.F., Phys.Letts. 32A (1970) 93.
- Spialter L., J.Chem.Doc. 4 (1964) 269.
- Spiegel M.R., 'Statistics' (1961), Schaum, N.Y.
- Spurling T.H. and Mason E.A., J.Chem.Phys. 51 (1969) 1684.
- Stein G.D., J.Chem.Phys. 51 (1969) 938.
- Stein G.D. and Wegener P.P., J.Chem.Phys. 46 (1967) 3685.
- Stogryn D.E. and Hirschfelder J.O., J.Chem.Phys. 31 (1959) 1531.
- Symon K.R., 'Mechanics' (1967) 432, Addison-Wesley, Reading, Mass.
- Thomson W., Proc.Roy.Soc. Edinburgh 7 (1870) 63.

- Turnbull D. and Cohen M.H., J.Chem.Phys. 34 (1961) 120.
- Urch D.S., 'Orbitals and Symmetry' (1970), Penguin, Middlesex, England.
- Urey H.C. and Bradley C.A., Phys.Rev. 38 (1931) 1969.
- van Hove L., Phys.Rev. 89 (1953) 1189.
- Volmer M. and Flood H., Z.Phys.Chem. A170 (1934) 273.
- Volmer M. and Weber A., Z.Phys.Chem. 119 (1925) 277.
- Vook R.W. and Otoono M.A., J.Appl.Phys. 38 (1967) 2471.
- Walsh G.R., 'Methods of Optimization' (1975), Wiley, London.
- Walton D., J.Chem.Phys. 37 (1962a) 2182
Phil.Mag. 7 (1962b) 1671.
- Watanabe D. and Miida R., J.Appl.Phys.Japan 11 (1972) 296.
- Weaire D., Ashby M.F., Logan J. and Weins M.J., Acta Met. 19 (1971) 779.
- Wegener P.P. and Parlange J-Y., Naturwissenschaften 57 (1970) 525.
- Weisskopf V., Phys.Rev. 52 (1937) 295.
- Werfelmeier W., Z.Physik. 107 (1937) 332.
- Whittaker E.T., 'Analytical Dynamics of Particles and Rigid Bodies'
(1944) Chapter 7, Dover Publications, N.Y.
- Williams M.L., Landel R.F. and Ferry J.D., J.Amer.Chem.Soc. 77 (1955) 3701.
- Wilson E.B., Decius J.C. and Cross P.C., 'Molecular Vibrations' (1955),
McGraw-Hill, York, PA.
- Woolley H.W., J.Chem.Phys. 21 (1953) 236.

Zeldovich J.B., J.Expt.Theo.Phys. 12 (1942) 525.

Acta.Phys.Chem. 18 (1943) 1.

Zettlemoyer A.C. (editor), 'Nucleation' (1969) 60, Dekker, N.Y.

Appendix A

Description of Major Computer Programs and Auxiliary Programs

A.1

The three major computer programs used in this research are:

- (1) Growth Algorithm
- (2) Optimization by the Method of Conjugate Gradients
- (3) Vibrational Analysis.

All programs are run on either the CDC6600 or CDC7600 at the University of London Computing Centre (U.L.C.C.). Single precision arithmetic is used throughout except in a few runs of the optimization program where double precision is required to achieve a minimum within the accuracy specified. Optimization to within a specified accuracy is necessary to ensure that all vibrational frequencies found in the vibrational analysis program are positive semi-definite (ie. the potential energy surface is concave). Programs are written in CDC Fortran, this being slightly more flexible than standard Fortran IV. Both the CDC FORTRAN Extended Compiler (FTN) and Minnesota Fortran (MNF) are used to compile the programs. Library subroutines from the IBM Scientific Subroutine Package (SSP) are used in the Growth Program, whilst comprehensive use is made of both the Dimfilm and the Microfilm facilities at U.L.C.C. to provide, respectively, much of the graphical output and the displays of various isomeric forms.

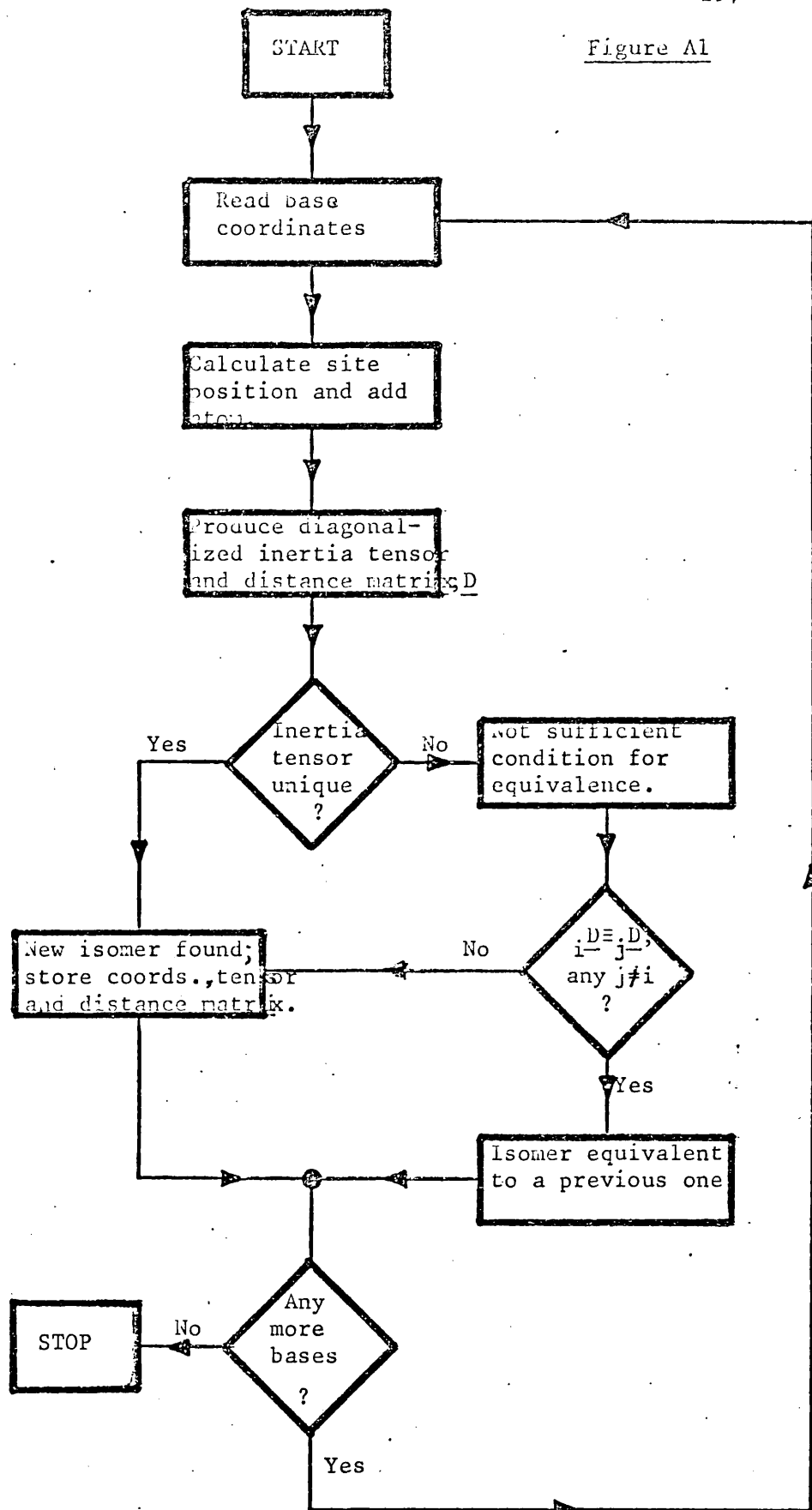
A.2

Full descriptions of the Growth, Optimization, and Vibrational Analysis Programs are contained in the relevant Chapters. Flow diagrams for these three programs are presented in Figures (A1) to (A3).

A.3

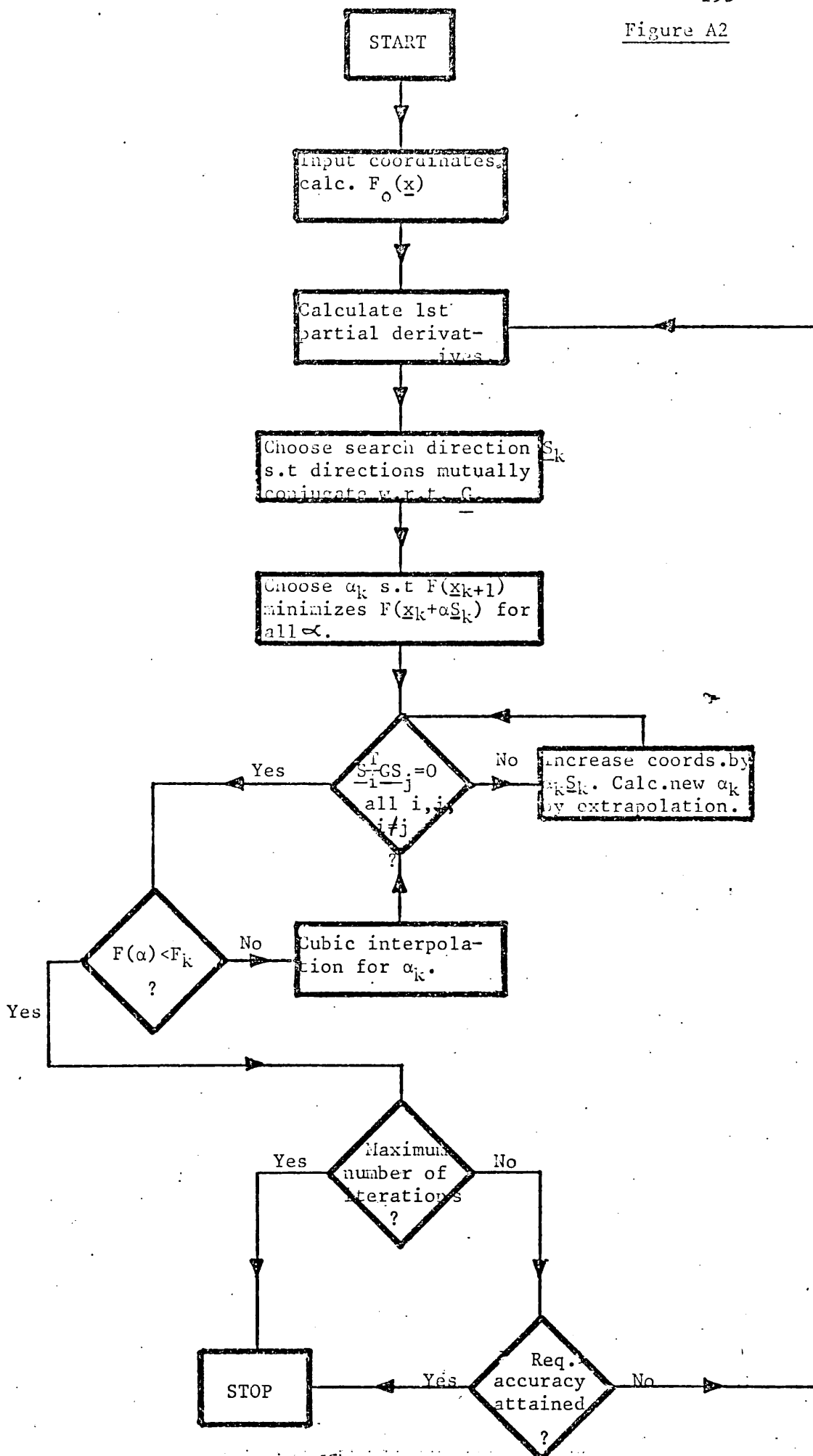
Specially written packages have been prepared using the sophisticated Dimfilm and Microfilm facilities available at U.L.C.C. to produce graphs, drawings of different isomeric configurations, and stereo views of microclusters. These packages combine flexibility with great accuracy and high speed production, and are invaluable for the reproduction of fine detail. Images on a cathode ray tube are photographed using 16mm or 35mm film: the developed film may then be used to produce either photographic plates or prints on photosensitive paper. Detailed information on the use of Dimfilm and Microfilm may be found in the U.L.C.C. Dimfilm and Microfilm manuals.

Figure A1



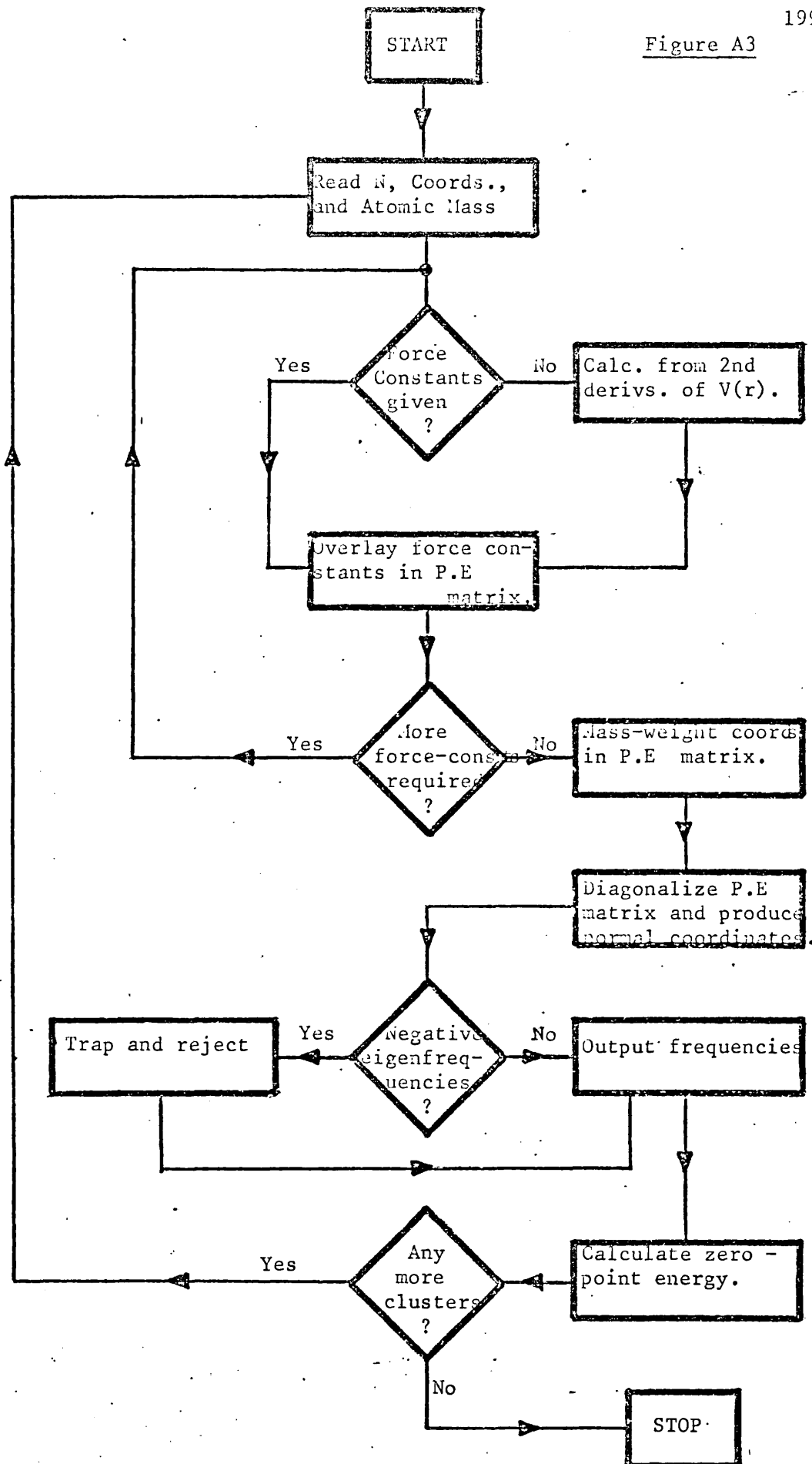
Flow Diagram of Growth Program

Figure A2



Flow Diagram of Optimization Program

Figure A3



Flow Diagram of Vibrational Analysis Program

Appendix B

Vibrational Multiconfigurational Thermodynamic Functions

The derivations of the explicit MC vibrational formulae, equations (5.17) to (5.20), are presented below.

Separating the exponential term implicitly included in equation (5.16) (see eq. (5.1)), the vibrational MCPF may be written

$$Z_{v,mc}^{(N)} = \sum_{i=1}^c Z_{v,sc}^{(N)}(i) \cdot e^{-\frac{E_{o,i}}{kT}} \quad (B.1)$$

where $E_{o,i}$ is the energy of the i^{th} minimum about which vibration occurs, and other terms are as previously defined. For explicit substitution of (B.1) into the standard formulae (5.2) to (5.5) it is apparent that the first and second derivatives of

$$\ln \sum_{i=1}^c Z_{v,sc}^{(N)}(i) \cdot e^{-E_{o,i}/kT}$$

with respect to temperature, are required.

$$\text{Let } \beta_{j,i} = Z_{v,sc}^{(N)}(i) \text{ and } \gamma_i = e^{-E_{o,i}/kT} \quad (B.2)$$

with $Z_{v,sc}^{(N)}(i)$ given by $\prod_j \alpha_{j,i}$ (see equations (5.6) and (5.21))

then the problem is an explicit evaluation of

$$\frac{\partial}{\partial T} \ln \sum_{i=1}^c \prod_j \alpha_{j,i} \gamma_i \quad (B.3)$$

and

$$\frac{\partial^2}{\partial T^2} \ln \sum_{i=1}^c \prod_j \alpha_{j,i} \gamma_i \quad (B.4)$$

For the first derivative:

$$\frac{\partial}{\partial T} \ln \prod_{i=1}^c \sum_j \Pi_{j,i} \alpha_{j,i} \gamma_i = \left\{ \prod_{i=1}^c \sum_j \Pi_{j,i} \alpha_{j,i} \gamma_i \right\}^{-1} \cdot \frac{\partial}{\partial T} \left[\prod_{i=1}^c \sum_j \Pi_{j,i} \alpha_{j,i} \gamma_i \right] \quad (\text{B.5})$$

The derivative on the right-hand side of (B.5) may be written

$$\frac{\partial}{\partial T} \left[\prod_{i=1}^c \sum_j \Pi_{j,i} \alpha_{j,i} \gamma_i \right] = \sum_{i=1}^c \left\{ \gamma_i \frac{\partial}{\partial T} \left[\prod_j \Pi_{j,i} \alpha_{j,i} \right] + \prod_j \Pi_{j,i} \alpha_{j,i} \frac{\partial}{\partial T} \gamma_i \right\} \quad (\text{B.6})$$

On performing the differentiation we find

$$\frac{\partial \gamma_i}{\partial T} = -\exp \left[\frac{|E_{o,i}|}{kT} \right] \cdot \frac{|E_{o,i}|}{kT^2} \quad (\text{B.7})$$

$$\frac{\partial}{\partial T} \left(\prod_j \Pi_{j,i} \alpha_{j,i} \right) = \prod_j \Pi_{j,i} \alpha_{j,i} \times \left(\sum_{i=1}^{3N-6} \frac{\partial \alpha_i}{\partial T} \cdot \frac{1}{\alpha_i} \right)$$

where α_i and $\partial \alpha_i / \partial T$ are given by equations (5.21) and (5.22) respectively. Use of equations (B.7) in (B.6) and the use of the resulting equation in (B.5) leads to an explicit formulation of (B.3) ie.

$$\frac{\partial}{\partial T} \ln \prod_{i=1}^c \sum_j \Pi_{j,i} \alpha_{j,i} \gamma_i = \frac{\sum_{i=1}^c \left\{ e^{-E_{o,i}/kT} \cdot \prod_j \Pi_{j,i} \alpha_{j,i} \times \sum_{i=1}^{3N-6} \left(\frac{\partial \alpha_i}{\partial T} \cdot \frac{1}{\alpha_i} \right) - \prod_j \Pi_{j,i} \alpha_{j,i} \frac{|E_{o,i}|}{kT^2} e^{-E_{o,i}/kT} \right\}}{\prod_{i=1}^c \sum_j \Pi_{j,i} \alpha_{j,i} \gamma_i} \quad (\text{B.8})$$

For the second derivative:

expressing (B.8) in terms of β , γ , and α , with their associated derivatives we obtain

$$\frac{\partial}{\partial T} \ln \prod_{i=1}^c \sum_j \beta_{j,i} \gamma_i = \frac{\sum_{i=1}^c \left(\gamma_i \frac{\partial \beta_{j,i}}{\partial T} + \beta_{j,i} \frac{\partial \gamma_i}{\partial T} \right)}{\prod_{i=1}^c \sum_j \beta_{j,i} \gamma_i} \quad (\text{B.9})$$

Differentiating (B.9) again with respect to T leads to an expression for $\frac{\partial^2}{\partial T^2} \ln \sum_{i=1}^c \beta_{j,i} \gamma_i$ in terms of β , γ and α , with combinations of the 1st and 2nd derivatives of these terms.

Explicitly:

$$\frac{\partial^2 \ln z_{v,mc}^{(N)}(i)}{\partial T^2} = \frac{\sum_{i=1}^c \left\{ \gamma_i \frac{\partial^2 \beta_{j,i}}{\partial T^2} + \beta_{j,i} \frac{\partial^2 \gamma_i}{\partial T^2} + 2 \frac{\partial \gamma_i}{\partial T} \frac{\partial \beta_{j,i}}{\partial T} \right\}}{\sum_{i=1}^c \beta_{j,i} \gamma_i} + \left[\sum_{i=1}^c \left\{ \gamma_i \frac{\partial \beta_{j,i}}{\partial T} + \beta_{j,i} \frac{\partial \gamma_i}{\partial T} \right\} \right] \times (-1) \left[\sum_{i=1}^c \beta_{j,i} \gamma_i \right]^{-2} \sum_{i=1}^c \left\{ \beta_{j,i} \frac{\partial \gamma_i}{\partial T} + \gamma_i \frac{\partial \beta_{j,i}}{\partial T} \right\} \quad (\text{B.10})$$

Inspection of (B.10) reveals a dependence on the 2nd derivatives of β and γ in addition to β , $\partial \beta / \partial T$, γ , $\partial \gamma / \partial T$.

$$\frac{\partial^2 \gamma_i}{\partial T^2} = \frac{-\partial \gamma_i}{\partial T} \cdot \left\{ \frac{|E_o|}{kT} + 2 \right\} / T = e^{-E_{i^o}/kT} \frac{|E_o|_i}{kT^3} \left\{ \frac{|E_o|_i}{kT} + 2 \right\} \quad (\text{B.11})$$

Using the 2nd line of (B.7) produces

$$\frac{\partial^2 \beta_{j,i}}{\partial T^2} = \frac{\partial \beta_{j,i}}{\partial T} \times \sum_i^{3N-6} \frac{\partial \alpha_i}{\partial T} \cdot \frac{1}{\alpha_i} + \beta_{j,i} \sum_{i=1}^{3N-6} \left\{ \frac{\partial^2 \alpha_i}{\partial T^2} \cdot \frac{1}{\alpha_i} - \frac{\partial \alpha_i}{\partial T} \frac{1}{\alpha_i^2} \right\} \quad (\text{B.12})$$

where $\partial^2 \alpha_i / \partial T^2$ is given by equation (5.23).

Use of equations (B.2), (B.7), (B.11) and (B.12) for $\beta_{j,i}$, γ_i , $\frac{\partial \beta_{j,i}}{\partial T}$, $\frac{\partial \gamma_i}{\partial T}$, $\frac{\partial^2 \gamma_i}{\partial T^2}$ and $\frac{\partial^2 \beta_{j,i}}{\partial T^2}$ respectively in equation (B.10) leads

to a formal representation of $\partial^2/\partial T^2 \ln Z_{v,mc}^{(N)}(i)$. Algebraic manipulation of the β s and γ s with their associated 1st and 2nd derivatives leads to the set of multiconfigurational vibrational equations for vibrational free energy, internal energy, entropy and heat capacity presented in equations (5.17) to (5.20).

Appendix C

Cluster Distributions in Configuration Space

The distances in $3N$ -space separating the most stable N -atom cluster from the other members of that set of minima are calculated according to equation (C.1) for the Lennard-Jones structures, with $8 < N < 10$.

$${}_j d_N^2 = \sum_{i=1}^N \left[(x_i - x_j)^2 + (y_i - y_j)^2 + (z_i - z_j)^2 \right] \quad (\text{C.1})$$

In equation (C.1) $\{X\}$, $\{Y\}$ and $\{Z\}$ are the Cartesian coordinates of the most stable cluster and the ${}_j\{x\}$, ${}_j\{y\}$ and ${}_j\{z\}$ are the coordinates of the j^{th} minimum.

The diagrams in Figure C1 indicate a mild correlation between these distances and the energy ratio $r_a = \frac{e_i}{E}$, where e_i is the cluster energy and E is the energy of the most stable cluster. For each N value the set of distances is statistically analyzed and the results presented in Table C1.

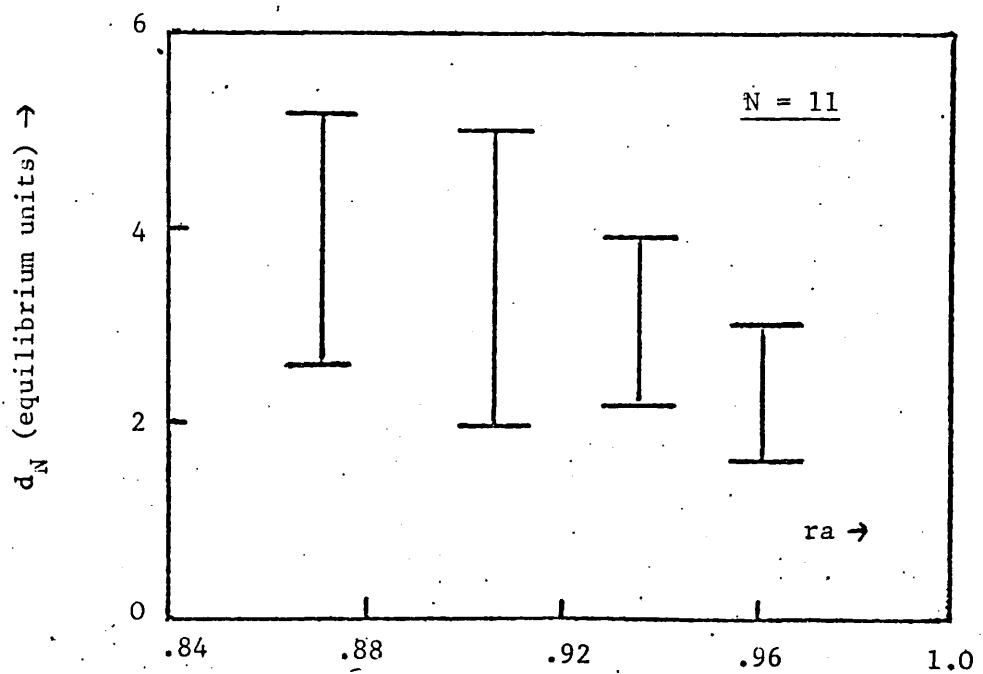
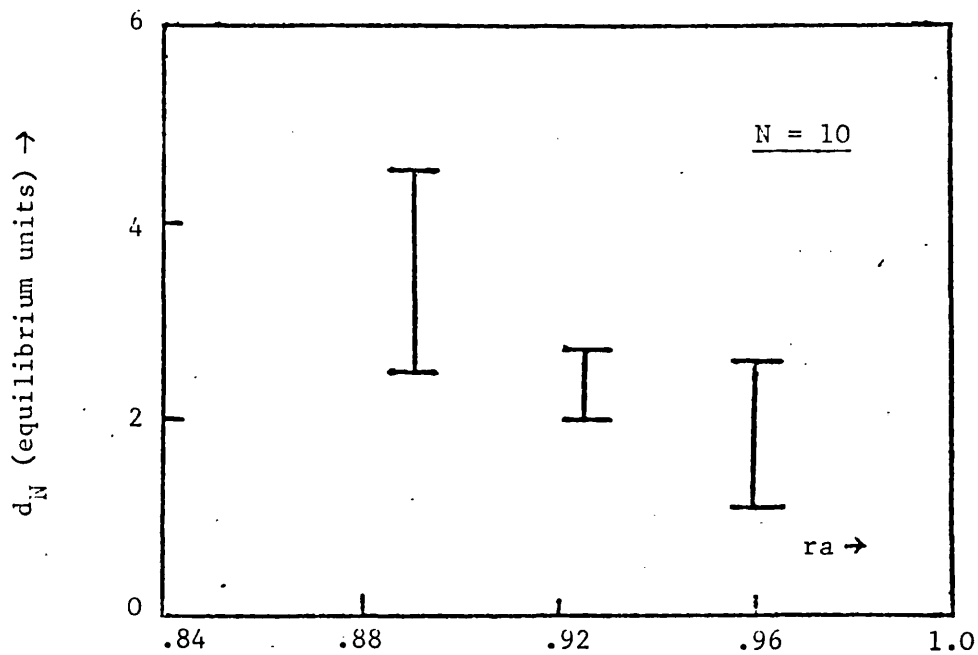
Table C1

N	$\overline{r_a}$	\overline{d}_N	Standard deviation in $\{d\}_N$	Skewness	Kurtosis
9	.939	2.66	0.74	0.07	- 1.35
10	.923	2.86	0.97	0.46	- 0.89
11	.916	3.39	0.95	0.51	- 0.86

We see from this table that the mean distance \overline{d}_N increases with N , as expected since \overline{d}_N is a function of N , whilst the mean energy ratio

\overline{ra} decreases comparatively slowly. With increasing N the distribution of distances becomes more skewed but less platykurtic. It seems that those clusters energetically near the most stable cluster also tend to be near this structure in configuration space.

Figure C1



The Distribution of Clusters in Configuration Space

Appendix DStandard Gibbs Free Energies of FormationTable D1

N/T^*	Neon $G_f^{\circ}(N, T^*, 1)$ Joules $\times 10^{21}$									
	.1	.2	.3	.4	.5	.6	.7	.8	.9	1.0
2	-.182	-.019	+.178	.397	.625	.858	1.102	1.348	1.599	1.851
3	-.578	-.180	+.294	.804	1.335	1.886	2.441	3.004	3.565	4.144
4	-1.164	-.425	+.438	1.360	2.305	3.274	4.248	5.230	6.213	7.205
5	-1.857	-.838	+.350	1.612	2.913	4.227	5.564	6.894	8.239	9.577
6	-2.568	-1.176	+.425	2.127	3.431	5.398	7.418	9.402	10.989	12.786
7	-3.532	-1.849	+.070	2.090	4.158	6.269	8.345	10.450	12.558	14.671
8	-4.403	-2.542	-.407	+1.845	4.149	6.483	8.829	11.182	13.525	15.877
9	-5.421	-3.170	-.634	+2.016	4.723	7.463	10.208	12.965	15.715	18.464
10	-6.500	-3.874	-.942	+2.092	5.173	8.274	11.389	14.512	17.630	20.745
11	-7.648	-4.728	-1.474	+1.900	5.334	8.792	12.261	15.724	19.198	22.653
12	-9.080	-5.709	-1.860	+2.071	5.971	9.854	13.743	17.624	21.500	25.364
13	-10.796	-6.937	-2.494	+2.179	6.822	11.303	15.724	20.112	24.494	28.867

Table D2

	Argon	$\Delta G_F^O(N, T^*, 1)$	Joules $\times 10^{21}$							
N/T^*	.1	.2	.3	.4	.5	.6	.7	.8	.9	1.0
2	-.905	-.134	+.697	1.561	2.441	3.361	4.259	5.227	6.159	7.094
3	-2.904	-1.015	+.982	3.016	5.071	7.156	9.239	11.369	13.483	15.634
4	-5.888	-2.406	+1.188	4.820	8.445	12.093	15.737	19.399	23.035	26.689
5	-9.250	-4.398	+.582	5.574	10.581	15.568	20.556	25.510	30.462	35.458
6	-12.900	-6.269	+.445	7.166	13.840	20.506	27.135	35.094	40.357	45.931
7	-17.324	-9.259	-1.143	+6.899	14.853	22.770	30.621	38.463	46.242	54.024
8	-21.326	-12.242	-3.097	+5.947	14.894	23.777	32.615	41.375	50.138	58.833
9	-26.085	-15.164	-4.319	+6.320	16.820	27.230	37.567	47.851	58.045	68.212
10	-31.027	-18.398	-5.839	+6.357	18.328	29.951	42.760	54.206	65.095	76.600
11	-36.174	-22.020	-8.010	+5.557	18.883	32.055	45.100	58.062	70.911	83.373
12	-42.422	-26.404	-10.146	+5.702	20.965	35.736	50.372	64.874	75.230	93.529
13	-50.045	-31.786	-13.174	+5.359	23.460	40.673	57.297	73.665	91.581	105.992

Table D3

	Krypton $\Delta G_f^{\circ}(N, T^*, 1)$ Joules $\times 10^{21}$									
N/T^*	.1	.2	.3	.4	.5	.6	.7	.8	.9	1.0
2	-1.311	-.143	+1.100	2.390	3.685	5.040	6.402	7.786	9.156	10.585
3	-4.243	-1.363	+1.596	4.607	7.644	10.700	13.792	16.919	20.024	23.181
4	-8.636	-3.365	+1.962	7.301	12.662	17.991	23.352	28.705	34.072	39.419
5	-13.579	-6.226	+1.154	8.518	15.859	23.194	30.476	37.795	45.037	52.287
6	-18.983	-8.934	+1.031	10.908	20.714	30.453	40.188	50.016	59.525	69.177
7	-25.469	-13.241	-.023	+10.624	22.334	33.927	45.448	56.889	68.290	79.653
8	-31.347	-17.515	-3.945	+9.383	22.542	35.576	48.539	61.413	74.217	86.976
9	-38.355	-21.746	-5.650	+10.034	25.467	40.747	55.892	70.938	85.916	100.768
10	-45.613	-26.422	-7.762	+10.207	27.767	45.135	62.293	79.332	96.295	113.147
11	-53.175	-31.653	-10.837	+9.162	28.735	48.055	67.173	86.161	105.011	123.732
12	-62.341	-37.611	-13.895	+9.443	31.796	53.552	74.982	96.208	117.248	138.176
13	-73.534	-45.811	-18.242	+9.007	35.564	60.778	85.112	109.081	132.813	156.371

Table D4

	Xenon	$\Delta G_f^{\circ}(N, T^*, 1)$ Joules $\times 10^{21}$								
N/T^*	.1	.2	.3	.4	.5	.6	.7	.8	.9	1.0
2	-1.757	-.267	+1.298	2.925	4.558	6.267	7.985	9.733	11.462	13.268
3	-5.636	-1.968	+1.795	5.624	9.467	13.335	17.249	21.208	25.138	29.065
4	-11.418	-4.666	+2.123	8.914	15.712	22.511	29.266	36.111	42.859	49.710
5	-17.924	-8.474	+.934	10.293	19.637	28.946	38.235	47.473	56.724	65.928
6	-25.028	-12.099	+.609	13.190	25.671	38.122	50.449	62.770	75.078	87.275
7	-33.543	-17.790	-2.413	+12.658	27.559	42.281	56.959	71.491	86.035	100.473
8	-41.250	-23.452	-6.110	+10.890	27.621	44.207	60.665	77.008	93.261	109.456
9	-50.447	-29.044	-8.458	+11.510	31.161	50.601	69.880	88.989	108.011	126.939
10	-59.973	-35.212	-11.354	+11.541	33.928	55.982	77.865	99.565	121.054	142.525
11	-69.879	-42.111	-15.473	+10.025	34.973	59.552	83.883	108.005	131.947	155.794
12	-81.886	-50.471	-19.612	+10.196	38.688	66.367	93.638	120.604	147.393	173.979
13	-96.534	-60.714	-25.416	+9.411	43.317	75.458	106.442	136.968	167.137	-97.153